The impact of influenza A virus protein phosphorylation and host cell protein kinases on viral replication

Inauguraldissertation
zur Erlangung des Grades eines Doktors der Humanbiologie (Dr.hum.biol.)
des Fachbereichs Medizin
der Justus-Liebig-Universität Gießen

vorgelegt von Liu, Lu
aus Hunan, China

Gießen, 2022

Aus dem Institut für Biochemie und dem Institut für medizinische Virologie
(Fachbereich Medizin)
der Justus-Liebig-Universität Gießen

Gutachter: Prof. Dr. M. Lienhard Schmitz

Gutachter: Prof. Dr. Stephan Pleschka

Tag der Disputation: 18.10.2022

TABLE OF CONTENTS

1 INTRODUCTION

1.1 Influenza viruses

Influenza viruses (IVs) belong to the family of *Orthomyxoviridae* and are classified as type A, B, C, or type D based on antigenic differences between their nucleocapsid (NP) and matrix proteins 1 (M1) (Kumar et al., 2018; Taubenberger et al., 2010). They are enveloped negative-strand RNA viruses with segmented genomes containing seven to eight gene segments. Before the COVID-19 pandemic, IVs were the leading cause of severe respiratory illness across the world and seasonal influenza viruses infect 5-15% of the global human population each year and result in ~650,000 deaths worldwide ((Stohr, 2002), https://www.who.int/news-room/fact-sheets/detail/influenza-(seasonal)). Infection with influenza A virus (IAV) or influenza B virus (IBV) accounts for the vast majority of the annual influenza burden. Compared to other types of IVs, IAV is the most pathogenic, causing seasonal epidemics and occasional pandemics due to the high degree of genomic plasticity and continued evolution that enables them to escape host immunity and adapt to new host species. Interestingly, a notable global reduction in influenza cases of both IAV and IBV has been seen in the SARS-CoV-2 pandemic due to the behavioral changes (social distancing, mask wearing, and hygiene measures) and travel and movement restrictions (Huang et al., 2021; Koutsakos et al., 2021). However, given that both IAV and SARS-CoV-2 have been co-circulating in the 2019/20/21/22 influenza seasons, and there have been documented cases of co-infections with these two viruses (Stowe et al., 2021; Yue et al., 2020), the impact of influenza alongside COVID-19 on morbidity and mortality will still be a major concern in the coming flu seasons.

1.1.1 Classification of IAV

According to the antigenic properties of the two major surface glycoproteins - hemagglutinin (HA) and neuraminidase (NA), IAVs are further grouped into 16 HA (H1-H16) and 9 NA (N1-N9) subtypes. Wild aquatic birds are the main natural reservoir for IAVs, from which all 16 HAs and 9 NAs have been isolated (Mostafa et al., 2018), whereas bats have recently been shown to harbor IAV-like viruses of the H17N10 and H18N11 subtype (Tong et al., 2013).

Avian influenza virus (AIV) infection is usually asymptomatic (Taubenberger & Kash, 2010), while some of the H5- and H7-type AIVs cause deadly, systemic disease (highly-pathogenic avian influenza virus [HPAIV]) and can cross to new species, occasionally infecting humans). Despite the high lethality of HPAIV, these strains typically do not show significant human-to-human transmission (Taubenberger & Kash, 2010). For example, the human H5N1 AIV isolate KAN-1 (A/Thailand/1(KAN-1)/2004) originating from an H5N1-HPAIV outbreak in Thailand in 2003 (Bao et al., 2008), is highly pathogenic in mice and ferret models (Govorkova et al., 2005; Manz et al., 2010). IAVs also circulate in a wild range of other host species, including marine mammals, poultry, and domestic mammals (whale, seal, swine, horses, dogs, cats). Human IAVs originate from birds and swine and only three IAV subtypes have been found to circulate in the human population causing several pandemics - 1918 and 2009 (H1N1), 1957 (H2N2), and 1968 (H3N2). Of these, A/H1N1$_{pdm09}$ and A/H3N2 subtype viruses currently cause seasonal influenza virus epidemics (Joseph et al., 2017).

1.1.2 Virus morphology

The eight genomic segments of IAV encode at least 10 viral proteins: polymerase basic protein 2 (PB2, segment 1), polymerase basic protein 1 (PB1, segment 2), polymerase acidic protein (PA, segment 3), HA (segment 4), nucleoprotein (NP, segment 5), NA (segment 6), matrix protein (M1 and its splicing product M2, segment 7), and non-structural protein (NS1 and its splicing product NS2 or nuclear export protein (NEP), segment 8) (Pleschka, 2013).

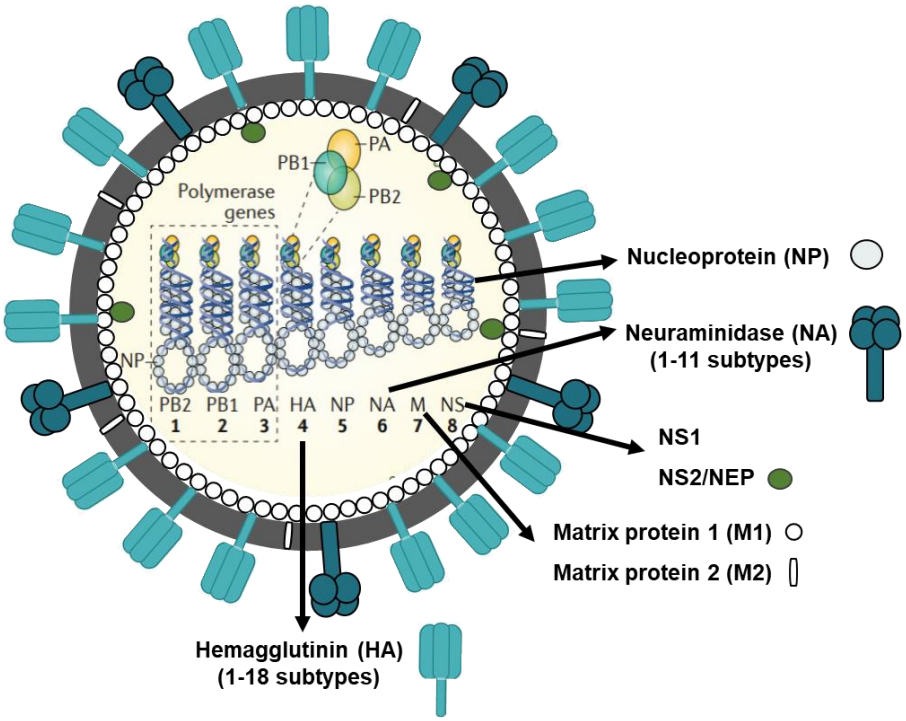

Figure 1: Structure of IAV.

The envelope of the IAV particle, which is derived from the host cell plasma membrane, contains three trans-membrane proteins; two surface glycoproteins designated as HA and NA, and the proton channel protein M2. The M1 underlies the inner surface of the viral envelope and associates with NEP and viral ribonucleoprotein complexes (vRNPs). The eight vRNPs comprise eight negative-strand RNA segments associated with the NP and three RdRp polymerase subunits (PA, PB1, PB2). Modified from (Krammer et al., 2018; Mostafa et al., 2018).

IAV particles are pleomorphic, presenting filamentous and spherical virions. Most of the clinically isolated IAVs exhibit filamentous particles, with a diameter reaching 80-100 nm, and an average length of 250 nm that is sometimes longer than 30 µm (Dadonaite et al., 2016). While upon passaging in eggs or MDCK II cells, laboratory-adapted IAV strains appear spherical and in elliptical virion shapes, with diameters ranging from 80 nm to 120 nm (Dadonaite et al., 2016). As illustrated in **Fig. 1**, IAV has a complex structure with a lipid bilayer envelope derived from the host cell membrane. The exterior of the IAV envelope is densely packed by the membrane-anchored glycoproteins HA, NA, and to a lesser extent the M2. The inner surface of the IAV envelope is tightly associated with M1, which interacts with viral vRNPs and the cytoplasmic tails of the viral glycoproteins HA and NA (Rossman et al., 2011). Each monomer of the trimeric HA in viral envelope consists of two disulfide-linked domains, HA1 and HA2. HA (550 aa) is transcribed initially as an inactive precursor molecule (HA0). HA0 is post-translationally glycosylated and cleaved into the HA1 and HA2 subunits to perform its fusion activity for membrane fusion (Garten et al., 1981). The larger part of the global head of the virus membrane

distal HA1 contains the receptor-binding site for specific sialic-acid moieties on the host cell to mediate viral entry; the smaller membrane-proximal HA2 forms a stalk domain and contains the fusion peptide, a region that bridges between the viral and endosomal membranes during entry after receptor-binding (Benton et al., 2020). The proteolytic cleavage of the HA0 is processed by proteases, which can recognize a single Arg or a Lys residue in a monobasic, dibasic, and tribasic cleavage site motif, with basic amino acids occurring once, twice, and three times, respectively, and varies between viral strains (Kido et al., 2008; Zhang et al., 2021). Except for the zoonotic H5/H7-type AIV, which possess a R-E-T-R or P-K-X-R cleavage site motif in the HA0, the other IAV including seasonal human H1/H3-type IAV have the consensus cleavage site motif Q(E)-T/X-R (Kido et al., 1999; Tsukamoto et al., 2008), which can be selectively recognized by several extra-cellular trypsin-type proteases from epithelial cells of the respiratory tract (Kido et al., 1999). As for the HPAIV (H5- and H7-subtypes), endoproteolytic processing of the HA0 occurs through ubiquitously expressed intra-cellular proprotein convertase “furin” and furin-like proteases (Stieneke-Grober et al., 1992), which selectively recognize the multi-basic consensus cleavage site motifs, such as R-X-K/R-R, and K-X-K/R-R, resulting in release of fully activated virions and severe systemic infection and rapid death of animals (Luczo et al., 2015). Therefore, the type of cleavage sites and the presence of HA-activating proteases in host cells is a major determinant for virus tropism and pathogenicity.

NA (454 aa) forms a homotetramer that is decorated in a mushroom shape on the viral envelope with a head domain, stalk domain, transmembrane domain (TMD), and cytoplasmic tail (**Fig. 1**) (Creytens et al., 2021). The primary function of NA is to act as a catalytic sialidase, releasing newly formed virions by cleaving sialic acids from glycoconjugates on the host cells (Benton et al., 2017; Creytens et al., 2021). In addition, certain subtypes of NA, particularly N7, possess receptor binding properties like HA, which are attributed to both a sialic acid binding site known as hemadsorption (Hb) site and an intrinsic sialidase activity (Uhlendorff et al., 2009). NA inhibitors, such as Relenza™ (zanamivir), Tamiflu™ (the phosphate salt of oseltamivir), Inavir™ (zanamivir octanoate), and Rapivab™ (peramivir), belong to one of the groups of anti-viral drugs currently available for treatment or prevention of influenza infections (Shie et al., 2019).

Another class of anti-IAV drugs target the M2 protein, a homotetrameric molecule embedded in the viral envelope, where it is arranged in a smaller proportion than HA and NA (approximately 16 to 20 molecules in a virus, compared to ca.300-400 HA and 50 NA copies) (Petrich et al., 2021; Samji, 2009). The M2 (54 aa, at nucleotide position 26 to 51 and 740 to 1007 of M) is encoded by a splice product of the M mRNA (1027 bp). M2 mainly functions as a proton channel activated by acidic pH in the endosomes and

leads to a proton influx lowering the virion-internal pH during virus entry resulting in the genome unpacking. M2 is also indispensable for virus replication, whereby M2 activity regulates transmembrane pH gradients in the trans-Golgi and stabilizes the conformation of the pH-sensitive H5/H7-type HAs (Alvarado-Facundo et al., 2015; Takeuchi et al., 1994). The M1 protein is translated from the unspliced M gene mRNA (252 aa, at nucleotide position 26 to 784 of M), and is underlying the viral envelope supporting viral morphology and integrity. As the most abundant protein in influenza virions, it has intrinsically versatile functions including a role in the nuclear export of vRNPs, uncoating viral particles, and assembly of virions (Krammer et al., 2018; Stauffer et al., 2014). M1 consists of an N- and C-terminal domain (NTD and CTD, respectively) (Sha et al., 1997), and is distributed in the cytosol and nucleus of infected cells. The nuclear localization of M1 is achieved by its nuclear localization signal (NLS), where M1 likely bridges the NEP and vRNPs, forming a complex that is in turn exported from the nucleus by the nuclear export sequence (NES) located in the N terminus of NEP (residues 12 to 21) (Cao et al., 2012; Ye et al., 1995). Another key role of M1 is its ability to recruit viral components at the budding site at the late stage of the IAV infection, which is in accordance with the fact that M1 interacts with cytoplasmic tails of HA, NA, M2, and the vRNPs (Ye et al., 1999). Along this line, the presence of the influenza M segment genes (M1 and M2) together with HA and NA are sufficient to induce the assembly of virus-like particles (VLPs) that structurally resemble native virions (Chlanda et al., 2015).

The vRNP consists of three subunits of the heterotrimeric RNA-dependent RNA polymerase (RdRp) complex including PB2 (759 aa), PB1 (757 aa) and PA (716 aa) subunits, and a NP (550 aa)-packed viral genome segment (**Fig. 1**) (Ye et al., 1999). In the context of the vRNP, the RdRp catalyzes the transcription and replication of the viral RNA. This highly flexible enzyme complex exhibits cap-binding, endonuclease, RNA-dependent RNA polymerase, and polyadenylation activities, supported by the concise interplay between each component (Wandzik et al., 2021). As shown in **Fig. 2**, the cap-binding activity of RdRp comes from the recognition of 5’ cap of methylated guanosine of host pre-mRNA by the PB2 cap-binding domain (residues 320-485). This directs the cleavage of the capped primer for the cap-snatching, a process in which the PA endonuclease (NTD resides 1-195) cleaves the cellular mRNA resulting in a 10-13 nucleotide primer used for viral transcription start. Finally, the catalytic core of the PB1 generates the capped-mRNA (Fodor, 2013; Pflug et al., 2018). Importantly, the RdRp activity is a major viral determinant of IAV pathogenicity and species specificity. The PB2 residue 627 is a good example of determining the host range (Subbarao et al., 1993). AIVs contain a Glu (E) at position 627 whereas this residue is commonly a Lys (K) in mammalian-adapted IAVs. Therefore, the PB2 E627K mutation is one of the

characteristic adaptaions for IAV, and it can be found in all circulating human IAVs of the 20th century, including the 1918 H1N1, 1957 H2N2, and 1968 H3N2 pandemic viruses (Taubenberger et al., 2005). Furthermore, PB2 residues 701 and 702 of the NLS domain are also strongly implicated in host adaptation. Atomic-resolution crystal data have suggested that within the RdRp complex, the PB1 is the central body connecting both PB2 and PA (**Fig. 2**). The PB1 exhibits the classic right-handed polymerase structure with a finger, a palm, and a thumb. The C-terminal subunit of PB1 is associated with the N-terminal 247 residues of the PB2 subunit, which forms the thumb side and triggers PA endonuclease activity. On the finger side, it is decorated by three consecutive short helices of the PA linker (196-257) that wrap around PB1 and connect the PA-N endonuclease to PA-C domain (258-714) (Pflug et al., 2014).

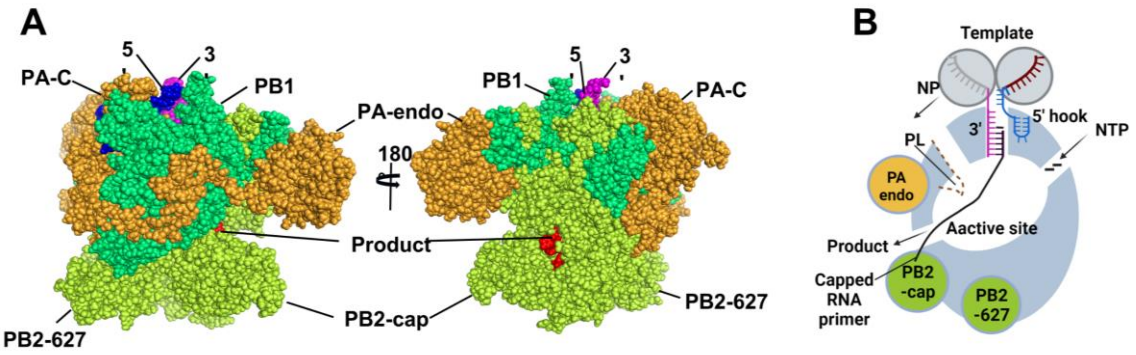

Figure 2: Structure of IAV polymerase.

(A) Surface presentation of the IAV RdRp (PDB 6RR7, PA: orange, PB1: green, PB2: lemon) bound to a capped mRNA primer and 5' and 3' vRNA termini (dark blue and pink respectively). The figure was generated by Pymol. **(B)** Schematic model for Figure A, presenting the active site of the polymerase, which is located at the edge of a large central cavity that is formed by PB1 and the N-terminus of PB2, and its connection to the solvent via template and nucleotide triphosphate (NTP) entry channels and product exit channels. The location of the priming loop (PL), as well as the 3' and 5' end hook of the vRNA, are indicated. Parts of the figure were created with BioRender.com. Modified from (Fodor et al., 2020).

Apart from the RdRp subunits, the vRNPs include vRNAs that are stoichiometrically wrapped around repeated NP subunits (approximately one NP molecule per 24 nucleotides) (Eisfeld et al., 2015). This structure of vRNP is highly dependent on NP oligomerization, in which extensive intermolecular contacts are formed between individual NP molecules and between NP and the genomic vRNA (Mondal et al., 2015). The NP (550 aa) molecule shows a crescent shape with a head domain (residues 150-276 and 429-452) and a body domain (residues 1-149 and 277-386) comprised of mainly alpha helices and beta strands (Tang et al., 2021) (**Fig. 3**). The tail-loop structure within residues 402-428 protruding outwards of the head domain, projects the NP

oligomerization with extensive interactions with the binding groove, particularly creating a salt bridge between residues 339 and 416 on different NP monomers (Shen et al., 2011). Self-assembly of NP is further facilitated by binding to the vRNA, which is attributed to the positive RNA binding groove of NP formed by a group of conserved residues on the surface of NP within the tail loop (Ye et al., 2006). Given the critical role of RdRp in viral replication, an antiviral drug that targets the PA endonuclease activity, baloxavir marboxil (Xofluza^{TM}) has also been clinically approved, and many of RdRp Inhibitors are in clinical trials (Giacchello et al., 2021).

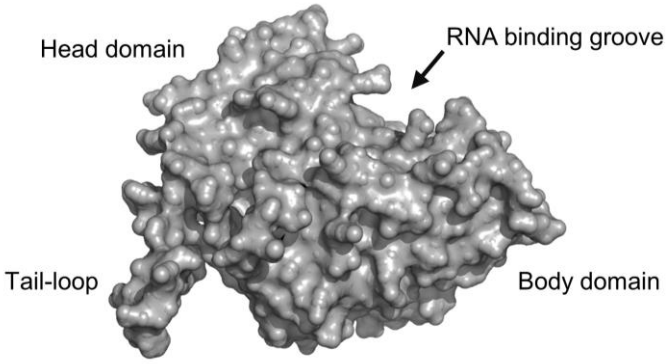

Figure 3: Structure of IAV NP.

Surface presentation of the H1N1 IAV NP monomer (PDB code: 2IQH) showing the head and body domains, Tail-loop, and the RNA binding groove. The figure was generated by Pymol.

The shortest vRNA segment of IVA encodes the NS1 (230 aa), NEP (121 aa), and NS3 (187 aa). NS1 is the product of the full-length mRNA, and forms a homodimer with two functional domains - double-stranded RNA binding domain (residue 1-73) and effector domain (residue 85-207), interspersed by a flexible linkage region. NS1 has been well known as an important immunomodulatory factor counteracting host interferon (IFN) responses through multiple mechanisms, including restricting the activation of retinoic acid-inducible gene 1 (RIG-I) pathway and the production of IFN-inducible proteins (Opitz et al., 2007; Price et al., 2000). Thus, the occurrence of NS1 in the early phase of infection with a continuous increase may reflect its importance in antagonizing the antiviral response of the host cell to ensure viral replication. In contrast, the NEP is translated from the spliced NS mRNA and expressed at the later stages of infection, mediating the nuclear export of vRNPs into the cytoplasm (Jaiswal et al., 2020; Neumann et al., 2000). Recently, many additional non-structural proteins of IAV (NSPs) have been discovered, including PA-X (Jagger et al., 2012), PB1 frame 2 (PB1-F2), PB1-N40 (Wise et al., 2009), PA-N155 (Muramoto et al., 2013), PA-N182 (Muramoto et al., 2013), M42 (Wise et al., 2012) and NS3 (Selman et al., 2012). Most of them are the product of viral

mRNA splicing, frameshift, and truncation of the coding region of IAV structural proteins, with implications in modulating viral replication, host defense suppression, virulence, and pathogenicity (Hao et al., 2020).

1.1.3 IAV life cycle

The IAV life cycle is divided into several consecutive steps (**Fig. 4**), namely (1) cell entry by clathrin-dependent and -independent mechanism, (2) membrane fusion and virus uncoating, (3) viral genome replication/transcription, (4) translation/post-translational processing of viral proteins, (5) virus assembly and genome packaging, (6) virus release and proteolytic activation of HA.

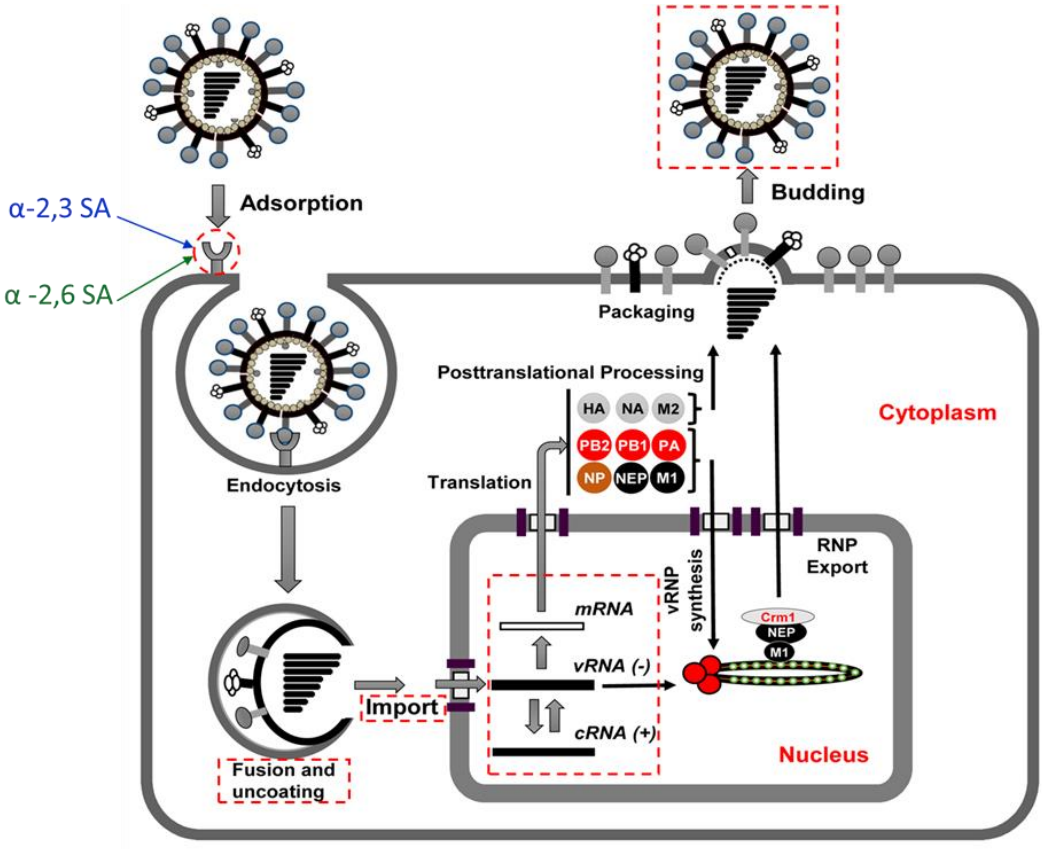

Figure 4: The IAV replication cycle.

The IAV HA recognizes and binds to the sialic acid receptor on the host-cell surface. Using clathrin-dependent and -independent endocytosis, the IAV is incorporated in an endosome for uptake into the host cell. The low pH (5.5-5.0) of the later endosome leads subsequently to the fusion of viral and endosomal membrane and release of the vRNP into the cytoplasm. The vRNP is transported into the nucleus to transcribe and replicate the viral genome. The newly synthesized viral mRNAs of the eight viral segments are transferred to the cytoplasm to start viral protein synthesis. A part of the viral proteins (HA, NA, and M2) undergo post-translational modifications (PTMs) and then are transported to the host cell membrane. Other

viral proteins (PB2, PB1, PA, NP) are imported back into the nucleus to generate the new vRNPs and by the help of M1 and NEP nascent vRNPs leave the nucleus through Crm1-dependant nuclear export to the cytoplasm. After the assembly of the eight viral vRNPs at the host cell membrane where the viral surface proteins and M1 are arranged, mature virions bud from the cell surface and releases to begin another replication cycle. Adapted and modified from (Pleschka, 2013).

1.1.3.1 Receptor binding and cell entry

IAVs initiate the infection process by virion attachment to the host cell through the binding of HA to surface sialic acid (SA) receptors that are species-specific, as illustrated in **Fig. 4**. It is generally perceived that AIV HAs preferentially bind to α2-3-linked SA whereas the HAs of human-adapted IAV show a high affinity for α2-6-linked SA (Stevens et al., 2006). However, the respiratory tract of humans displays high numbers of “avian receptor” type SA (Walther et al., 2013), and the “human receptor” is also found in tracheal epithelia of several bird species (Ellstrom et al., 2009), suggesting the potential ability of IAVs to cross into species. Also, SA of both avian and human receptor types are found in pigs, rendering this species a mixing vessel, susceptible to both, human and avian strains.

1.1.3.2 Membrane fusion and virus uncoating

Virion attachment to the host cell triggers endocytosis of the virion via clathrin-dependent and -independent entry pathways, such as micropinocytosis (Mercer et al., 2009; Rossman et al., 2012). After virion internalization, IAVs travel from the early endosome to the late endosome. As shown in **Fig. 5**, the IAV uncoating proceeds in early endosomes, where the mildly acidic pH (pH 6.5-6.0) activates M2 channel activity, leading to the influx of protons and K^+ ions that further loosen interactions within the M1 core and between vRNPs, in a process called priming (Stauffer et al., 2014). Subsequently, the penetration of the primed core into the cytosol occurs by low pH-triggered (pH 5.5-5.0), HA-mediated membrane fusion in late endosomes (Maeda et al., 1981; Miyake et al., 2019). This process involves the conformation change of the pH-sensitive HA, exposing its fusion peptide of the HA2. HA2 is then inserted into the endosomal membrane, mediating the fusion of the endosomal and the viral membrane and ultimately the release of the viral core to the cytosol (Bullough et al., 1994). The second step of the uncoating of IAV takes place at the cytosolic surface or in the close vicinity of the late endosome, where the host factor histone deacetylase 6 (HDAC6) is recruited to promote breakup of the M1 shell (Banerjee et al., 2014). Further removal of

M1 from the surface of the vRNPs involves an importin kapβ2 (also called transportin-1 (TNPO1)), which binds to PY-NLS sequence motif exposed in the primed M1 (Lee et al., 2006; Miyake et al., 2019).

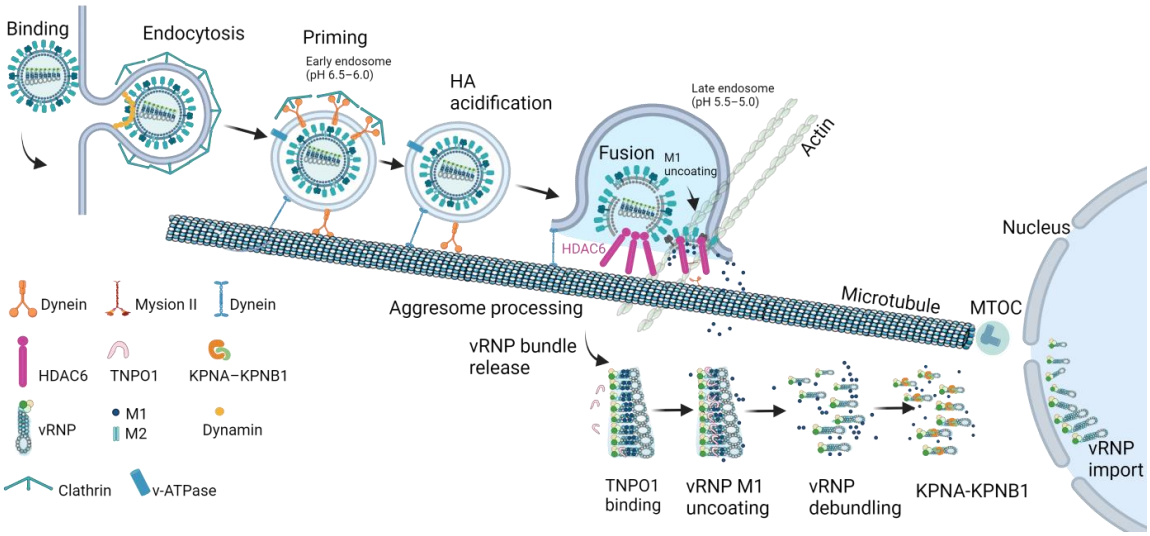

Figure 5: Schematic representation of stepwise IAV uncoating.

After viral uptake into endosomes, the M2 ion channels open, resulting in an influx of protons and K^+ ions that loosen interactions within the M1 core and between vRNPs. This induces the conformational change of M1 that exposes the PY-NLS close to the N terminus. Following the fusion of the viral-endosomal membranes by HA, the M1 core binds to the HDAC6 N terminus. Together with other components of the aggresome-processing machinery, such as the motors dynein and myosin II, microtubules, and actin filaments, HDAC6 facilitates M1 shell release from the endosome surface. After bundled vRNPs are released into the cytosol, TNPO1 associates with the PY-NLS exposed in the primed M1. TNPO1 removes residual M1 from the vRNP surface, which allows the dissociation of vRNPs from each other. KPNA and KPNB1 bind to the classical NLS in NP, resulting in the nuclear import of fully or partially debundled vRNPs. MTOC, microtubule-organizing center. The figure was adapted from (Miyake et al., 2019). Parts of the figure were created with BioRender.com.

1.1.3.3 Viral genome transcription/replication

The transcription and replication of the viral genome takes place when uncoated vRNPs are transported into the nucleus (Jackson et al., 1982; Walker et al., 2019). A pioneering round of primer-dependent transcription from the incoming RNPs is initiated before the replication. As shown in **Fig. 6**, this process involves the synthesis of capped and polyadenylated mRNA derived from template viral RNA (vRNA) segments by the viral RdRp. 5' terminal caps of viral mRNA are stolen from cellular mRNA by a cap-snatching mechanism. First, the viral polymerase binds to the carboxy-terminal domain of the host RNA polymerase II, promoting the association between viral polymerase and host

nascent RNA (Walker & Fodor, 2019). Second, the PB2 cap-binding domain binds the 5’ cap short oligonucleotide derived from the host mRNA, which is then downstream cleaved off by the PA endonuclease. Third, the 3’ end of the capped RNA primer flips in the polymerase active site where it base-pairs with the 3’ end of the vRNA template. This further promotes the transcription at the polymerase active sites on PB1 and follows the typical steps of initiation, elongation, termination, and recycling. Finally, the elongated viral transcription product terminates at a sequence motif of uridine residues near the 5’ end of the vRNA template, generating the addition of a poly(A) tail through RdRp stuttering (Fodor & Te Velthuis, 2020; Plotch et al., 1981). Synthesis of PB2, PB1, PA, NP and NS1 mRNAs takes place at the early stage of virus infection, whereas HA, NA and M1 mRNA synthesis is a more predominant process at the late stage. Viral transcripts encoding M and NS undergo splicing by hijacking the host spliceosome before translation (Dubois et al., 2014). The initially synthesized mRNAs are then exported from the nucleus for translation by cytoplasmic ribosomes, whereases the membrane-associated proteins (HA, NA and M2) are translated by endoplasmic reticulum (ER)-associated ribosomes (Dou et al., 2018; Jorba et al., 2009).

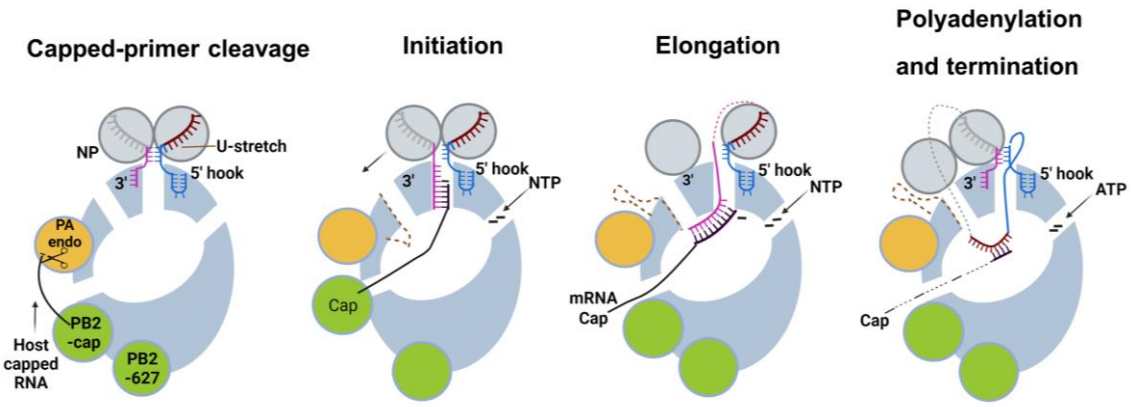

Figure 6: Schematic representation of models of viral mRNA transcription.

The viral RdRp is depicted in the transcription pre-initiation state as in Fig. 2B. Host capped RNA (black) is bound by the PB2 cap-binding domain and cleaved by the PA endonuclease domain. The cap-binding domain rotates to enable the 3’ end of the capped RNA primer to flip into the active site through the product exit channel. The 3’ end of the negative-sense vRNA template (pink) also inserts into the active site through the template entry channel, and NTPs enter through the NTP entry channel. Transcription is initiated by the addition of an NTP to the 3’ end of the capped primer, complementary to the second (shown) or third residue in the vRNA template. During elongation, this duplex further grows up to 9 bp and retracts the PL out of the active site. As the template is pulled into the active site, the viral NP detaches from the entering vRNA, then is translocated via the surface of the polymerase, and joins the vRNA template as it emerges through the template exit channel in the end. The 5’-cap of the mRNA product is removed from the PB2 cap-binding domain as the polymerase enters elongation. Termination occurs when polyadenylation initiates at repeated copying of the U-stretch (red) of the vRNA template. The 5’ end (dark blue) of the vRNA remains bound to its binding site formed by amino acid residues from PB1 and PA, and it may be stabilized by base-pairing

with the 3’ end of the vRNA, which rebinds at its binding site near the surface of the polymerase during elongation. The figure was adapted and modified from (Fodor & Te Velthuis, 2020; Te Velthuis et al., 2016; Wandzik et al., 2021). Parts of the figure were created with BioRender.com.

After the first round of viral mRNA synthesis and translation, newly synthesized vRNPs are relocalized to the nucleus to catalyze transcription of further mRNAs and vRNA/cRNA replication (Pflug et al., 2017). The M1, NS1, and NEP proteins are transported back to the nucleus. In contrast to transcription, replication is primer-independent and produces a positive-sense cRNA intermediate that serves as a template to make more vRNA (Hay et al., 1977). The first step of replication is to form positive-sense complementary cRNA from the vRNA template. Similar to the transcription, this process is initiated by the base-paired 5’ proximal region (nucleotides 1-10) of the vRNA promoter, which forms an intramolecular stem-loop, the so-called “hook,” that is tightly bound in a pocket formed between PA and PB1 (**Fig. 6**) (Pflug et al., 2014). The 5’ hook is protected additionally by a latch formed by the so-called PA-arch (aa 366–397) and PB1 β-hairpin (aa 353–370). It serves as an allosteric activator to order the correct polymerase structure (e.g., by correctly structuring the peptides of fingertips) and place the vRNA template to the polymerase active site. Next, the nucleotides 1-9 at the 3’ end of vRNA promoter translocate into polymerase active site through the template channel (Robb et al., 2019), followed by *de novo* initiation at the 3’ terminal UC of the vRNA template to generate a pppApG dinucleotide. Particularly a PL (PB1 residues 631–660) within the polymerase active region supports this state by stabilizing the initiation complex, however, it subsequently moves away from the polymerase active site, providing space for cRNA extension. To protect the cRNAs from degradation, the cRNA is packed with newly formed polymerase and NP oligomers into cRNPs (Vreede et al., 2004). In the second step of IAV genome replication, the polymerase copies cRNA back into vRNA. Similar to cRNA synthesis, it starts with the cRNPs binding to the 5’ and 3’ terminal cRNA promoter. 5’ cRNA differs in sequence from the vRNA 5’ end (being complementary to vRNA 3’ end), it forms a similar hook structure as the vRNA. Interestingly, vRNA and cRNA initiate replication differently. Unlike the initiation on the vRNA template at the 3' end at positions 1 and 2 (1-UC), the initiation on the cRNA template occurs at positions 4 and 5 and produces a ppApG dinucleotide that next acts as a primer for realignment to bases 1 and 2 of the cRNA 3’ terminus, before elongation (Oymans et al., 2018). This step requires the PL and a regulatory polymerase (Fan et al., 2019). Of note, cRNP-associated polymerase contacts a second regulatory polymerase thereby forming a dimer that modulates cRNA replication (Fan et al., 2019).

1.1.3.4 ER targeting and post-translational processing of the IAV proteins

Similar to cellular secretory proteins, the viral envelope proteins (HA, NA and M2) are translocated into the rER for glycosylation (except M2) and form HA trimer or tetramers of NA and M2. These proteins next are trafficked through the Golgi apparatus where HA and M2 undergo palmitoylation of cysteine residues. The mature HA, NA and M2 proteins are ultimately destined for the lipid rafts of the host cell membrane (Dou et al., 2018). The freshly synthesized NP proteins and polymerase subunits are translocated into the nucleus where they form novel vRNPs to assist in transcription and replication of vRNA. Likewise, the NEP and M1 proteins are imported into the nucleus to traffic vRNPs out of the nucleus (Akarsu et al., 2003; Shimizu et al., 2011). M1 could bridge the NEP to interact with the vRNP, forming the vRNP-M1-NEP complex. The nuclear export of this complex to the cytosol relies on the CRM1/exportin1-mediated pathway, followed by transport along microtubules to the cell membrane (Kawaguchi et al., 2012; Momose et al., 2007; K. Watanabe et al., 2014). Furthermore, previous studies showed that the nuclear RNP export is trigged by membrane accumulated HA via activation of the Raf/MEK/ERK signal cascade (Marjuki et al., 2007) and promoted by virus-induced apoptotic caspase-dependent widening of the nuclear pores (Muhlbauer et al., 2015).

1.1.3.5 IAV assembly and budding

IAV envelopes are enriched in cholesterol and sphingolipids that are acquired from host cell apical plasma membrane (PM) regions often referred to as “rafts” during the viral budding (Gerl et al., 2012). Membrane-decorated or proximal IAV proteins are arranged by different mechanisms (Dou et al., 2018). For example, HA is directed to the lipid rafts by the C-terminal cysteine that carries fatty acid modifications (Takeda et al., 2003), while the association of the NA to the membrane is attributed to its transmembrane domain (Barman et al., 2004). The eight vRNPs are transported by RAB11A to the budding zones where they are arranged in a “1+7” pattern (Noda et al., 2018) and bind to M1s, which are decorated beneath the cell membrane and linked to the cytoplasmic HA- and NA tails (Eisfeld et al., 2011). The assembly of viral components at the budding site triggers the budding processes, which includes bud initiation, bud growth, and bud release (Nayak et al., 2009). Several studies have indicated that the accumulation of HA and NA at the membrane is sufficient to induce the curvature, which is a prerequisite for budding and is promoted by the presence of M1 and M2 (Chen et al., 2007; Chlanda et al., 2015; Lai

et al., 2010). Eventually, IAV release relies on the NA, which can cleave SA from cell surface receptors and prevent HA binding of newly formed virions at the cell surface (Gottschalk, 1957).

1.1.4 Analysis of IAV by reverse genetic systems

The *de novo* synthesis of wild-type, mutant, and reassortant influenza viruses from viral cDNAs by reverse genetics (RG) systems is currently a common and powerful molecular virology technique to answer important questions in the biology of IAV that would not be possible using conventional virological or biochemical procedures (Nogales et al., 2016). One commonly used RG-system for IAV, is a bidirectional plasmid-based system, in which eight viral cDNAs (each a DNA copy of a specific vRNA segment) are inserted in negative-sense orientation between the human Pol-I promoter (p_{Ih}) and the Pol-I terminator (t_I) (Hoffmann et al., 2000). As illustrated in **Fig. 7**, the Pol-I transcription cassette in positive-sense orientation is flanked by a Pol-II promoter (p_{II}CMV) of the human cytomegalovirus and the polyadenylation signal (a_{II}BGH) of the bovine growth hormone gene, thereby enabling this unit produce mRNAs with 5' cap structures and 3' poly(A) tails that are eventually translated into viral proteins. The Pol-I promoter (p_{Ih})-t_I unit produces vRNA-like transcripts with exact unmodified ends. All eight cDNA copies (e.g. RG-plasmids) of the eight viral segments are transfected into co-cultures of 293T and MDCK cells, in which the 293T ensured high transfection efficiency, and the MDCK cells facilitated efficient IAV replication, the generated recombinant IAVs can be propagated and further analyzed.

RG-systems can be used, for example, to characterize the functional importance of specific residues in IAV proteins, mutations can be introduced by PCR-based site-directed mutagenesis (SDM) into the cDNAs of the viral genome segments which encode the viral proteins. By further co-transfection of the other RG-plasmids, the engineered recombinant IVs with the desired mutation can be generated and functionally tested. Thus, RG-systems enable the analysis of specific amino acids in viral protein function and also for IAV replication in general (Dawson, Wilson, Freiberger, et al., 2020; Giese et al., 2017; Weber et al., 2019). Likewise, risks of reassortant IAVs can be assessed by RG. In this scenario the reassortant IAVs are produced with various combinations of the eight RG-plasmids representing the viral genome segments from different genetic sources (F. Li et al., 2021; Waters et al., 2021).

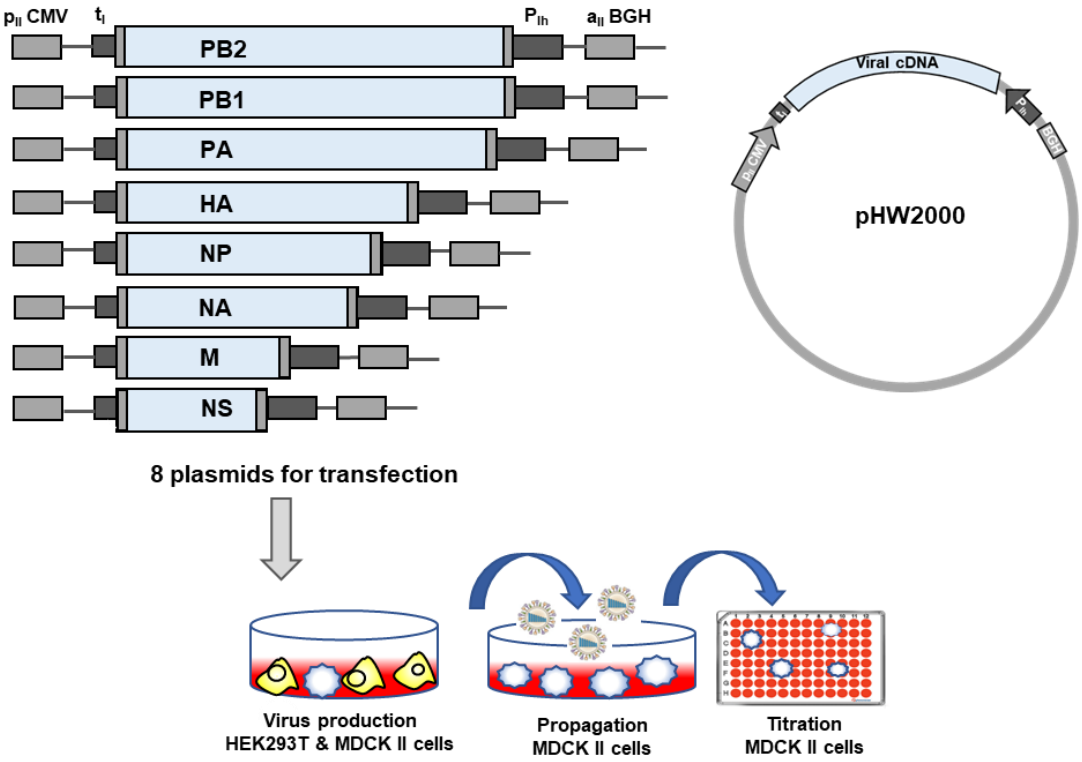

Figure 7: Schematic representation of the bi-directional plasmid-driven RG system for the rescue of recombinant IAV.

In the dual promoter RG-system in which eight cDNAs, representing the different genomic vRNA segments, are contained in a pHW2000 vector. These Pol-I/Pol-II-driven plasmids for the generation of vRNA and mRNA are transfected into co-cultures of 293T and MDCK II cells to generate recombinant IAV. The rescued recombinant IAVs can be propagated subsequently in MDCK II cells and titrated by foci assays. The figure was adapted and modified from (Hoffmann et al., 2000).

1.2 Protein phosphorylation

PTMs are enzyme-mediated covalent modifications of proteins. Known PTMs include proteolytic cleavage of precursor proteins or constitute a modifying group, such as phosphoryl, acetyl, methyl, glycosyl and ubiquitin or ubiquitin-like moieties (Ramazi et al., 2021). Such PTMs occur in a highly regulatory and reversible manner and give rise to new functionalities of proteins by affecting the protein folding, -stability, -activity, -localization, and protein-protein interactions among diverse cellular processes. Among the reported PTMs, phosphorylation was among the first described (Fischer et al., 1955) and the most studied PTM (Ramazi & Zahiri, 2021). This reversible biological process results in the addition or removal of phosphate groups and has been found to play key roles in nearly every aspect of cell life (Johnson, 2009). Phosphorylation in eukaryotes mainly target on serine (Ser), threonine (Thr), and tyrosine (Tyr) residues (Huang et al.,

2019), and phosphorylation between these is asymmetrically distributed: 85% Ser, 11.8% Thr, and 1.8% Tyr residues (Olsen et al., 2006). This chapter elucidates the functions of PTMs with focus on phosphorylation and how they can be detected by MS and substrate peptide-based assays.

1.2.1 Protein kinases as catalysts of protein phosphorylation

Protein kinases are responsible for catalyzing phosphorylation by transfer of the γ - phosphate of ATP to a Ser, Thr, or Tyr residue in protein substrates. Thus, kinases generally are categorized into three groups with respect to their substrate specificity: Ser/Thr protein kinases, Tyr protein kinases, and dual-specificity protein kinases (Hanks et al., 1988; Kim et al., 2015). They are activated by phosphorylation which in turn triggers a cascade of events leading to the phosphorylation of different amino acids of proteins in signaling networks (Ardito et al., 2017). Based on the results from the human genome project, at least 538 protein kinases were discovered in the human genome (Edwards et al., 2011), and at least 70% of all cellular proteins undergo phosphorylation modulated by these kinases (Olsen et al., 2010; Sharma et al., 2014). Numerous studies have unveiled the relevance of protein kinases in regulating signaling pathways and cellular processes, including metabolism, transcription, cell-cycle progression, differentiation, cytoskeleton arrangement, cell movement, apoptosis, intercellular communication, neuronal and immunological functions (Johnson, 2009). Concomitant with prominent roles in almost all aspects of cellular physiology, dysregulation of protein kinases is involved in various diseases such as cancer (Ledford, 2010), but interestingly the vast majority of kinases is heavily under-investigated or not studied at all. Available methods for the detection of these phosphorylation events, including the specific phosphorylation sites in kinases and substrates, largely rely on the specificity of phosphorylation by protein kinases.

1.2.2 Mechanisms of specificity in protein phosphorylation

As a consequence of being part of a large gene family, the specificity of protein kinase to regulate phosphorylation is essential for proper protein functions. It is well known that the protein kinases selectively target specific substrates with the involvement of several types of physical interactions (Miller et al., 2018). As shown in **Fig. 8**, protein kinase domains consist of a small N-terminal lobe that is predominantly responsible for coordinating ATP binding and a large C-terminal lobe, consisting mostly of α-helices and

loops, that mainly contributes to protein substrate binding and catalysis of phosphorylation (Taylor et al., 2011; Wilson et al., 2018). Protein kinases have evolved multiple mechanisms to ensure specificity in targeting residues for phosphorylation.

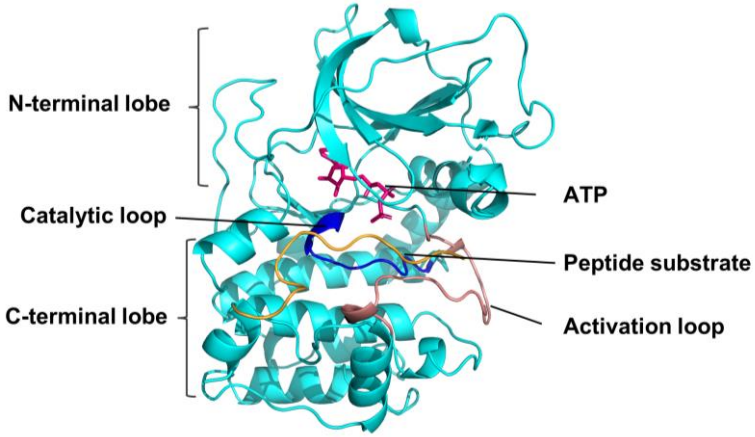

Figure 8: Schematic representation of protein kinase domain.

X-ray crystal structure of ATP bound to PKA (protein kinase A) (PDB code: 1ATP) showing distinct subdomains in the ATP binding site. PKA (~260 residues) consists of an N-terminal lobe (top) and a larger C-terminal lobe (bottom). The ATP binds to the N-terminal lobe whereas the substrate (orange) binds in the active site between the two lobes.

1.2.3.1 Phospho-acceptor specificity

As mentioned above, protein kinases are grouped into Ser/Thr-specific kinases, Tyr-specific kinases, and dual-specificity kinases. One mechanism by which kinase can discriminate between Tyr and Ser/Thr residue is largely attributed to the intrinsic specificity of the catalytic kinase domain, particularly the structure of the catalytic cleft between the N- and C-terminal lobes of the catalytic domain (Bradley et al., 2021; Ubersax et al., 2007). The catalytic domains have maintained nearly similar structures (Wilson et al., 2015). Tyr specific kinases are characterized by a deep catalytic cleft to accommodate the bulk Tyr side chain (Ubersax & Ferrell, 2007). Likewise, Ser/Thr kinases possess conserved signature residues within the catalytic domain, which is important for accommodating a small, aliphatic Ser/Thr residue at the active site (Chen, Ha, et al., 2014; Taylor et al., 1995).

Kinase activation occurs through an allosteric mechanism or phosphorylation of a canonical kinase segment known as the activation loop (**Fig. 8**) (Ardito et al., 2017; Zheng et al., 2018). Phosphorylation of residues in the activation loop will induce a conformational change that stabilizes the kinase in an active conformation. This loop

typically begins with an invariant “DFG” motif (Asp-Phe-Gly) near the ATP-binding cleft. A part of the activation loop interacts with the substrate peptide via β-sheet-like hydrogen bonding, whereas its region within the catalytic cleft defines its shape and biophysical characteristics to determine phosphorylation site specificity, which varies substantially among kinases (Miller & Turk, 2018). For example, human extracellular-signal regulated kinase (ERK) 1 and ERK2 contain the Thr-Glu-Tyr motif in their activation loop and are phosphorylated on both Thr and Tyr when they are activated, while most other kinases have a Thr within the loop (Mehdizadeh et al., 2016; Olea-Flores et al., 2019). However, in general target sites within the activation loop are not representative of the kinase substrate specificity, as reflected by the fact that there is no clear evidence of sequence-based determinants in the kinase active site for dual-specificity kinases (Lindberg et al., 1992).

Importantly, the Ser/Thr phospho-acceptor specificity of kinases co-varies with a residue downstream of the conserved DFG motif at the N terminus of the activation loop (‘DFG+1’). In line with this, an analysis of aligned kinase domain sequences unveiled larger hydrophobic residues (predominantly Leu, Phe, and Met) at this position for Ser-selective kinases, while most Thr-specific kinases possess the β-branched aliphatic residue Ile at this site (Chen, Ha, et al., 2014; Miller & Turk, 2018). More recently, kinase specificity determining residues on the kinase active site for Ser/Thr kinases were identified (Bradley et al., 2021).

1.2.3.2 Protein kinase substrate specificity

Another indispensable mechanism that ensures specific phosphorylation is determined by kinase phosphorylation site motifs, i. e., preferential phosphorylation of phospho-acceptor residue surrounded by particular patterns of amino acids in the context of specific sequence motifs (Zhu et al., 2005). A sequence motif is traditionally comprised of the phospho-acceptor residue and five N- and C-terminal residues next to it. The sequence motif of ERK2 kinases for example is P-X-S/T-P, this kinase tends to phosphorylate Ser and Thr residues that have proline at position −2 and +1 relative to the phospho-acceptor (Roskoski, 2019).

A protein kinase substrate motif can be characterized either by the mutational analysis of the known substrate or by *in vitro* biochemical analyses of the kinase reaction in the presence of phosphorylatable synthetic peptides. These two experimental approaches are generally combined due to the fact that the most conserved substrate sites will also be the most important for the efficient phosphorylation of the peptide. Such an example

is the first discovered substrate motif for PKA (PKA: R-R-x-S), where either substrate variants or mutation of arginine in a synthetic target peptide caused a drastic reduction in the phosphorylation levels (Kemp et al., 1975; Roskoski, 2019). More sophisticated peptide library screens enable rapid analysis of the substrate specificity and consensus phosphorylation sites of protein kinases (Songyang et al., 1994; Ubersax & Ferrell, 2007) (**Table 1**).

Table 1: Consensus sequences recognized by protein kinases.

Kinase	Full name	Kinase consensus motifs	Refence
PKA	Protein kinase A or cAMP-dependent protein kinase	R-R/K-x-S-ϕ	PMID: 194899
AKT	Or Protein kinase B	R-x-R-x-x-S/T-ϕ	PMID: 8985174
AMPK	AMP-activated protein kinase	ϕ-x-R-x-x-S-x-x-x-I/L	PMID: 7698321 PMID: 18439900
CDKs	Cyclin-dependent kinases	S/T-P-x-K/R	PMID: 7874496
MAPKs	Mitogen-activated protein kinases	P/ϕ-x-S/T-P	PMID: 1939237
CaMK2	Calmodulin-dependent protein kinase-2	R-X-X-S/T	PMID: 8887677
EGFR	Epidermal growth factor receptor	E-E-E-Y-F	PMID: 7845468
Src	Rous sarcoma virus Tyr kinase	E-E-I-Y-E/G-X-F	PMID: 7845468

The table shows consensus sequences that have been derived from selected kinases with PubMed Unique Identifiers (PMIDs) shown here. x: any amino acid; underlined: phosphorylated residue; ϕ: hydrophobic residue. Adapted and modified from (Miller et al., 2016).

1.2.3.3 Other specificity determinants of protein kinase

Another aspect of determining substrate affinity and specificity comes from docking interactions, in which allosteric sites outside the kinase active site recognize sequence motifs on the substrate (**Fig. 8**). For example, in the Ser/Thr kinase PRK2 a phosphorylated hydrophobic motif (HM) FXXF-S/T-F is located in the C-terminal lobe of the kinase domain that can function as a docking site for its substrate the kinase PDK1 (Balendran et al., 2000). For Tyr kinases, a SH2 domain wildly serves as a docking module for the binding of phosphorylated Tyr motifs (Roskoski, 2004; Sipeki et al., 2021). In addition, kinase specificity is also modulated by adaptor and scaffold proteins in the sense that these modules can result in either the higher local effective concentration of

the kinase to a specific substrate or less likelihood of kinase inhibition by other substrates (Miller & Turk, 2018).

1.3 Analysis of protein phosphorylation: methods for studying kinases and their substrates

Protein phosphorylation, which is tightly controlled by protein kinases and phosphatases, has fundamental roles in signal transduction, which in turn regulates a diverse variety of cellular processes and also the pathophysiological events. Therefore, continuous attempts have been made to determine the protein phosphorylation-mediated cell physiology and disease mechanisms. In earlier times phosphorylation of proteins was detected either by radiolabeled phosphates, 2D gels or specifically raised antibodies (Raggiaschi et al., 2005). New advances have been made with more robust and comprehensive methodologies for assessing protein phosphorylation, which will be briefly discussed here.

1.3.1 Phosphoproteomic studies

Quantitative mass spectrometry (MS)-based phosphoproteomics is currently the most powerful technique for the analysis of cellular signaling networks employing phosphorylation. A typical shotgun phosphoproteomic analysis involves the digestion of total cellular proteins, followed by liquid chromatography-tandem MS analysis (LC-MS/MS) of sorted phosphorylated peptides. As phosphorylation is typically substoichiometric and of low abundance, phosphopeptides only represent a tiny fraction (Bonne Kohler et al., 2020). Phosphopeptides will then be enriched (TiO_2, IMAC, etc) and analyzed using MS and quantification (Douglass et al., 2012).

There are several remarkable advantages of this methodology. First, phosphoproteomic profiling provides deep insight into the global picture of the phosphorylation landscapes with characterization of tens of thousands of phosphosites under a specific experimental condition. It also contributes to a much broader and more detailed overview of physiological and pathological alterations of signaling pathways and how these might affect cell function. Second, comprehensive bioinformatics enables the further identification of activated kinases of the quantitative phosphoproteome for a given system. For that, different approaches for assessing kinase activation on a kinome-wide level can be applied. For example, the kinases mediating protein phosphorylations can be predicted from assessing the over- or under-represented sequence motifs combined

with database comparisons of known kinase substrates or sequence specificities (Lachmann et al., 2009; Zagorac et al., 2018). The cellular kinase activation states can alternatively be deduced from the phosphorylation state of key residues present in the activation loop, which is contained in most kinase domains (Kornev et al., 2015; Schmidlin et al., 2019). Thus, the phosphorylation state of the kinase activation loop is often used as proxy to analyze the activation state of the respective kinase (Schmidlin et al., 2019; Sharma et al., 2014; Weber et al., 2019). Understanding the role of the interplay between kinases and phosphatases on the net phosphorylation seen in global phosphoproteomic data is essential to identify abnormal phosphorylation-driven cell signaling in disease. Also, the identification of key novel kinases in the pathogenesis of numerous diseases promising novel targets for pharmacological interventions (Savage et al., 2020).

1.3.2 Peptide-based kinase activity assay

In vitro experiments can be very good indicators of specific phosphorylation mediated by a kinase. Based on the fact that in general each kinase prefers to phosphorylate the substrates embedded into a particular sequence which typically follows a consensus phosphorylation motif, *in silico* prediction of kinase-substrate relationships has been commonly utilized in various approaches as shown in **Fig. 9** (Sugiyama et al., 2019). Kinase activity toward substrates is commonly measured by *in vitro* kinase assay in which the purified kinase is incubated with an exogenous peptide substrate in the presence of ATP. The phosphorylation of a substrate by a purified kinase can be assessed by several reporter systems including colorimetric, radioactive, or fluorometric detection (Johnson et al., 2005; Xue et al., 2013). However, this method requires the purification of an active kinase, and the phosphorylation may not necessarily reflect what occurs under physiological conditions in the cell (e.g., concentration of a given kinase) (Xue & Tao, 2013).

The peptide-based kinome array profiling allows for in-depth and global-scale analysis of multiple kinases activity in a natural cell lysate, which also maintains kinomic network integrity in this biological sample. For this technique, a randomized peptide library immobilized on beads (Wu et al., 1994) or arrays (Hutti et al., 2004; Mok et al., 2010), natural protein-derived peptides (Schutkowski et al., 2004) and protein arrays (Ptacek et al., 2005) as potential downstream targets of the profiled kinase are employed. Kinase activity profiling with PamChip® peptide microarrays is one such protein-derived peptide-based approach (Alack et al., 2020; Creeden et al., 2020; Weiss et al., 2019). This

platform applies 144 Tyr or 144 Ser/Thr kinase peptide substrates containing 4 positive controls spotted on a chip. When these peptide spots are exposed to experimental samples, they can be phosphorylated by the activated kinases within a given sample. Phosphorylation events correspond to the enzymatic activity of the active kinases contained in the lysate. Fluorescently tagged phospho-antibodies then recognize the phosphorylated peptides and generate the signal proportional to the amount of phosphorylated peptides contained within the sample. The intensities reported by a PamChip® provide a signature that can be used to predicate the kinases responsible for the observed phosphorylation intensity.

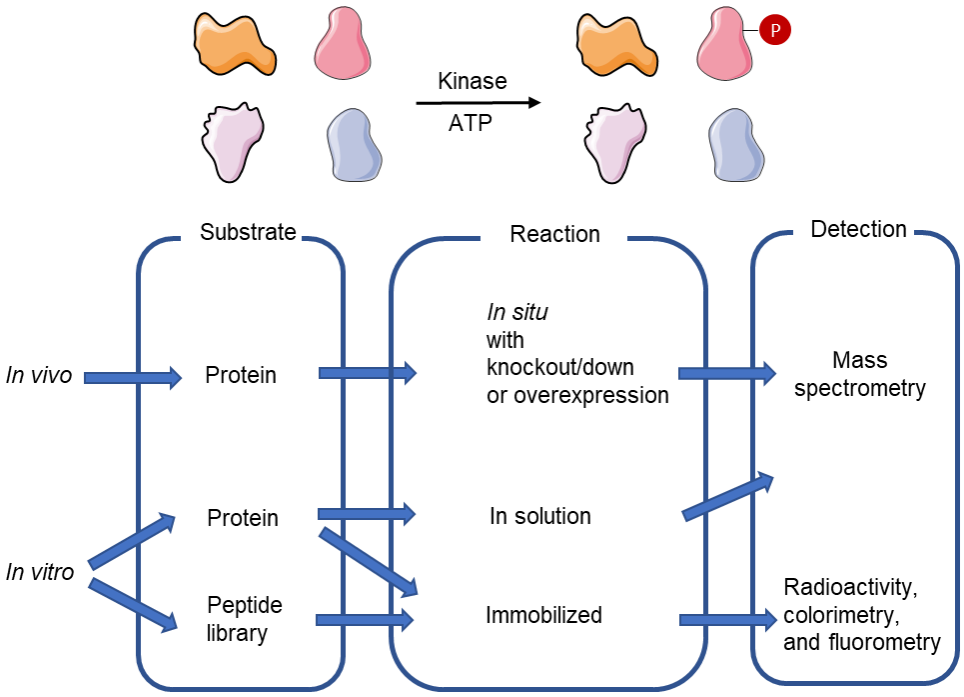

Figure 9: Approaches for the profiling of kinase substrate specificities.

Schematic display of typical combinations of substrate sources, reaction conditions and detection methods for the profiling of kinase substrate specificities. Adapted and modified from (Sugiyama, 2020).

1.4 Importance of identification of protein phosphorylation in IAV-infected cells

Throughout various stages of its life cycle, infection with IAVs necessarily induces specific signaling cascades, that either support or antagonize viral propagation or that occur as an indirect result of ongoing infection due to changes in cell architecture or the occurrence of cell damage (Kash, Goodman, et al., 2006; Kash, Tumpey, et al., 2006; Schmitz et al., 2014). These virus-regulated signaling pathways employ diverse types of

PTMs including acetylation, ubiquitination, and phosphorylation. Phosphoproteomic analyses largely contribute to the characterization of IAVs infection-associated changes of the protein phosphorylation status (Hu et al., 2020). These investigations provide abundant evidence on the relevance of phosphorylation of viral and cellular proteins, and phosphorylation-regulated pathway cascades at every step of the virus replication cycle, and their role to regulates viral replication and host responses to infection (Hu et al., 2020). Amongst the distinct roles of virus-induced protein phosphorylation, the kinases responsible for virus-supportive protein phosphorylation either on cellular or viral proteins are of particular interest, as they have been proposed to be attractive targets for the development of novel antivirals. But yet, a large number of these phosphorylation events remain to be discovered, which would be relevant for ongoing development of an effective anti-influenza therapy (Yanguez et al., 2018).

1.4.1 Role of IAV-induced phosphorylation-dependent signaling events

During IAV infection, host cells can trigger the immune response by changing the functions of cellular proteins via phosphorylation. However, viruses also hijack host cellular machinery to break through these defenses for efficient replication (Hu et al., 2020). Kinases-mediated protein phosphorylation has been identified as a central player in mediating cell signaling pathways in response to IAV infection. The understanding of the relevance of kinase signaling for IAV infection can be achieved by the approaches mentioned in section 1.3 : **(I)** IAV-dependent changes of phosphorylations in kinase activation loops can be used as a proxy for their relative activation state, an approach that has been used in previous phosphoproteomic studies in our lab (Weber et al., 2019). **(II)** IAV-mediated phosphorylation changes can also be determined using the peptide-based kinome array profiling, such as PamStation® analysis. By now, a large group of kinases critical for IAV propagation has been reported, which is active at different steps of the IAV life cycle as shown in **Table 2**. Despite the fact that anti-virals against IAV currently in use exclusively target viral factors, such as NA or the M2 ion channel, pro-viral host factors or kinases of intracellular signaling cascades which are essential for virus replication have been unraveled as novel targets for pharmacological intervention (Ludwig, 2009). The pharmacologic possibilities of Ser/Thr kinase inhibitors that target essential cellular pathways on which IAV relies for propagation, such as the pathway that leads to activation of the transcription factor nuclear factor kappa-B (NF-κB) and the classical mitogenic Raf/MEK/ERK kinase cascade, are good examples for understanding

the relevance of kinases profiling in anti-influenza intervention (Laure et al., 2020; Pinto et al., 2011).

Table 2. Overview of the role of cellular kinases in different stages of IAV replication.

	Name	IAV effect	*In Vitro, In Vivo or Ex Vivo*	Inh. vs. KO or knock-down	Reference
Tyr	FAK	-Virus entry -Polymerase activity	*In vitro*	Inhibition	PMID: 27743963 PMID: 24696469
	TrkA	-vRNA synthesis -RNP export -Budding	*In vitro*	Inhibition	PMID: 21209112 PMID: 21930873
	Btk	-Neutrophil regulation	*In vivo*	Inhibition	PMID: 29516781
	c-Abl	-Pathogenicity mediator	*In vivo*	Inhibition	PMID: 25052580 PMID: 25367299
	Tyk2	-Cytokine regulation	*Ex vivo*	Inhibition	PMID: 28705941
Ser/ Thr	JNK1/JNK2	-vRNA synthesis -Autophagy -Cytokine regulation	*In vivo*	Inhibition	PMID: 24780373 PMID: 30316042 PMID: 26559961
	P38 MAPK	-vRNA synthesis -RNP export -Prevents apoptosis -Cytokine regulation -Virus entry	*In vitro*	Inhibition	PMID: 27346133 PMID: 24189062 PMID: 20702616 PMID: 25154738
	MEK	-RNP export	*In vivo*	Inhibition	PMID: 21854809 PMID: 23523553 PMID: 28377100
	ERK	-RNP import -RNP export	*In vivo*	Inhibition	PMID: 11231581 PMID: 16608852
	RSK2	-Antiviral responses	*In vitro*	Knockdown	PMID: 19129453
	IKK	-Cytokine regulation -Caspase regulation -RNP export -Antiviral response modification	*In vitro*	Inhibition	PMID: 23320394 PMID: 22891964 PMID: 23811282 PMID: 15269376
	IRAK-M	-Neutrophil interaction -Cytokine reg.	*In vivo*	KO	PMID: 20042589
	PKC	-Endosomal entry -RNP assembly -Polymerase activity -Prevents apoptosis	*In vivo*	Inhibition	PMID: 1698925 PMID: 12477851 PMID:19523156 PMID: 19264651 PMID: 28758638
	GRK2	-Viral uncoating	*In vivo*	Inhibition	PMID: 30206219
Lipid	PI3K	-Virus entry -Prevents apoptosis -vRNA synthesis -RNP export -Antiviral response modification	*In vitro*	Inhibition	PMID: 21129142 PMID: 19290913 PMID:16882036 PMID: 17229704 PMID: 17325368
	SphK1/SphK2	-vRNA synthesis -RNP export	*In vivo*	Inhibition	PMID: 24137500 PMID: 30125617

Adapted from (Meineke et al., 2019).

1.4.1.1 The role of Ser/Thr kinases in classic MAPK signaling for IAV replication

As shown in **Fig 10**, activation of Ser/Thr mitogen-activated protein (MAP) kinase proceeds by a cascade employing three subsequently activated kinases (MAP3K→MAP2K→MAPK) resulting in the activation of the actual Ser/Thr kinase MAPK. All MAPKs are activated via phosphorylation of their specific TXY motif by mixed lineage kinases (MKKs) or their upstream kinases, thereby maintaining substrate specificity and MAPK signaling stringency (Ludwig et al., 2021; Pearson et al., 2001). The Ras-dependent Raf/MEK/ERK MAPK signaling pathway regulates important cellular functions involved in proliferation, differentiation, apoptosis, and immune response (Cargnello et al., 2011). Aberrant activation of this pathway often turns into oncogenic signaling and causes tumor development. Pharmacologic inhibitors have been developed that inhibit the pathway on the level of MAPK/ERK kinase (MEK) to interfere with ERK activation under pathophysiological conditions (Ludwig et al., 2021; Zhao et al., 2014). For this, compounds have successfully passed clinical trials and some are now licensed for clinical use (Cheng et al., 2017), such as trametinib, which is approved by the FDA for melanoma treatment (Zhao & Adjei, 2014). More importantly, previous findings point toward the activation of protein kinase C (PKC)-dependent Raf/MEK/ERK signaling which occurs late in the infection cycle via HA accumulation in the cellular membrane. This cascade leads to phosphorylation at specific sites of the NP, which in turn creates a docking site for binding of the M1 protein as a prerequisite for forming vRNP export complexes (Marjuki et al., 2006; Pleschka et al., 2001; Schreiber et al., 2020). Given its critical roles in supporting IAV growth by supporting vRNP nuclear export, the inhibition of this pathway by MEK or ERK inhibitors is also reflected by decreased titers of IAV. Further repurposing of licensed MEK inhibitors as anti-infective agents is therefore conceivable, based on the fact that this inhibitor has been proven to display efficient anti-influenza activity and cytokine expression *in vitro* and in the mouse model without major toxicity (Schrader et al., 2018). In line with this, a further MEK inhibitor (ATR-002, EudraCT 2019-000784-25), has made further progress into a Phase I clinical trial (Laure et al., 2020) and another Phase II clinical trial to evaluate the suitability to treat adult hospitalized patients with COVID-19 (ClinicalTrials.gov Identifier: NCT04776044).

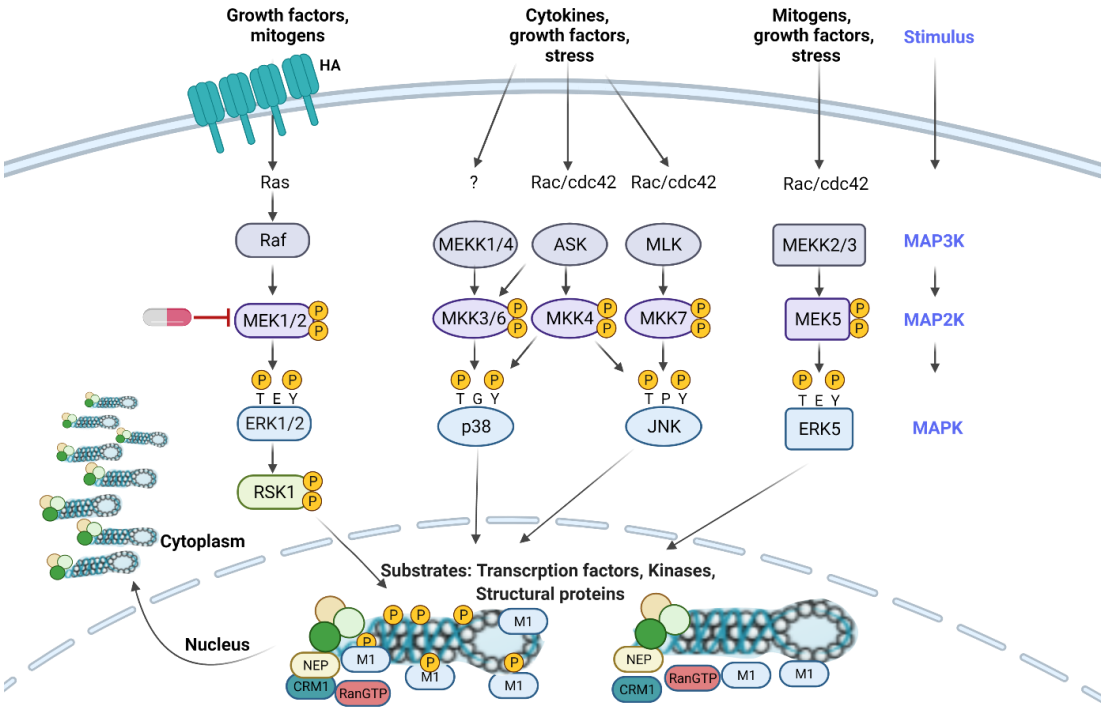

Figure 10: Schematic representation of different MAPK signaling pathways.

MAPK signaling cascades are organized hierarchically into three-tiered modules. MAPKs are phosphorylated and activated by MAPK kinases (MAP2K), which in turn are phosphorylated and activated by MAP2K kinases (MAP3K). MAP3Ks are activated by several modes, including interaction with the family of small GTPases and/or other protein kinases, connecting the MAPK module to cell surface receptors or external stimuli. MAPK cascades activation results in a diverse set of biological responses depending on stimulus and cellular context. Ras: Rat sarcoma, Rac: Ras related C3 botulinum toxin substrate 1, Cdc42: cell division cycle 42. Modified from (Ludwig et al., 2021; Pleschka, 2008; Schreiber et al., 2020).

1.4.2 Role of IAV-protein phosphorylation

IAVs also utilize the host kinase machinery to phosphorylate viral proteins, and this phosphorylation can be well detected by phosphoproteomic MS analysis (Hutchinson et al., 2012; Jacob et al., 2011; Patil et al., 2021; Weber et al., 2019). The functions of IAV protein phosphorylation are quite diverse. They have either no discernible effect or they support or antagonize viral replication. Some phosphorylations are of critical relevance while others only allow a fine-tuning of effector functions (Hu et al., 2020). For example, a wide range of functions of multiple phosphorylated sites in the NS1 protein has been reported. The relevance of several phosphorylation sites of IAV NS1 (S42, T49, T80) in attenuating the IFN-antagonistic activity of IAV NS1 has been established with regard to decreasing its RNA-binding affinity (Hsiang et al., 2012; Kathum et al., 2016) or affecting

NS1-RIG-I binding (Kathum et al., 2016), while phosphorylation of Y73 and S83 has been demonstrated to be necessary for the effective inhibition of IFN (Cheng et al., 2019). In addition, NS1 S205 phosphorylation is required for efficient binding of NS1 to DDX21 and contributes to the enhanced viral polymerase activity, which is likely to be regulated by casein kinase 2 (CK2) (Patil et al., 2021). The remaining NS1 phosphorylation events (S48, T215) could not be linked to specific NS1 functions yet, since they did not significantly affect viral replication (Hale et al., 2009; Hsiang et al., 2012; Kathum et al., 2016). Furthermore, the importance of Y132 phosphorylation of M1 mediated by Janus kinases (JAK) has been reflected as either necessary for nuclear import and viral replication using a RG system (Wang et al., 2013), or for virion assembly in real IAV infection (Mecate-Zambrano et al., 2020).

Distinct functional mechanisms of NP phosphorylation have also been reported. In the context of vRNPs, the NP protein is present in an oligomeric form, consisting of multiple copies, around which the viral RNA genome is wrapped. During the assembly of vRNPs, an NP monomer is initially recruited through direct interaction with the viral polymerase. Upon binding to the nascent 5' end of the viral genome, monomeric NP undergoes oligomerization along the length of the genomic RNA via NP/NP homo-oligomerization. Interestingly, the profound negative effect of NP phosphorylation on vRNP assembly has been seen in several studies. For example, the phosphorylation of two NP sites (S407 and S413) on the opposite sides of the NP-NP interface has been shown to block homotypic interactions thus maintaining the monomeric form of NP (Mondal et al., 2015). Further investigation reveals that the human PKC family members are responsible for the phosphorylation of vRNP subunits, including the NP S165 and S407 phosphorylation, thereby disturbing the RNP assembly (Mondal et al., 2017). In contrast, NP can be dephosphorylated by phosphatase CDC25B, which leads to enhanced NP self-oligomerization, nuclear export of NP, viral polymerase activity, and vRNA production (Cui et al., 2018). Dynamic phosphorylation of NP at these sites therefore plays a role in directing ordered assembly of vRNP throughout virus life cycle (Mondal et al., 2017; Turrell et al., 2015). The negative effect of phosphorylation on vRNP nuclear export has been seen on residues NP T188 and Y296 (Li et al., 2018; Zheng et al., 2015). Likewise, the phosphorylation at S9 or Y10 in the NLS of NP impairs its nuclear import by decreasing the association with nuclear import receptors-e.g. importin-α (Zheng et al., 2015).

The studies of phosphorylation on IAV polymerase subunits, however, point to their impact on the prohibition of polymerase activity and the inference with production of infectious virus. This phenomenon has been seen for phosphorylation at PB1 T223, S478, and S673 (Dawson, Wilson, Freiberger, et al., 2020). Regulatory phosphorylation

at PA T157 is linked to vRNA replication by mediating the proteolytic activity of PA (Perales et al., 2000).

1.5 Aim of the study

The aim of this thesis is to address the functional relevance of IAV-regulated phosphorylation events that occur on host cellular proteins as well as on IAV proteins. In the first part of this thesis, I aimed to identify the novel IAV-regulated kinases. For this, PamStation® peptide microarrays should be utilized to profile the kinetics of kinase activation triggered by two medically relevant IAVs, namely A/Hamburg/4/09 ($H1N1_{pdm09}$) and the highly pathogenic avian IAV human isolate A/Thailand/1(KAN-1)/2004 (H5N1). The function of identified upregulated kinases on IAV replication should be characterized via perturbation of the activity of these kinases using highly specific small molecule inhibitors (where available) or siRNAs.

As previous phosphoproteomic studies in our laboratory identified novel phosphorylation sites on SC35 or SC35M, the aim in the second part of my thesis, was to elucidate the function and the molecular consequences of novel IAV-protein phosphorylation sites as well as those previously reported. All IAV-protein phosphorylation sites from the existing literature should be combined and then filtered according to pre-defined criteria. Furthermore, the consequences of candidate phosphorylation sites on viral protein for IAV propagation should be characterized with recombinant IAVs generated by RG. Important phosphorylation sites, whose phosphorylation either enhance or antagonize protein function, should be investigated in more detail by exploring the functional significance of this modification, including its role in regulating protein stability, subcellular location, polymerization, protein/protein interactions, and enzymatic activities.

2 MATERIALS AND METHODS

2.1 Materials

2.1.1 Antibodies

2.1.1.1 Primary antibodies

Specificity	Species	Supplier	Dilution	Cat.N
anti-phospho-ERK1/2 (T202/Y204)	Rabbit mAb (D13.14.4E)	Cell Signaling	1:1000	4370S
anti-ERK2 (D-2)	Mouse mAb	Santa Cruz	1:500	SC-1647
anti-phospho-JNK (T183, 185)	Rabbit pAb	Cell Signaling	1:1000	9251S
anti-phospho-Akt (S473)	Rabbit pAb	Cell Signaling	1:1000	9271S
anti-IAV NP	Rabbit pAb	Thermo Scientific	1:2000	PA5-32242
anti-IAV NP	Mouse mAb	Dr. S. Ludwig, Münster (Germany)	Immunohistochemistry or IF 1:100	
anti-IAV PB1	Rabbit pAb	Gene Tex	1:1500	GTX125923
anti-IAV PA	Rabbit pAb	Gene Tex	1:1500	GTX118991
anti-IAV M1	Rabbit pAb	Gene Tex	WB: 1:1000 IF: 1:2000	GTX125928
anti-IAV M2	Mouse mAb	Thermo Scientific	IF: 1:1000	MA1-082

anti-IAV NS1 (SC35M)	Mouse mAb	Dr. S. Ludwig, Münster (Germany)	1:100	
anti-IAV NS1 (pdmH1N1)	Mouse mAb	Santa Cruz	1:1000	SC-130568
anti-IAV HA (H7)	Rabbit pAb	Abcam	1:1000	ab195565
anti-STRN	Mouse mAb	BD Biosciences	WB: 1:2000 IF: 1:500	610838
anti-STRN3	Mouse mAb	Novus Bio	WB: 1:1500 IF: 1:500	NB110-74572SS
anti-α-Tubulin	Mouse mAb	DSHB	1:1000	12G10
anti-Vinculin	Mouse mAb	Sigma	1:1000	V9131
anti-H3	Rabbit pAb	Abcam	1:1000	ab1791
anti-GAPDH (6C5)	Mouse mAb	Abcam	1:2000	ab8245

2.1.1.1 Secondary antibodies

Specificity	Conjugated to	Supplier	Dilution
goat-anti-mouse IgG	HRP	Dianova	1:5000
goat-anti-rabbit IgG	HRP	Dianova	1:5000
goat-anti-rat IgG	HRP	Dianova	1:5000
goat-anti- mouse IgG	Cy3	Dianova	1:3000
goat-anti- rabbit IgG	Alexa Fluor 488	Dianova	1:1000

2.1.2 Antibiotics

Type	Working conc.	Selection	Source
Ampicillin	100 µg/ml	prokaryotes	Sigma
Kanamycin	50 µg/ml	prokaryotes	Sigma

2.1.3 Cells

2.1.3.1 Prokaryotic cells

Strain	Genotype	Source
TOP10	F– *mcr*A Δ(*mrr-hsd*RMS-*mcr*BC) Φ80*lac*ZΔM15 Δ*lac*X74 *rec*A1 *ara*D139 Δ(*ara leu*) 7697 *gal*U *gal*K *rps*L (StrR) *end*A1 *nup*G	Invitrogen
XL1-blue	recA1 endA1 gyrA96 thi-1 hsdR17 supE44 relA1 lac [F proAB lacIqZΔM15 Tn10 (Tetr)]	Agilent

2.1.3.2 Eukaryotic cells

Name	Genotype/Feature	Source
293T	Human embryonic kidney cells stably expressing the large T antigen of SV40 virus	Schmitz Lab
MDCK II	MDCK II - Madin-Darby Canine Kidney II is a subclone derived from the heterogenous parent line MDCK	Pleschka Lab
A549	Human alveolar epithelial cells	Pleschka Lab
MLE-15	Mouse lung epithelial cell line deriving from transgenic mice harbouring T antigen of SV40 virus	Pleschka Lab

2.1.4 Viruses

Strain	Source	BSL level
A/Seal/Massachusetts/1/80 (H7N7, SC35M)	Virus collection, Institute of Medical Virology, Justus-Liebig University Giessen, Germany	3
A/Thailand/1(KAN-1)/2004 (H5N1)	Virus collection, Institute of Medical Virology, Justus-Liebig University Giessen, Germany	3
A/Hamburg/4/09 (H1N1)	Virus collection, Institute of Medical Virology, Justus-Liebig University Giessen, Germany	3

2.1.5 Chemicals and general materials

Name	Source
2-propanol (Isopropanol)	Roth
4-(2-hydroxyethyl)-1-piperazineethanesulfonic acid (HEPES)	Sigma
ABsolute qPCR SYBR green ROX Mix	Thermo
Acetic acid	Roth
Acrylamide/bisacrylamide mix (37.5:1)	Roth
Adenosine triphosphate (ATP)	Thermo
AEC (3-amino-9-ethylcarbazole)	Sigma
Agar	AppliChem
Agarose	AppliChem

Name	Source
Ammonium persulfate (APS)	Sigma
Aprotinin	Sigma
Avicel	FMC Biopolymer
BlueSlick	Serva
Bovine serum albumin (BSA)	Sigma
Bromophenol blue	Merck
BSA (Solution, 30% (w/v))	Sigma
Calcium chloride ($CaCl_2$)	Merck
Cell culture consumables	Sarstedt
Chloroform	Sigma
DEAE Dextran (MW: 500,000)	Pharmacia biotech
N, N-Dimethylformamid (DMF)	Sigma
Dimethyl sulfoxide (DMSO)	Sigma
Dithiothreitol (DTT)	Invitrogen
D-Sucrose	Roth
Disuccinimidyl glutarate (DSG)	CovaChem
Disodium hydrogen phosphate (Na_2HPO_4)	Roth
Disuccinimidyl suberate (DSS)	Thermo
DMEM, high glucose + GlutaMAX	Life Technologies
DNA sample buffer	Thermo
DNA Molecular Weight Marker XIII (50 bp ladder)	Roche,Sigma

Name	Source
Dual-Luciferase reporter assay system kit	Promega
Ethanol	Sigma
Ethidium bromide	Roth
Ethylene glycol-bis(β-aminoethyl ether)-N,N,N',N'-tetraacetic acid (EGTA)	Sigma
Ethylenediaminetetraacetic acid (EDTA)	Sigma
Fetal calf serum (FCS)	Life Technologies
GeneRuler 100 bp & 1 kb DNA ladder	Thermo
Glucose	Merck
Glycerol	Roth
Glycine	Roth
Hoechst 33342	Invitrogen
Hydrochloric acid (HCl)	Sigma
Hydrogen peroxide (H_2O_2)	Merck
Igepal CA-630	Sigma
IgG Sepharose 6 Fast Flow beads	Cytiva
Leupeptin	Sigma
Lipofectamine 2000	Invitrogen
Lipofectamine 3000	Invitrogen
Magnesium chloride ($MgCl_2$)	Sigma
Magnesium sulfate ($MgSO_4$)	Sigma
Manganese (II) chloride ($MnCl_2$)	Sigma

Name	Source
MicroSpin G-25 Columns	Cytiva
Microtiter plate (96 wells)	Greiner
Minimum Essential Media (MEM) (10x)	Life Technologies
Methanol	Sigma
Mowiol Mounting Medium	Roth
Nuclease free water	Ambion
N,N,N',N'-tetramethylethylendiamin (TEMED)	Roth
Opti-MEM	Life Technologies
Paraformaldehyde	Roth
Page Ruler Plus pre-stained protein ladder	Thermo
Phenylmethanesulfonyl fluoride (PMSF)	Sigma
Polyethylenimine, linear (PEI)	PolyScience
Poly-L-Lysine hydrobromide	Sigma
Potassium acetate	Roth
Potassium chloride (KCl)	Sigma
Potassium hydroxide (KOH)	Merck
Potassium phosphate (KH_2PO_4)	Sigma
Polyvinylidene difluoride (PVDF) membrane	Thermo
Protein G Plus/Protein A-Agarose	Millipore
QIAshredder	Qiagen
RiboLock RNase Inhibitor	Thermo

Name	Source
ROTIPHORESE®Sequencing gel concentrate	Roth
ROTIPHORESE®Sequencing gel diluent	Roth
ROTIPHORESE®Sequencing gel buffer concentrate	Roth
Skimmed milk powder	Merck
Sodium acetate	Roth
Sodium azide (NaN_3)	Sigma
Sodium chloride (NaCl)	Sigma
Sodium deoxycholate	Sigma
Sodium dodecyl sulfate (SDS)	Bio-Rad
Sodium fluoride (NaF)	Roth
Sodium hydrogen phosphate (Na_2HPO_4)	Roth
Sodium hydroxide (NaOH)	Roth
Sodium orthovanadate (Na_3VO_4)	Sigma
Tris (hydroxymethyl)aminomethane (Tris)	Roth
Triton X-100	Sigma
Tryptone	Roth
Trypsin 0.05% EDTA	Life Technologies
Tween 20	Gerbu
Western Lightning ECL solutions	Perkin Elmer
Yeast extract	AppliChem
β-glycerophosphate	Sigma

Name	Source
β-mercaptoethanol	Roth

2.1.6 Enzymes

Type	Source
DNase I	Thermo
FastAP Thermo-sensitive Alkaline Phosphatase	Thermo
Proteinase K	Invitrogen
Phusion HF DNA polymerase	Thermo
Restriction enzymes and buffers	Thermo
RNase A	Thermo
T4 DNA Ligase	Thermo
T4 Polynucleotide Kinase	Thermo
Taq DNA Polymerase	Thermo
TEV protease	NEB
Trypsin/0.05 % (v/v) EDTA	Life Technologies

2.1.7 Inhibitors

Name	Target	Source
Tofacitinib (CP-690550)	JNK3, also inhibits JNK1	Sigma
TAE684	FER and FES	AdooQ® Bioscience

Name	Target	Source
WZ4003	NUAK1, also inhibits NUAK3	AdooQ® Bioscience
ZM306416	FLT1, VEGF-R1	Cayman chemical

2.1.8 Kits

Name	Source
GeneJET Plasmid Maxiprep Kit	Thermo
GeneJET Plasmid Midiprep Kit	Thermo
GeneJET Plasmid Miniprep Kit	Thermo
SmartPure Plasmid Kit	Eurogentec
QuikChange II XL Kit	Aligent
Nano-Glo® Luciferase Assay Kit	Promega
RNeasy Mini Kit	Qiagen
SuperScript™ IV One-Step RT-PCR	Thermo
PrimeScript RT Master Mix cDNA synthesis Kit	Takara
QIAquick Nucleotide Removal Kit	Qiagen
PageSilver Silver Staining Kit	Thermo

2.1.9 Oligonucleotides

2.1.9.1 Oligonucleotides used as primers for PCR

NCBI Primer-BLAST tool was used to design all the primers. All oligonucleotides were were purchased by Sigma, Germany, dissolved in autoclaved Milli-Q water, aliquoted and stored at -20 °C.

Name	Sequence (5'-3')	Target	Objective
hEphA1-For	GTGGACACTGTCATAGGAGAAGG	EphA1	qPCR
hEphA1-Rev	GGTCTTAATGGCCACAGTCTTG	EphA1	qPCR
hEphA3-For	GTTCTCTGGGAGGTGATGTCTT	EphA3	qPCR
hEphA3-Rev	GGGTCTGTTGTTCCTGTCTTTC	EphA3	qPCR
hBLK-For	CTCCCAAGGCTGATTGACAT	BLK	qPCR
hBLK-Rev	GTGAAGACCCCGAAGTGGAT	BLK	qPCR
hCDK15-For	ATGTCTCAGCATCCAGGAGG	CDK15	qPCR
hCDK15-Rev	CCCTGTGAAGAACGTGTTGG	CDK15	qPCR
hBeta-actin-For	CATGTACGTTGCTATCCAGGC	Beta-actin	qPCR
hBeta-actin-Rev	CTCCTTAATGTCACGCACGAT	Beta-actin	qPCR
M1-T108A-For	GCTCAAAAGGGAAATTGCATTCCATGGGGCCAAGGAGGTAC	IAV-M1	Mutagenesis
M1-T108A-Rev	CTTGGCCCCATGGAATGCAATTTCCCTTTTGAGCTTCCTGTAC	IAV-M1	Mutagenesis
M1-T108E-For	GCTCAAAAGGGAAATTGAATTCCATGGGGCCAAGGAGGTAC	IAV-M1	Mutagenesis
M1-T108E-Rev	CTTGGCCCCATGGAATTCAATTTCCCTTTTGAGCTTCCTGTAC	IAV-M1	Mutagenesis
PB2-T471A-For	CGACATGACCCCAAGTGCTGAGATGTCGCTGAGGGGA	IAV-PB2	Mutagenesis
PB2-T471A-Rev	GCGACATCTCAGCACTTGGGGTCATGTCGGGTAATATCCCG	IAV-PB2	Mutagenesis
PB2-T471E-For	CGACATGACCCCAAGTGAGGAGATGTCGCTGAGGGGA	IAV-PB2	Mutagenesis

PB2-T471E-Rev	GCGACATCTCCTCACTTGGGGTCATGTCGGGTAATATCCCG	IAV-PB2	Mutagenesis
PA-YS393,395FA-For	CAGCGATTTGAAACAGTTTGACGCCGATGAGCCAGAACAAAGATC	IAV-PA	Mutagenesis
PA-YS393,395FA-Rev	GTTCTGGCTCATCGGCGTCAAACTGTTTCAAATCGCTGACATCCTTG	IAV-PA	Mutagenesis
PA-Y393E-For	CAGCGATTTGAAACAGGAGGACAGCGATGAGCCAGAACAAAGATC	IAV-PA	Mutagenesis
PA-Y393E- Rev	GTTCTGGCTCATCGCTGTCCTCCTGTTTCAAATCGCTGACATCCTTG	IAV-PA	Mutagenesis
PA-S395E-For	CAGCGATTTGAAACAGTATGACGAGGATGAGCCAGAACAAAGATC	IAV-PA	Mutagenesis
PA-S395E-Rev	GTTCTGGCTCATCCTCGTCATACTGTTTCAAATCGCTGACATCCTTG	IAV-PA	Mutagenesis
PA-YS393,395EE-For	CAGCGATTTGAAACAGGAGGACGAGGATGAGCCAGAACAAAGATC	IAV-PA	Mutagenesis
PA-YS393,395EE-Rev	GTTCTGGCTCATCCTCGTCCTCCTGTTTCAAATCGCTGACATCCTTG	IAV-PA	Mutagenesis
NP-Y148F-For	GAATGATGCTACATTTCAGAGAACAAGGGCACTTG	IAV-NP	Mutagenesis
NP-Y148F-Rev	CTTGTTCTCTGAAATGTAGCATCATTCAGGTTGGA	IAV-NP	Mutagenesis
NP-Y148E-For	CTGAATGATGCTACAGAGCAGAGAACAAGGGCACTTGTGC	IAV-NP	Mutagenesis
NP-Y148E-Rev	GCCCTTGTTCTCTGCTCTGTAGCATCATTCAGGTTGGAATG	IAV-NP	Mutagenesis
NP-T378A-For	CAATGGAATCCAGTGCTCTTGAATTGAGGAGCAG	IAV-NP	Mutagenesis

NP-T378A-Rev	TCAATTCAAGAGCACTGGATTCCATTGTCTCCATG	IAV-NP	Mutagenesis
NP-T378E-For	GACAATGGAATCCAGTGAGCTTGAATTGAGGAGCAGATATTGG	IAV-NP	Mutagenesis
NP-T378E-Rev	TGCTCCTCAATTCAAGCTCACTGGATTCCATTGTCTCCATGTTC	IAV-NP	Mutagenesis
NS1-T197A-For	GAATCTCTGTAGAGCTTCAGAGACTCGAACTGTGTTATCAT	IAV-NS1	Mutagenesis
NS1-T197A-Rev	ATGATAACACAGTTCGAGTCTCTGAAGCTCTACAGAGATTC	IAV-NS1	Mutagenesis
NS1-T197E-For	CTTCTCCAAGCGAATCTCTGTAGCTCTTCAGAGACTCGAACTGTGTTAT	IAV-NS1	Mutagenesis
NS1-T197E-Rev	ATAACACAGTTCGAGTCTCTGAAGAGCTACAGAGATTCGCTTGGAGAAG	IAV-NS1	Mutagenesis

2.1.9.2 Oligonucleotides used for siRNA knockdown

siRNAs were purchased from Ambion Silencer® Select siRNA, Thermo Fisher, or Origene, Germany. siRNAs were dissolved in RNAse-free water, aliquoted and stored at -20°C.

Name	Species	Supplier	CAT#
Silencer select Strn siRNA	Mouse	Origene	SR420066
Silencer select Strn3 siRNA	Mouse	Thermo Fisher Scientific	Assay ID s97012
Silencer select EphA1 siRNA	Human	Thermo Fisher Scientific	Assay ID s223490
Silencer select EphA3 siRNA	Human	Thermo Fisher Scientific	Assay ID s4724

Name	Species	Supplier	CAT#
Silencer select BLK siRNA	Human	Thermo Fisher Scientific	Assay ID s199570
Silencer select CDK15 siRNA	Human	Thermo Fisher Scientific	Assay ID 1140
Control scramble siRNA	Human/mouse/ rat	Thermo Fisher Scientific	D-001810-10-05
Silencer™ Select Negative Control No. 2 siRNA	Human/mouse/ rat	Thermo Fisher Scientific	4390846

2.1.10 Plasmids

Construct	Vector backbone	Source
pCAGGS-SC35M-PB1	pCAGGS	Kind gift from Prof. M. Schwemmle, Freiburg
pCAGGS-SC35M-PA	pCAGGS	Kind gift from Prof. M. Schwemmle, Freiburg
pCAGGS-SC35M-NP	pCAGGS	Kind gift from Prof. M. Schwemmle, Freiburg
pCAGGS-SC35M-HA	pCAGGS	Kind gift from Prof. M. Schwemmle, Freiburg
pCAGGS-SC35M-NA	pCAGGS	Kind gift from Prof. M. Schwemmle, Freiburg
pCAGGS-SC35M-M1	pCAGGS	Kind gift from Prof. M. Schwemmle, Freiburg
pCAGGS-SC35M-M2	pCAGGS	Kind gift from Prof. M. Schwemmle, Freiburg
pHW2000-SC35M-PB2	pHW2000	Schmitz Lab

Construct	Vector backbone	Source
pHW2000-SC35M-PB1	pHW2000	Schmitz Lab
pHW2000-SC35M-PA	pHW2000	Schmitz Lab
pHW2000-SC35M-NA	pHW2000	Schmitz Lab
pHW2000-SC35M-HA	pHW2000	Schmitz Lab
pHW2000-SC35M-NP	pHW2000	Schmitz Lab
pHW2000-SC35M-NS	pHW2000	Schmitz Lab
pHW2000-SC35M-M	pHW2000	Schmitz Lab
pHW72-Luci	pHW72	Schmitz Lab
pCI-neoRenilla-Luci	pCI-neo	Schmitz Lab
pPOLI-CAT-RT	pUC19	Pleschka Lab

2.1.11 Instruments

Type	Source
Cell culture incubator (NU-58xx)	IBS tecnomara
Cell culture microscope	Hund
Cell culture centrifuge 5810	Eppendorf
Centrifuge RC6 Plus	Thermo
Centrifuge 5424R	Eppendorf
ChemiDoc Touch	Bio-Rad
Confocal LSM810 microscope	Zeiss

Type	Source
Culture Hood (MSC 1.2)	Thermo
Western blot developing machine	Afga
Fine scale (Mettler PM460)	Mettler Toledo
Heat block	Thermomixer pro
Luminometer	Berthold technologies
GloMax Discover Microplate Reader	Promega
Magnetic stirrer	Qiagen
Microwave oven	Thermo
pH meter	Mettler Toledo
T100™ Thermal Cycler	Bio-Rad
Power Supply	Cleaver scientific
Real time PCR machine 7300	Applied biosystem
Scale	Mettler Toledo
Bioreader®-6000 FZ	BioSys
SDS-PAGE gel system	Bio-Rad
Semi-dry membrane transfer device	Bio-Rad
Stirrer	IKA
C25 incubator shaker	New Braunswick
Sonicator	Branson
Spectrophotometer	Eppendorf
Typhoon scanner	Cytiva

Type	Source
Ultracentrifuge LE-80	Beckman Coulter
UV 1800 crosslinker	Stratagene Stratalinker
Vacuum drier (Savant SpeedVac Concentrator)	Thermo
Vortex (8VTX-3000L)	LMS
Water bath	Julabo, GFL

2.1.12 Software

Image Lab 6.0.1 (Bio-Rad) was used to analyze Western blot data. Fiji was used for densitometric analysis of Western blot data. GraphPad Prism 9 (GraphPad Software, La Jolla, CA, USA) was used to prepare graphs and perform statistics. Data representation was done using MS-Office. The statistical significance of differences between the indicated groups was tested by using the unpaired Student's t-test in SPSS 19. Protein structures were visualized using PyMOL (Schrödinger LLC). Processing of Confocal microscopy pictures and calculation of scale bars was done using Zen Lite software (ZEN3.1, blue edition).

2.1.13 Buffers and solutions

All buffers and solutions were prepared in fresh deionized Milli-Q water unless stated otherwise. Recipes for buffers are given at the beginning of the corresponding methods described in the methods section. Autoclaved Milli-Q water was used for molecular and cell-culture experiments.

50x Tris-acetate-EDTA (TAE)
0.05 M EDTA
2 M Tris (pH 8.3)
1 M Acetic acid

10x Tris buffered saline (TBS-T)

250 mM Tris (pH 7.4)
1.37 mM NaCl
50 mM KCl
7 mM $CaCl_2$
1 mM $MgCl_2$
0.1% (v/v) Tween 20

DMEM/BSA/P/S (infection medium for MDCK-II, A549, MLE-15 and 293T)

492 ml DMEM
5 ml Penicillin/Streptomycin (P/S, 100x)
3 ml BSA (30% (v/v))

Phosphate-Buffered Saline (10x PBS)

0.137 M NaCl
0.27 mM KCl
8.1 mM Na_2HPO_4
1.47 mM KH_2PO_4
Total volume was adjusted to 1 L with H_2O and autoclaved.

Ca^{2+}/Mg^{2+} (100x) (100ml)

1.32 g $CaCl_2$
1 g $MgCl_2$
These reagents were dissolved in 100 ml ddH_2O and then autoclaved and filtered through 0.2 µm membrane disc filters.

PBS/Ca^{2+}/Mg^{2+}/BSA/P/S (100 ml)

10 ml 10x PBS (see above)
87.4 ml ddH_2O (sterile)
1 ml Penicillin/Streptomycin (10000 U/mL Penicillin, 10000 µg/mL Streptomycin)
0.6 ml BSA (30% (v/v))
1 ml 100x Ca^{2+}/Mg^{2+} (see above)

Avicel Stock (2.5% (w/v))

5 g Avicel-powder was dissolved in 200 ml ddH_2O and then autoclaved.

Avicel Medium (100 ml) for focus assay

10 ml 10x MEM

33 ml ddH_2O
1 ml Penicillin/Streptomycin liquid (10000 U/mL Penicillin, 10000 µg/mL Streptomycin)
1 ml BSA (30% (v/v))
50 ml avicel stock (2.5% (w/v))
1 ml 1% (v/v) DEAE-Dextran
4 ml $NaHCO_3$ (7.5% (v/v), pH=9.0)

Acetate buffer (1x)
7.708 g ammonium acetate powder
534 µl H_2O_2 (30% (v/v))
1950 ml dH_2O
pH was adjusted to 5.0 and fill up till 2 L

AEC staining solution (for one 96 well titration plate, 4.5 ml)
4.5 ml 1x acetate buffer
225 µl 20x AEC substrate (25 mg AEC in 2.5 ml Dimethylformamide)
10 µl H_2O_2 (30% (v/v))

2.1.14 Biosafety

All experiments using infectious virus were performed in accordance with German biosafety regulations pertaining to the propagation of IAVs. All experiments involving H5N1-type and H7N7 (SC35M) HPIAV IAV were performed using Biosafety Level 3 containment laboratories approved for such use by the local authorities (RP, Giessen, Germany).

2.2 Methods in molecular biology

2.2.1 Transformation of chemically competent bacterial strains

Lysogeny broth (LB) medium:	1 % (w/v) tryptone; 0.5 % (w/v) yeast extract; 1 % (w/v) NaCl
Lysogeny broth (LB) agar:	LB medium with 1.5 % (w/v) agar with respective antibiotics

Super optimal broth (SOC) medium:	Super optimal broth (SOC) medium: 2 % (w/v) tryptone; 0.5 % (w/v) yeast extract; 10 mM NaCl; 2.5 mM KCl; 10 mM $MgCl_2$; 10 mM $MgSO_4$; 20 mM Glucose

To transform chemically competent *Escherichia coli* Top 10 or XL1-blue strains, 100 µl of the competent cells were thawed on ice. Then up to 50 ng of plasmid DNA or 10 µl of a ligation mixture (section 2.2.6) were added to the competent cells and gently mixed thoroughly. After 30 minutes incubation on ice, the mixture of chemically competent bacteria and DNA were heated at 42 °C for 90 seconds and then incubated on the ice for 2 minutes. 750 µl of prewarmed SOC medium or LB medium with no selective antibiotic were added and the tubes were incubated at 37 °C for 1 hour with shaking at 225 rpm. Afterwards, 150 µl of the transformation mixture concentrated by centrifuging at 3000 rpm for 2 minutes was plated on LB-ampicillin agar plates. Following the incubation at 37 °C overnight, single colonies were picked and inoculated in LB medium with ampicillin and grown on a shaker overnight at 37 °C. The next day, plasmid DNA was isolated from this bacterial culture. The long-time storage of bacterial isolates was prepared by mixing 930 µl bacterial culture with 70 µl sterile 100% (v/v) DMSO. The stocks were kept at -80 °C for future use.

2.2.2 Isolation of plasmid DNA

For rapid and small-scale preparation of plasmid DNA from transformed *E. coli* cultures, the GeneJET Plasmid Miniprep Kit (source see section 2.1.9) was used according to the manufacturer´s instructions. Briefly, individual clones were picked and grown in 3 ml LB medium supplemented with ampicillin (100 µg/ml) and grown overnight at 37 °C while shaking at 200 rpm. Then the 1.5 ml bacterial culture were harvested by centrifugation at 5000 rpm for 2 minutes at room temperature (RT). The supernatants were removed and the bacterial pellets were resuspended in 250 µl of the resuspension solution. For bacterial lysis, 250 µl lysis solution were then added and mixed by gentle inverting of the microcentrifuge tubes. Thereafter the lysate was neutralized with 350 µl of neutralization solution and mixed thoroughly. The mixtures were centrifuged at 14000 rpm for 5 minutes and the supernatants without white precipitate were then transferred to the supplied GeneJET spin column. After centrifugation at 14000 rpm for 1 minute, the flow-through was then discarded and the “GeneJET spin column” was washed by adding 500 µl washing buffer and centrifuged at 14000 rpm for 1 minute. The spin column was washed

again using 500 µl of washing buffer and centrifuged at 14000 rpm for 1 minute. The flow-through was discarded and the empty spin column was then centrifuged at 14000 rpm for an additional 1 minute to remove the residual wash buffer. To elute DNA, the "GeneJET spin column" was transferred to a clean 1.5 ml microcentrifuge tube, 50 µl of elution buffer were loaded to the center of the column. After 2 minutes at room temperature, the column was centrifuged at 14000 rpm for 2 minutes. The purified DNA was kept in -20 °C until use.

For large-scale preparation, plasmid DNA was extracted and purified using the GeneJet Plasmid Maxiprep purification kit. The bacterial cultures containing the correct plasmids of interest, confirmed by restriction digestion and sequencing of the extracted plasmid DNA from small-scale preparations, were grown in 250 ml of LB media with dilution of 1:1000 in 37 °C with shaking at 220 rpm for 16 hours. Pelleted bacterial cells are concentrated by centrifugation at 5000 × g for 10 minutes and resuspended in 6 ml of resuspension buffer containing RNase A and then 6 ml of the lysis buffer were added. The whole mixture was mixed gently and incubated at RT for 2 minutes and neutralized with 6 mL of neutralization solution. 0.8 mL of the endotoxin binding reagent was the added. After incubation 5 minutes at room temperature, the mixture was centrifuged at 20000 rpm and 4 °C for 20 minutes. The supernatant mixed with 1 volume of 96% ethanol was then applied to the Gene JET Maxi purification columns. After centrifugation for 3 minutes at 2000 × g in a swinging bucket rotor. The flow-through was discarded and the column was placed back into the same collection tube. For further washing, the column was treated with 8 ml of wash solution I once and 8 ml of wash solution II twice. The plasmid DNA was then eluted with 750 µl elution buffer.

The concentration of the DNA was quantified by measuring the OD at 260 nm. An OD260 of 1.0 corresponds to 50 µg/ml of DNA. The ratio of the OD_{260nm}/OD_{280nm} was used to control the purity of the samples; DNA samples having a ratio between 1.8 and 2 were further used in experiments and also stored at -20 °C.

2.2.3 Site-directed point mutagenesis

Candidate phosphorylation sites were mutated either in order to prevent phosphorylation (Ser/Thr to Ala or Tyr to Phe) or to mimic phosphorylation by changing to Glu. Mutations were introduced by point mutagenesis with Stratagene Quikchange II site-directed mutagenesis kit according to manufacturer's protocol. The procedure utilizes a plasmid with an insert of interest as a template and two synthetic oligonucleotide primers, both

containing the desired mutation. The PCR reaction was prepared 0.2 ml PCR tubes on a T100 Thermal Cycler (Bio-Rad) with the following reagents:

Reaction Mixture	**Cycle steps**		
2.5 U *PfuUltra* HF DNA polymerase	Initial activation:	1 min at 95 °C	
5 µl 10x reaction buffer	Denaturation:	50 sec at 95 °C	x 20 cycles
1 µl dNTP mix (10 mM each)	Annealing:	50 sec at 55-65 °C	
125 ng forward primer	Elongation:	1 min/kb at 68 °C	
125 ng Reverse primer	Final elongation:	5 min at 68 °C	
10 ng plasmid (Template)	Hold	4 °C	
Milli-Q water (ad to 50µl)			

After completion of PCR cycling program, 1 µl of DpnI (10 U/µl) was directly added to each reaction and kept at 37 °C/2 hours to digest the parental methylated and hemi-methylated plasmid DNA strands. An aliquot of 8 µl of each reaction was then transformed into XL1-blue competent cells or Top 10 competent *E. coli* cells and the entire transformation reaction was plated on LB-Amp agar plates (section 2.2.1). The mutated plasmid DNA was isolated from the bacteria and further characterized by restriction digestion and sequencing.

2.2.4 Agarose gel electrophoresis

Tris-acetate-EDTA (TAE) buffer:	4 mM Tris (pH 8.3); 50 mM acetic acid; 1 mM EDTA

To prepare 0.8-1% agarose gel, appropriate amounts of agarose powder were completely melted in 50 ml 1x TAE buffer using a microwave oven. Before pouring to the casting platform, 2 µl ethidium bromide (EtBr, 10 mg/ml) were added to the liquid agarose. The DNA samples were then mixed with 6x loading dye before loading to the polymerized gel slots. The agarose gel electrophoresis was conducted in 1x TAE buffer with a constant voltage of 80 V for 45-60 minutes. The separated DNA bands was visualized under ultraviolet light (UV).

2.2.4.1 DNA extraction from agarose gels

After agarose gel electrophoresis, the DNA fragment of interest was excised from the gel using a clean scalpel for purification. The DNA was purified using the SmartPure Plasmid Kit (source see 2.1.9) according to the manufacturer's instructions.

2.2.5 Restriction digestion of DNA

For analytical cleavage of plasmid DNA or PCR products at specific sites, the following reaction mix was incubated for 1 hour at an enzyme-specific temperature (in general 30 °C or 37 °C):

Reaction Mixture	
DNA	0.5 µg
Restriction enzyme 1	1 U
Restriction enzyme 2	1 U
10x restriction buffer (or 2x Tango buffer)	2 µl
Milli-Q water	*ad* 20 µl

For cloning by restriction digest and ligation, the appropriate restriction enzymes were chosen to cut open a plasmid (backbone) and insert a linear fragment of DNA (insert) that has been cut by compatible restriction enzymes at an enzyme-specific temperature for 4 hours according to the following 40 µl reaction:

Reaction Mixture	
Plasmid DNA (backbone or insert)	3.5 µg
Restriction enzyme 1	10 U
Restriction enzyme 2	10 U
10x restriction buffer (or 2x Tango buffer)	4 µl
MilliQ water	*ad* 40 µl

2.2.6 Dephosphorylation of vector DNA

Dephosphorylation of vector DNA is recommended to avoid re-ligation of vector DNA in case of a single digest. 5' phosphate group from digested vector DNA was removed using 1 U of FastAP, followed by incubation at 37 °C for 1 hour. FastAP was inactivated by heating at 75 °C for 10 minutes.

2.2.7 Ligation of DNA fragments

Ligation of DNA fragments and vector plasmids was performed via enzymatic ligation. Dephosphorylated vector DNA (2.2.6) was mixed with insert DNA in a molecular ratio of 1:3 or 1:7. Ligation was performed in the following reaction with a decreasing temperature gradient for 16 hours.

Reaction Mixture	
vector DNA	100 ng
Insert DNA	1:3 or 1:7
10x T4 DNA ligase buffer	1 µl
T4 DNA ligase	1 U
MilliQ water	*ad* 10 µl

2.2.8 RNA extraction

2.2.8.1 Viral RNA extraction for sequencing full-length amplification of IAV genome

To confirm the occurrence of phosphosite mutations in IAVs, viral RNA was extracted from the supernatants of virus infected MDCK II cells using the “RNeasy Mini Kit” (Invitrogen) according to the manufacturer's instructions. 140 µl of virus-infected MDCK II supernatant was mixed with 600 µl Buffer RLT containing 1% (v/v) β-mercaptoethanol (β-ME) in a 1.5 ml microcentrifuge tube. Afterwards, 1 volume of 70% (v/v) ethanol was added to the sample, and mixed well by pipetting. After mixing, the tube was briefly centrifuged to remove drops from inside the lid and all the solution was loaded to the “RNeasy spin column”. The mixtures were centrifuged at 12000 rpm for 30 seconds. The filtrate was then discarded and the column was washed by adding 700 µl buffer RW1

and centrifuged at 12000 rpm for 30 seconds. The column was washed twice using 500 µl of buffer RPE and centrifuged at 12000 rpm for 30 seconds. The flow-through was discarded and the empty column was then centrifuged at 12000 rpm for an additional 2 minutes to remove the residual wash buffer. To elute DNA, 30–50 µl RNAse-free water was added to the “RNeasy spin column” and the solution was transferred to a clean 1.5 ml microcentrifuge tube.

2.2.8.2 Cellular RNA extraction

For cellular RNA extraction, 1.2 x 10^6 cells were harvested and washed with cold PBS (350 x g, 2 minutes). Lysis and DNA shearing was performed with RNeasy Mini kit (source see 2.1.9) and QIAshredder (Qiagen) according to the manufacturer’s instructions. Purified RNA was eluted with 25-50 µl RNase-free water and stored at -80°C. RNA concentration and purity was measured by an Eppendorf photometer using a microliter cuvette.

RNA concentration: 1 $OD_{260\ nm}$ = 40 µg/ml RNA

RNA purity: $OD_{260\ nm}/OD_{280\ nm}$ = 2.0

2.2.9 Full-length RT-PCR amplification of the segments of SC35M

The extracted viral RNA was reverse transcribed and amplified by PCR in a single reaction using SuperScript™ IV One-Step RT-PCR System. This System combines high-processivity SuperScript IV reverse transcriptase and high-fidelity Invitrogen™ Platinum™ SuperFi™ DNA polymerase to provide superior one-step RT-PCR performance. Using specific primers (Universal Hoffman primers), the PB2, PA, NP, M or NS segment of the recombinant SC35M virus, in which the mutation was introduced, was amplified in separate reactions.

Universal Hoffman primers

Segment		Primer Name
PB2	Forward primer	TATTGGTCTCAGGGAGCGAAAGCAGGTC
	Reverse primer	ATATGGTCTCGTATTAGTAGAAACAAGGTCGTTT
PA	Forward primer	TATTCGTCTCAGGGAGCGAAAGCAGGTAC
	Reverse primer	ATATCGTCTCGTATTAGTAGAAACAAGGTACTT
M	Forward primer	TATTCGTCTCAGGGAGCAAAAGCAGGTAG

	Reverse primer	ATATCGTCTCGTATTAGTAGAAACAAGGTAGTTTTT
NS	Forward primer	TATTCGTCTCAGGGAGCAAAAGCAGGGTG
	Reverse primer	ATATCGTCTCGTATTAGTAGAAACAAGGGTGTTTT
	Designed primers	
NP	Forward primer	AGCGAAAGCAGGGTAGATAATC
	Reverse primer	AGTAGAAACAAGGGTATTTTTCT

Reaction components of one-step RT-PCR

Component	**Volume**
2X Platinum™ SuperFi™ RT-PCR Master Mix	25 µl
Forward primer (10 µM)	1.25 µl
Reverse primer (10 µM)	1.25 µl
SuperScript™ IV RT Mix	0.25 µL
Template RNA (0.01 pg to 1 µg total RNA)	7.25 µL
Milli-Q water	(*ad* to 50 µl)

After gently mixing the reaction solution, the reaction was performed with the following parameters:

Cycling program		
Reverse transcription:	10 min at 55 °C	
RT inactivation/initial denaturation:	2 min at 98 °C	
Denaturation:	10 sec at 98 °C	x 35 cycles
Annealing	10 sec at 56 °C	
Elongation:	10 sec /kb at 72 °C	
Final elongation:	5 min at 72 °C	

The amplified PB2, PA, NP, M1 or NS1 gene of SC35M in separate reactions was purified by agarose gel purification, further confirmed by restriction digestion and sequencing. to confirm the occurrence of phosphosite mutations in IAVs.

2.2.10 Reverse transcription of cellular RNA

Total RNA extracted from (2.2.9.1) was converted to cDNA by reverse transcription using PrimeScript RT Master Mix cDNA synthesis Kit (2.1.9). The RNA sample (0.5 µg) was mixed with 1X PrimeScript RT Master Mix (containing PrimeScript RTase, RNase Inhibitor, Random 6 mers, Oligo dT Primer, dNTP Mixture, and reaction buffer) to a total volume of 10 µl RNase-free water. Reverse-transcription reaction was performed at 37 °C for 20 minutes, followed by heat inactivation of reverse transcriptase at 80 °C for 10 seconds. The resulting cDNA was diluted 1:10 and stored at -20 °C.

2.2.11 Real-time quantitative PCR (qPCR)

Relative expression of target genes was analyzed by real-time quantitative PCR (qPCR). PCR reactions were performed on a StepOnePlus Real-Time PCR system (Applied Biosystems) in 96 well PCR plates using the following cycling program:

Reaction Mixture	**Cycling program**		
1x SYBR Green ROX mix	Initial denaturation:	10 min at 95 °C	
0.2 µM primer 1	Denaturation:	15 sec at 95 °C	x 35 cycles
0.2 µM primer 2	Annealing:	30 sec at 60 °C	
2 µl cDNA (1:10)	Elongation:	30 sec at 72 °C	
Milli-Q water (*ad* 10µl)	Final elongation:	30 sec at 72 °C	

SYBR green was used as a fluorescence reporter for cDNA levels during amplification by PCR. During each cycle, fluorescence was emitted by the binding of SYBR-Green to the cDNA. This fluorescence in the reaction was measured and collected as fluorescent spectra. The intensity of fluorescence, directly proportional to the amount of DNA in each sample, was expressed as C_T value. The background detection threshold was set automatically by the StepOnePlus software. Every reaction was performed as triplicates and quantified with the $\Delta\Delta C_T$-method. The amount of PCR product in each sample was determined relative to that of the housekeeping gene (β-Actin) using the $\Delta\Delta C_{T-}$ method. The difference between CT values (ΔC_T) of the target gene and the housekeeping gene in each sample was calculated. These values were then transformed into absolute values

using the formula: $R = 2^{-\Delta\Delta_T}$ to compare a target gene's expression level. To confirm the specificity of the reactions, a melting curve analysis for each primer pair was included.

2.3 Methods in cell biology

2.3.1 Eukaryotic cell culture and maintenance

DMEM complete medium:	DMEM, high glucose + GlutaMAX with 10 % (v/v) FCS; 1 % (v/v) Penicillin/Streptomycin
Freezing medium:	10 % (v/v) DMSO in FCS

All cell lines used in this study (2.1.3) were cultured in Dulbecco's Modified Eagle Medium (2.1.6) supplemented with FCS and penicillin/streptomycin (DMEM complete medium) at 37 °C in a humidified atmosphere, with 5 % (v/v) CO_2. Cells were cultured in sterile 75 cm^2 or 175 cm^2 flasks (Sarstedt) (depending upon the cell number requirement) and routinely passaged at densities above 70 %. For passaging, cells were washed once with warm PBS and incubated with Trypsin/EDTA at 37 °C for 3 minutes for 293T cells, 5-7 minutes for MLE-15 and A549 cells, and 16 minutes for MDCK II cells. Trypsinization was stopped with fresh DMEM complete medium. An appropriate fraction of cells was distributed to new culture flasks or cells were counted and seeded according to the experimental plan. For long-term frozen storage, the pelleted cells were resuspended in freezing medium and transferred to CryoPure tubes (Sarstedt) and were slowly frozen down to -80°C, followed by transfer to -150 °C. For re-culturing, frozen cells were quickly thawed by incubation at 37 °C water bath for 2 minutes, washed with warm DMEM complete medium (300 x g, RT, 3 minutes), and seeded in prepared cell culture flasks.

2.3.2 Cell counting

To seed the appropriate number of cells according to the experimental plan or mere passaging, cell numbers were counted with a LUNA-II™ automated cell counter (Logos Biosystems). Cells were harvested by trypsinization and washed in DMEM complete medium (300 x g, 3 minutes, RT). The pellet was resuspended in an appropriate amount of fresh DMEM complete medium. Subsequently, 10 µl of cell suspension was mixed with 10 µl of Trypan blue dye and cells were counted according to the manufacturer's instructions. Cell concentration, size, and viability in the LUNA-II™ are measured based on the dye exclusion method. The basic principle is that the live cells possess intact cell membranes, hence excluding certain dyes, such as trypan blue, whereas dead cells with

a disrupted cellular membrane take up the dye and get stained. The cell counting algorithm was set automatically by the LUNA-II™ software.

2.3.3 Transfection of eukaryotic cells

Plasmid DNA was introduced into mammalian cells by transfection. One day before transfection, cells were plated to 50-70 % density in 10 cm cell culture Petri-dishes with DMEM complete medium. On the day of transfection, cells were washed with warm PBS, and an appropriate amount of transfection medium was added to the cells. Depending upon the requirement of transfection (transient or stable), different transfection reagents were used. For stable transfection, a DNA mixture was prepared by adding an appropriate amount of plasmid DNA (generally up to 4 µg) to Opti-MEM medium (Life Technologies). A Lipofectamine 2000 mixture was prepared by mixing Lipofectamine 2000 (1.25 µl per µg DNA) in Opti-MEM medium. After incubation for 5 minutes at RT, both the mixtures were mixed and vigorously mixed, followed by incubation for 30 minutes at RT. After that, the transfection mix was carefully added to the cells in a dropwise manner. For transient transfection, plasmid DNA was mixed with linear PEI (3 µg per µg of DNA, source see section 2.1.6) in DMEM without supplements. Cells were replaced with transfection medium (DMEM supplemented with 10 % (v/v) FCS). After approximately 6 hours, the transfection medium was replaced with DMEM complete medium, and cells were grown for 24-48 hours to allow for protein expression.

2.3.4 Virus propagation and infection in cell culture

PBS^{++}/BSA:	PBS containing 0.2% (w/v) BSA, 1 mM $MgCl_2$, 0.9 mM $CaCl_2$, 100 U/ml penicillin and 100 µg/ml streptomycin
Infection medium:	DMEM supplemented with 0.2% (w/v) BSA and 100 U/ml penicillin and 100 µg/ml streptomycin. The $H1N1_{pdm09}$ viruses were grown in the presence of 1 µg/ml of tosylsulfonyl-phenylalanyl-chloromethyl keton (TPCK)-treated trypsin.

The virus inoculum was prepared by adding the according amount of virus stock to a defined volume of PBS++/BSA depending on the desired multiplicity of infection (MOI) used for the experiment. The calculation of MOI was done as follows:

$$\frac{1000\ \mu l\ X\ \mu l\ virus}{Virus\ titer\ (FFU)} = \frac{X\ \mu l\ virus}{MOI x\ cell\ amount\ in\ the\ culture}$$

In general, cells (MDCK II, A549, MLE-15 or 293T) were grown to 90% confluency and infected with the desired viral stocks. For virus propagation, MDCK II cells in 165 cm^2 culture flask were washed once with PBS and 5 ml of PBS^{++}/BSA containing virus dilution corresponding to a MOI of 0.001 were added. This was followed by 1 hour of incubation at a RT. Subsequently the inoculum was removed, cells were washed with PBS and further incubated in Infection medium at 37 °C for 2 days. The supernatant was collected and virus titer was determined by a foci-forming assay. For virus infection, cells were washed once with PBS^{++}/BSA, followed by the addition of the MOI-adjusted inoculum. Single cycle infections of A549 cells were synchronized on ice 1 hour, while multi-cycle infections were done at RT. After the adsorption time, the inoculum was removed and replaced by an appropriate amount of infection medium and cells were incubated for the desired periods at 37 °C. The supernatant was collected and virus titer was determined by a foci assay.

2.3.5 Generation and amplification of reassorted viruses by RG

Viral growth medium:	Opti-MEM supplemented with 0.2% (w/v) BSA and 100 U/ml penicillin and 100 µg/ml streptomycin

The recombinant wildtype (WT) or mutated IAVSC35M (A/seal/Mass/1-SC35M/1980 (H7N7)) were generated by RG technology using 1 µg each of the 8 plasmids (pHW2000 system) encoding the different virus segments. For this, a co-culture of 293T and MDCK II cells (ratio 3:1) was seeded in 6 well plates 24 h before transfection and were grown to 70% confluence. Then they were transfected using 10 µl Lipofectamine 2000 (section 2.3.3) with a combination of each of the 8 plasmids carrying the desired mutation. 6 hours after transfection, the transfection mixture was removed and the cells were incubated with 2 ml of viral growth medium. To verify the successful *de novo* propagation of influenza virus, the transfected dishes were screened for appearance of a cytopathic effect (CPE) and the harvested medium was screened for infectious particles (2.3.6, foci assay in MDCK II cells). The progeny viruses were amplified on MDCK II cells in 165 mm flasks by infection and titrated on MDCK II cells by foci assays as described in section 2.3.6, viruses were stored at -80 °C. The generation of all viruses was carried

out at biosafety level 3.

2.3.6 Foci assay

Fixing solution	PBS++ containing 4% (w/v) paraformaldehyde; 1% (v/v) Triton X-100
Washing solution	PBS++ containing 0.05% (v/v) Tween20
Acetate buffer (1x)	50 mM ammonium acetate; 8.8 mM H_2O_2; pH was adjusted to 5.0
20x AEC substrate	10 mg/ml AEC in DMF
AEC staining solution	10 µl H_2O_2 (30% (v/v)) and 1x AEC substrate in 4.5 ml 1x Acetate buffer

Infectious particles in the supernatants of the cells were quantified by foci assay on MDCK II cells grown in 96-well plates at 90% confluency. Cells were wash once with pre-warmed PBS^{++}. Virus dilutions were performed in the 96 well microtiter plates with U-form bottom. 20 µl virus samples were serially diluted in PBS++/BSA from 10^{-1} to 10^{-7} and then incubated 1 h at RT. The inoculum was replaced by 150 µl Avicel-medium. In the case of $H1N1_{pdm09}$, TPCK-treated trypsin (1 µg/ml) was added. The cells were further incubated for 24 h at 37 °C, 5 % (v/v) CO_2. To detect foci of infected cells resulting from an infectious particle, cells were fixed and permeabilized with 150 µl fixing solution in PBS^{++} and incubated at 4 °C overnight. The solution was then discarded and cells were washed 3x with washing solution. Next, the cells were incubated with 50 µl/well primary antibody recognizing the IAV NP protein diluted 1:100 in PBS^{++} containing 3% (w/v) BSA for 1 h at RT. Then cells were washed 3x in washing solution and incubated with 50 µl/well secondary antibody (Horse Radish Peroxidase (HRP)-conjugated anti mouse, 1:1000 diluted in PBS^{++}/3% BSA) diluted 1:1000 in PBS^{++} containing 3% (w/v) BSA, for 1 h at RT. Cells were then washed 3x with washing solution and incubated with 40 µl AEC staining solution for 40 minutes at 37 °C in the dark. After staining the substrate was removed and cells were washed 2x with H_2O to remove salts. To detect and quantify foci, the dried 96 well plates were scanned using a BioSys Bioreader® (BioSys, Karben, Germany). The viral foci were then counted to determine the viral titer using the following equation:

FFU/ml (stock) = (1/virus dilution) *(number of foci) *(Dilution factor)

where ffu is foci forming unit.

1/virus dilution: The reciprocal of virus dilution at which the foci were counted.

Dilution factor: 1000 / (µl of inoculum/well). Therefore, the well was infected with 50 µl of viral dilution solution, the dilution factor=1000/50=20.

The statistical analysis of data was done by unpaired t-tests which compared each condition with the respective control.

2.3.7 Preparation of cell extracts

Igepal buffer:	20 mM Tris/HCl (pH 7.4); 150 mM NaCl; 10 % (v/v) glycerol; 1 % (v/v) Igepal CA-630 (Sigma); freshly added: 10 mM NaF; 1 mM Na_3VO_4; 2 µg/ml aprotinin; 1 µg/ml leupeptin; 1 mM PMSF
M-PER lysis buffer	Commercially available Thermo Scientific™ 78503; freshly added: of 1x protease inhibitor cocktail (100x, Cell Signaling Technology, Cat#5871P3) and Halt™ phosphatase inhibitor cocktail (Thermo Fisher Scientific, Cat#1862495)
RIPA lysis buffer:	50 mM Tris/HCl (pH 7.4); 150 mM NaCl; 1 mM EDTA; 0.1 % (w/v) SDS; 0.5 % (w/v) sodium deoxycholate; 1 % (v/v) NP-40; freshly added: 10 mM NaF; 0.5 mM Na_3VO_4; 2 µg/ml aprotinin, 1 µg/ml leupeptin; 1 mM PMSF
5x SDS sample buffer:	250 mM Tris/HCl (pH 6.8); 10 % (w/v) SDS; 40 % (v/v) glycerol; 15 % (v/v) β-mercaptoethanol; 0.1 % (w/v) bromophenol blue

Cell lysis for protein extraction was done either under native or denaturing conditions. Native conditions were used to maintain protein interactions or enzymatic activity and achieved with buffers containing non-ionic detergents. Cell lysis for co-immunoprecipitation (co-IP) was performed with Igepal lysis buffer and lysis for kinase enzymatic assays in PamChip® analysis (PamGene International, s-Hertogenbosch, Netherlands) was performed with M-PER lysis buffer. Cell lysis for protein extraction under denaturing conditions was performed with RIPA lysis buffer. According to the experimental plan, cells were washed once with ice-cold PBS, harvested with a cell scraper, and pelleted by centrifugation (300 x g, 3 minutes, 4 °C). The cell pellet was resuspended in an appropriate volume of lysis buffer. For example, for cells grown on 10

cm dish 300 µl of Igepal buffer or RIPA lysis buffer was used. 150 µl of M-PER lysis buffer supplemented with 0.5% (v/v) Triton X-100 (inactive the virus), with fresh protease and phosphatase inhibitors in PamChip® analysis was used for up to 8.8 x 10^6 cells in 10 cm dishes. Subsequently, samples were incubated on ice for 30 minutes, followed by centrifugation (16000 x g, 10 minutes, 4 °C). The supernatant was transferred into a new tube for further use. Lysates were then used for downstream applications or were directly mixed with an appropriate volume of 1x SDS-sample buffer, boiled at 95 °C for 5 minutes and used for SDS-PAGE and Western blotting.

2.3.8 Subcellular fractionation of cells

Buffer A: 10 mM HEPES (pH 7.9); 10 mM KCl; 0.1 mM EDTA; 0.1 mM EGTA; 1 mM β-mercaptoethanol freshly added: 10 mM NaF; 1 mM Na_3VO_4; 2 µg/ml aprotinin; 1 µg/ml leupeptin; 0.5 mM PMSF

To check the sub-cellular localization of any target protein, subcellular fractionation is performed based on sedimentation of cellular organelles at differential centrifugation speeds in different lysis buffer. Cells in 6 cm dish were washed once with ice-cold PBS, harvested by scraping, and pelleted by centrifugation (3000 rpm, 2 minutes, 4 °C). Pellet was resuspended in 200 µl buffer A and incubated 10 minutes on ice. Subsequently, 5 µl of a 10 % (v/v) Igepal CA-630 solution was added to the lysates, and the samples were briefly vortexed. The lysate was cleared by centrifugation (13000 x rpm, 10 seconds, 4 °C). The supernatant was taken as the cytoplasmic fraction (C). The remaining pellet was washed three times with 500 µl buffer A and resuspended in 225 µl 1x SDS sample buffer. The samples were then sonicated twice for 30 seconds and were taken as the nuclear/chromatin fraction (N). All samples were mixed with 5x SDS sample buffer, boiled at 95 °C for 5 minutes and analyzed by SDS-PAGE and Western blotting.

2.3.9 Coating of glass coverslips

Coating solution: 0.02 mg/ml poly-L-lysine in distilled H_2O

To enhance adhesion of 293T cells to the coverslips for immunofluorescence staining assays (2.3.10), the coverslips were coated with poly-L-lysine. Lysine can be polymerized to any desired length, and poly-L-lysine will bind to most solid supports

through its charged side chains. The positively charged polymerized poly-L-lysine can facilitate binding of cells which carry an overall negative charge. Sterile 18 mm coverslips were placed in 12 well plates containing 250 µl poly-L-lysine (0.02 mg/mL) and incubated at 37 °C for 1 hour. Coverslips were pressed with a pipette tip every 15 minutes to make sure that the coverslips are not floating. After that, the poly-L-lysine solution was removed and collected for further re-use. The coverslips were air-dried under the hood for 15 minutes and the desired number of cells was subsequently plated.

2.3.10 Immunofluorescence staining

Fixation solution:	4 % (w/v) paraformaldehyde in PBS (pH 6.9)
Blocking solution	PBS with 10 % (w/v) BSA; 0.5 % (v/v) Triton X-100
Antibody solution:	PBS with 1 % (w/v) BSA; 0.5 % (v/v) Triton X-100

Immunofluorescence was performed to visualize the abundance and localization of proteins in single cells. Therefore, 293T cells were coated and grown on coverslips in 12 well plates. The treated cells were washed three times with PBS and fixed with 500 µl 4 % (v/v) paraformaldehyde at RT for 8 minutes. After having been washed for three times with PBS, cell membranes were permeabilized with 0.5 % (v/v) Triton X-100 and unspecific antibody binding was blocked with 10 % (w/v) BSA at RT for 1 hour. Cells were incubated with primary antibody solutions at 4 °C for 16 hours. Cells were washed three times with PBS and incubated with secondary antibodies for 2 hours at room temperature. Because secondary antibodies conjugated to fluorescent dyes were used, samples were covered from this step on. After incubation, cells were washed three times, and DNA was stained with 1 µg/ml Hoechst 33342. Coverslips were washed again and mounted on microscope slides with Mowiol mounting medium (Carl Roth). Slides were stored at 4 °C while being protected from light. Stained cells were analyzed and pictures taken with Zeiss Confocal LSM810 microscope. Samples were illuminated using a diode 405-nm laser, a DPSS 561-nm laser, and an Argon laser for 488-nm excitation. Pictures and calculation of scale bars were prepared with Zen Lite system (ZEN3.1, blue edition).

2.3.11 Determination of cell viability

The cytotoxicity of applied inhibitors was assessed by PrestoBlue™ (Thermo Fisher Scientific), which is a resazurin-based cell permeable reagent to assess cell viability as indicated by a color change. Cells (1x 10^4) were seeded on a 96-well plate and one day later cells were exposed to various concentrations of the inhibitors or DMSO in 90 µl of culture medium as a control. Viability was scored upon addition of 10 µl PrestoBlue™ reagent (10x stock), followed by incubation for 30 minutes at 37 °C in darkness and subsequent determination of absorbance at 570 nm using a GloMax Discover Microplate Reader (Promega).

2.3.12 SiRNA-mediated gene silencing

Expression of specific target genes was silenced using specific siRNA (from Thermo Fisher Scientific or Origene). siRNA from Origene comprises of a heterogeneous pool of unmodified siRNAs, all targeting the same mRNA sequence, resulting in high specificity of knockdown and minimal off-taget effects. One day before transfection, cells were plated to 10-15 % density with DMEM complete medium. On the day of transfection, cells were washed with warm PBS, and an appropriate amount of transfection medium (DMEM supplemented with 10% (v/v) FCS) was added to the cells. A siRNA mixture was prepared by mixing an appropriate amount of siRNA (generally up to 40 nM) with Opti-MEM. A Lipofectamine 3000 mixture was prepared by mixing Lipofectamine 3000 (1.25 µl per µg DNA) in Opti-MEM medium. After incubation for 5 minutes at RT, both the mixtures were mixed and vigorously mixed, followed by incubation for 30 minutes at RT. After that, the transfection mix was carefully added to the cells in a dropwise manner overnight. The medium was replaced with fresh growth medium 24 h after transfection. Cells were then transfected the second time two days after the first transfection using the same protocol. The cells were further incubated at 37 °C for 48 h prior to either infection or RNA purification and RT-qPCR. Knockdown of the target gene at mRNA level was confirmed by qPCR and/or Western blotting.

2.4 Methods in biochemistry

2.4.1 Sodium dodecyl sulfate polyacrylamide gel electrophoresis (SDS-PAGE)

Stacking gels:	4 % (v/v) acrylamide; 125 mM Tris/HCl (pH 6.8); 0.1 % (w/v) SDS; 0.1 % (v/v) APS; 0.1 % (v/v) TEMED
Separating gels:	6-15 % (v/v) acrylamide; 375 mM Tris/HCl (pH 8.8); 0.1 % (w/v) SDS; 0.05 % (v/v) APS; 0.05 % (v/v) TEMED
SDS running buffer:	25 mM Tris; 200 mM glycine; 1 % (w/v) SDS

Sodium dodecyl sulfate polyacrylamide gel electrophoresis (SDS-PAGE) allows the separation of proteins in an acrylamide gel matrix according to their molecular weight. Lysates obtained from cell lysis were mixed with 5x SDS sample buffer to achieve a final concentration of 1x SDS sample buffer (2.3.7). The sample was denatured by boiling at 95 °C for 5 minutes. Depending upon the molecular weight of the protein of interest, gels with different pore size can be prepared to contain 6-15 % (v/v) acrylamide. SDS-PAGE was carried out in a mini-gel apparatus (Bio-Rad), using a discontinuous SDS running buffer system. Gels were run at 80 V for 2-3 hours. A pre-stained molecular weight marker was loaded as a reference.

2.4.2 Western blot and immune detection

Transfer buffer:	50 mM Tris; 40 mM glycine; 20 % (v/v) methanol; 0.04 % (w/v) SDS
Tris Buffered Saline (TBS-T):	25 mM Tris (pH 7.4); 137 mM NaCl; 5 mM KCl; 0.7 mM $CaCl_2$; 0.1 mM $MgCl_2$; 0.1 % (v/v) Tween 20
Blocking buffer:	5 % (w/v) skimmed milk powder or BSA in TBS-T
Primary antibody solution:	1 % (w/v) skimmed milk powder or BSA in TBS-T; 0.05 % (v/v) NaN_3
Secondary antibody solution:	1 % (w/v) skimmed milk powder or BSA in TBS-T

For immune detection, proteins separated via SDS-PAGE (2.4.1) were immobilized on polyvinylidene fluoride (PVDF) membranes by Western blotting. The Western blot sandwich was prepared with two layers of Whatman papers soaked in transfer buffer and one layer of PVDF membrane pre-activated with methanol in between. Western blots were assembled from anode to cathode in a semi-dry blotting apparatus (Bio-Rad). The electrophoretic transfer was performed at 24 V for 1-3 hours, depending on the size of the proteins (at least 1 hour/gel). After protein transfer onto the PVDF membrane, unspecific antibody binding was blocked with skimmed milk or BSA as blocking buffer at RT for 1 hour. The membrane was then transferred to TBS-T solution containing the primary antibody and incubated at 4 °C for 16 hours. After that, the membrane was washed three times with TBS-T at RT (10 minutes/wash), followed by incubation with secondary antibody solution at RT for 1 hour. Secondary antibodies were directed against the species of the respective primary antibodies and conjugated with horse reddish peroxidase (HRP). After incubation with secondary antibodies, the membrane was washed three times with TBS-T at RT (10 minutes/wash). Proteins were detected on a ChemiDoc Touch imaging system (Bio-Rad) using freshly prepared enhanced chemiluminescence (ECL) solution.

2.4.3 Stripping of PVDF membrane for reprobing

Mild stripping buffer:	1.5% (w/v) glycine; 0.1-1% (w/v) SDS; 1% (v/v) Tween 20; pH 2.2

Stripping of PVDF membrane was done to detect different proteins on the same membrane. The membrane was stripped in stripping buffer at RT (5 minutes/wash), followed by two washes with PBS at RT (10 minutes/wash). Stripping was completed by two washes with TBS-T (5 minutes/wash). Stripped PVDF membrane was then incubated in blocking buffer, followed by incubation in primary antibody and ECL detection as described above.

2.4.4 Luciferase reporter assay

To test which mutation in the vRNP subunits affects viral polymerase activity, the Dual-Luciferase reporter assay system kit (Promega) was used according to manufacturer's protocol. Briefly, 293T cells were seeded in 6-well plates ($2x10^5$ cells/well) and co-transfected with either 1 µg each of pHW2000-SC35M-PB2, pHW2000-SC35M-PB1,

pHW2000-SC35M-PA, pHW2000-SC35M-NP, 200 µg each of the firefly luciferase reporter gene (pHW72-Luci) encoding the vRNA-like polI-transcript and 20 µg pCI-neoRenilla-Luci using PEI (Protocol see section 2.2.3). pCAGGs expressing plasmids encoding PB2, PB1, PA (each 125 ng) and NP (800 ng) were co-transfected with the firefly luciferase-encoding viral minigenome construct pHW72-Luci (50ng) and a plasmid (pCI-neoRenilla-Luci, 20 ng) coding for Renilla luciferase in 293T cells. Transfection was performed using PEI for 5 hours (see section 2.3.3). After 24 h post-transfection, the cells were harvested, washed, lysed 15 minutes with 150 µl of 1x passive lysis buffer. 10 µl LARII substrate was mixed with 2 µl of cell lysate in a luminometer tube and firefly luciferase activity was measured. After addition of 10 µl of stop and glow buffer, the bioluminescence of Renilla luciferase was determined using a luminometer (Berthold technologies). The relative activities were calculated after the normalization of the Renilla luciferase activities to the activities of the firefly luciferase.

2.4.5 Immunoprecipitation (IP)

Igepal buffer: 20 mM Tris/HCl (pH 7.4); 150 mM NaCl; 10 % (v/v) glycerol; 1 % (v/v) Igepal CA-630; freshly added: 10 mM NaF; 1 mM Na_3VO_4; 2 µg/ml aprotinin; 1 µg/ml leupeptin; 0.5 mM PMSF

For co-IP experiments, proteins from a cell lysate prepared in Igepal buffer were precipitated with antibodies bound to protein A/G sepharose beads (Millipore). In general, 25 µl beads per sample were equilibrated with IP buffer and mixed with 1 µg of antibody. Cell lysates were added and samples were rotated at 4 °C, while 10 % of the supernatants were collected as input controls. After 3 to 4 hours or overnight, beads were washed five times with 1 ml IP buffer at 4 °C for 10 minutes. Eluted proteins were subjected to further analysis such as MS or SDS-PAGE and Western blotting.

2.4.6 Intracellular crosslinking of protein complexes

Quench buffer: 200 mM Tris in PBS; pH 7.5

Crosslinkers: 2 mM of DSS or DSG in PBS

Because of the high abundance of lysine residues in M1, membrane-permeable and bifunctional lysine-to-lysine crosslinkers DSS and DSG (source see section 2.1.5), with

spacer arm lengths of 7.7 Å, and 11.4 Å, respectively, were used for *in vivo* crosslinking of M1 protein complexes. The 293T cells in 6 well plates expressing the 8-plasmid RG system expressing SC35M-WT M1 or M1T108A/E mutants were harvested 24 hours post-transfection (h.p.t.) and washed 3 times in cold PBS. The cells were subsequently crosslinked by the addition of DSS or DSG dissolved in 100 µl PBS to a final concentration of 2 mM. The reaction mixture was incubated for 30 minutes at room temperature. Crosslinking was quenched at RT for 15 minutes by the addition of 900 µl of PBS containing 200 mM Tris (pH 7.5) to a final concentration of 20 mM. The cells were then washed twice with PBS containing 20 mM Tris and lysed in Igepal buffer prior to analysis by SDS-PAGE.

2.4.7 IAV VLP production and purification

293T cells were seeded in 10-cm dishes in complete DMEM and were co-transfected with 6 µg each of pCAGGS-SC35M protein expression plasmids encoding HA, NA, and WT M1 or M1 T108A/E proteins by Lipofectamine 2000 (transfection protocol see section 2.3.3). 48 hours after transfection, the cell culture supernatants were clarified from cell debris by centrifugation at 2500 rpm for 5 minutes. The virus like particles (VLP) in the semi-purified supernatant (9.5 ml) were pelleted by careful layering 9.5 ml of the VLP preparation onto 5 ml of 30% (w/w) sucrose cushion, followed by ultracentrifugation with 28000 rpm for 2.5 h at 4 °C using Beckman SW32Ti rotor. The sediments were dissolved in 200 µl PBS and mixed with 1x SDS sample buffer for SDS-PAGE.

2.4.8 Primer extension analysis

For the *in vitro* reconstitution of the SC35M polymerase, five plasmids were co-transfected into 293T cells. The first plasmid, pPOLI-CAT-RT, contains the CAT open reading frame in minus sense as a reporter gene, flanked by the 3’ and 5’ noncoding regions of the NS RNA segment of influenza virus A/WSN/33 (H1N1). Expression of the influenza virus-like RNA is driven by a human RNA pol I promoter and a ribozyme sequence that generates the desired 3' end by autocatalytic cleavage. The other four plasmids, pCAGGS-PB1, -PB2, -PA, and -NP express the influenza SC35M PB1, PB2, PA, and NP proteins. These proteins are able to amplify and transcribe the influenza virus-like RNA expressed by pPOLI-CAT-RT into v-, c- and mRNA in the transfected 293T cells. The PA was expressed as WT and in the mutant forms carrying the indicated mutations at position 393 and 395. Using specific radioactive labeled primers, the

different forms of viral RNA (v-, c-, mRNA) and the 5S RNA (loading control) were separated by gel electrophoresis and detected by autoradiography.

2.4.8.1 Isolating RNA (Trizol Method)

To isolate total RNA from transfected cells, 293T cells were grown on 6 well plates to 70% confluency and transfected with 250 ng of plasmids encoding the vRNP components pCAGGS-SC35M-PB2, pCAGGS-SC35M-PB1, and pCAGGS-SC35M-PA wt or PA phospho-mutants,1 µg pCAGGS-SC35M-NP, together with 1 µg pPOLI-CAT-RT which expresses a vRNA-like Pol I-transcript encoding the CAT using PEI (transfection protocol see section 2.3.3). 48 hours after transfection, the total RNA (viral and cellular) was extracted with Trizol reagent (Invitrogen). Briefly, the medium was aspirated from transfected cells, 1 ml of Trizol was added to the cell monolayer in each dish and incubated together for 5 minutes at RT. Trizol-treated cells were transferred into a microcentrifuge tube and incubated at RT for 10 minutes. 200 µl of chloroform was added to each reaction tube, mixed properly and incubated for 10 minutes at RT with intermittent shaking. The microcentrifuge tubes were then centrifuged at 13000 rpm and 4 °C for 30 minutes. Later, 500 µl of the upper phase was transferred into fresh microcentrifuge tubes containing 500 µl isopropanol, mixed properly and incubated at RT for 10 minutes. Afterwards, the tubes were centrifuged at 13000 rpm and 4 °C for 20 minutes. The supernatant was then discarded carefully and 1 ml of 70% ethanol was added to the pellet and centrifuged at 13000 rpm for 5 minutes at 4 °C. Alcoholic supernatant in each tube was removed carefully, the pellet was air dried and dissolved in 30 µl of nuclease free water. The extracted RNA was used directly or kept at -70 °C until use. The concentration of extracted RNA was measured. 10 µg of RNA was taken from each sample and vacuum-dried and resuspend in 1 µl of nuclease free water.

2.4.8.2 Primer and marker labeling

Primers for primer extension of CAT		
Segment	**vRNA**	**cRNA and mRNA**
pPOLI-CAT-RT	CGCAAGGCGACAAGGTGCTGA	ATGTTCTTTACGATGCGATTGGG
Primers for primer extension of 5S rRNA		
5S rRNA	TCCCAGGCGGTCTCCCATCC (human 5S RNA)	

The gene-specific primers listed above were diluted into the concentration of 10 pmol/µl in RNase free H_2O and labelled along with 50 bp DNA Ladder (Roche DNA molecular weight marker XIII) according to the following 10 µl reaction:

1. Marker labelling

Reaction Mixture	
50 bp DNA Ladder (Roche marker XIII)	1 µl
RNase-free water	6 µl
10x PNK Buffer (Fermentas)	1 µl
(γ-^{32}P) ATP (3000 Ci/mmol, 10 µCi/µl)	1 µl
PNK (T4 polynucleotide kinase, 10 U/µl)	1 µl

2. Primer labelling

Reaction Mixture	
Primer (10 pmol/µl)	3 µl
RNase-free water	2 µl
10x PNK Buffer (Fermentas)	1 µl
(γ-^{32}P) ATP (3000 Ci/mmol, 10 µCi/µl)	3 µl
PNK (T4 polynucleotide kinase, 10 U/µl)	1 µl

The reaction mixture was well mixed and incubated at 37 °C for 1 h and then cleaned from the residual radioactive material using the “Qiagen Nucleotide Removal kit”. Briefly, 100 µl of PNK-buffer was added to each 10 µl labelling reaction mixture (10:1 (v/v)), mixed and applied to “QIAquick spin column” in 2 ml collection tubes. The column was then centrifuged at 6000 rpm for 1 minute. The collection tube containing the radioactive flow-through is appropriately discarded in radioactive waste. The column was then placed into a clean 2 ml collection tube, washed 2 times with 500 µl PE-buffer and centrifuged at 6000 rpm for 1 minute. The collection tube was discarded and replaced with a clean 1.5 ml microcentrifuge tube. To elute the labelled primers or DNA ladder, 40 µl nuclease-free water was added to the center of the column, followed by incubation for 1 minute at RT and centrifugation for 1 minute at 13000 rpm. The radioactively labelled

primers or DNA marker were directly used or stored at -20 °C in the isotope room for further work (~2 weeks). Before loading the sequencing gel, 40 µl of Fu-mix (6 M Urea, 80% (v/v) Formamide (deionized), 1x TBE, 0.1% (w/v) Bromophenol blue, 0.1% (w/v) Xylene cyanol FF) were directly added to the labeled DNA marker (40 µl). After heating at 95 °C for 5 minutes samples were cooled on ice 2 minutes, collected by brief centrifugation an and then immediately loaded onto the denaturing sequencing gel.

2.4.8.3 Reverse Transcriptase Reaction

For one cDNA reaction, 1 µl of Trizol-purified total RNA (10 µg) was mixed with 4 µl of the following primer-mix:

RNA-Primer Reaction Mixture	
RNase-free water	3 µl
^{32}P labelled Primer for vRNA (10 mmol/µl)	0.25 µl
^{32}P labelled primer for cRNA and mRNA (10 mmol/µl)	0.25 µl
^{32}P labelled primer for 5s rRNA100 (10 mmol/µl)	0.25 µl
Primer for 5s rRNA100 (unlabelled) (10 mmol/µl)	0.25 µl

The reaction mixture in a 1.5 µl microcentrifuge tube was heated at 95 °C for 3 minutes in a heat block and then incubated on ice for 5 minutes. The reaction mixture was then collected by centrifugation and 5 µl of the following 5 µl superscript mix was added:

Superscript Mixture	
RNase-free water	1.25 µl
5x RT buffer (Invitrogen)	2 µl
100 mM DTT (Invitrogen)	1 µl
100 mM dNTP (25 mM each, (Invitrogen))	0.5 µl
Superscript III (Invitrogen, 10 units/ µl)	0.25 µl

The mixture was then incubated at 45 °C for 1 hour for the reverse transcription (RT) reaction, then at 70 °C for 10 minutes to inactivate the Superscript III enzyme and cooled to 4 °C. The synthesized cDNA(s) was then precipitated and cleaned up by adding 3 µl

of 3 M sodium acetate (NaOAC, pH=5.2), 100 µl of absolute ethanol and incubated at -20 °C. The mixture was then centrifuged at 13000 rpm and RT for 30 minutes. The supernatant was discarded and the pellet was air-dried. The cDNA pellet was further cleaned by dissolving in 6 µl of RNase A mix which is composed of 1 µl RNase A (10 mg/ml) plus 49 µl of ddH_2O (1:50) and incubated at 37 °C for 20 minutes. Afterwards, 2.5 µl of K mix (2 µl proteinase-K (Invitrogen, 20 mg/mL) in 18 µl of ddH_2O) was added and incubated at 55 °C for minutes in a heat block.

2.4.8.4 Denaturing urea polyacrylamide gel electrophoresis

Sequencing gels: 8 % (v/v) acrylamide; 7 M urea; 0.1 % (v/v) APS; 0.1 % (v/v) TEMED in 1X TBE

8% Urea-Polyacrylamide small gel (Sequencing gel) (solutions are from Roth) was used**:**

Small gel (30 ml)	**8%**
Acrylamide concentrate (Solution #1)	9.6 ml
Acrylamide diluent (Solution #2)	17.4 ml
Acrylamide buffer (Solution #3)	3 ml
10% APS	250 µl
TEMED	25 µl

The above solution was mixed very well and poured between the assembled glass plates. These have been preassembled and have to be clean and free of grease using ddH_2O and 70% (v/v) ethanol and then precoated on one side (outer glass plate) with BlueSlick™ (Serva) to prevent the adhesion of the polymerized gel to the glass plate. After pouring the gel mixture the gels were incubated for 1 hour at RT until the gel polymerized and the gel was then fixed in the gel tank. The gel was pre-run at 40 W for 1 hour until the temperature of the gel has raised to 50 °C. Afterwards, 8.5 µl of Fu-mix loading dye was added to each sample, mixed and heated to 95 °C for 5 minutes. Then the samples were cooled on ice 2 minutes, collected by brief centrifugation and then 10 µl of each sample together with 5 µl labeled marker were loaded onto the sequencing

gel. The gel was run at 40 W until the blue dye was approximately 3 cm away from the bottom of the plate (2 h).

2.4.8.5 Quantification of cDNA bands derived from v-, c-, mRNA

When the gel run was finished, the glass plates were separated very carefully and the gel should stick to one of the glasses. The gel on the glass plates was transferred to Whatman paper and wrapped in cling film (plastic foil side at the top). After the gel was vacuum dried at 80 °C for 75 minutes, it was placed into the screen cassettes together with a phosphor image screen (Fuji Photo Film Co. Ltd.). The gel side should be exposed to the white side of the screen overnight. The screen was then scanned on a Amersham™ Typhoon™ and the bands were quantified using “Quantity One” software (Bio-Rad).

2.5 Methods in bioinformatics

2.5.1 Bioinformatic analyses of PamStation® and MS

The statistical analyses of the PamStation® platform were performed by Dr. Astrid Weiß (Department of Internal Medicine, Cardio-Pulmonary Institute, University of Giessen) and Dr. Vera V. Saul (Institute of Biochemistry, University of Giessen) with whom I closely cooperated in the discussion and data analysis. The prediction of corresponding upstream kinases responsible for selective peptide substrate phosphorylation was performed using Bionavigatornv. 6.2 software (PamGene). To identify kinase hubs, physical, genetic and functional interactions between the identified kinases were further analyzed using the STRING database (Version 11.5). The phosphosite consensus motifs were derived using using the Weblogo tool. The Statistical analyses of MS were performed by Dr. Axel Weber and Prof. Michael Kracht (Institute of Pharmacology, University of Giessen), and I participated in visualizing the Volcano plots. Proteomic data were realized by self-created scripts in R statistical language (R Core Team, 2017) including packages for R or for R/Bioconductor. Volcano plots were generated using the ggplot R package.

2.5.2 Sequence collection and alignment

All previously published full-length protein sequences of avian and human IAV (before August 2018) were collated from the Influenza Virus Resource at the National Center for Biotechnology Information (NCBI) (www.ncbi.nlm.nih.gov/genomes/FLU). laboratory strains were excluded from the analyses to eliminate sample biases. Identical sequences were collapsed and filtered to ensure that each strain was only represented once in the dataset. All assembled protein sequences were aligned using MAFFT v7 2 as available in the Cipres Science Gateway (https://www.phylo.org) with subsequent manual adjustment to correct frame shift errors using BioEdit. The downstream analyses were based on a data set of 16979 of PB2, 12956 of PB1, 16631 of PA, 1890 of HA-H7, 12599 of NP, 781 of NA-N7, 11755 of M, 12,643 of NS isolated from avian, 17719 of PB2, 16297 of PB1, 17040 of PA, 142 of HA-H7, 13875 of NP, 4 of NA-N7, 11591 of M, 11218 of NS human IAV sequences.

3 RESULTS

3.1 Comparative analysis of IAV-dependent kinase activity changes in human cells through peptide-based kinase activity profiling

3.1.1 H1N1$_{pdm09}$- and H5N1 induce distinct phosphorylation patterns based on PamStation® analysis

To comparatively analyze the IAV-dependent kinase activity changes, peptide-based kinase activity profiling was conducted using two IAV strains H1N1$_{pdm09}$ and H5N1. For this, the replication kinetics of both viruses in A549 alveolar epithelial cells (Ding et al., 2016) were firstly determined by monitoring viral proteins of H1N1$_{pdm09}$ or H5N1 at various time points of infection by Western blotting. Although detectable NP protein expression occurred slightly earlier in H5N1-infected cells, the expressed HA protein showed a similar kinetics at late time points (**Fig. 11A**). The virus replication was also assessed by indirect immunofluorescence, in which the H1N1$_{pdm09}$ or H5N1- infected A549 cells were fixed and analyzed for NP localization. NP, as a surrogate for vRNP, appeared in the nuclei of infected cells already a few hours post infection (h.p.i.) and started nuclear export at 5 h.p.i. (**Fig. 11B**). Further quantitative analysis of intracellular NP distribution confirmed that replication cycle kinetics of these two viruses were largely similar, although slightly faster for H5N1 (**Fig. 11C**).

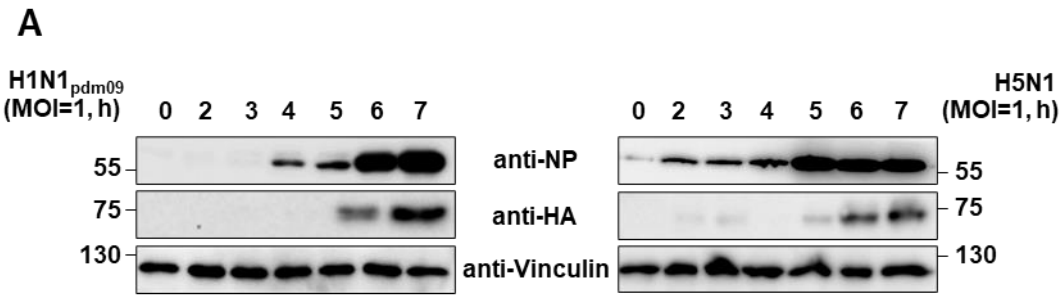

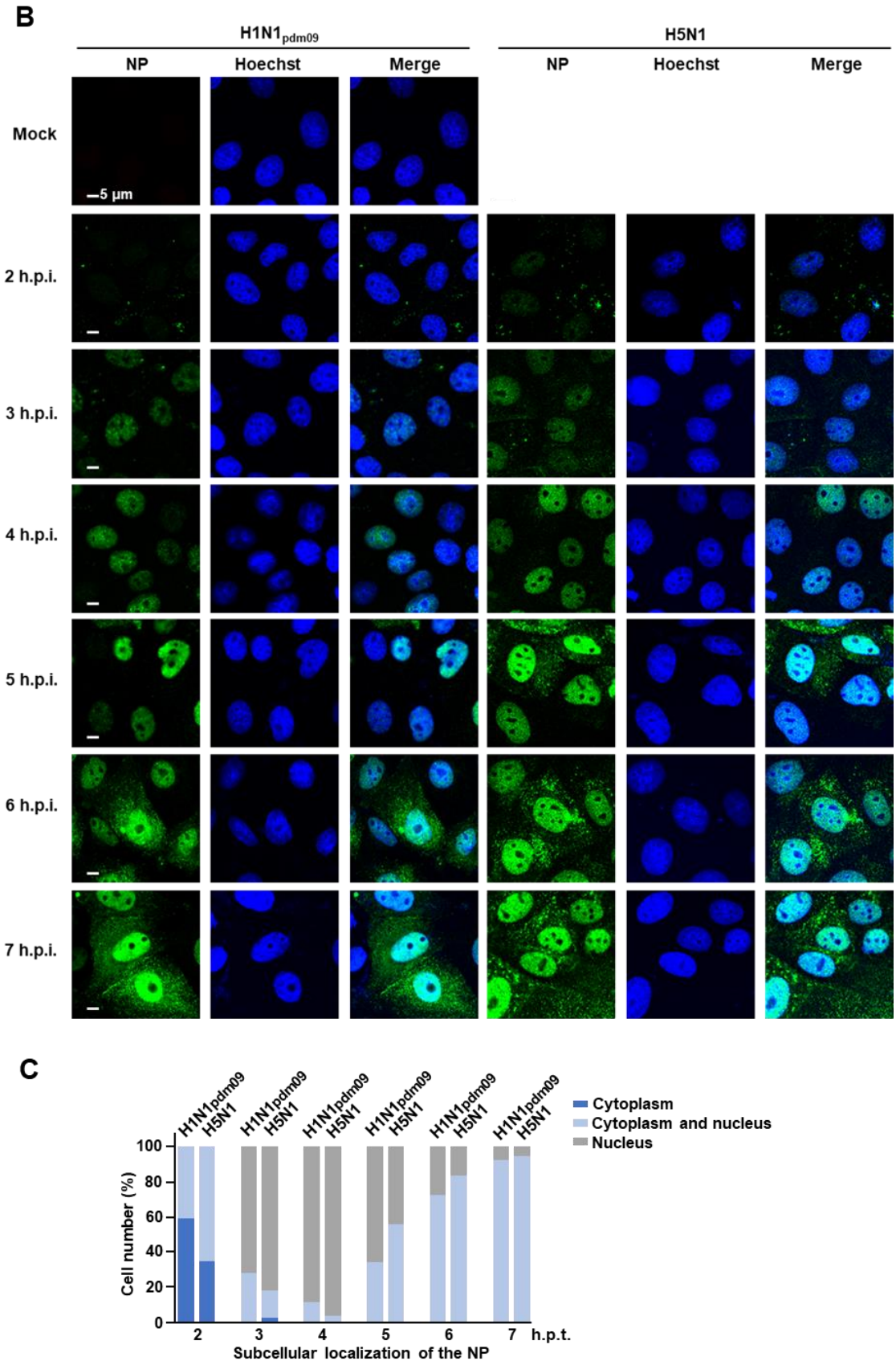

Figure 11: Replication kinetic analysis of H1N1$_{pdm09}$ or H5N1 in A549 cells.

(A) A549 cells were infected at 4°C for 1 h with $H1N1_{pdm09}$ or H5N1 (MOI = 1) and harvested at indicated times post infection. The expression of viral NP and HA proteins in cell lysates was detected by Western blotting. Three independent experiments were performed. The positions of molecular mass markers are indicated on the side of each panel, a representative experiment is shown. **(B)** Infected A549 cells (MOI = 1) were stained for IAV NP protein at the indicated time points and analyzed by indirect immunofluorescence. Nuclei were stained with Hoechst 33342, pictures are representatives of two independent experiments. **(C)** The experiment was performed as in (B). The intracellular distribution of NP was quantified for each condition from at least 150 interphase cells expressing NP under a confocal microscopy. The cellular location of NP was scored as predominantly cytoplasmic, nuclear and cytoplasmic, or predominantly nuclear, and the percentage of cells is shown.

To further profile the kinase activities in $H1N1_{pdm09}$ or H5N1 infected cells, a peptide-based PamChip® assays were performed, as schematically displayed in **Fig. 12A**. These PamChip® micro-arrays immobilized with peptides either allow the detection of phosphorylation by Tyr kinases (PamChip® PTK, 196 peptides) or by Ser/Thr kinases (PamChip® STK, 144 peptides). PamChip® system contains less than 1% of the human phosphoproteome (Morens et al., 2011), but represent many main kinase pathways and thus serve as a frequently used proxy to estimate the contribution of relevant kinase networks (Kheirollahi et al., 2019; Schwill et al., 2019). Active kinases present in cell extracts allow phosphorylation of distinct sets of peptides coupled to the respective chips. The phosphorylation patterns of these peptides are subsequently quantified by phosphorylation-specific antibodies, followed by computational prediction of the activity status of the upstream kinases with specificity for individual substrate peptides. Using this strategy, $H1N1_{pdm09}$- or H5N1 infection trigged the cellular phosphorylation responses in the A549 cells were examined at various stages of IAV replication cycle, namely 1-, 5-, and 8 h.p.i. prepared in two biological independent experiments.

Samples from the respective lysates prepared either from uninfected or virus-infected cells were first used to confirm kinase activity by detection of phosphorylation in the activation loop of several kinases, which are well-documented to be activated by IAV, such as c-jun N-terminal kinase (JNK), ERK, and protein kinase B (AKT) by Western blot analysis using phospho-specific antibodies (Pleschka et al., 2001; Sharma et al., 2020). These experiments showed that the phosphorylation levels of ERK, JNK, and AKT were steadily increasing over the course of H5N1 infection. In contrast, in the context of the human IAV strain $H1N1_{pdm09}$, the virus-induced ERK and JNK activation in A549 cells showed an immediate rise after infection (1 h.p.i.), and then a drop back to background level at 5 h.p.i, followed by a sharp increase again at 8 h.p.i.. AKT phosphorylation increased over time in $H1N1_{pdm09}$-infected cells, while there was no significant phosphorylation detected in H5N1-infected cells. Infection of the cells was controlled by

detection of the IAV-encoded NP protein (**Fig. 12B**). Overall, these experiments proofed the occurrence of virus-regulated phosphorylation in IAV-infected A549 cells, though with varying pattern between both strains.

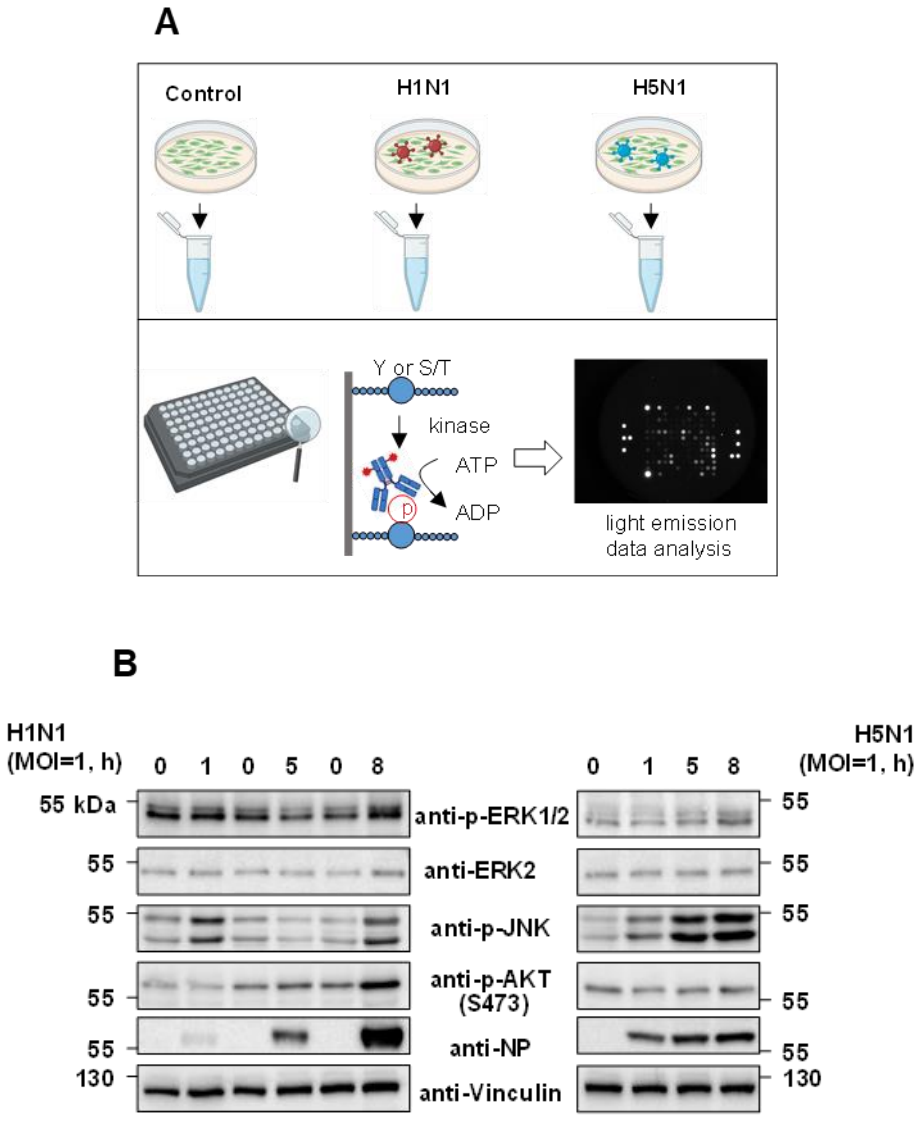

Figure 12: PamChip® analysis of IAV-induced kinases activity.

(A) Schematic display of the experimental workflow for PamChip® analysis. To generate cell lysates, A549 cells were infected with IAV strains $H1N1_{pdm09}$ or H5N1. Cell extract were further processed on PamChips® with a different set of substrate peptides immobilized on the chip surface. Active kinases present in the lysates phosphorylate their distinct peptide substrates, which can be detected by phospho-specific antibodies and appropriate FITC-labeled secondary antibodies to create a signal that can be quantified using a CCD sensor. Parts of the figure were created with BioRender.com. **(B)** A549 cells were infected at 4°C for 1 h with $H1N1_{pdm09}$ (refer as H1N1 for simplicity in the figure) or H5N1 (MOI = 1) as shown and incubated for the indicated time. Cell extracts were prepared, one part of which was used for the analysis of kinase activity and expression of the viral NP protein by Western blotting, while remaining material was used for the analysis

of kinase activities on PamChips®. The positions of molecular weight markers are indicated, a representative experiment is shown.

In a next step the remaining cell lysates were used for PamChip® experiments to determine phosphorylation at Tyr or Ser/Thr. For this, phosphorylation patterns between uninfected and $H1N1_{pdm09}$ or H5N1-infected cells at various h.p.i. were compared in biological and technical replicates. 100 highest-ranked peptides undergoing Tyr or Ser/Thr phosphorylation changes are displayed in **Fig. 13**. Phosphorylation patterns induced by two subtypes of IAV were overall distinct. With regard to the level of Tyr phosphorylation, $H1N1_{pdm09}$ infection induced strong phosphorylation changes at 5 h.p.i., whereas earlier and later time points showed only a few alterations (**Fig. 13A**). This kinetic was completely different in H5N1-infected cells, in which dynamically induced phosphorylation was observed at all time points of infection. At the level of Ser/Thr phosphorylation, $H1N1_{pdm09}$ infection led to a time-dependent increase of phosphorylation with a maximum at 8 h.p.i., while H5N1 infection caused a significant decrease in phosphorylation at 5 h.p.i.. (**Fig. 13B**).

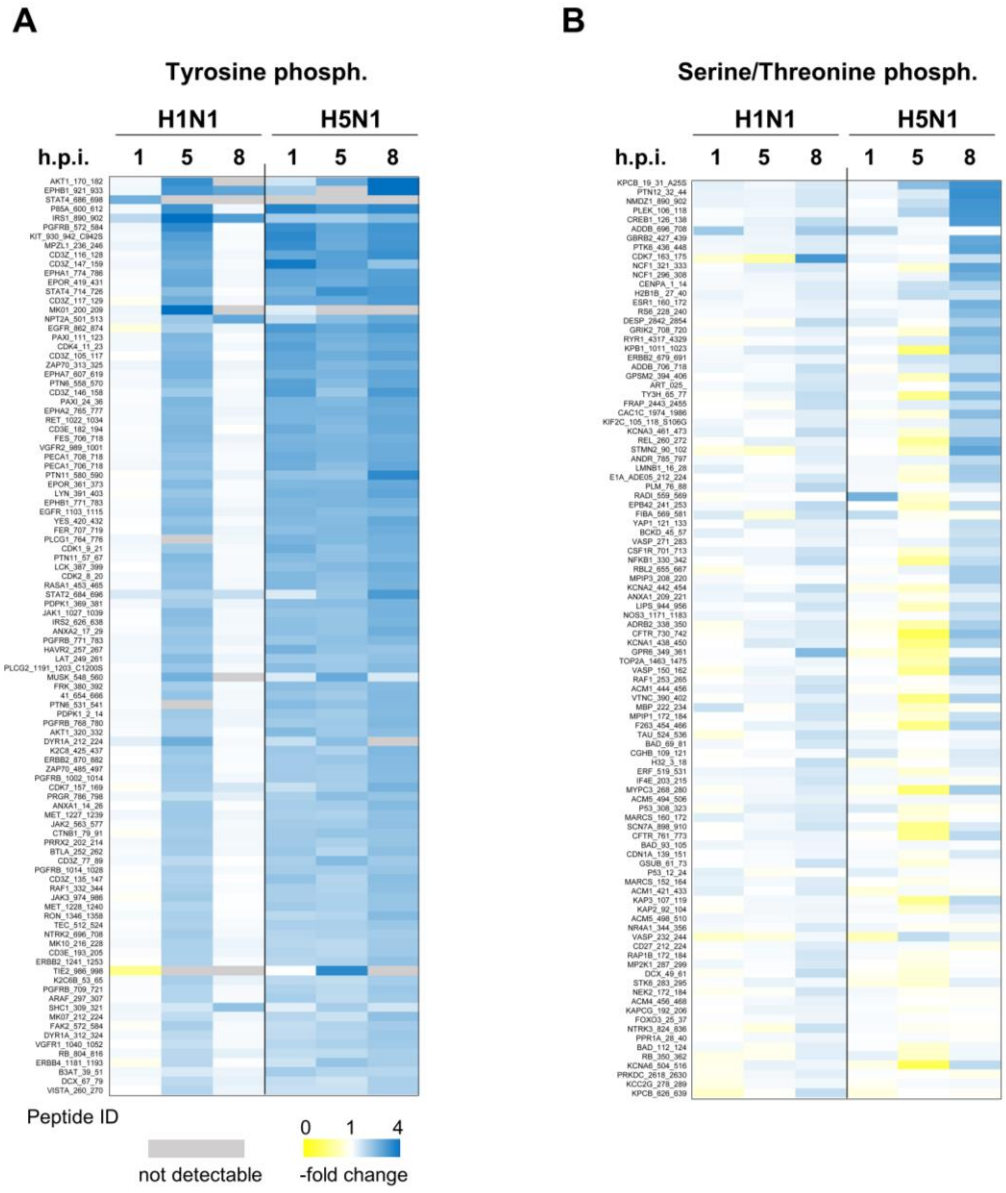

Figure 13: Dynamics of peptide phosphorylation pattern trigged by IAV-infected cells lysates.

(A) Pairwise comparisons of peptides (infected/uninfected) with a significant change in Tyr phosphorylation are displayed. Raw data of substrate peptide phosphorylation quantified from densitometry of fluorescence signals were used to calculate the mathematical mean value for both biological replicates. Ratios are given as relative fold change versus un-infected (for H5N1) or trypsin-treated un-infected control (for $H1N1_{pdm09}$) samples. **(B)** The experiment was done as in (A) with the difference that phosphorylation on STK PamChips® was analysed. Grey fields indicate that the signal was not detectable (= n.d.). PamChip® experiments were conducted in collaboration with Dr. Astid Weiß (Department of Internal Medicine, Cardio-Pulmonary Institute (CPI)).

Focusing on time-resolved Tyr phosphorylation, $H1N1_{pdm09}$-induced Tyr phosphorylation on peptides at 5 h.p.i also detected in H5N1 infection (**Fig. 14A**). Moreover, there was prominent and large overlapping phosphorylation between all time points of H5N1 infection. Furthermore, the characteristic of Tyr-phosphorylation sequence motifs for the

69 peptides regulated by $H1N1_{pdm09}$ and H5N1 at all time points were compared. This analysis revealed one motif containing an aliphatic amino acid at position +3 and another motif with acidic amino acids at position -3 (**Fig. 14B**). However, peptides with Ser/Thr phosphorylation showed no ($H1N1_{pdm09}$) or limited (H5N1) overlap between the different time points of infection (**Fig. 14C**). Only 4 peptides were undergoing regulated Ser/Thr phosphorylation by both viruses (**Fig. 14D**), which is in stark contrast to Tyr phosphorylation, which is largely shared between $H1N1_{pdm09}$ and H5N1. A motif analysis revealed that many peptides showing regulated Ser/Thr phosphorylation contain a basic amino acid at positions -2 and/or -3 (**Fig. 14E**). Taken together, these analyses imply that despite the apparently different kinetics of phosphorylation induced between $H1N1_{pdm09}$ and H5N1, both viruses preferentially induce Tyr kinases that phosphorylate a largely overlapping number of peptide substrates.

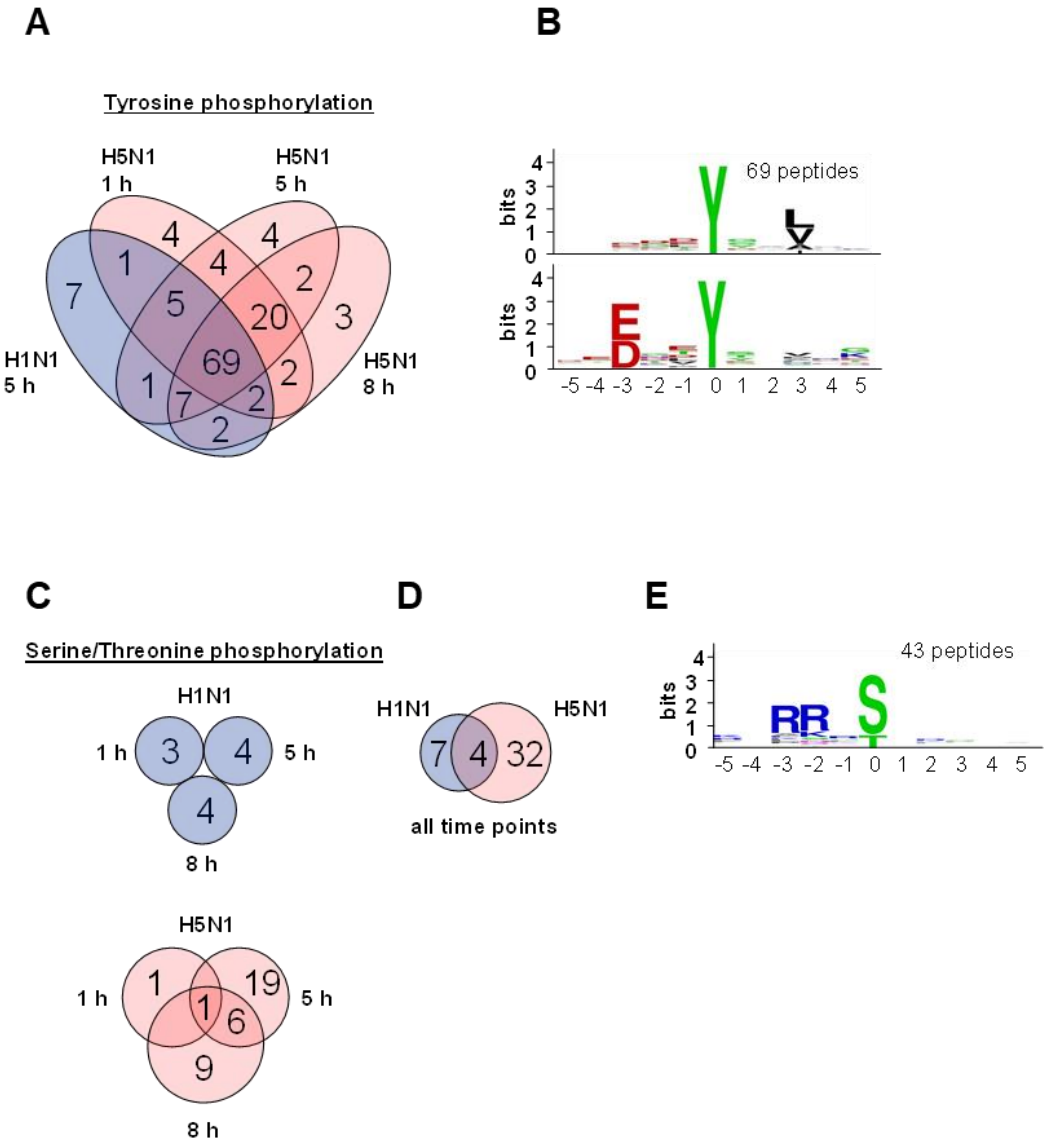

Figure 14: Time-resolved analysis of IAV-regulated protein phosphorylation events.

(A) Venn diagram of overlap between any two viruses in terms of regulated Tyr phosphorylation with a statistically significance ($p<0.05$, up- or down-regulation), corresponding to the time of their occurrence. As the number of peptides regulated by $H1N1_{pdm09}$ infection after 1 or 8 h.p.i. was too small to be included in this analysis, only the value 5 h.p.i. was considered. **(B)** Consensus motifs of 69 peptides uundergoing Tyr phosphorylation co-regulated by both viruses under all conditions were identified by Weblogo. Sequence frequency graphs of significantly enriched de novo motifs for centered Tyr are shown; the number of different peptides used for the generation of the logos is indicated at the top. **(C)** The analysis was done as for (A) with the exception that peptides undergoing significant differential phosphorylation at Ser/Thr were analysed. **(D)** Venn diagram of overlap between any two viruses in terms of regulated Ser/Thr phosphorylation with a statistically significance ($p<0.05$, up- or down-regulation), corresponding to the time of their occurrence. **(E)** A sequence motif of 43 peptides undergoing dynamic regulation at Ser/Thr by both viruses was generated by Weblogo as in (B).

3.1.2 Computational prediction of $H1N1_{pdm09}$- and H5N1-induced kinases allows the discovery of signaling hubs

Based on the alterations of phosphorylation patterns in these peptides, a computational analysis was preformed to predict the statistically significant changes in the activity of upstream kinase, which known to mediate these phosphorylations (**Fig. 15A, B**). This prediction assigned these phosphorylation events to 25 differentially regulated kinases in $H1N1_{pdm09}$-infected cells, including members of the PKC family and EphA receptor kinases. Multiple receptor Tyr kinases as well as a large number of kinases with down-regulated activity were predicted in H5N1-infected cells. Moreover, there was little overlap in the regulated-kinases between the two viruses, although kinases including PKCα, CDK10, EphA2, and RET were up-regulated by both viruses (**Fig. 15C**). In particular, activity changes in kinases of EphA family were overrepresented in the datasets for both IAV strains, and these kinases are known to act on large numbers of targets - ephrin-A ligands, thus probably providing extensive cross-talk between pathways through a single “junction” kinase regulated by both viruses (Darling et al., 2019).

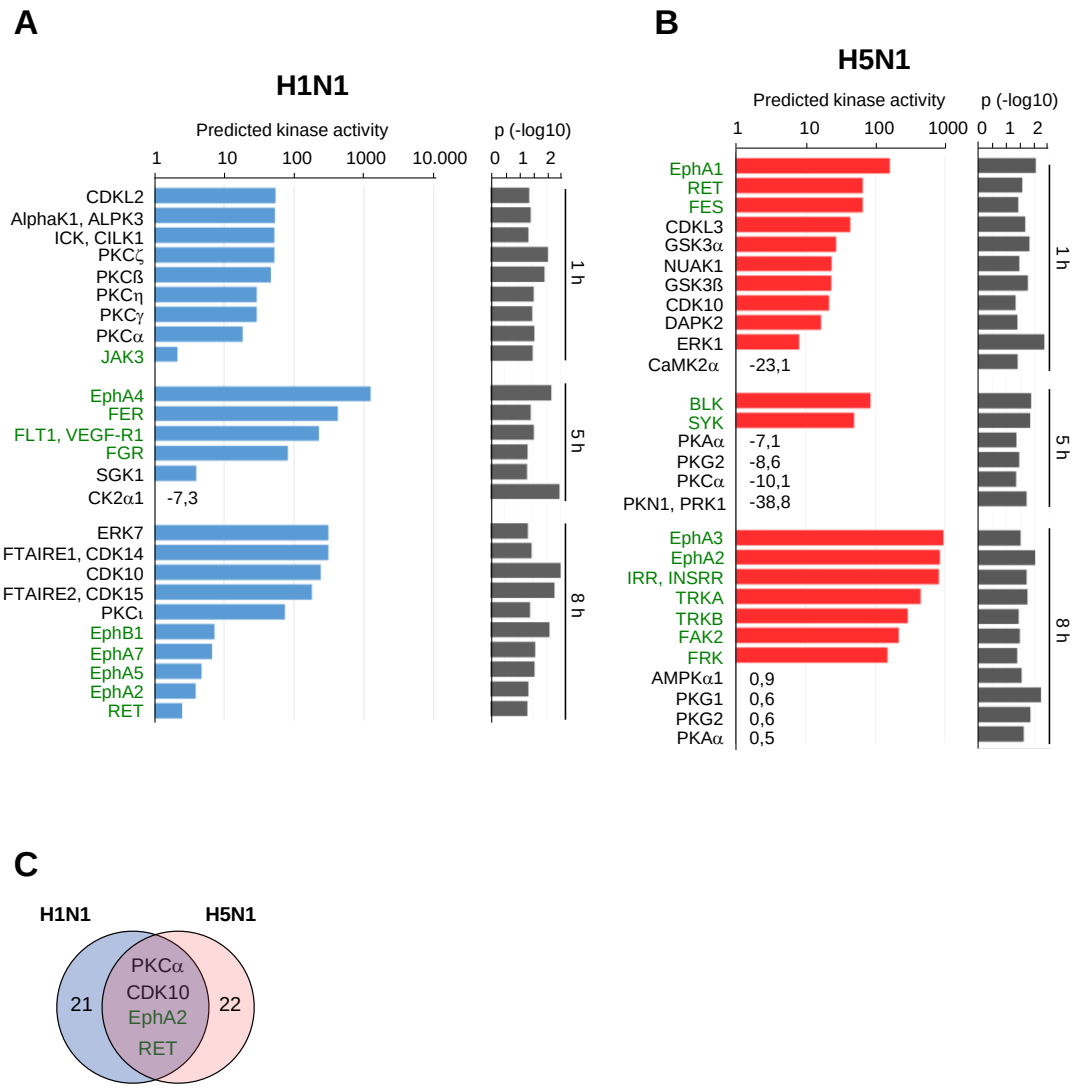

Figure 15: Computational prediction of kinase activity regulated by H1N1$_{pdm09}$ and H5N1.

(A) The corresponding upstream kinases and their activities responsible for selective peptide substrate phosphorylation were computationally predicted by normalized kinase statistics using Bionavigator v. 6.2 software (PamGene). H1N1$_{pdm09}$ refers as H1N1 for simplicity in the figure. **(B)** Venn diagram showing kinases to be regulated by H1N1$_{pdm09}$ and/or H5N1. Tyr kinases are shown in green.

Among the predicted kinases, approximately one half (26 of 47) of them were known to be associated with IAV infection, as shown in **Table 3**.

Table 3. Literature review of the regulated kinases identified in this study.

Kinase	Known role in IAV infection (PMID)/ inhibition strategy	Kinase	Known role in IAV infection (PMID)/ inhibition strategy
AlphaK1, ALPK3	PMID: 28132841	GSK3α	
AMPKα1	PMID: 20716159	GSK3ß	PMID: 20027183
BLK	*siRNA*	ICK, CILK1	
CaMK2α	PMID: 31972088	IRR, INSRR	PMID: 30174303
CDK10	PMID: 20027183	***JAK3***	*Tofacitinib, also inhibits JAK1 (PMID: 20478313)*
CDKL2	PMID: 29642015	***NUAK1***	*WZ4003, also inhibits NUAK2 (PMID: 24171924)*
CDKL3	PMID: 28132841	PFTAIRE1, CDK14	
CK2α1		***PFTAIRE2, CDK15***	*siRNA*
DAPK2	PMID: 20027183	PKAα	PMID: 12466482
EPHA1	*siRNA*	PKCα	PMID: 19523156
EPHA2	PMID: 28132841	PKCß	PMID: 12477851
EPHA3	*siRNA*	PKCγ	PMID: 11038382
EPHA4	PMID: 20027183	PKCη	
EPHA5		PKCι	
EPHA7	PMID: 20027183	PKCζ	
EPHB1		PKG1	PMID: 21731751
ERK1	PMID: 32601201	PKG2	PMID: 21731751
ERK7		PKN1, PRK1	
FAK2	PMID: 30996098	RET	PMID: 18615016
FER	*TAE684 (PMID: 22520759)*	SGK1	PMID: 23487453
FES	*TAE684 (PMID: 22520759)*	SYK	PMID: 33472080
FGR		TRKA	PMID: 21209112
FLT1, VEGF-R1	*ZM306416 (PMID: 22573732)*	TRKB	PMID: 21209112
FRK	PMID: 20027183		

The kinases known to be involved in IAV infection are shown with assigned PubMed Unique Identifiers (PMIDs). The kinases highlighted in bold and italics were further determined for their possible role in IAV infection using siRNAs or small molecule inhibitors with the indicated specificities and the appropriate references. Tyr kinases are shown in green.

This analysis also revealed the other half of novel kinases for IAV infection. It was then interesting to identify highly connected kinases in an integrative network, as dense network hubs can serve as ideal perturbation entry points (Colinge et al., 2014; Invergo et al., 2020). To this end, the functional interactions among identified kinases were analyzed using the STRING database (Szklarczyk et al., 2019). In $H1N1_{pdm09}$-infected cells, 60% of the kinases were clustered into two different networks including EphA receptor Tyr kinases, various PKC family members and JAK3 (**Fig. 16A**). Notably, 71,4% of predicted kinases modulated by H5N1 infection were grouped on one large interaction cluster (**Fig. 16B**). A functional network analysis of all kinases regulated by at least one of the two viruses was subsequently performed to identify kinases of potential pharmacological significance. This revealed extensive interaction within the predicted biological network, from which 7 kinases and also CDK15 as a control for an

unconnected kinase were selected for further analysis (**Fig. 16C**). Therefore, I assessed the effect of selective inhibition of these kinases on IAV infection through highly specific small molecule inhibitors (where available) or siRNAs, as specified in **table 3**.

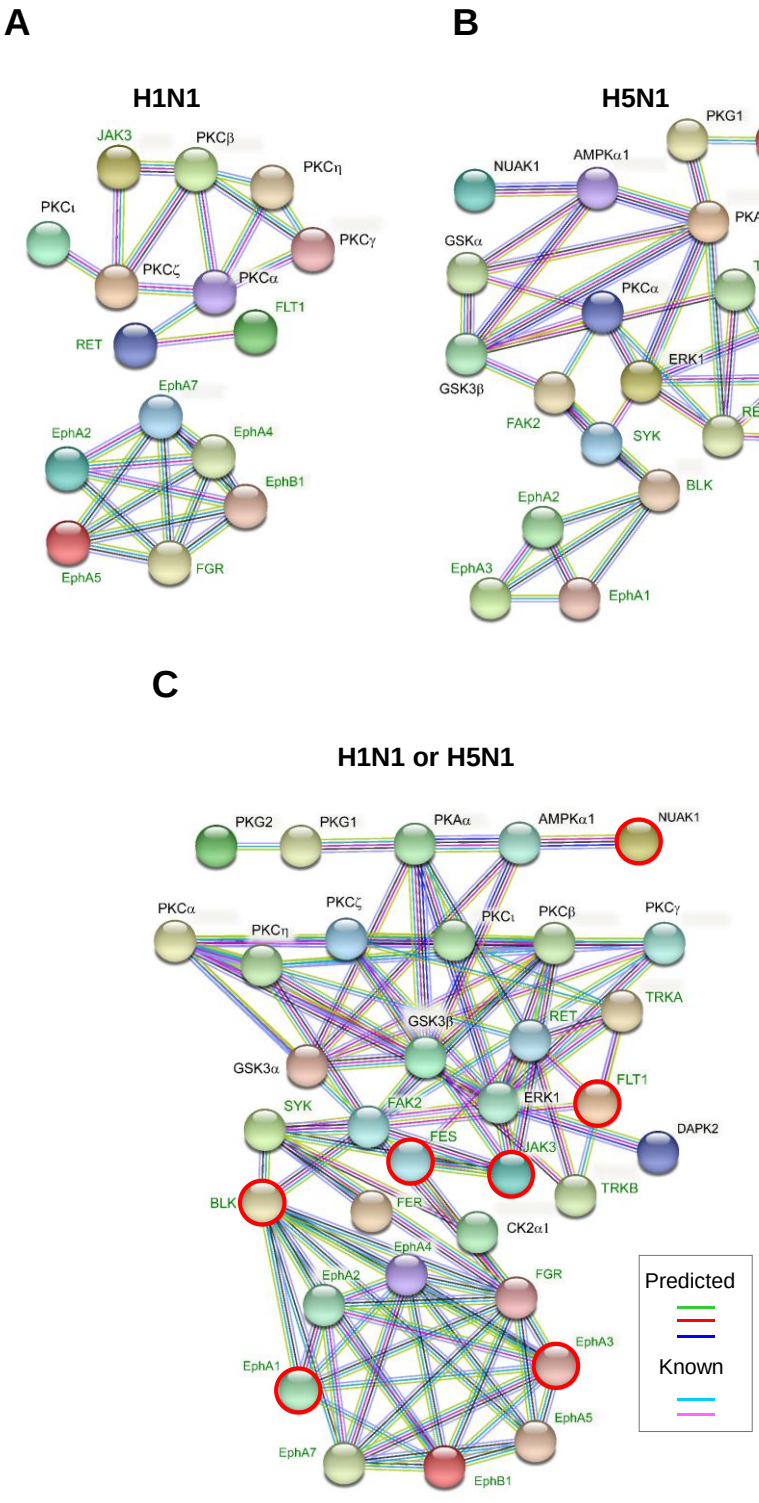

Figure 16: Network analysis of kinase signaling hubs.

The network view displays the physical, functional and genetic interactions of the kinases identified in Fig. 15. This figure was generated by the STRING database version 11.5. Kinase hubs activated by $H1N1_{pdm09}$ **(A)**, H5N1 **(B)** or both viruses **(C)** are shown. The kinases highlighted in red circles were further tested to determine their functional role in IAV replication.

3.1.3 Functional analysis of $H1N1_{pdm09}$- and H5N1-regulated kinase networks

Cytokine receptor-induced signaling pathways in immune cells are regulated by the JAK family kinases, including one of the family members JAK3 (Pesu et al., 2008), which is also regulated upon IAV infection (**Table 3**). Since this kinase can be specifically inhibited by Tofacitinib (VS-6063, PF-04554878), it was then used to test the effects of JAK3 on IAV replication. Firstly, Tofacitinib treatment at concentrations ranging from 1-50 µM had no deleterious effects on the cell viability of A549 (**Fig. 17A**). Secondly, determination of the virus titers 24 h.p.i. plus Tofacitinib treatment revealed that inhibition of JAK3 caused $H1N1_{pdm09}$ titer reduction in a dose-dependent manner while the effect on the H5N1 titer was only minor (**Fig. 17B, C**). The bias of JAK3 inhibition for the $H1N1_{pdm09}$ virus might also be reflected by the fact that this kinase was only predicted from $H1N1_{pdm09}$ infected cells (see **Fig. 16A**). The selectivity of Tofacitinib for interference with $H1N1_{pdm09}$ replication was still apparent when titers were determined 48 h.p.i. (**Fig. 17D)**. A further increase of Tofacitinib concentration or incubation time did not result in a more pronounced inhibition of $H1N1_{pdm09}$ replication and only slightly reduced H5N1 replication.

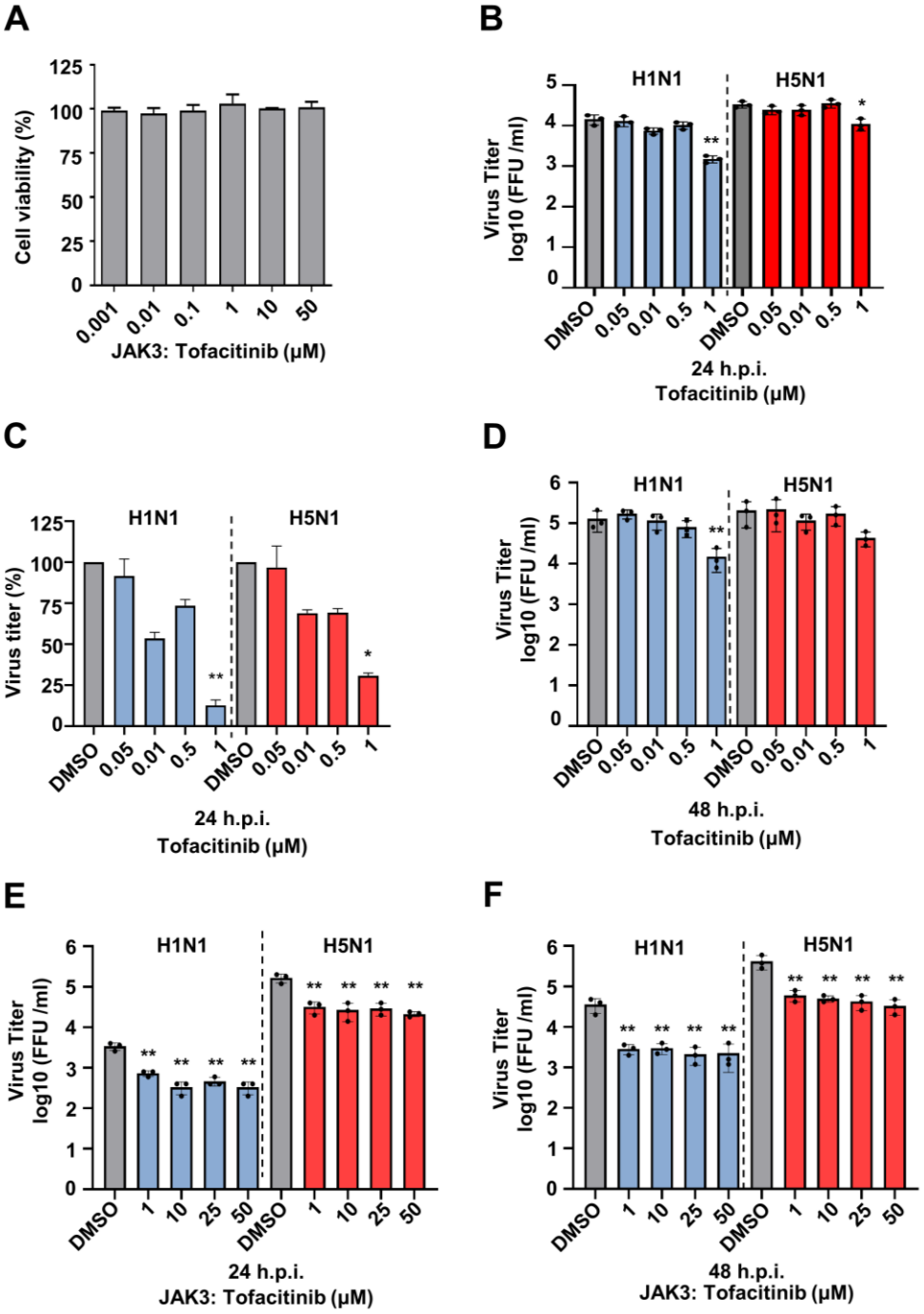

Figure 17: Dose-dependent suppression of IAV replication by Tofacitinib.

(A) A549 cells were treated for 24 h with DMSO (vehicle control) or Tofacitinib at indicated concentration, followed by the determination of cell viability via PrestoBlue assays. Cell viability of control cells was set as 100%. **(B, C, E)** A549 cells were pre-treated for 1 h with Tofacitinib at indicated dose or DMSO as a solvent control, followed by infection with $H1N1_{pdm09}$ or H5N1 (MOI = 0.001). Treatment with Tofacitinib or DMSO was also maintained at the same concentration following infection. Viral titers of cell culture supernatants were determined 24 h.p.i., titers are displayed in absolute numbers (B) and in relative numbers with the DMSO control set to 100% (C). **(D, F)** The experiment was performed as in (B, C, E) with the exception that

viral titers were determined 48 h.p.i. Shown are means ± standard deviations from three independent experiments performed in triplicates. Data were processed with unpaired t-tests (comparing Tofacitinib to DMSO), asterisks indicate p values (*p ≤ 0.05, **p ≤ 0.01).

Likewise, two members of the FES (FEline Sarcoma) family kinases, FES and FER, as well as vascular endothelial growth factor receptor (VEGFR) family kinase VEGFR1, were newly predicted to be regulated upon either $H1N1_{pdm09}$ or H5N1 infection. Given that no specific and selective inhibitors of FES or FER have been reported to date, I chose a multi-kinase inhibitor, TAE684, which is known to inhibit both kinases as well as the well-known target ALK, to measure its possible impact on viral replication. Neither the FES/FER inhibitor nor the VEGFR1 inhibitor showed significant effect on IAV replication at nontoxic concentration (**Fig. 18B** and **Fig. 18D**). The slightly reduced viral titer occurred when cells were treated with 10 µM TAE684, which was more likely due to the cytotoxicity of this compound rather than its effect on the viral growth (**Fig. 18B**).

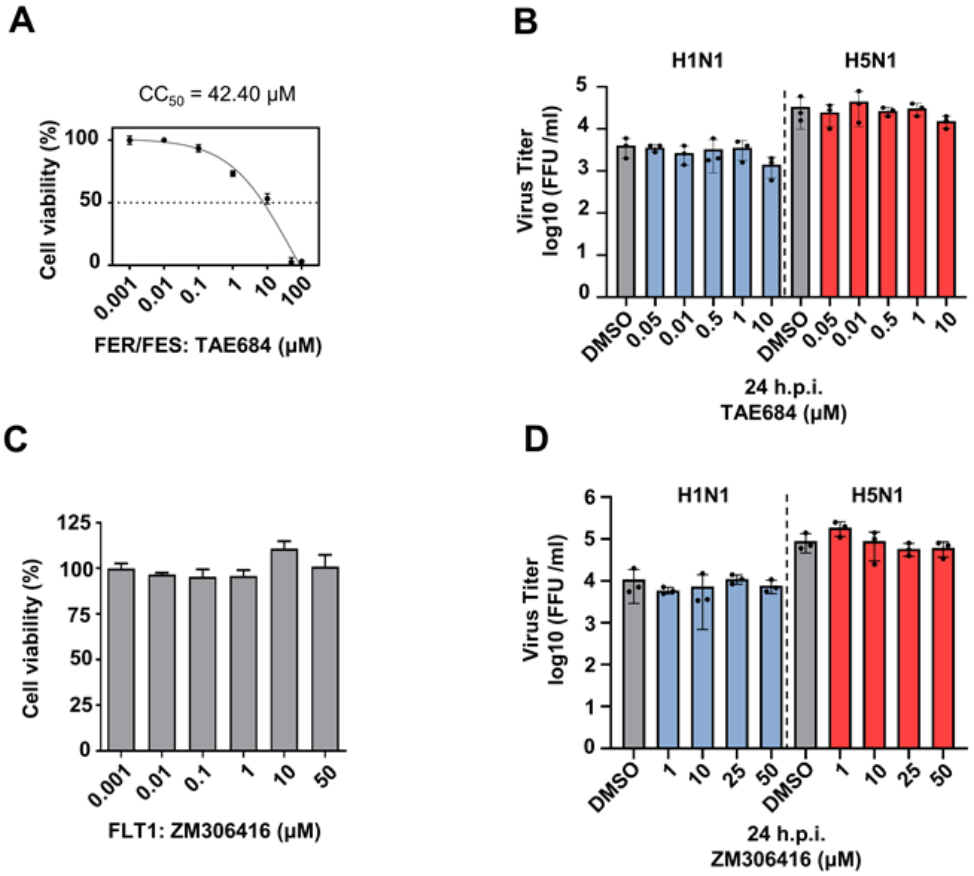

Figure 18: The impact of kinases inhibitor on IAV replication.

(A) A549 cells were treated for 24 h with DMSO (vehicle control) or TAE684 at indicated concentration, followed by the determination of cell viability A549 cells and calculation of the half-maximal cytotoxic (CC_{50}) concentration of TAE684. **(B, D)** A549 cells were pre-treated for 1 h with the indicated dose of TAE684 (B),

ZM306416 (D), or DMSO as a solvent control, then infected with $H1N1_{pdm09}$ or H5N1 (MOI = 0.001) for 24 h in the presence of indicated inhibitor. Viral titers of cell culture supernatants were determined and are displayed in absolute numbers. **(C)** The experiment was performed as in (A) with the exception that A549 cells were incubated with ZM306416. After 24 h cell viability was determined by PrestoBlue assays. Cell viability of control cells was set as 100%.

novel (nua) kinase (NUAK) 1, also known as ARK5, is one of 12 kinases with sequence homology to the catalytic α-subunits of the metabolic regulator AMPK, which has been described as an anti-viral factor for IAV replication via PPARα/γ-AMPK-SIRT1 pathway (Bei et al., 2021; Monteverde et al., 2018). Since NUAK1 was also found to be activated in H5N1-infected samples at 1 h.p.i., the selective NUAK1 inhibitor WZ4003 was applied to assess the impact on the viability of A549 cells (**Fig. 19A**) and viral replication (**Fig. 19B**). Inhibition of NUAK1 increased the virus titers of $H1N1_{pdm09}$ and H5N1 at a dose-dependent manner, suggesting an anti-viral function of this kinase.

Four novel kinases (EphA1, EphA3, CDK15 and BLK) were further assessed for their particular importance to IAV replication by using sequence-specific small interfering RNAs (siRNAs). In this particular experiment (**Fig. 19C, D**), a second siRNA transfection (double transfection) was conducted 48 h following the first siRNA transfection, and the cells were either collected and the knockdown efficiencies were analyzed 48 h after the second transfection, or infected at a low MOI (0.001) by $H1N1_{pdm09}$ or H5N1. The qRT-PCR (**Fig. 19C**) results showed >50% knockdown efficiency at RNA level for each gene was achieved by the corresponding siRNA transfection, except for siRNA-EphA3, which showed only 35% depletion at the mRNA level, compared with control scrambled siRNA (si Scramble). While no effects were observed after knockdown of CDK15 or BLK, knockdown of EphA1 and EphA3 together resulted in increased viral titers (Fig. 19D), consistent with a cooperative anti-viral effect of both members of this redundantly acting Tyr kinase family.

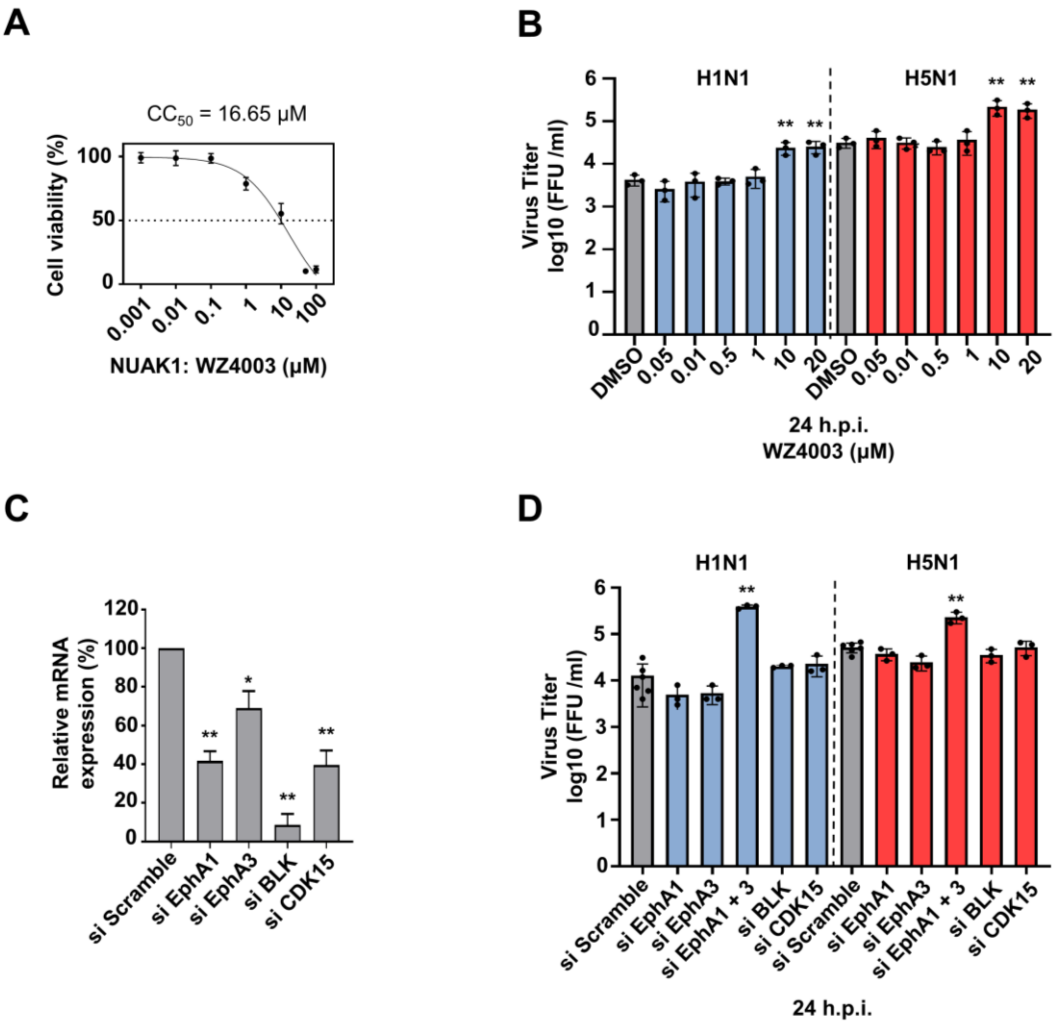

Figure 19: Effects of individual kinases on IAV infection.

(A) A549 cells were treated for 24 h with DMSO (vehicle control) or WZ4003 at indicated concentration, followed by the determination of cell viability A549 cells and calculation of the CC_{50} concentration of WZ4003. **(B)** A549 cells were pre-treated for 1 h with indicated concentration of WZ4003 or DMSO. Cells were further infected with $H1N1_{pdm09}$ or H5N1 (MOI = 0.001) for 24 h in the presence of WZ4003. Viral titers of cell culture supernatants were determined. **(C, D)** A549 cells were transfected twice with siRNAs using a 48-h interval between transfections. At 48 h after the second transfection, one part of the cells was harvested for the analysis of gene expression by RT-qPCR to control knockdown efficiency (C), or infected with $H1N1_{pdm09}$ or H5N1 (MOI = 0.001) (D). Viral titers of cell culture supernatants were determined 24 h.p.i.. Shown are means ± standard deviations from three independent experiments performed in triplicates. Data were processed with unpaired t-tests. Asterisks indicate p values (*$p \leq 0.05$, **$p \leq 0.01$).

3.2 Overview of IAV protein phosphorylation

3.2.1 Criteria for the selection of candidate phosphorylation sites

Previous phosphoproteomic analysis of MLE-15 cells infected by SC35 or its mouse-adapted derivative SC35M from our laboratory allowed the identification of phosphorylated residues within viral proteins (Weber et al., 2019). This work identified 12 novel phosphorylation sites and confirmed 8 already known modified amino acids in several IAV-encoded proteins (**Table 4**) (Weber et al., 2019). To comprehensively characterize the functionally relevant phosphorylation events within IAV-encoded proteins, our data set was combined with published data sets generating a list of 69 phosphorylation sites contained in 10 different viral proteins encoded by several different IAV strains (**Table 4**). This list was then filtered by the following criteria to select sites to be further examined: (I) the site should not yet been previously studied, (II) it should be highly conserved between IAV strains (**Fig. 20**). and, (III) the site should be located in regions with a known function and available structural information were considered.

Table 4: Summary of IAV phosphorylation sites.

IAV Protein	Published	Confirmed	New
PB2	S742		T471
PB1	T223		Y657
PA	T151, T157, T162, T200, S224, S225		Y393, S395
HA	T358		Y155, Y218
NP	S3, S28, S50, S60, S69, S84, S165, S297, S377, T378, S403, S407, S457, T472, S473, S486	S9, Y10, Y97, Y296, S402	Y148, Y289
NA	S160, S164, S166		
M1	S2, T5, T9, Y10, T37, Y132, T168, S195, S196, S224, S225, S226	T108	S118, Y119, T121, Y240
M2	S64, T65		
NS1	S42, T80, T197, T215	S48, T49	
NEP	S23, S24, S25		

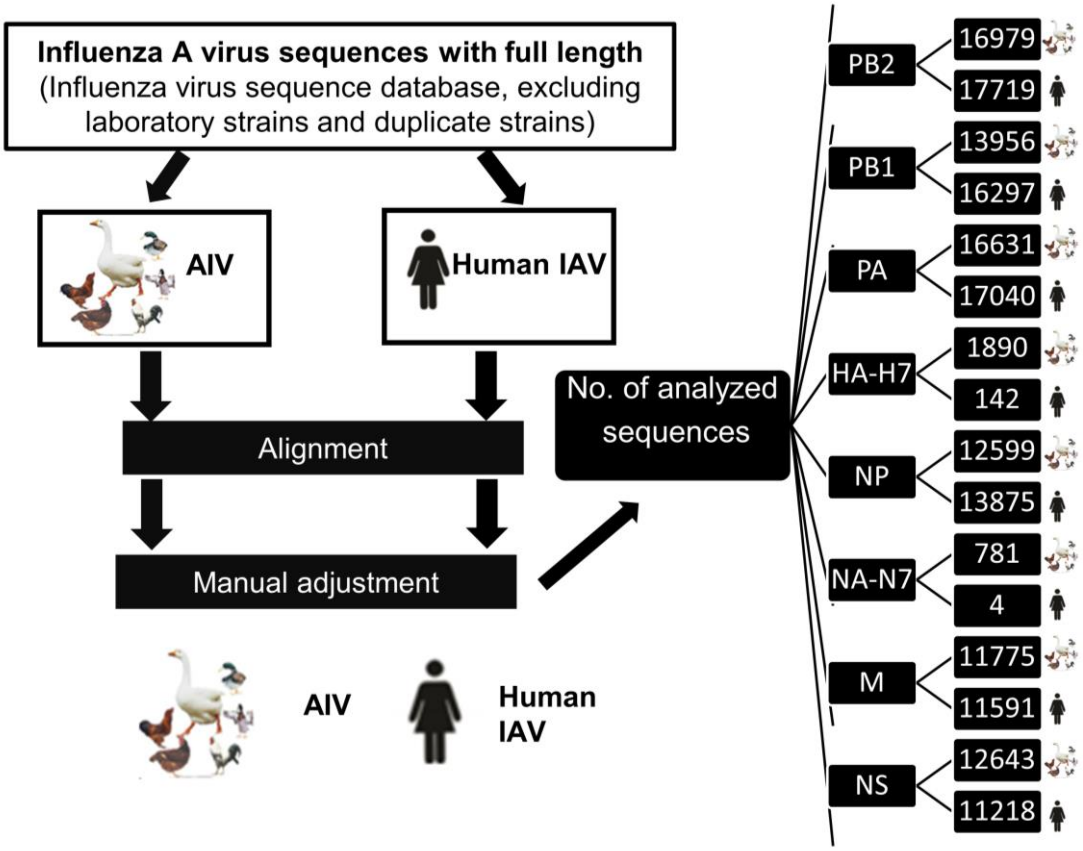

Figure 20: Computational analysis of the evolutionary conservation of phosphorylation sites on IAV proteins.

Schematic display of the workflow: All previously published full-length protein sequences of avian and human IAV (before August 2018) were collated from the Influenza Virus Resource at the National Center for Biotechnology Information (NCBI) (www.ncbi.nlm.nih.gov/genomes/FLU). laboratory strains were excluded from the analyses to eliminate sample biases. Identical sequences were collapsed and filtered to ensure that each strain was only represented once in the dataset. All assembled protein sequences were aligned using MAFFT v7.2 as available in the Cipres Science Gateway (https://www.phylo.org) with subsequent manual adjustment to correct frameshift errors using BioEdit. The number of protein sequences used to calculate the frequency of residue (Ser/Thr/Tyr) at a given phosphorylation site is listed on the right.

3.2.2 Phosphorylation of the polymerase subunits and the NP

The known phosphorylation sites occurring on the polymerase subunits are listed in **Table 5**, and further filtered according to the criteria mentioned above.

One candidate phosphorylation site of PB2 is T471, a highly conserved residue and positioned in one of NLS within PB2, suggesting a functional relevance for nuclear import of PB2 and for interactions with nuclear import factors. Additionally, this residue is located at the cap-binding domain of PB2, which is tightly involved in the unique cap-

snatching mechanism needed for IAV transcription (Pflug et al., 2014). Moreover, the structure of the polymerase complex implies PB2 T471 is surface-exposed in a region of the cap-binding domain of PB2. It would therefore presumably be accessible to kinases. Thus, PB2 T471 matches all the selection criteria and was therefore further investigated.

Table 5: Summary of IAV phosphorylation sites in the polymerase subunits.

Protein	Phosphorylation site	Virus strains where it was found	Avain IAV	Human IAV	Comments	Reference
			Residue conservation(%)	Residue conservation(%)		
PB2	Thr471	SC35/SC35M	99.49	99.17	Located at NLS1 and cap binding domain (319–481)	PMID: 26008706 PMID: 25409142
	Ser742	WSN	99.93	99.96	Adjacent to NLS2, forms part of a flexible C-terminal tail containing the protein's bipartite NLS; But the surrounding sequence is not conserved in SC35	PMID: 26008706 PMID: 17310249 PMID: 23144613
PB1	Thr223	WSN	99.84	99.99	Located at the "Finger Tips". Our analysis shows that phosphorylation of Thr223 inhibits the enzymatic function	PMID: 25409142
	Tyr657	SC35/SC35M	99.97	99.98	Priming loop	PMID: 25409142
PA	Thr151	Vic	99.00	99.90	Already analyzed; not essential	PMID: 10627541
	Thr157	Vic	99.45	99.77	Already analyzed; important for the capacity of viral polymerase to synthesize cRNA	PMID: 12719592 PMID: 10627541
	Thr162	Vic	99.62	99.92	Already analyzed; not essential	PMID: 12719592 PMID: 10627541
	Thr200	Vic	99.96	99.99	Already analyzed; not essential	PMID: 10627541
	Ser224	WSN/Vic	99.61	99.75	Already analyzed; S224A was shown not to affect RNP activity or the apparent proteolytic activity of PA	PMID: 12719592 PMID: 10627541
	Ser225	WSN	99.60	38.40	Located at the amino-terminal third of the molecule (positions 1 to 247),activate proteolysis	PMID: 10627541
	Tyr393	SC35/SC35M	99.98	99.95	Located in the C-terminus of PA, which wraps around the PB1 complex (PA arch)	PMID: 25409142
	Ser395	SC35/SC35M	99.42	99.83	Located in the C-terminus of PA which wraps around the PB1 complex (PA arch)	PMID: 25409142

WSN: A/WSN/1933 (H1N1); Vic: A/Victoria/3/75 (H3N2); SC35: A/Seal/Massachusetts/1/80 (H7N7); SC35M: A/Seal/Massachusetts/1/80 (H7N7) mouse-adapted.

Eight phosphorylation sites of PA were reported. Among them, two novel phosphorylation sites Y393 and S395 previously detected in our laboratory, are highly conserved in influenza A viruses. Of particular interest, these two phosphorylation sites are located at the C-terminus of the PA, a region that wraps around the PB1 complex, suggesting a relevance for regulating the interaction with PB1. Additionally, PA Y393 and S395 are close to the 5' vRNA/cRNA binding pocket in the polymerase structure (**Fig. 21**). Thus, PA phosphorylation sites Y393 and S395 might plausibly affect 5' vRNA/cRNA binding.

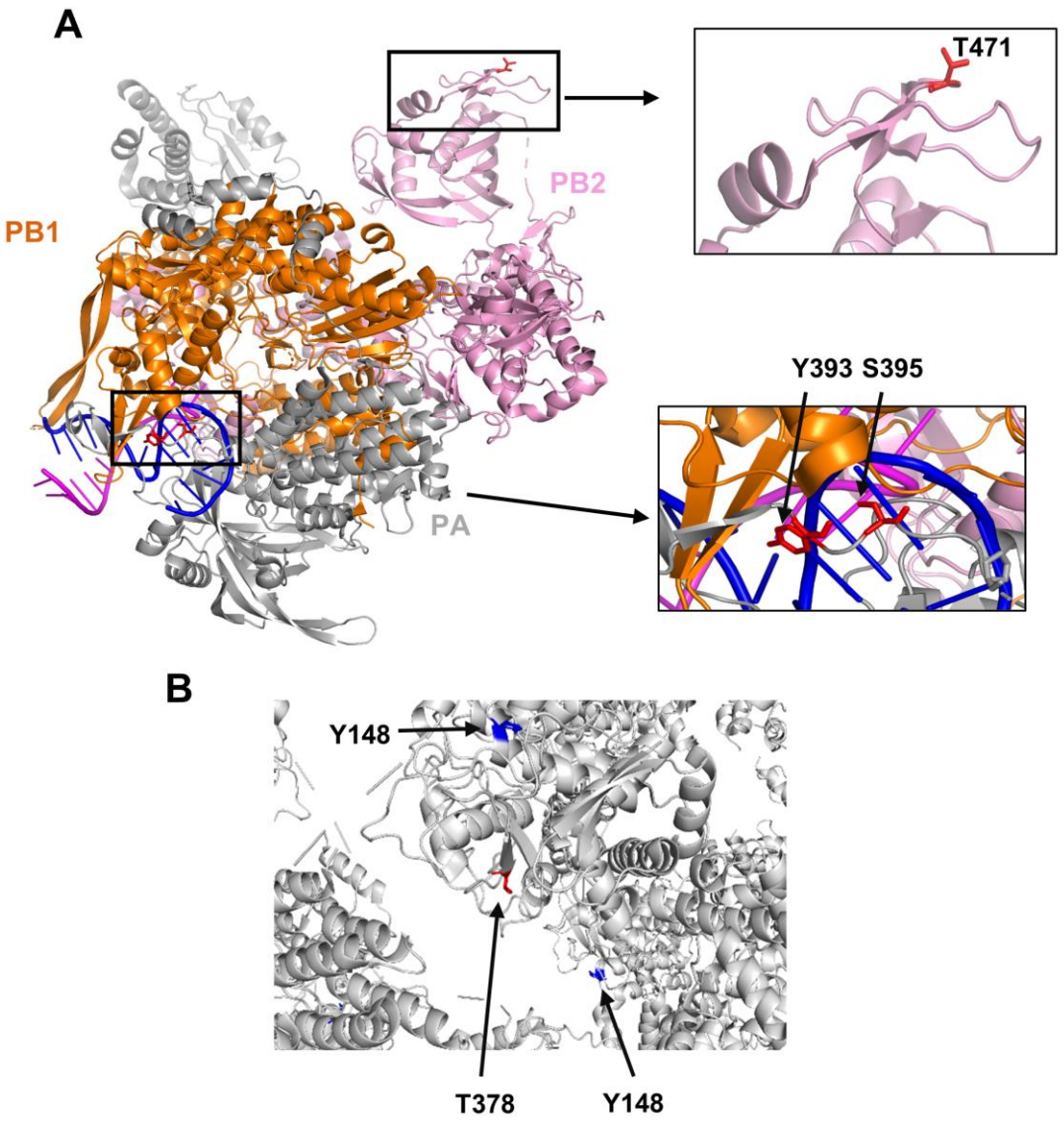

Figure 21: Location of functionally relevant phosphorylated residues in the IAV polymerase and NP.

(A) Display of the positions of functionally relevant phosphorylation sites PB2 T471 and PA Y393, S395 in the three-dimensional structure of the IAV polymerase (PDB: 4WSB). The PB2, PB1, and PA subunits are shown in light pink, orange, and gray, respectively. The boxed areas were enlarged on the right. **(B)** Display of the positions of functionally relevant phosphorylation sites Y148 and T378 in the structure of the IAV NP multimer (PDB: 4BBL).

The NP is the most abundant protein of IAV after the M1 and is known to be a phosphoprotein (Hutchinson et al., 2012). As illustrated in **Table 6**, NP phosphorylation occurs at multiple sites during infection, and these phosphorylation patterns vary throughout the infectious cycle and are dependent on the viral strain as well as the host cell type. Several functional studies have reported that NP phosphorylation inhibits its oligomerization in cells and defines the molecular mechanisms by which this modification impairs RNP formation. Amongst novel NP phosphorylation sites, Y148 phosphorylation

occurs at the end of helix alpha 4, a region that is important for RNA binding. The molecular modeling of NP showed that Y148 is at one end of the RNA groove and stacks against the bound RNA to extend the quasi-helix (Lejal et al., 2013; Tarus et al., 2015; Ye et al., 2006). Intramolecular localization of another candidate phosphorylation site at T378, is not far away from the interaction zone between individual NP proteins within the RNP thus proposing a possible functional relevance (**Fig. 21** as above). Furthermore, this site is highly conserved in both avian and human IAV and contained in the region which is important for the NP oligomerization. Thus, NP Y148 and T378 phosphorylation sites were selected for further analysis.

Table 6: Summary of IAV phosphorylation sites in the NP.

Protein	Phosphorylation site	Virus strains where it was found	Avain IAV	Human IAV	Comments	Reference
			Residue conservation(%)	Residue conservation(%)		
NP	Ser3	Vic	98.81	99.70	Already analyzed; Critical for phosphorylation at the N-terminal end of the NP, but not essential for the protein function in the replication and transcription of the viral genome	PMID: 8648669
	Ser9	SC35/SC35M/WSN	99.69	99.98	Already analyzed; control the nuclear import of NP, essential for viral growth and the regulation of polymerase activities	PMID: 25787277
	Tyr10	SC35/SC35M/WSN	98.90	99.97		
	Ser28	Vic	99.94	99.99	Already analyzed; not essential	PMID: 8648669
	Ser50	Vic	96.94	91.92	Already analyzed; not essential	PMID: 8648669
	Ser60	Vic	99.96	99.99	Already analyzed; not essential	PMID: 8648669
	Ser69	Vic	99.97	99.94	Already analyzed; not essential	PMID: 8648669
	Ser84	Vic	98.59	99.67	Already analyzed; not essential	PMID: 8648669
	Tyr97	SC35/SC35M	99.98	100.00	Located at NP body domain; unknow function region	PMID: 19471866
	Tyr148	SC35/SC35M	99.99	100.00	Close to surface of the groove, might affect RNA binding	PMID: 17151603
	Ser165	WSN	99.96	100.00	Already analyzed; S165 was shown to have a negative effect on the viral polymerase and the dissociation of the NP oligomers	PMID: 25787277
	Tyr289	SC35/SC35M	99.59	66.41	Important for NP homo-oligomerization	PMID: 20463064
	Tyr296	SC35/SC35M/WSN	99.71	99.99	Already analyzed; Y296 plays an important role in the nuclear export: essential for viral growth and the regulation of polymerase activities	PMID: 25787277
	Ser297	WSN	99.98	99.99	Already analyzed; Y296 s adjecent to S297, being in close proximity to NES3, which functions in the CRM1-dependent nuclear export pathway	PMID: 25787277
	Ser377	WSN	75.39	63.63	Important for oligomerization	PMID: 20463064
	Thr378	WSN	99.93	100.00	Important for oligomerization	PMID: 20463064
	Ser402	SC35/SC35M/WSN /PR8	99.85	99.96	Already analyzed; in the 'tail loop, S402A mutation caused a relatively small defect in growth (5-fold)	PMID:23144613
	Ser403	WSN /PR8	0.02	0.08	Already analyzed; in the 'tail loop', important for viral growth	PMID: 23144613
	Ser407	WSN	99.99	100.00	Already analyzed; prevents RNP assembly, and severely impairs viral replication	PMID: 25867750
	Ser413	WSN	99.98	99.99	Already analyzed; not essential	PMID: 25867750
	Ser457	WSN	99.98	100.00	Already analyzed; important for viral growth	PMID: 23144613
	Thr472	WSN	99.42	84.31	Already analyzed; not essential	PMID: 23144613
	Ser473	WSN	0.38	0.48	Already analyzed; not essential	PMID: 25867750 PMID: 23144613
	Ser486	WSN	99.94	99.97	Already analyzed; located at the binding groove entrance, contributes to regulated assembly by preventing hyper-oligomerization	PMID: 25867750

WSN: A/WSN/1933 (H1N1); Vic: A/Victoria/3/75 (H3N2); PR8: A/Puerto Rico/8/34 (H1N1); SC35: A/Seal/Massachusetts/1/80 (H7N7); SC35M: A/Seal/Massachusetts/1/80 (H7N7) mouse-adapted.

3.2.3 Phosphorylation of the NS1

The NS1 is phosphorylated at different residues during infection, which depends on the viral strain and cells used. Six phosphorylation sites were reported when I started this

study, whereas a recent paper investigated another novel phosphorylated residue at S205 and its critical role in supporting polymerase function (Patil et al., 2021). Amongst the phosphorylation sites of NS1, only one site (T197) found in the WSN strain is functionally unknown, while all remaining sites have been functionally analyzed. Remarkably, it was noted that T197 is part of the NS1 effector domain according to a previous structural analysis of NP by Bornholdt *et al*., 2008 (Bornholdt et al., 2008) (**Fig. 22**). T197, together with the nearby S195 and D92 (a virulence determinant of H5N1), forms strong hydrogen-bonding interactions with each other. It has been proposed that phosphorylation of either S195 or T197 may destabilize NS1 and thus potentially disrupt the dimerization of NS1.

Table 7: Summary of IAV phosphorylation site in the NS1.

Protein	Phosphorylation site	Virus strains where it was found	Avain IAV	Human IAV	Comments	Reference
			Residue conservation(%)	Residue conservation(%)		
NS1	Ser42	Udorn	79.85	99.76	Already analyzed; affecting virus replication during infection	PMID: 22787231
	Ser48	SC35/SC35M/ Udorn	83.45	13.82	Already analyzed in previous study and our own analysis; NS1 ST48,49EE did not impair virus production	PMID: 22787231
	Thr49	SC35/SC35M/ WSN/ PR8	99.94	99.78	Already analyzed in previous study; dissolving of NS1-TRIM25 binding as well as NS1-RIG-I complex	PMID: 22787231 PMID: 26687707
	Thr80	WSN	67.04	98.76	Already analyzed; regulating the replication of IAV by reducing the binding affinity with RIG-I	PMID:27376632
	Thr197	WSN	66.97	14.53	Part of the NS1 effector domain; phosphorylation of either S195 or T197 may destabilise NS1, potentially disrupting its dimerization	PMID: 16715094 PMID: 23144613
	Thr215	WSN/Udorn	1.59	62.43	Already analyzed; T215 is not required for human infection and transmissibility. Although the residue is important for viral growth, mutational analysis suggests that its phosphorylation is not required in tissue culture	PMID: 19007960 PMID: 22787231 PMID: 23144613

Udorn=A/Udorn/72 (H3N2); WSN: A/WSN/1933 (H1N1); PR8: A/Puerto Rico/8/34 (H1N1); SC35: A/Seal/Massachusetts/1/80 (H7N7); SC35M: A/Seal/Massachusetts/1/80 (H7N7) mouse-adapted.

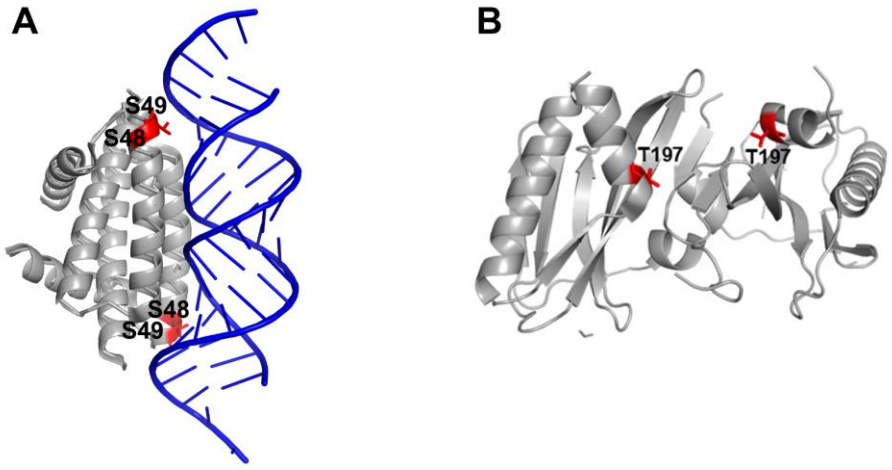

Figure 22: Location of functionally relevant phosphorylated residues in the IAV NS1.

Display of the positions of functionally relevant phosphorylation sites **(A)** S48, S49 in the IAV NS1 RNA binding domain (PDB: 2ZKO) and **(B)** T197 in the dimeric NS1 effector domain (residues 79–207) (PDB 2GX9). Residues 206–230 and residues 73–78 are disordered. RNA is shown in blue.

3.3 Functional consequences of phosphorylation of IAV proteins on viral propagation

By analysis of all phosphorylation sites within the different virus proteins know to be phosphorylated (**Table 4**) applying the above-mentioned selection criteria, a total of 9 phosphorylation sites (PB2:1, PA:2, NP:2, M1:1, NS1:3) were selected for further functional evaluation through generation of phosphorylation-defective (STY/AF) and phospho-mimicking (STY/E) mutations. RG using eight co-transfected plasmids encoding the viral RNAs was employed to create recombinant SC35M virus mutants in a co-culture of 293T/MDCK II cells. Repeatedly, I was not able to rescue recombinant viruses with mutations in M1 (T108A) and in two vRNP components, namely PA (Y393E), NP (Y148E, T378E). All rescued viruses were then compared in a multi-cycle replication assay and showed roughly similar replication kinetics at 12, 24, and 36 h.p.i. in MLE-15 cells (**Fig. 23C**).

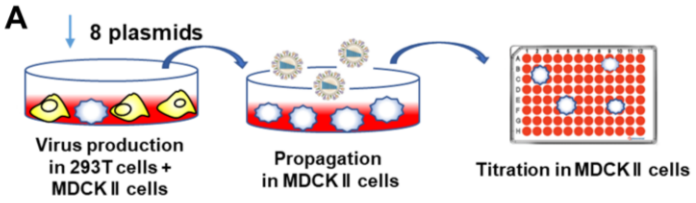

B

Recombinant virus	Rescue
SC35M WT	+
PB2 T471A	+
PB2 T471E	+
PA YS 393,395 FA	+
PA YS 393,395 EE	-
PA Y393E	-
PA S395E	+
NP Y148F	+
NP Y148E	-
NP T378A	+
NP T378E	-
NP YT 148,378 FA	+
M1 T108A	-
M1 T108E	+
NS1 STT 48,49,197 AAA	+
NS1 STT 48,49,197 EEE	+

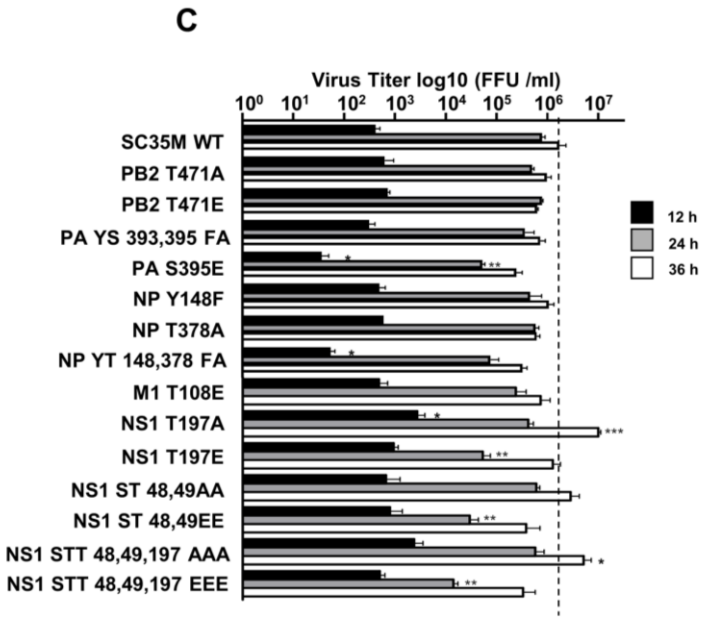

Figure 23: The effects of IAV protein phosphorylation on viral replication and growth.

(A) Schematic display of the workflow for the production of recombinant IAV SC35M viruses encoding mutated viral proteins. **(B)** Summary of the rescue of recombinant viruses ablating or mimicking constant phosphorylation on candidate phosphorylation sites. Plus indicates successful rescue of recombinant viruses. (**C)** MLE-15 cells were infected with the indicated viruses at an MOI of 0.001 and viral growth was monitored 12, 24, and 36 h.p.i. by foci assay. Dashed lines represent the detection limit. *p < 0.05, **p < 0.01 and *** p < 0.001. Error bars represent standard deviation from three independent experiments. Differences from WT were tested using unpaired t-test, asterisks indicate p values (*p ≤ 0.05, **p ≤ 0.01, and ***p < 0.001).

3.4 Functional consequences of phosphorylation of vRNP components

To test whether the modifications occurring at the vRNP components PB2, PA and NP affect polymerase activity, a plasmid-based minireplicon system to perform minigenome replication assays by RNP reconstitutions in cells was employed. A plasmid expressing

a polymerase I (Pol I)-driven vRNA-like transcript encoding the luciferase reporter gene was co-transfected into 293T cells together with plasmids encoding the viral PB2, PB1, PA, and NP proteins or their phospho-deficient/phospho-mimetic derivatives. Quantification of the luciferase activity 24 h.p.t. showed a strong reduction in reporter activity when PA mutants (Y393E and PA S395E) were expressed instead of WT PA, thus suggesting that the failure to rescue the respective mutant viruses results from defective RdRp activity (**Fig. 24**). The NP Y148E mutant which did not allow to rescue virus led to reduced reporter protein activity while the NP T378E mutation, which also did not permit the rescue of virus had no effect on the luciferase activity. The other polymerase subunit mutants PB2 (T471A/E), PA (YS393,395FA), NP (Y148F, T378A, YT148,378FA), which all allowed to recused virus with replication efficiencies comparable to WT SC35M, also demonstrated reporter/polymerase activity similar to WT.

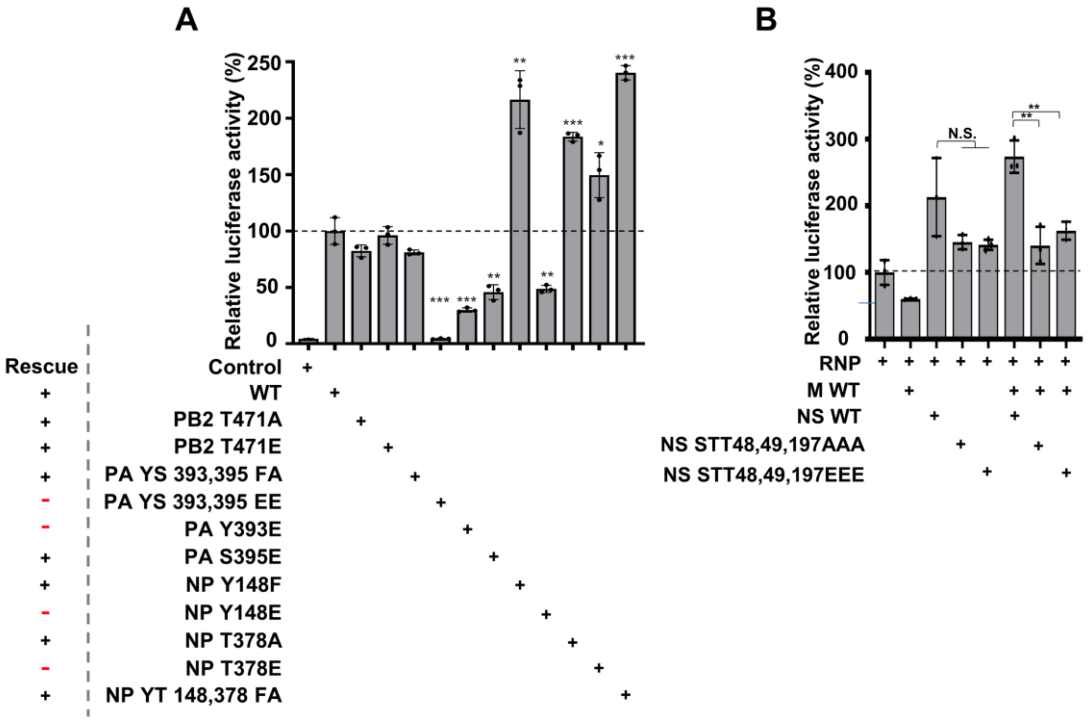

Figure 24: Overview of the impact of phosphorylation sites of IAV proteins on polymerase activity.

(A) Polymerase reconstitution assay in the presence of the indicated IAV protein mutants. 70% confluent 293T cells were transfected with 1 µg each of WT or mutated pHW2000-SC35M-PB2, pHW2000-SC35M-PB1, pHW2000-SC35M-PA, pHW2000-SC35M-NP, 200 µg pHW72-Luci, and 20 µg pCI-neoRenilla-Luci plasmids in 6-well-plates by using PEI. After 24 h, the cells were washed with PBS and lysed for 15 minutes with 150 µl of 1x passive lysis buffer. 10 µl LARII substrate was mixed with 2 µl of cell lysate in a luminometer tube and firefly luciferase activity was measured. After the addition of 10 µl of stop and glow buffer, the bioluminescence of Renilla luciferase was determined using a luminometer. The relative activities were calculated after the normalization of the Renilla luciferase activities to the activities of the firefly luciferase.

(B) The experiment was performed as in (A) with the difference that vRNP complexes were further co-expressed with indicated NS1 phospho-mutants in the presence or absence of M1 protein. Polymerase activity is shown as mean and standard deviation (s.d). of at least three independent experiments. Differences from WT were tested using unpaired t-test, N.S.: not significant, asterisks indicate p values (*$p \leq 0.05$, **$p \leq 0.01$ and ***$p < 0.001$).

3.4.1 Phosphorylation status of PA Y393 affects the ability of the polymerase to produce vRNA and infectious virions

Mutational analysis revealed that PA phospho-residues impact IAV propagation. In this context, constitutive phosphorylation Y393E is incompatible with the production of infectious viruses (**Fig. 23B**) and led to a remarkable reduction in polymerase activity (**Fig. 24A**). To further determine whether the PA phospho-site mutants have an impact on the synthesis of the specific viral RNA species (vRNA, cRNA, and mRNA), a primer extension assay was performed. For this, 293T cells were transfected with plasmids expressing the vRNP components (PB2, PB1, PA, NP) containing WT or phospho-mutant PA, together with a plasmid (pPOLI-CAT-RT), which expresses a vRNA-like Pol I-transcript encoding the CAT open reading frame. Using specific radioactive labeled primers, the different forms of viral RNA (v-, c-, mRNA) and the cellular 5S RNA (loading control) in the extracted total RNA can be detected (**Fig. 25A**) and quantified (**Fig. 25B**). Comparing the result for the negative control (lane 2) to the positive control (lane 3), which both express WT PA, demonstrates that the polymerase is not active without PB2. The PA YS393,395FA mutant had no major effect on the amounts of the three viral RNAs (lane 4). The PA YS393,395EE (lane 5) and PA Y393E (lane 6) mutations resulted in complete loss of viral c- and mRNA. It must be noted that due to the constant expression of the vRNA from the pPOLI-CAT-RT a background level of vRNA was detected in all experiments. The PA S395E mutation (lane 7) resulted in a markedly reduced amount of mRNA and no detectable levels of cRNA. These results are well in agreement with the fact that recombinant SC35M virus can only be rescued with WT PA and that the virus carrying the PA YS393,395FA mutations replicates to similar titers as WT virus, while the virus with the PA S395E mutation, replicates to significantly reduced titers. In summary, these results suggest that permanent phosphorylation of PA at Y393 and S395E prohibits the activity of the RdRp.

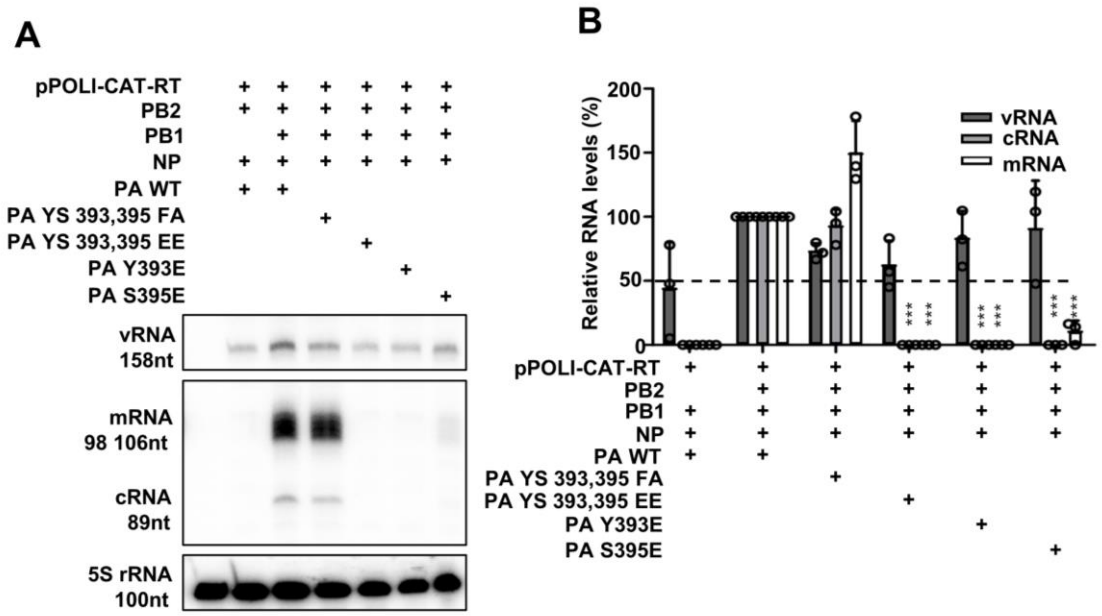

Figure 25: Effect of mutating phosphorylated residues in the PA on transcription and replication.

(A) To assess the function of mutated PA proteins in transcription and replication, RNP reconstitutions were performed in 293T cells and RNA species at 48 h.p.t. measured by primer extension and autoradiography. A representative image is shown. **(B)** Autoradiography signals from (A) were quantified from three independent experiments and normalized to WT levels. Bars indicate standard deviations obtained by unpaired t-test for two-group comparisons, asterisks indicate p values (*$p \leq 0.05$, **$p \leq 0.01$, and ***$p < 0.001$).

3.4.2 PA Y393 and S393 phosphorylation does not affect the ability of PA to interact with PB1

As mentioned before, the residues Y393 and S395 are contained in a region of PA, which is critical for the interaction with PB1 protein. The polymerase activity requires multiple steps for successful transcription and replication, starting with protein expression, the assembly of trimeric polymerase complex, RNA binding, RNP assembly, and ultimately the synthesis of new RNA products (Dawson, Wilson, Freiberger, et al., 2020; Mondal et al., 2017), and the cumulative success of this process can be monitored with the primer extension assay. To decipher whether PA Y393 phosphorylation might be critically involved in regulating the PA/PB1 interaction, further investigations were performed. To this point, PA/PB1 interaction was assayed by expressing WT- and PA mutants along with either PB1 (**Fig. 26A**), or PB2 and PB1 (**Fig. 26B**), or PB2, PB1 and NP without (**Fig. 26C**) or with (**Fig. 26D**) viral RNA in 293T cells, immuno-purifying PA with a PA-specific antibody, and probing for co-precipitation of PB1. The results showed that the levels of co-precipitated PB1 with WT PA or all PA mutants were at approximately WT

levels in all above settings, independent of whether the mutations of the expressed PAs were phospho-ablative or phospho-mimetic, indicating that PA/PB1 interaction is unaffected by the PA Y393 and S395 phospho-mutations.

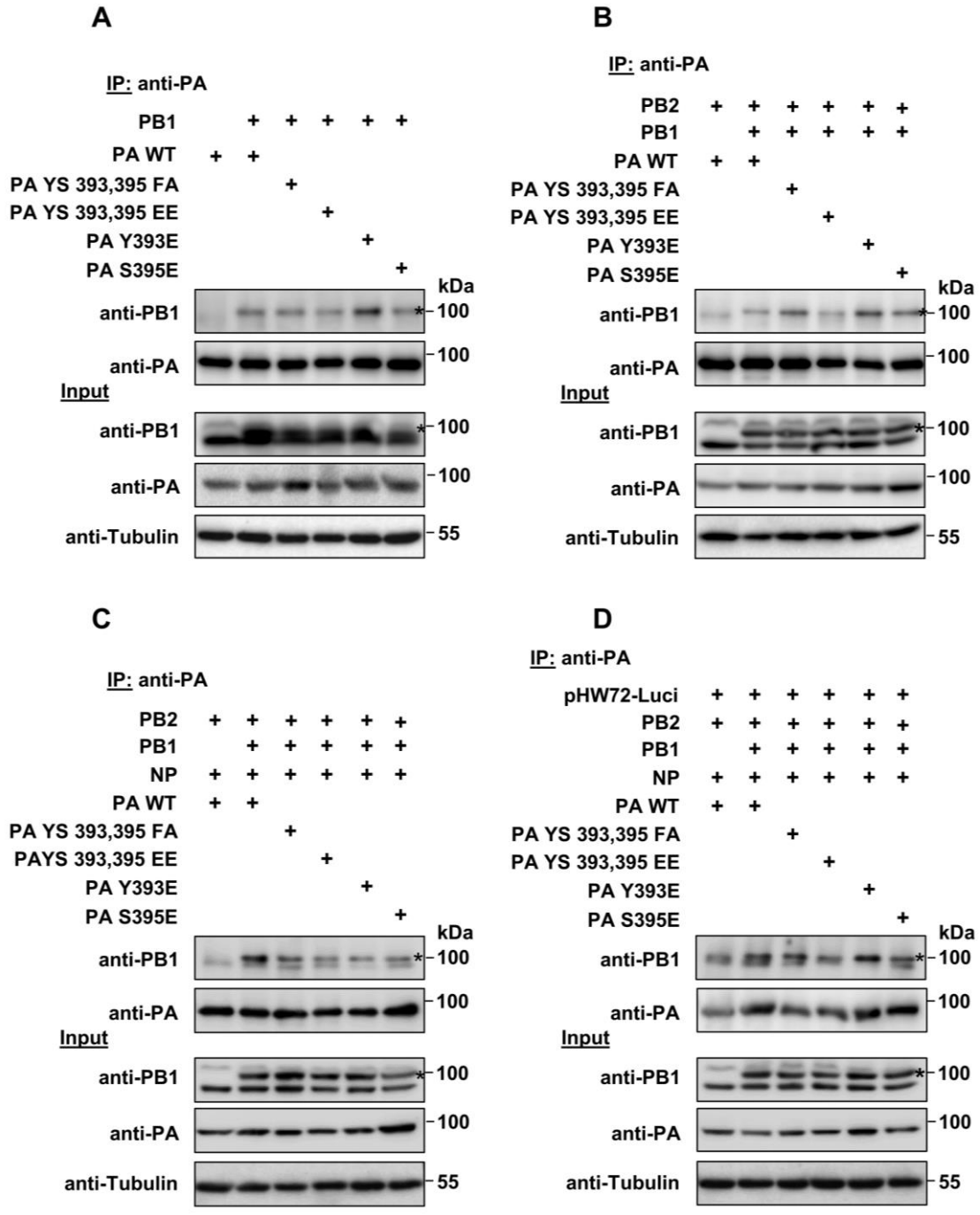

Figure 26: PA Y393 and S395 phospho-mutants do not affect PB1-PA interaction.

(A) PB1 and indicated PA Y393 and S395 phospho-mutants were expressed in 293T cells and cell lysates were subject to PA immunoprecipitation. Immunoprecipitates and input samples were western blotted for PB1 and PA proteins. **(B)** The experiment was performed as in (A) with the difference that PB2 was further co-expressed to test PB1-PA interaction in the presence of polymerase proteins. **(C)** The experiment was

performed as in (B) with the difference that NP was further co-expressed. **(D)** The experiment was performed as in (C) with the difference that vRNA-like reporter gene was further co-expressed expressed to test PB1-PA interaction in the presence of RNP components. Data are representative of two independent experiments.

3.5 Functional consequences of M1 T108 phosphorylation

3.5.1 Phosphorylated M1 T108 is highly conserved among different IAV strains

The phosphorylation sites found in viral matrix protein M1 of influenza A viruses are summarized in **Tables 8**. As described there, IAV M1 phosphorylation occurs at multiple sites on Ser, Thr, and Tyr residues, and can vary between viral strains and host species. Among these candidates, M1 T108 meets the afore mentioned selection criteria. Firstly, the alignment of the primary amino acid sequences of M1 protein showed that the M1 T108 residue is almost 100% identical in all subtype IAV strains from both avian (11759) and human (11590) species, with the exception of two human $H1N1_{pdm09}$ isolates (GeneBank accession no. AGL04668.1 and AFU09343), which present a Met at this site. Secondly, M1 T108 is contained in several described functional regions (**Fig. 27**), suggesting the possible functional roles of a phosphorylation at this site. For example, on the one hand it is close to the known M1 NLS (101RKLKR105), which regulates the nuclear M1 import. On the other hand, it is located in the M1/M1 interacting domain, which is essential for the M1 multimerization.

Table 8: Summary of IAV phosphorylation site in the M1 proteins.

Protein	Phosphorylation site	Virus strains where it was found	Subtypes	Avain IAV	Human IAV	Comments	Reference
				Residue conservation(%)	Residue conservation(%)		
M1	Ser2	WSN/PR8	All	99.93	99.97	Residues 1–20 are critical for the interaction between the / terminus of M1 and importin α1 protein	PMID: 24743939
	Thr5	WSN/PR8	All	99.84	99.93		
	Thr9	WSN/PR8	All	99.91	99.96		
	Tyr10	WSN/PR8	All	99.97	99.97		
	Thr37	PR8	All	89.30	98.89	Unknow function region	
			H7N9	19.12	4.50		
	Thr108	SC35/SC35M/ WSN	All	99.96	99.98	Close to the NLS(^{101}RKLKR^{105})of M1, regulating the nuclear import of M1	PMID: 26008706 PMID: 23536660
	Ser118	SC35/SC35M	All	99.40	99.86		
	Tyr119	SC35/SC35M	All	99.97	99.99	NEP binding region of M1 protein (residues 89 -164) , vRNP nuclear export is mediated by the nuclear presence of M1 and NEP	PMID: 12970177
	Thr121	SC35/SC35M	All	98.35	33.99		
			H3N2	95.54	0.37		
	Tyr132	WSN	All	100.00	99.99	Already analyzed; NLS-neighboring Y132 is critical to control the nuclear import of M1 and virus replication.	PMID: 23536660
	Thr168	WSN	All	83.52	98.79		PMID: 11222100 PMID: 17597902
			H5N1	16.06	16.25		
	Ser195	WSN	All	99.89	99.93		
	Ser196	WSN	All	99.83	99.84	C-terminal part of M1 (residues 165–252), binding to RNPs	PMID: 10799781
	Ser224	WSN	All	74.73	97.75		
	Ser225	WSN	All	96.86	100.00		PMID: 11222100
	Ser226	WSN	All	99.94	99.99		
	Tyr240	SC35/SC35M	All	99.89	99.99		

WSN: A/WSN/1933 (H1N1); PR8: A/Puerto Rico/8/34 (H1N1); Vic: A/Victoria/3/75 (H3N2); SC35: A/Seal/Massachusetts/1/80 (H7N7); SC35M: A/Seal/Massachusetts/1/80 (H7N7) mouse-adapted.

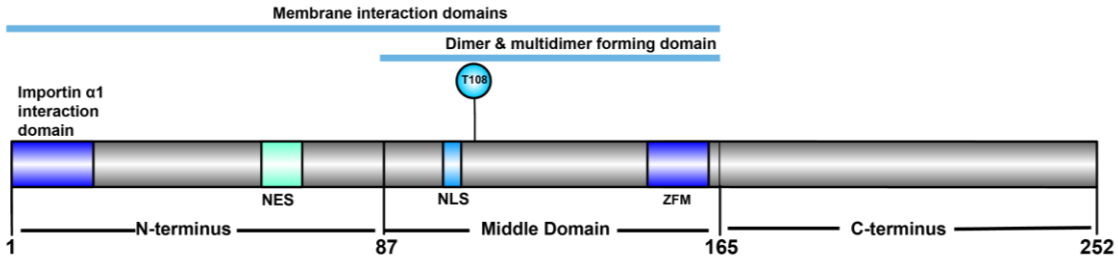

Figure 27: Display of the position of functionally relevant phosphorylation M1 T108.

Schematic domain structure of M1. The amino acid residue M1 T108 is indicated above in blue. The colored boxes represent different functional domains of the M1 protein. ZMF: Zinc finger motif. A detailed description of each protein domain is provided in the text. Amino acid details are adapted from (Liu et al., 2018).

3.5.2 Phosphorylation of M1 at position 108 is required for SC35M propagation

To assess the functional importance of phosphorylation M1-T108 on viral replication, this site was mutated either to prevent phosphorylation (T/A) or to mimic phosphorylation (T/E). Subsequently genetically engineered recombinant SC35M viruses carrying these mutations were generated by RG (**Fig. 28A**). Three attempts to rescue viruses upon mutation of M1 T108A repeatedly failed, while the M1 T108E phospho-mimicking SC35M mutant could be rescued and showed only a minor decrease in replication efficiency compared to WT SC35M (**Fig. 28B**). Taken together, this experiment implies that the phosphorylation of M1 at position 108 is required for SC35M propagation.

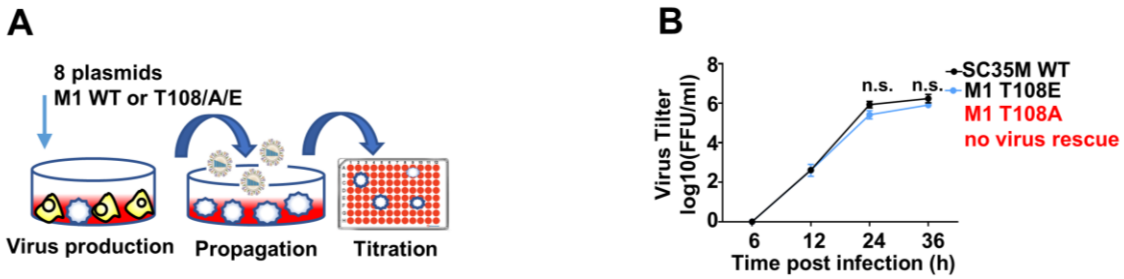

Figure 28: Phosphorylation at M1 T108 is required for viral rescue.

(A) Schematic display of the workflow. Eight plasmids encoding SC35M were expressed to produce viruses mutated in the SC35M M1 proteins. **(B)** The recombinant viruses were produced in 293T/MDCK II cells and then titrated to infect MLE-15 cells (MOI = 0.001). Virus supernatant was harvested at the indicated time points and viral titers were determined via foci assays. The relative virus titers and SEM derived from three independent experiments performed in triplicates are shown on a log10 scale. Differences to WT M1 were tested using unpaired t-test, n.s.: not significant.

To investigate whether the substitutions on M1 T108 affect the stability of M1 proteins, 293T cells were transfected to express 8 plasmids encoding the viral genome and allowing to express all viral proteins. Cells were lysed at 12 h.p.t. and 24 h.p.t., followed by expression analysis of the major viral proteins (WT M1 or M1 T108A/E mutants and NP) via Western blotting (**Fig. 29A)** and subsequent quantification (**Fig. 29B**). The Western blots showed that the expression levels of WT M1 and M1 T108A/E were not significantly changed at both early and late time points after transfection. The quantification of M1 proteins levels revealed slight variations, but this was not statistically significant. The NP displayed a rather minor reduction in protein levels on cells expressing mutated M1 T108A/E proteins in comparison to the WT M1. This suggests that the substitutions T108A/E do not affect expression and stability of M1.

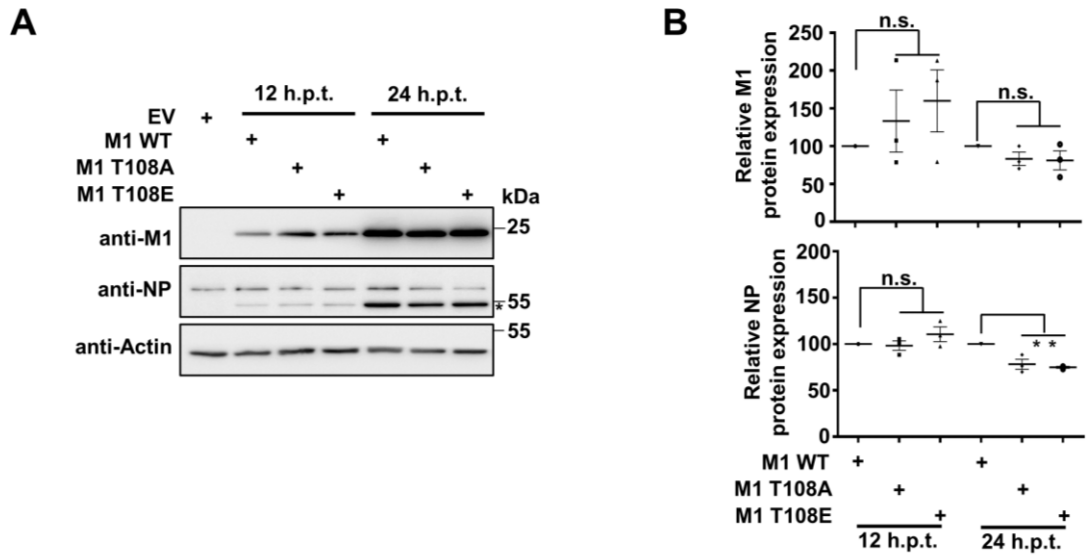

Figure 29: Substitutions at M1 T108 do not affect the M1 protein expression level.

293T cells transfected with 8 plasmids for RG were lysed for Western blot analysis at 12 and 24 h.p.t. **(A)**. M1 and NP were detected with respective antibodies, β-Actin was probed as a loading control (blank lane: cells transfected with empty vector (EV)). Asterisks indicate specific bands detected by immunoblotting. **(B).** Quantitative analysis of M1 and NP protein expression from three independent experiments. The experiment was performed as described in (A), protein amounts of M1, NP, and β-Actin were quantified. Relative protein amounts were normalized to β-Actin and WT M1 or NP expression was set as 100%, the mean is plotted and error bars indicate standard error of the mean (SEM) by unpaired t-tests, n.s.: not significant, asterisks indicate p values (*p ≤ 0.05, **p ≤ 0.01).

3.5.3 Phosphorylated M1 T108 contributes to the nuclear import of M1

Phosphorylation within or adjacent to NLSs has been shown to be important in regulating nuclear import, acting through a range of stimulatory and inhibitory mechanisms (Hutchinson et al., 2012). M1 shuttles between the cytosol and nucleus at early stages of virus replication to modulate viral polymerase activity and guide newly synthesized vRNP complexes from the nucleus into the cytoplasm (Mecate-Zambrano et al., 2020). In late stages, M1 is mainly localized at the PM to initiate budding and assembly of progeny virions. The fact that the phospho-acceptor site M1 T108 is close to the NLS of M1 protein (**Fig. 27**), raises the question whether this phosphorylation is involved in the regulation of the nuclear M1 import. To address this question, subcellular localization of WT M1 or M1 mutants was analyzed in 293T cells transfected with 8 plasmids (**Fig. 30**). Cells were harvested and fractionated into cytosolic and nuclear extracts at the 4 indicated time points. Quantitative evaluation of Western blot experiments revealed an increased amount of M1 T108A in the cytosolic fraction and a reduced amount in the

nuclear fraction, when compared to WT M1 or the M1 T108E mutant at all four time points. These data suggest that M1 phosphorylation can affect the intracellular distribution of M1.

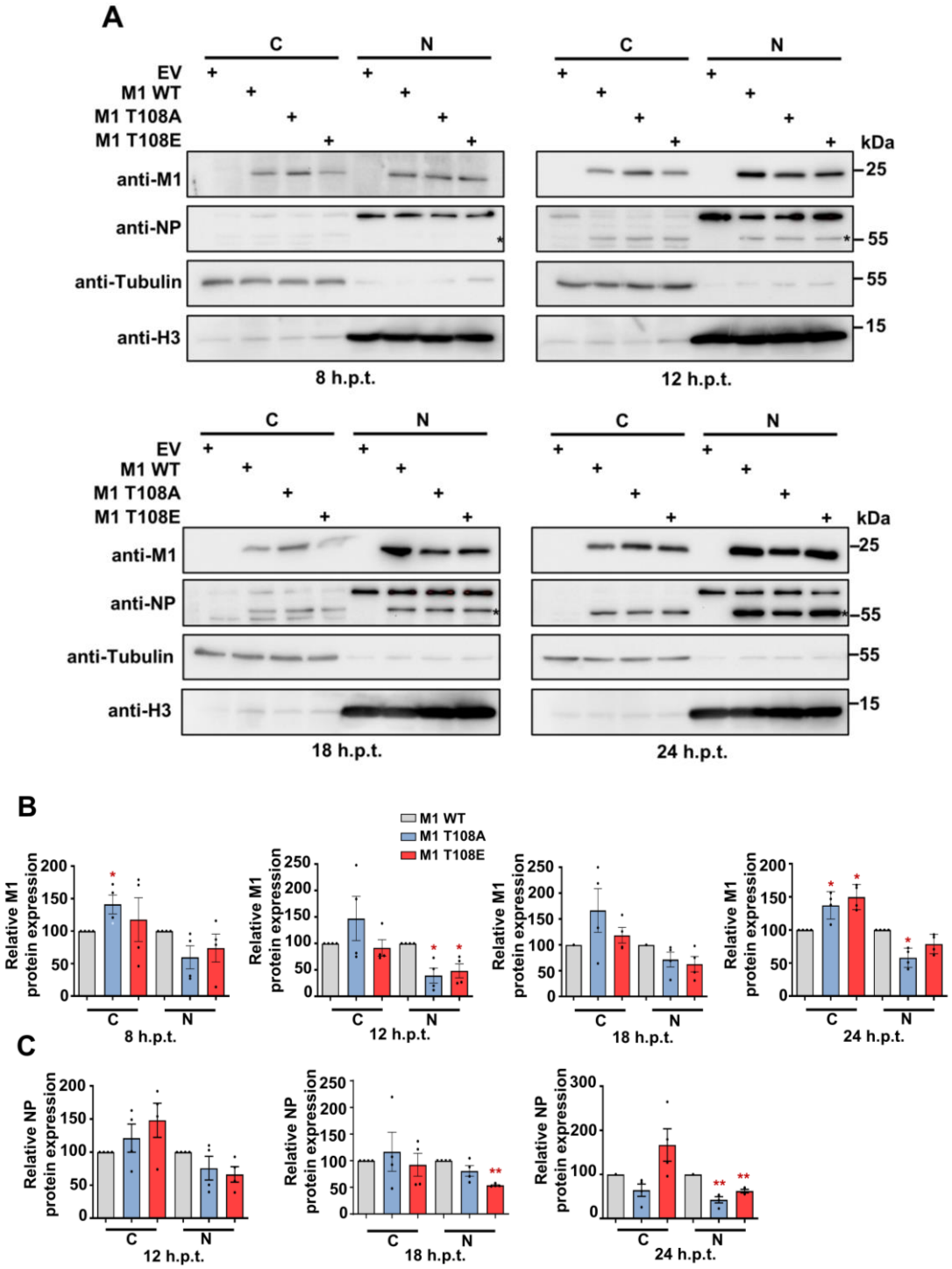

Figure 30: M1 T108A mutant causes the cytoplasmic accumulation of M1 protein.

Immunoblot analysis of the cytoplasmic and nuclear distribution of M1 and NP proteins. 293T cells were transfected with 8 plasmids for RG of SC35M expressing either WT M1 or M1 T108 phospho-mutants. **(A)**

At 8, 12, 18, and 24 h.p.t., nuclear and cytoplasmic fractions were obtained. The upper panels show protein levels determined by quantification of Western blots. β-Tubulin and histone H3 were used as fractionation-specific markers. **(B)** and **(C).** The experiment was performed as in A, and the M1 (B) and NP expression (C) were quantified compared to WT M1, which was set at 100%. The data of NP protein expression at 8 h.p.t was not included due to the low expression level of NP at this time point. Values display means ± sd. from four independent experiments. Differences to WT M1 were tested using unpaired t-test, red asterisks indicate p values (*p ≤ 0.05 and **p ≤ 0.01 ***p < 0.001). C: cytoplasmic fraction; N: nuclear fraction.

In addition, an immunofluorescence assay was also performed to examine the intracellular location of M1 and vRNPs in 293T cells transfected with the SC35M-encoding 8 plasmids at the indicated time points. Here, WT M1 displayed a homogenous distribution between nucleus and cytoplasm at each of the four tested time points. As the major protein component of vRNPs, the NP protein accordingly underwent dynamic nucleocytoplasmic shuttling, with predominant nuclear localization at 18 h.p.t., translocation from the nucleus to the cytoplasm at 24 h.p.t., localization throughout the cells at 36 h.p.t., and nuclear redistribution at 48 h.p.t. (**Fig. 31A**). This phenomenon could also be observed in cells expressing M1 T108E mutant, which displayed cellular localization similar to that of WT M1 (**Fig. 31A**). However, quantitative analysis of the immunofluorescence experiments of cells expressing M1 T108A exhibited cytoplasmic accumulation of M1 and nuclear retention of vRNP (**Fig. 31B**). Accordingly, these experiments show that phosphorylation on M1 T108 contributes to the nuclear import of M1 and nuclear export of NP.

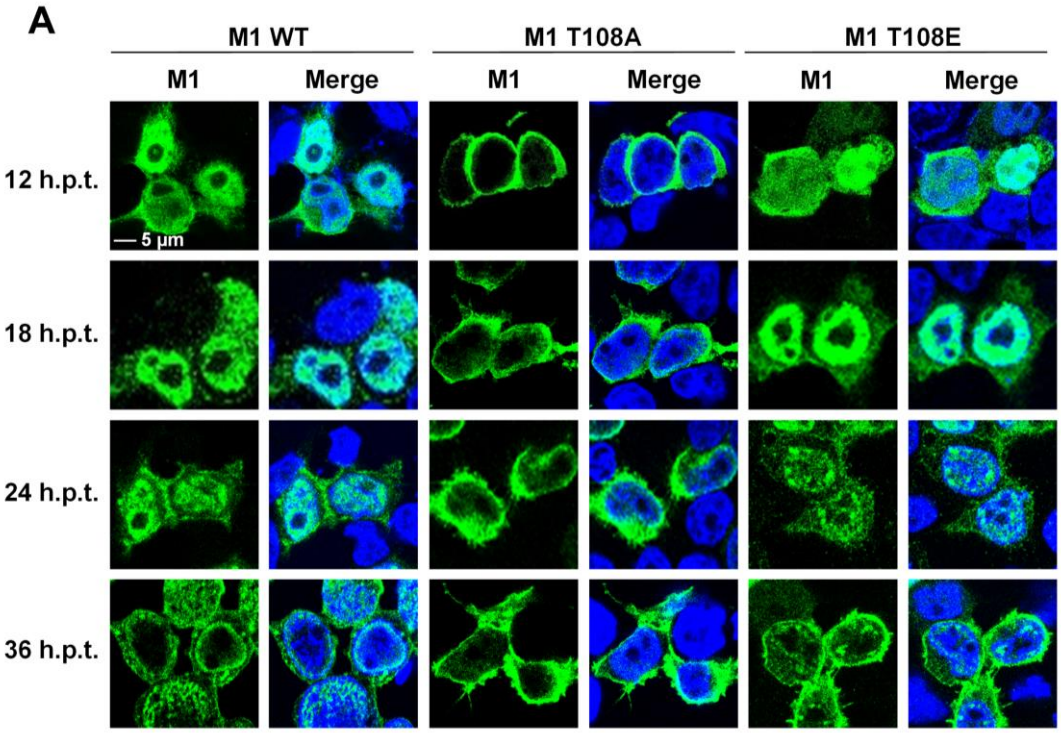
A
M1 WT
M1 T108A
M1 T108E
M1
Merge
M1
Merge
M1
Merge
12 h.p.t.
18 h.p.t.
24 h.p.t.
36 h.p.t.
5 µm

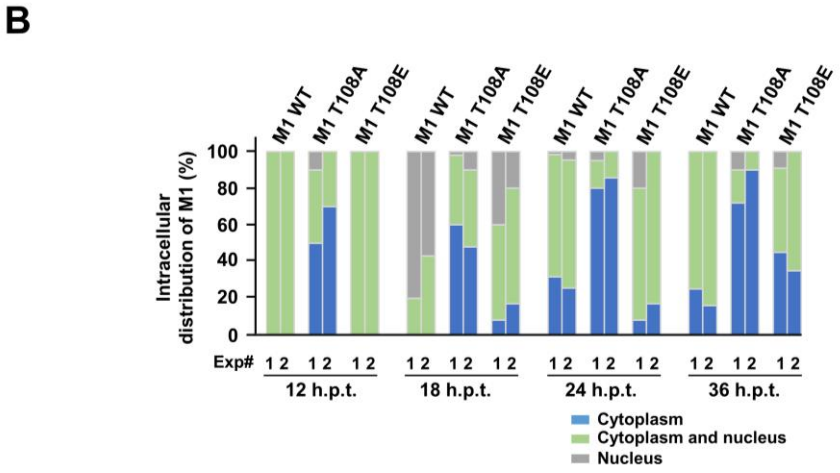
B
M1 WT
M1 T108A
M1 T108E
Intracellular distribution of M1 (%)
100
80
60
40
20
0
Exp# 1 2 1 2 1 2 1 2 1 2 1 2 1 2 1 2 1 2 1 2 1 2 1 2
12 h.p.t.
18 h.p.t.
24 h.p.t.
36 h.p.t.
Cytoplasm
Cytoplasm and nucleus
Nucleus

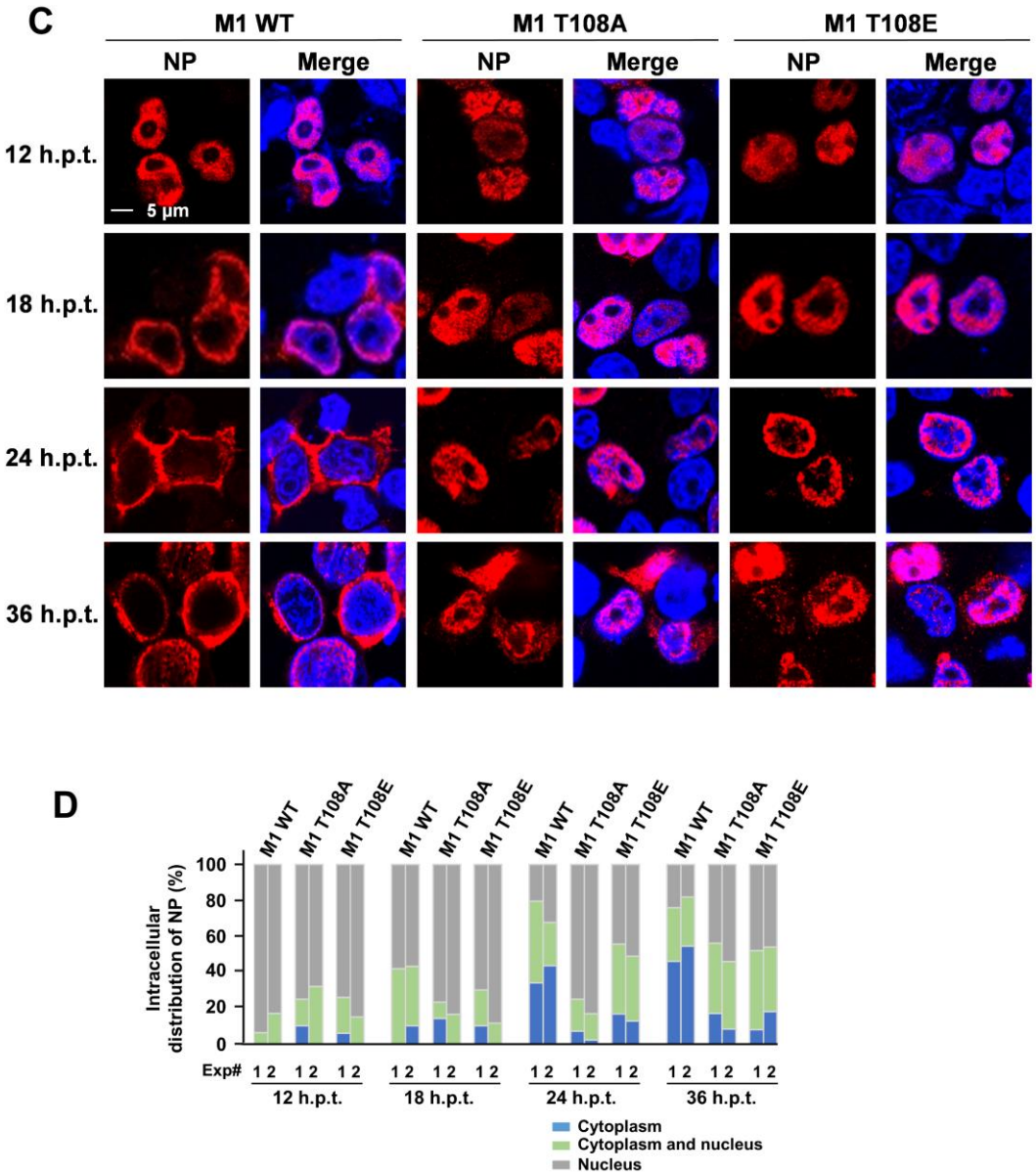

Figure 31: Phosphorylation M1-T108 contributes to the nuclear import of M1 and nuclear export of vRNP.

Immunofluorescence assay to detect the cellular location of WT and mutated M1 (M1 T108A/E) in 293T cells transfected with an 8-plasmid reverse genetic system for SC35M. At 12, 18, 24, and 36 h.p.t., cells were fixed and stained with anti-M1 antibody (green) **(A)** and anti-NP antibody (red) **(C)**. Nuclei were stained with Hoechst 33342 (blue), scale bars: 5 µm. Pictures are representatives of two independent experiments. **(B, D)** The experiment was performed as in (A,C), and the intracellular distribution of M1 and NP in the cells was scored as shown. The percentage of cells representing each score is shown. M1 and NP expression were quantified from at least 150 interphase cells for each condition.

.

3.5.4 The M1 T108A mutation does not alter the membrane association of M1 and the production of IAV particles

In later stages of infection, M1 is mainly localized at the PM where it recruits other viral envelope proteins (HA, NA, M2), initiating the assembly and budding of progeny virions (Hilsch et al., 2014; Nayak et al., 2009; Rossman & Lamb, 2011). T108 is also found in the region interacting with the PM of infected cells (**Fig. 27**). Therefore, it was also important to test the relevance of M1 phosphorylation for its association with the cell membrane. To this end, a direct method relying on co-staining M1 together with the M2 protein, which carries M1 in a piggyback mechanism to the PM (Chen et al., 2008; McCown et al., 2006), was applied on the 293T cells upon transfection of 8 plasmids expressing all SC35M proteins. After 24 h.p.t., WT viral progeny should be produced in cells expressing WT SC35M proteins, and consistent with this, a fraction of the WT M1 protein was detected at the PM where it co-localized with M2 (**Fig. 32**). This phenomenon was also seen for the M1 T108E mutant. Interestingly, M1 T108A was also observed in close proximity to the membrane, but showed a reduced nuclear presence, which is consistent with the fractionation and immunofluorescence experiments (**Fig. 30**, **Fig. 31**). In the meanwhile, a clear colocalization of both M1 and M2 proteins at the PM was observed. Collectively, these results suggest that M1 T108A is efficiently transported to the PM and does not influence the PM association of the M1 protein.

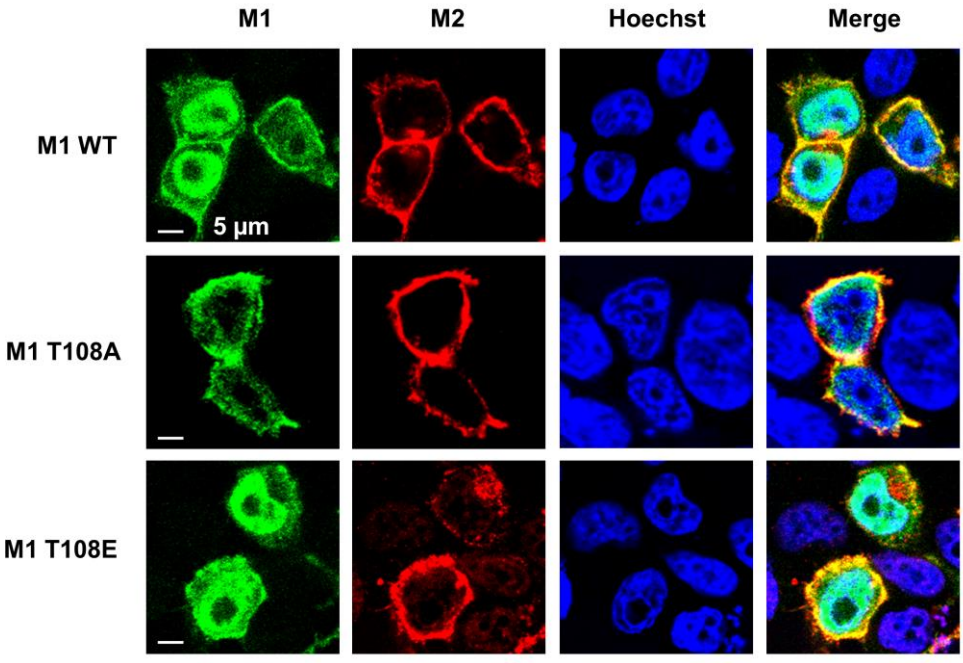

Figure 32: The T108A mutation does not influence the PM association of M1.

Immunofluorescence assay for the cellular location of M2 and WT or mutated M1 (M1 T108A/E) in 293T cells transfected with the 8-plasmid reverse genetic system for SC35M. Cells were fixed 24 h.p.t. and analyzed for localization of M1 (green) and M2 (red), nuclei were stained with Hoechst 33342 (blue), scale bars: 5 µm. Pictures are representatives of two independent experiments.

VLPs are widely used to assess the efficiency for influenza virus assembly and budding (Das et al., 2012; Wang et al., 2017). Thus, the generation of VLPs was determined to analyze whether M1 T108 phospho-mutants affect VLP formation. To do that, three different VLPs were generated in 293T cells transfected with plasmids expressing the SC35M genome together with WT or mutated M1, along with HA, NA, and M2, all of which are known components sufficient to produce VLPs with structures identical to the WT virions (Peukes et al., 2020). Western blotting experiments were subsequently performed to analyze presence of these viral proteins within purified and concentrated VLPs in cell culture supernatants as well as in cells. Notably, HA occurred in the culture supernatant of transfected cells even in the absence of the M1 protein (**Fig. 33**, lane 2), due to the fact that HA and NA are sufficient for VLP formation and budding (Chlanda et al., 2015; Das et al., 2012). Comparable robust M1 and HA protein levels in all purified VLPs were detected for WT SC35M M1 and mutant M1, indicating the efficient incorporation of M1 T108 phospho-mutants into VLPs.

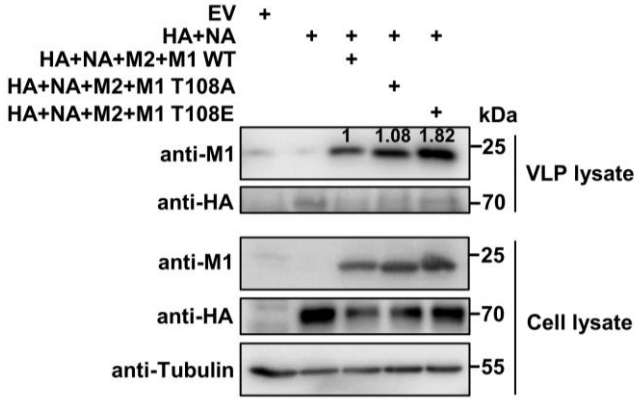

Figure 33: Effect of the M1 T108 mutations on M1 incorporation into VLPs.

293T cells were co-transfected with pCAGGS-SC35M-HA, pCAGGqS-SC35M-NA and pCAGGS-SC35M-M2 expressing plasmid alone, or together with pCAGGS-SC35M-WT M1 or M1 T108A/E mutants. After 48 h.p.t., VLPs in the supernatants were pelleted through a 30% sucrose cushion by ultracentrifugation. Proteins in the cell lysates and VLP samples were examined by Western blotting. The M1 intensity of VLP lysate and cell lysate was quantified with Image Lab 6.0.1 software (BioRad). Relative VLPs production was calculated on the basis of the protein band intensities and expressed as the ratios of VLP lysate M1/cell lysate M1, the ratio of IAV VLPs from the cells expressing WT M1 was set to 1.

3.5.5 M1 T108 phosphorylation plays a role in regulating M1 polymerization

The data gained so far point to a key function of M1 T108 phosphorylation on viral propagation by regulating the nuclear import of M1, thus affecting the nuclear export of vRNP. The position of M1 T108 within the protein suggests a possible role in the regulation of M1/M1 interactions, as seen by the structural analysis of M1 multimers (**Fig. 34A**) (Peukes et al., 2020). It is known that association M1 with the PM triggers its oligomerization as a consequence of an increased affinity to other monomers, ultimately providing structural integrity and stability to the virion (Calder et al., 2010; Dahmani et al., 2019; Mohd-Kipli et al., 2021). Notably, regions on M1 previously identified as being involved in priming M1 for oligomerization can also be phosphorylated, including helix 1 (S2/T5 and T9/Y10) and the loop between helices 2 and 3 (T37) (Mohd-Kipli et al., 2021). In order to test the possibility that M1 T108 phosphorylation regulates M1 polymerization, its self-association was tested by crosslinking experiments. 293T cells were transfected to express the SC35M genome together with WT M1 or its phosphorylation-defective or phospho-mimicking versions. Proteins in close proximity were crosslinked using the membrane-permeable, bifunctional lysine-to-lysine crosslinkers disuccinimidyl glutarate (DSG) or disuccinimidyl suberate (DSS). After crosslinking by DSG or DSG, M1 multimerization was revealed by Western blotting where crosslinked protein species were seen by multiple upshifted bands. Interestingly, the phosphorylation-deficient M1 T108A mutant displayed a stronger signal of the dimer (a band at 50 kDa that could be a M1 dimer) and also high molecular weight smear in comparison to WT M1 or M1 T108E mutant (**Fig. 34B, C**). This phenomenon was even more apparent after crosslinking with DSG, which has shorter spacer arms (**Fig. 34B**). These data indicate that the M1 T108 phosphorylation plays a role in restricting M1 multimerization.

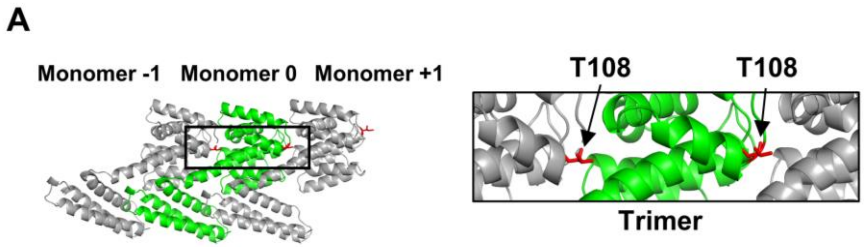

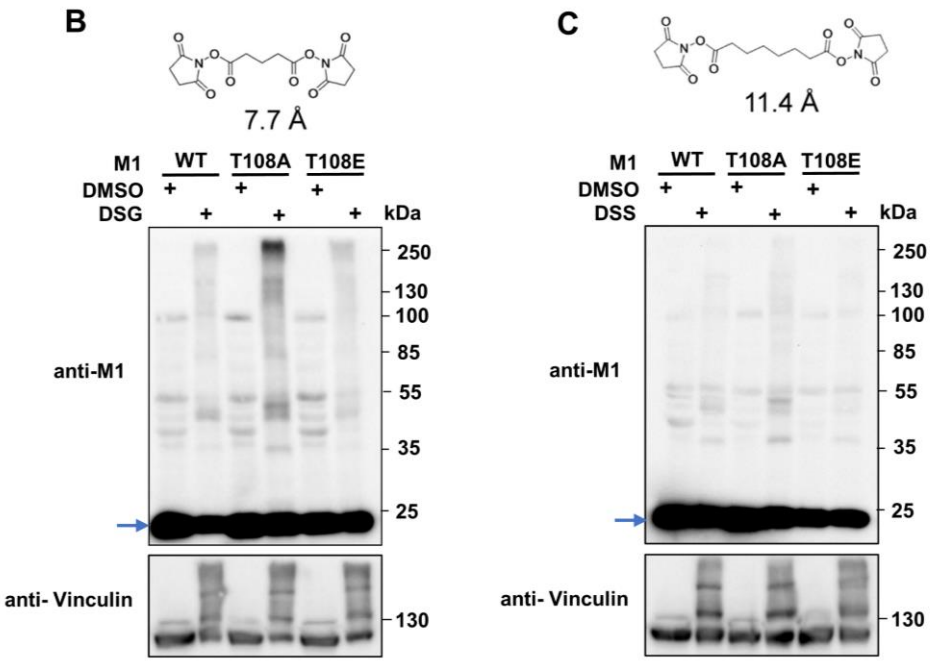

Figure 34: The mutation of T108A affects the M1 polymerization.

(A) The position of phosphorylation M1 T108 is shown within the multimerized M1 protein (PDB: 1EA3) and the boxed areas were enlarged. The structures were displayed using Pymol. **(B)** The indicated transfected 293Tcells were harvested 24 h.p.t., and *in vivo* crosslinked with DSG (2 mM) or **(C)** DSS (2 mM). The cells were then lysed and analyzed by Western blotting using an M1-specific antibody. Uncrosslinked M1 monomer migrates at ~22 kDa (blue arrow). Vinculin was used as loading control.

3.5.6 M1 T108 phosphorylation regulates the protein/protein interactions

To investigate a potential effect of regulated M1 T108 phosphorylation on protein/protein interactions by an unbiased approach, Co-IP experiments coupled to mass spectrometric analysis were performed, as illustrated in **Fig. 35A**. 293T cells were transfected with 8 plasmids to express the SC35M genome together with the WT M1 or its T108 phospho-mutants or the empty vector. Cell lysates were prepared and used for Co-IP using the anti-M1 antibody or a nonspecific control rabbit Immunoglobin G (IgG) (**Fig. 35B**). The immunoprecipitates were subsequently subjected to mass-spectrometric analysis. The analysis of three independent experiments showed that the WT M1 protein specifically interacts with a number of proteins (**Fig. 35C**). The analysis of the M1 T108E interactome showed that this mutant had largely lost the ability to interact with proteins attached to M1 WT (**Fig. 35C**). Mapping of the M1 interacting proteins to gene ontology (GO) pathways using Metascape software revealed the association of proteins regulating TNFα/NF-κB singling, RNA splicing and components of the STRIPAK (striatin-interacting

phosphatases and kinases) complex, that did not interact with the T108A mutant anymore (**Fig. 35D**).

Among the 71 detected WT M1-asscoated proteins as shown in the Venn diagrams (**Fig. 35E**), 12 proteins (KLHDC10, tubulin isotypes (TUBA1A; TUBA1B; TUBA1C; TUBA3E; TUBA4A; TUBA8), PHGDH, RPL12, RPS3, RPS26; RPS26P11, EEF1A1; EEF1A1P5; EEF1A2, C1QBP, RPL21, RPL35A, NUDT21, NCL) specifically bound to WT M1. Of these proteins, KLHDC10 (kelch repeat protein), ubiquitous cytoskeleton components-tublin isotypes, NUDT21(Gaucherand et al., 2019), ribosomal proteins including RPS3 and RPL21 (Wang et al., 2018), cell surface nucleolin (NCL) (Chan et al., 2016), were previously annotated as binding factors of IAV proteins, such as PA, PA-X and HA. RPS3 is linked to the mouse resistance to the H5N1 IAV infection (Boon et al., 2009). PHGDH (Nigdelioglu et al.), RPS3 (Capitanio et al., 2012), RPS26 (Capitanio & Wozniak, 2012), RPL21 (Capitanio & Wozniak, 2012), EEF1A1 (Sammaibashi et al., 2018), NUDT21 (Gaucherand et al., 2019), and NCL (Chan et al., 2016) serve as pro-viral factors for IAV replication.

Most importantly, a numerous of proteins showed their involvement in M1 T108 phosphorylation-regulated association, with different binding affinity between WT M1 and and M1 T108A/E mutants (**Fig. 35E)**. Specifically, 108 proteins displayed a higher binding affinity towards the M1 T108A mutant, some of which are directly related to the pathways such as regulation of mRNA metabolic process (**Fig. 35D**). In particular, some of them (HSP90AA1, KHSRP DSP, RPS20) were noted as essential host factors required for IAV replication (Konig et al., 2010). In contrast, the T108E mutant largely lost its ability to bind to 86 proteins, 14 of which also had a lower binding affinity with M1 T108A mutant than WT M1. Of these, SFPQ and NONO are members of the paraspeckle complex (Fox et al., 2018) and associated with antiviral immune response (Imamura et al., 2014; Ma et al., 2017). These proteins were also identified as SINV viral RNA interactor (Pennemann et al., 2021) and play role in regulate posttranscriptional HIV-1 replication (Lahaye et al., 2018; Pennemann et al., 2021; Sarracino et al., 2018; Zolotukhin et al., 2003). In summary, the phosphorylation status of M1 T108 also affects the ability of M1 protein to interact with other proteins.

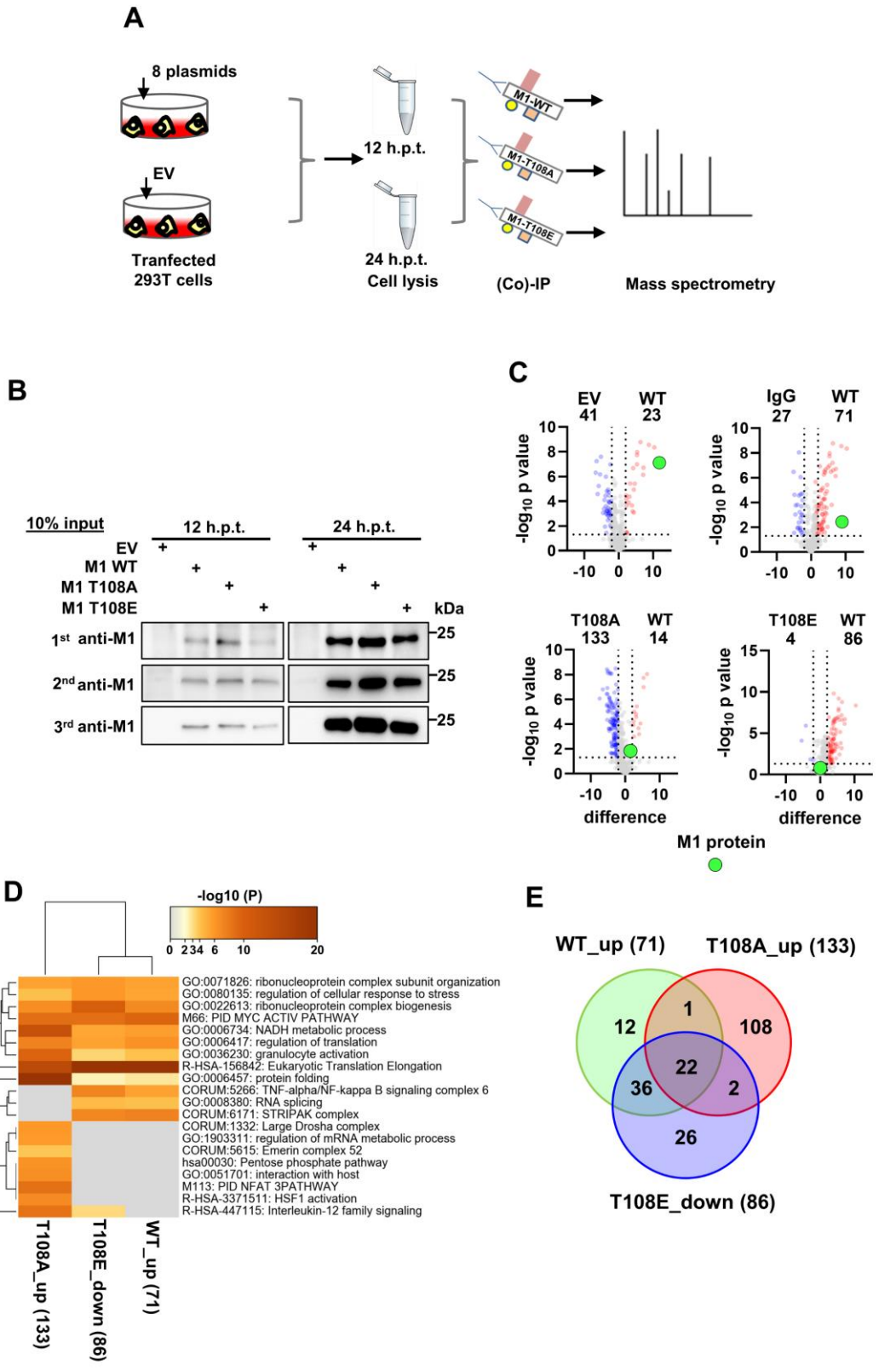

Figure 35: M1 T108 phosphorylation plays a role in regulating the association of M1 with other proteins.

(A) Schematic display of the experimental setup used to identify WT M1 & M1 T108A/E mutant-interacting proteins. 293T cells expressing 8 plasmids encoding SC35M together with WT M1 or M1 T108 phospho-mutants or empty vector (EV) were lysed. Lysates were subjected to Co-IP using anti-M1 antibody or a

nonspecific control rabbit IgG. **(B)** The input material was analyzed by Western blotting for M1 protein expression levels. **(C)** The M1 interactomes of the cells expressing M1 for 24 h.p.t. were subjected to the pairwise comparisons as shown. Colored spots in Volcano plots show proteins with intensity values significantly enriched (LFC ≥ two-fold) and statistically significant ($p \leq 0.05$). Data are from three biological and two technical replicates. The M1 protein intensities are highlighted in green in all graphs. **(D)** Overrepresentation (ORA) analysis for enriched interactors. Numbers in brackets correspond to the protein sets shown in (C). **(E)** Overlap of specifically enriched interactors binding to WT M1 or the T108 mutants.

3.5.7 The interaction between M1 and STRN/STRN3 is regulated by M1 T108 phosphorylation

10 Proteins (STRN, PPP2R1A, FGFR1OP2, SLMAP, MOB4, STK26/STK25, STRIP1, SIKE1, PPP2CA/PPP2CB) belonging to STRIPAK complex bound preferentially to WT M1 (**Fig. 36A**). To confirm these regulated physical interactions between WT M1 and its phospho-mutants, Co-IP experiments were performed. In these experiments, striatin (STRN) and STRN3, which function as central scaffolding proteins of the STRIPAK complex, were detected. 293T cells expressing 8-plasmids encoding SC35M together with WT M1 or M1 T108 phospho-mutants were lysed and extracts were further used for Co-IP experiments. Subsequent Western blot experiments confirmed the preferential interaction of STRN and STRN3 with WT M1 at both 12 h.p.t. and 24 h.p.t. (**Fig. 36B, C**). In addition, the interaction between STRN or STRN3 and M1 was also established in a genuine infection of 293T cells and MLE-15 cells by SC35M (**Fig. 36D**).

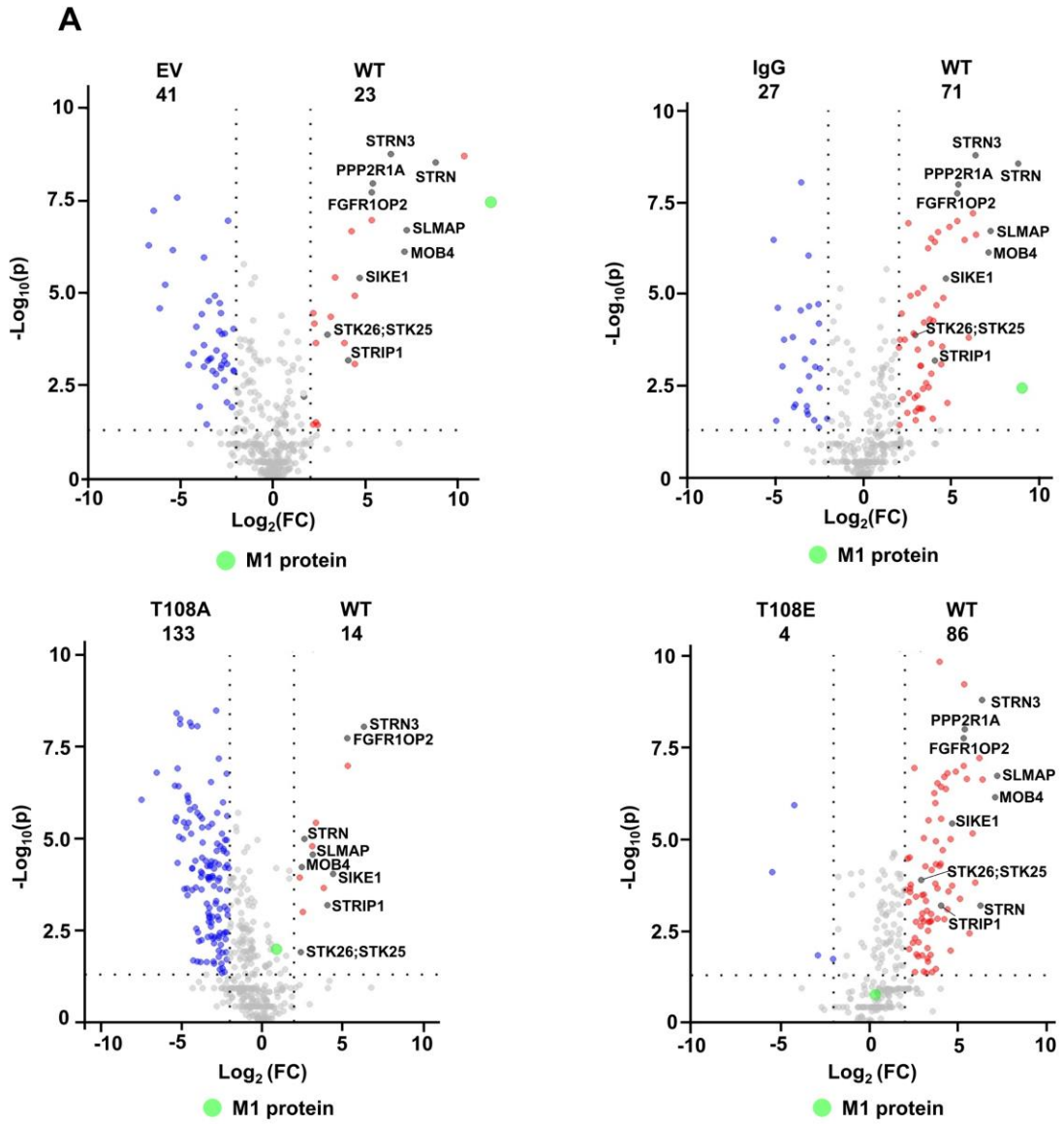
A
EV
41
WT
23
IgG
27
WT
71
T108A
133
WT
14
T108E
4
WT
86
STRN3
PPP2R1A
STRN
FGFR1OP2
SLMAP
MOB4
SIKE1
STK26;STK25
STRIP1
-Log10(p)
Log2(FC)
M1 protein

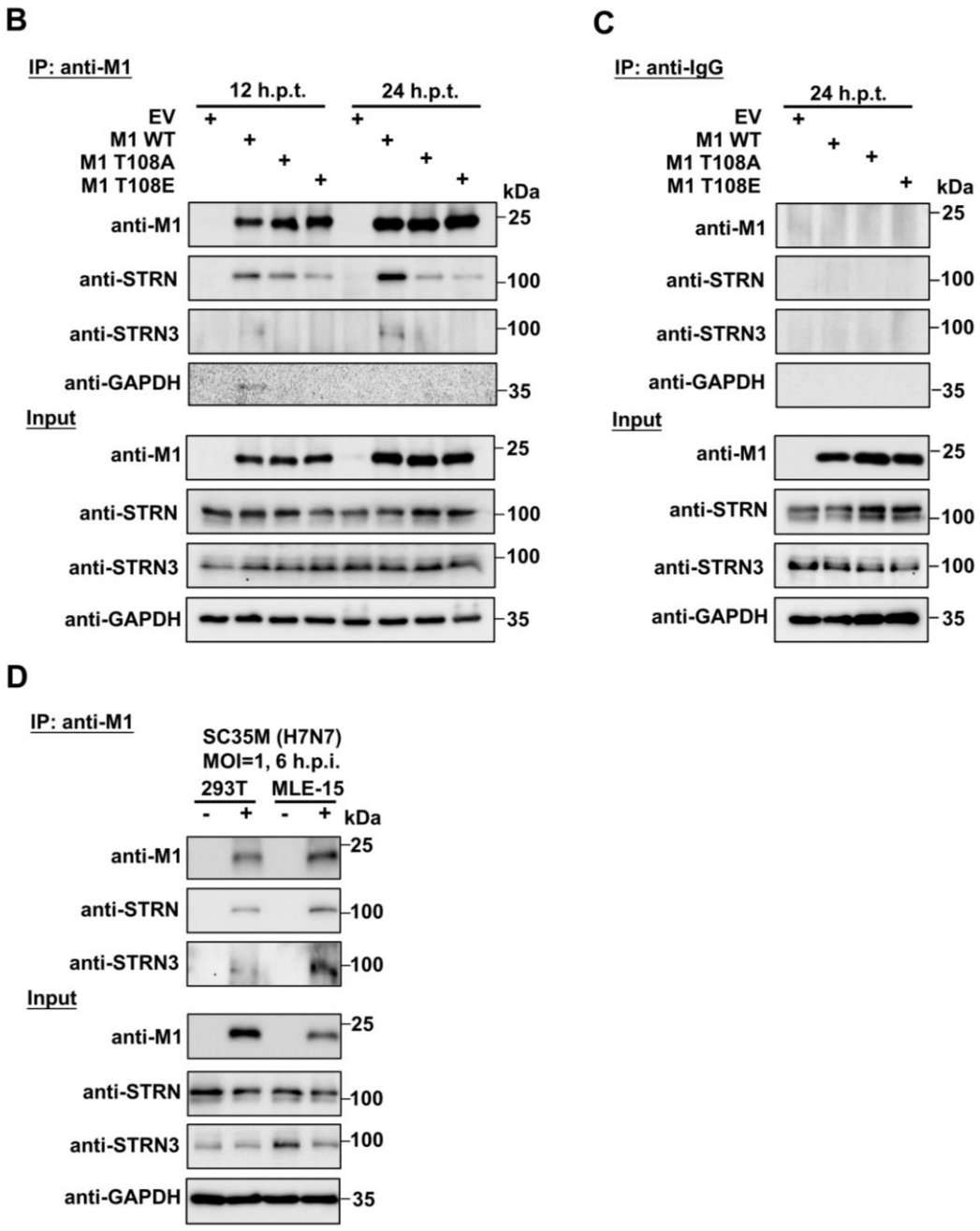

Figure 36: M1-T108 phosphorylation mediates the binding of M1 to STRN and STRN3.

(A) The Volcano plots show pairwise comparisons, members of the STRIPAK complex are shown in dark grey dots. **(B)** and **(C)** 293T cells were transfected with 8 plasmids for RG of SC35M and analyzed at 12 and 24 h.p.t. by Co-IP as shown. **(D)** 293T cells or MLE-15 cells infected by SC35M (MOI=1) were harvested 6 h.p.i., and immunoprecipitated using anti-M1 antibodies or control anti-IgG antibodies. Precipitated eluates and non-precipitated whole cell lysates of transfected cells as input were subjected to SDS gel electrophoresis, the indicated proteins were detected by Western blot analysis with specific antibodies.

3.5.7.1 The role of the identified M1 interactors STRN/STRN3 in viral replication

To investigate a possible function of Strn and Strn3 for IAV replication, both adapter proteins were knocked down in MLE-15 cells. Western blot experiments conducted to confirm the effective knockdown showed that downregulation of Strn increased the levels of Strn3 and vice versa downregulation of Strn3 resulted in a similar increase of Strn levels, suggesting that different Strn family members can compensate for each other (**Fig. 37A**). Depletion of Strn or Strn3 alone did not significantly affect the SC35M replication, while the combined knockdown of Strn together with Strn3 resulted in a decrease in levels of viral proteins (M1, NS1, and NP) as well as in viral titers by one order of magnitude. This effect was seen starting at 14 h.p.i. and a slight reduction was still seen at 24 h.p.i (**Fig. 37B**). Similarly, knockdown of Strn/Strn3 interfered with replication of another human IAV subtype, the pandemic IAV strain A/Hamburg/04/2009 ($H1N1_{pdm09}$) (**Fig. 37B**), indicating that the virus-supportive function of the STRIPAK complex is not restricted to one virus strain.

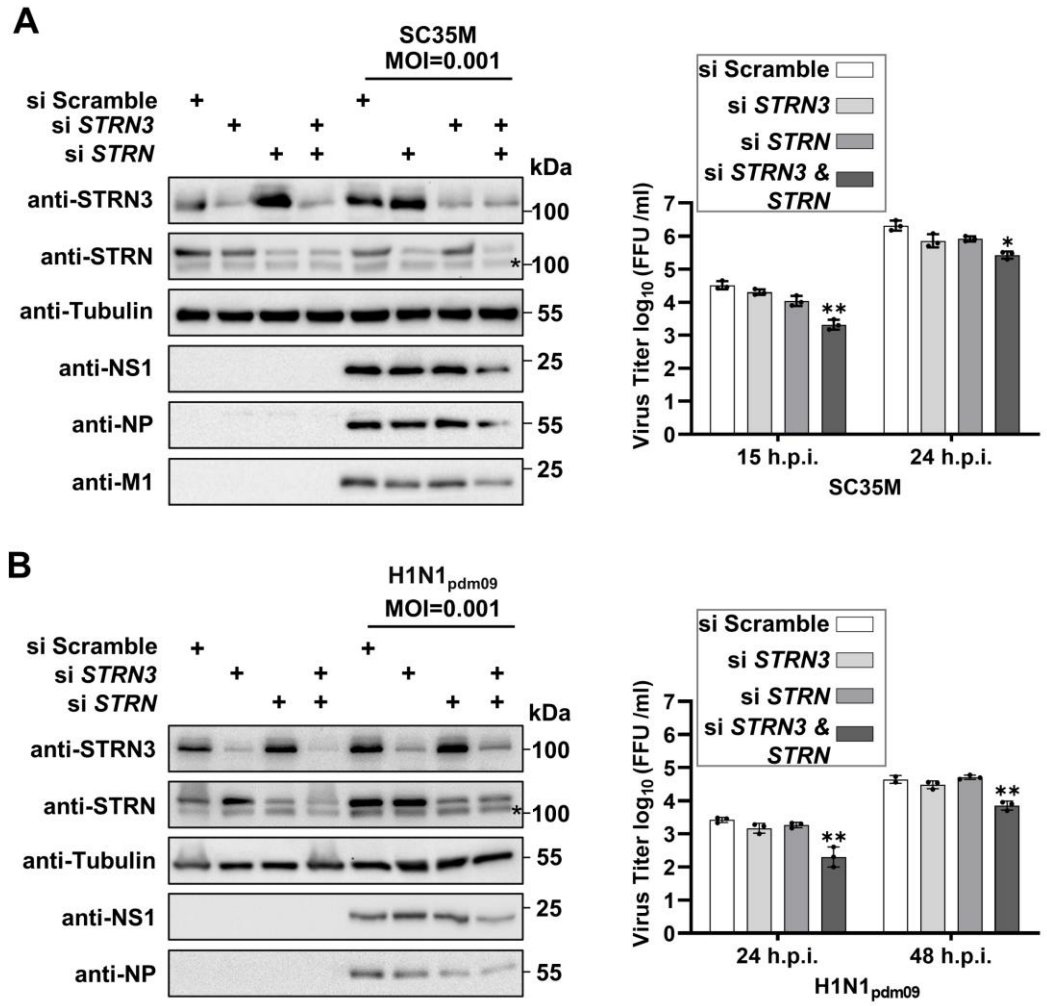

Figure 37: Pro-viral effect of Strn/Strn3.

(A) MLE-15 cells were seeded and transfected one and three days later with siRNAs targeting mRNAs encoding the indicated proteins or an adequate scrambled control as shown. One part of the cells was lysed and characterized by Western blotting to control knockdown efficiency and expression of viral proteins from cells infected with SC35M (left) or viral titers of cell culture supernatants were determined at the indicated time points (right). Titers are displayed. Bars indicate standard deviations obtained by unpaired t-tests, asterisks indicate p values (*p ≤ 0.05, **p ≤ 0.01). **(B)** The experiment was done as in (A), but virus infection was done using H1N1pdm09 (MOI = 0.001).

3.5.7.2 The colocalization of M1 with STRN and STRN3 in IAV-infected cells

In order to gain more insight into spatiotemporal dynamics of interactions between M1 and STRN/STRN3 in IAV infection, I further determined the subcellular localization and kinetics of M1 and STRN/STRN3 over time in SC35M-infected 293T cells and found that at different time points p.i., M1 mainly colocalized with endogenous STRN in the cytoplasm and in the perinuclear region (**Fig. 38A**). Weak diffuse M1 staining throughout the cytoplasm and the nucleus was detectable as early as 2 h.p.i., indicating that expression of M1 already proceeded at this time point. (Larson et al., 2019). This staining signal subsequently increased throughout the cytoplasm and the nucleus of the cells. Consistent with previous reports, STRN staining in uninfected cells or virus-infected cells at an early time point (2 h.p.t.) revealed a homogeneous puncta pattern with a main localization at the cell cortex and a partial localization throughout the cytoplasm in 293T cells (Lahav-Ariel et al., 2019). After 4 h.p.i., the punctate distribution of STRN in the cell cortical region decreased, while the accumulation in the cytoplasm tended to increase slightly.

Similarly, there was an apparent co-localization between STRN3 and M1 since when the M1 staining was visible at 4 h.p.i.. In addition, the staining pattern of STRN3 showed as small puncta along the cellular membrane and throughout the cytoplasm, with high concentrations close to the nuclear membrane in the absence and presence of virus infection (**Fig. 38B**). Strikingly, after infection, STRN3 appeared to form clusters, which considerably increased in number and size starting at 4 h.p.i and extending to 8 h.p.i., suggesting that STRN3 forms aggregates in response to viral infection (**Fig. 38B**)

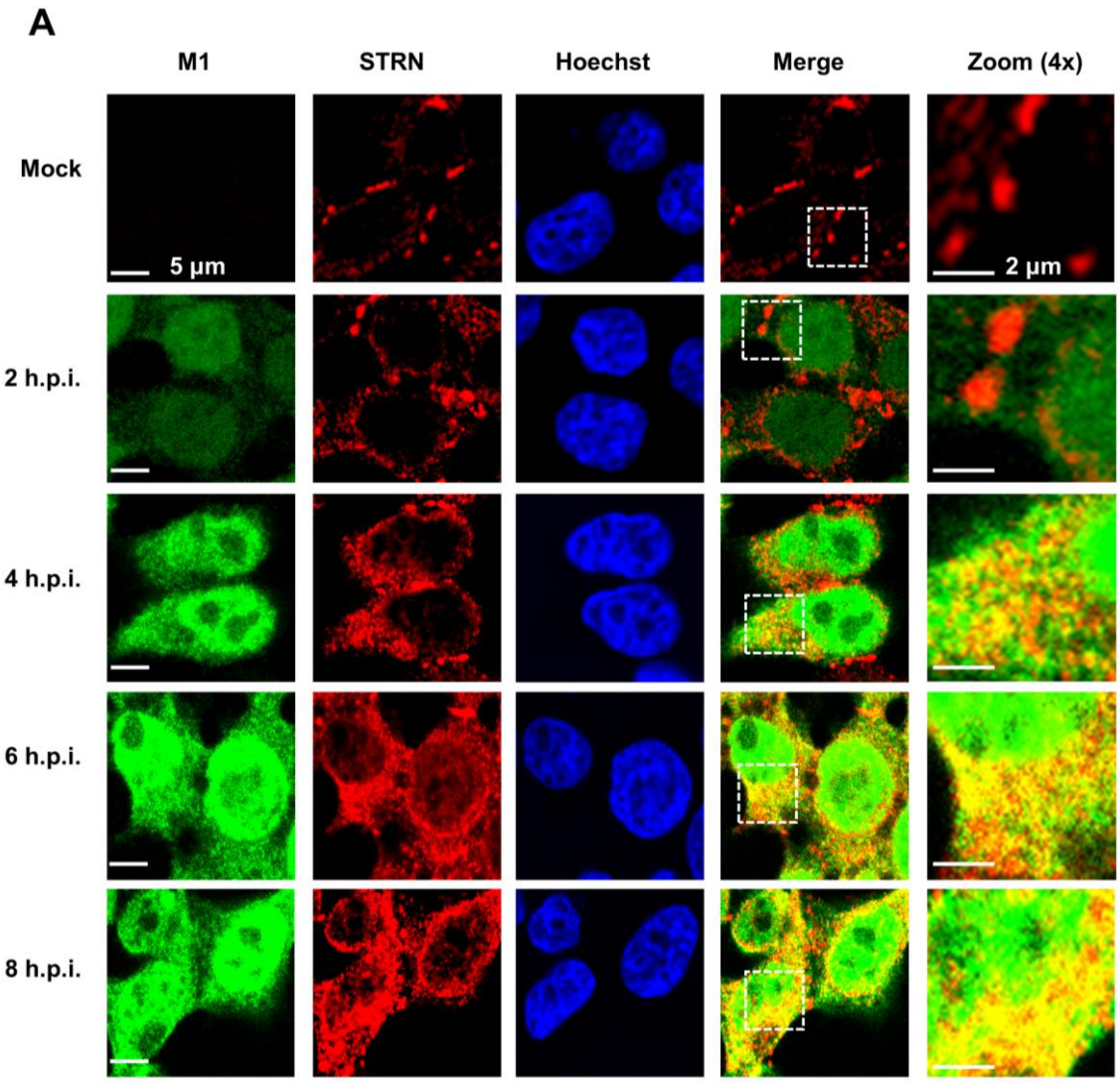
A
M1
STRN
Hoechst
Merge
Zoom (4x)
Mock
2 h.p.i.
4 h.p.i.
6 h.p.i.
8 h.p.i.
5 µm
2 µm

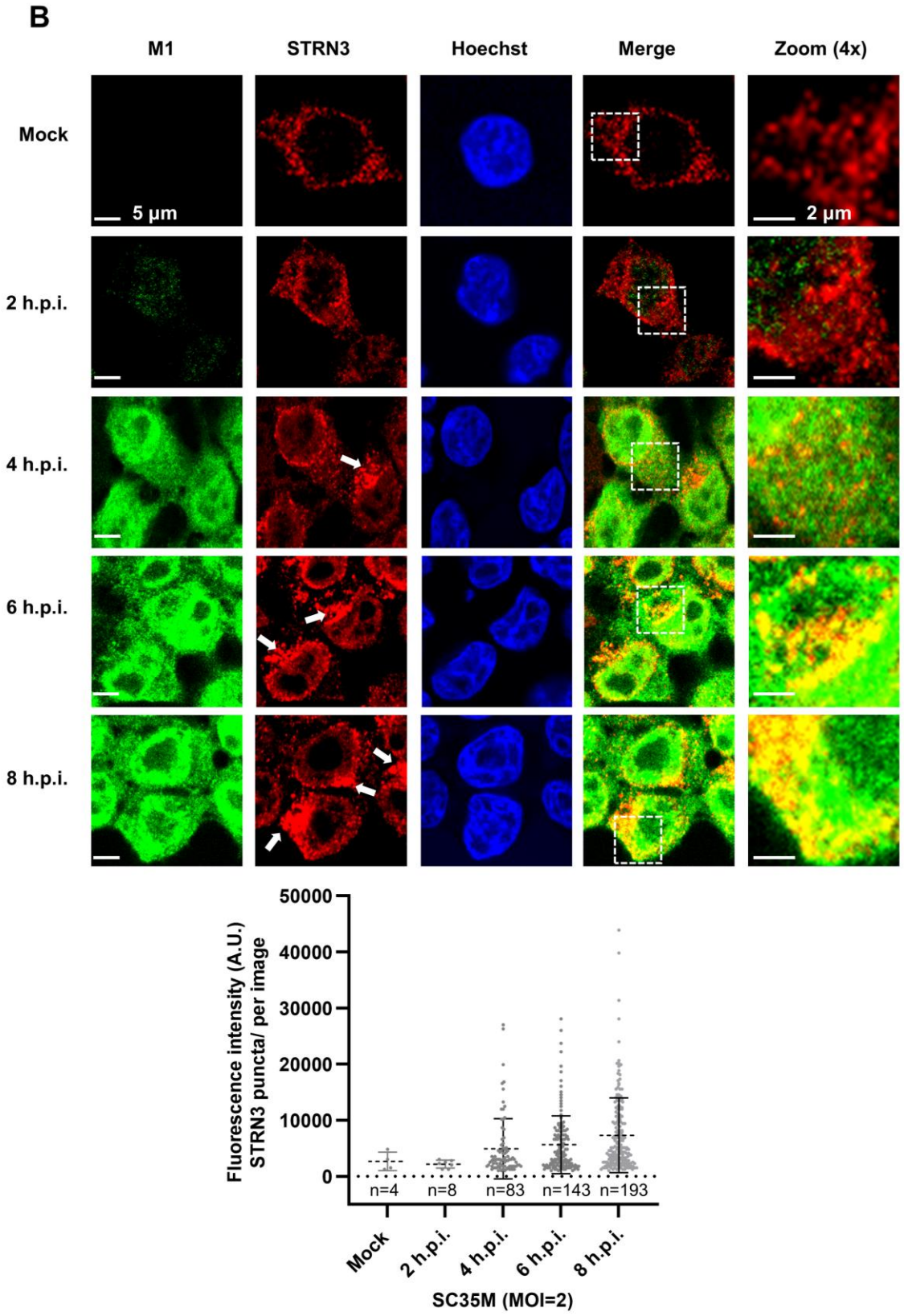

Figure 38: Colocalization of endogenous STRN/STRN3 and M1 in infected cells.

(A) Representative confocal images from two independent experiments show intracellular colocalization of STRN and viral protein M1 in the 293T cells at different time points after SC35M infection (2 h.p.i., 4 h.p.i., 6 h.p.i., and 8 h.p.i., MOI of 2) compared to noninfected cells (green, influenza A M1; red, STRN; blue,

Hoechst 33342). Scan zoom of 2, resulting in a pixel resolution of 0.13 µm; Scale bars: 5 µm. **(B)** The experiment was performed as in (A) with the exception that M1 was co-stained with STRN3. The boxed areas are displayed in 4× magnification. Quantification of the number of STRN3 puncta per image generated by pre-zoom of 0.6, with a pixel resolution of 0.344 µm, was performed in ImageJ using a threshold of 2× background intensity, followed by “Analyze Particles” algorithm with the following parameters: size 0-Infinity; circularity 0.20–0.50. (Cao et al., 2018). Fluorescence intensities were quantified with ImageJ and analyzed using GraphPad Prism. Data show mean ± s.d. from one representative experiment where at least 150 cells per condition (n ≥150) were quantified.

4 DISCUSSION

4.1 Comparative kinase activity profiling between seasonal ($H1N1_{pdm09}$) and highly pathogenic influenza A viruses reveals new anti- and pro-viral protein kinases

4.1.1 IAV-induced Ser/Thr and Tyr phosphorylation in $H1N1_{pdm09}$- and H5N1-infected cells

In the first part of this study, I interrogated virus-dependent changes in the kinetics of kinase-driven activation pathways in response to infection with a human 2009 pandemic strain ($H1N1_{pdm09}$) or a highly pathogenic avian H5N1-type strain (H5N1). The kinase ERK is an example of a kinase whose activity is required for IAV replication capacity (Marjuki et al., 2007). Here, the kinetics of upregulated ERK phosphorylation observed in A549 cells by $H1N1_{pdm09}$ infection were similar to those observed in MDCK cells infected with early seasonal H1N1 type IAV (Pleschka et al., 2001), but differs from that of H5N1-type IAV-infected cells, where the ERK phosphorylation level steadily increased over the time course of infection. Similarly, I observed a discrepancy in the kinetics of JNK activation between $H1N1_{pdm09}$ and H5N1 infection. In contrast, AKT activation steadily increased in $H1N1_{pdm09}$-infected cells, while no major increase could be detected for H5N1-infected cells. Of note, the infection by the H5N1 virus in A549 cells is slightly more advanced when compared to $H1N1_{pdm09}$ at the time point 5 h.p.i.. Interestingly, the high NP amount in $H1N1_{pdm09}$-infected cells is not reflected in virus titers as H5N1 always achieved higher titers (**Fig. 17E, F**), which has also been described previously (Simon et al., 2016). Nevertheless, I always observed a much stronger cytopathic effect (CPE) of $H1N1_{pdm09}$-infected cells compared to H5N1-infected A549 cells (data not shown), which might reflect an overall enhanced cytopathogenicity for $H1N1_{pdm09}$ on the human A549 cells. In addition, subsequent more detailed PamStation® analysis revealed an overall distinct intracellular kinase activity trigged by $H1N1_{pdm09}$ and H5N1. In conclusion, $H1N1_{pdm09}$ and H5N1 show a different capacity in ERK-, JNK- and AKT, as well as overall kinase activation strength and kinetics in A549 cells, which might be related (i) to slight differences in viral replication kinetics but (ii) also illustrate that the genotype of the virus dictates the activity of kinases and probably also phosphatases. In fact, IAV species specificity is determined by species-specific interactions between virus and host cell factors (Long et al., 2019; Mehle et al., 2012). Therefore, it is conceivable that the distinct

kinase signaling pathways would be triggered between the human $H1N1_{pdm09}$ and the avian-origin H5N1, due to the fact that these viruses are differently well adapted to the human A549 cells. Furthermore, it has been reported in previous studies that H5N1 provoked a more pronounced induction of a number of cytokines and chemokines in human lung tissue, compared to several seasonal and pandemic viruses, including $H1N1_{pdm09}$ (Weinheimer et al., 2012). Taken these findings into account, it must be assumed that the dissimilarity of kinase-driven phosphorylation between the human $H1N1_{pdm09}$ and the avian H5N1 might be a direct consequence of distinct viral determinants of IAV host adaption. Accordingly, a phosphoproteomic study comparing the phosphorylation patterns regulated by SC35 and the highly regulated SC35M virus revealed that only one half of the phosphorylations were affected by both virus variants (Weber et al., 2019). Another a non-negligible part of the early kinase response is also triggered by soluble factors contained in the virus stock. Although this part of the signaling response is indirect, it resembles the physiological situation of an *in vivo* infection. Furthermore, it is plausible that a significant part of the late response will be indirectly caused by the virus-induced cell damage.

Interestingly, the PamStation® results showed that virus-regulated differential Tyr phosphorylation (68,8%) was much more prominent than modification at Sers/Thrs (29,9%). This strikingly contradicts Tyr phosphorylation of endogenous host proteins, which only accounts for less than 1% of total protein phosphorylations (Sharma et al., 2014). It thus raises the possibility that the actual degree of relevant Tyr phosphorylation of host proteins, particularly in a biological state of IAV-infection, might be underestimated. This bias for Tyr phosphorylation might be attributable to various reasons. First, the low number of Tyr phosphorylations on endogenous proteins might be due to the high activity of phospho-Tyr phosphatases causing a short half-life of this modification. It will be interesting to investigate whether IAV infection also triggers the phosphorylation of other "non-canonical" amino acids, but their phosphorylation is difficult to detect as the modification is relatively instable under the standard methods of phosphoprotein characterization (Hardman et al., 2019). Second, the abundance of tyrosines might be due to the overrepresentation of phosphorylatable tyrosines (196 peptides), when compared to serines/threonines (144 peptides) on the PamChips®, thus potentially causing an experimental bias. Despite these uncertainties, Tyr kinases might be also valuable therapeutic anti-viral targets against IAV, as also emphasized by the high degree of shared target sites that largely overlap between $H1N1_{pdm09}$ and H5N1 in this study (**Fig. 14A**).

The peptide-based approach used here allows the fast, cheap and unbiased identification of regulated kinases with a limited bioinformatic effort. On the other hand,

this approach definitively has some limitations, as the discovery of kinases is hampered by two factors: (I) The relatively small number of peptides represents a clear limit, as illustrated by the example of missing detection of JNK activation. Here, the peptide library does not contain the part of the activation loop that is detected by the phosphospecific antibodies. (II) The number of detectable kinases is further reduced by the fact that only kinases that phosphorylate well-defined consensus sequences can be predicted by the computational algorithm. Another limitation of this strategy is based on the fact that cell extracts are used, so that intracellular regulation of the kinases is lost.

4.1.2 Identification of new anti- and pro-viral protein kinases

A computational prediction of activity changes of kinases responsible for these phosphorylation events allowed the identification of novel kinases, which yet have not been shown to be relevant in IAV infection (**Table 3**). Subsequent functional analysis revealed the pro-viral function of JAK3 and the anti-viral function of NUAK. The anti-viral effect of Tofacitinib (JAK1/3 inhibitor) (**Fig. 17**) points to a pro-viral function of the JAK/STAT signaling pathway, as observed for several other viruses, including HBV, HCV and human CMV (Chang et al., 2018). With regard to the relevance of JAK kinases in IAV replication, similar observations were made for other JAK inhibitors Ruxolitinib and A77 1726, both demonstrating the IAV-supportive function of JAK1 and JAK2 (Wang, Sun, et al., 2020; T. Watanabe et al., 2014). It is currently unclear whether the $H1N1_{pdm09}$-specific anti-viral effect of Tofacitinib is solely due to its inhibitory effect on JAK3, as higher concentrations of this inhibitor can also inhibit JAK1 and JAK2 (Choy, 2019; Furumoto et al., 2013). A previous study showed that H5N1-HA could induce the activation of JAK2/3 and STAT1/NF-κB signaling resulting in a large release of cytokines/chemokines, whereas targeting to JAK3 blocked these signal transduction cascades and protected the JAK3 knockout mice from acute hyper-cytokinemia caused by H5N1 challenge (Xu et al., 2012). However, despite of the protective role of JAK3 inhibition against IAV changeling *in vivo*, the infectivity and replication kinetics of IAV tested in these conditions remains unknown. In contrast, JAK1 and JAK2 have been identified as crucial cellular factors involved in IAV replication (Han et al., 2018; T. Watanabe et al., 2014). Thus, it is important to note that tofacitinib is a pan JAK inhibitor and that anti-viral effect of Tofacitinib for $H1N1_{pdm09}$ as well as H5N1 cannot exclusively be traced back to JAK3 based on the presented experiments. Therefore, it will be interesting to investigate the relative contribution of the individual JAK kinases using genetic models targeting individual JAK kinases with high selectivity in the future.

The underlying mechanism of pro-viral function of the NUAK kinase inhibitor WZ4003 (**Fig. 18B**) was not addressed in this study, but a possible explanation could be that NUAK1 and NUAK2 belong to the family of AMP-activated protein kinases (AMPKs), which function as metabolic regulators and have been implicated in IAV replication via the PPARα/γ-AMPK-SIRT1 pathway (Bei et al., 2021; Garcia et al., 2017; Monteverde et al., 2018). Since also NUAK1 and NUAK2 are regulated by metabolic stress (Escalona et al., 2020; Inazuka et al., 2012), a similar role of these kinases for AMPK activity in viral replication might be proposed, in accordance with their ability to regulate the metabolic state to limit IAV replication. Alternatively, the relevance of NUAKs for the regulation of virus growth might be due to their role in AKT signaling, which has virus-supportive function during later stages of replication in IAV infection (Ehrhardt et al., 2006; Ehrhardt et al., 2007).

Furthermore, I observed an anti-viral function of Eph (erythropoietin-producing hepatoma) receptor Tyr kinases (EphA1 and EphA3) (**Fig. 19D**). A total of 14 Eph receptors have been found in humans, which can be subdivided into two subfamilies including EphA and EphB (Wang, Zheng, et al., 2020). The group of EphA receptors consist of 9 members, which bind promiscuously to ephrin-A ligands (five members), thus creating many combinatorial activation patterns (Miao et al., 2012). Both EphA and EphB have a known role in many infectious diseases by viruses, as well as bacterial and fungal pathogens (Darling & Lamb, 2019; Wang, Zheng, et al., 2020). A pervasive role of Ephs in viral infection was manifested in multiple mechanisms, including being used as virus entry receptors (10 of 14 Eph receptors) (Bonaparte et al., 2005; Hahn et al., 2013; Hahn et al., 2012; Lupberger et al., 2011; Wang, Zheng, et al., 2020; Wong et al., 1999), mediators of immune signaling (Lai et al., 2004) as well as involving in cell/cell contact and adhesion (de Boer et al., 2020). Along the same lines, the role of Ephs in IAV replication has been described as either supporting or suppressing viral replication (Atkins et al., 2014; Karlas et al., 2010; Willemsen et al., 2017). For example, EphA2 has been implicated as an anti-viral factor in seasonal H1N1 infection by regulating anti-viral RIG-I/IRF3 pathway (Atkins et al., 2014; Willemsen et al., 2017). In contrast, EphB6 has been shown to be required for the replication of several subtypes of IAV (Karlas et al., 2010). However, it remains unclear whether the other EphAs and EphB1 screened in this study played role in IAV replication (**Fig. 15A, B**). Therefore, revealing the function of the Ephs/Ephrin network in response to IAV infection will be an important task in the future.

In the recent years, genome-wide screening methods including siRNA, proteomics and CRISPR/Cas9 screens, have been widely used in a large body of studies to identify key host factors required for IAV replication (Benitez et al., 2015; Karlas et al., 2010; Konig

et al., 2010; Li et al., 2020; Su et al., 2013). Within this increasing list of pivotal host factors, some belong to kinases or involve kinase-regulated signaling (Konig et al., 2010). Although the overlap of the identified hits is limited, a comprehensive analysis of the kinases identified in these numerous studies is recommended, with further determination of kinase networks and discovery of their structural organization. This analysis would therefore allow for the classification of highly interconnected kinase networks with multi-layered signaling regulated by IAV infection , in which the general controller kinases that phosphorylate the next lower level of kinases of this process (Colinge et al., 2014) and mediate regulatory interactions/crosstalk between two processes (Invergo et al., 2020), would be of particular interest to be functionally test.

4.2 IAV protein phosphorylations regulate polymerase activity, viral proteins trafficking, polymerization and protein-protein interaction

4.2.1 Regulatory phosphorylations on IAV polymerase subunits and NP regulate the polymerase activity

Multiple mechanisms, including phosphorylation of IAV polymerase (RdRp) subunits and NP, have been reported to regulate the IAV polymerase to produce mRNAs, cRNAs cRNA or genomic vRNA (Dawson et al., 2018; Dawson, Wilson, Coon, et al., 2020). For example, previous studies have reported that NP S165 phosphorylation regulates NP oligomerization (Mondal et al., 2015), and the core polymerase subunit PB1 is phosphorylated at multiple conserved sites (**Table 6**). Some of these phosphorylation events mediate PB1 binding to viral RNA and transcription activity of IAV RdRp (Dawson, Wilson, Freiberger, et al., 2020). However, the occurrence of phosphorylation sites on the other vRNP core components (PB2, PA) and their possible functional relevance remains largely unexplored. Previous phospho-proteomic studies identified several phosphorylation sites on H7N7-type mouse-adapted SC35M-encoded proteins, including sites on the vRNP protein components (Weber et al., 2019). The PA Y393E, NP Y148E and NP T378E recombinant IAVs could not be rescued, suggesting that vRNPs do not tolerate complete and permanent deposition of a negative charge at these sites. In contrast, the phospho-mimetic mutation PB2 T471E did not affect the yield of infections virus or the replication efficiency of PB2 mutants. Furthermore, the replacement of residues PA Y393, S395 or NP Y148 with the phospho-mimetic E

severely impaired polymerase activity, implying that in these cases, disruption of polymerase function may lead to defective production of infectious virus. Further support that permanent phosphorylation of PA at both Y393 and S395 is prohibiting the activity of the RdRp comes from the fact that these two phosphorylations derogate the function of the RdRp in transcription and replication (**Fig. 25**).

One copy of the heterotrimeric RdRp comprised of PA, PB1, and PB2, binds to one end of the conserved 5' and 3' termini encoding the replication/transcription promoter, of each of the eight viral RNA (vRNA) genome segments, while the remaining RNA associates with multiple copies of the viral NP, thus packaging the RNA into a vRNP (Wandzik et al., 2020). In the context of the vRNP, the RdRp is a highly flexible enzyme complex to conduct transcription and replication of the viral genome, which is tightly regulated by appropriate interactions between the three subunits (Deng et al., 2005; Sugiyama et al., 2009). Although the investigated PA Y393 and S395 residues are located at the PA-PB1 dimer interface, phosphorylation of these two sites had no apparent effect on the PA-PB2 dimer interaction and further assembly of the RdRp/vRNP complex (**Fig. 26**).

Recent studies have structurally described the specific binding sites for the 5' and 3' vRNA ends with the RdRp during the RNA synthesis (Carrique et al., 2020; Pflug et al., 2014; Wandzik et al., 2020). Specifically, the 5' and 3' vRNA and cRNA promoters both form similar hook structures, which bind with high affinity in a single pocket formed by the PB1 β-hairpin and the so called "PA arch". To validate the observed negative effect of the PA Y393E and S395E it is important to note that PA phosphorylation on Y393 and S395 occurs at the "PA arch", which forms a phosphate-binding loop close to the 5' vRNA/cRNA binding pocket that is far away from the PA endonuclease domain and all other known 3' vRNA/cRNA binding sites (Carrique et al., 2020; Pflug et al., 2014; Wandzik et al., 2021; Wandzik et al., 2020). Therefore, it will be relevant to test whether Y393 phosphorylation affects the PA ability to interact with 5' vRNA/cRNA promoter in future studies. For this, a method developed by Prof. Ervin Fodor (University of Oxford, Oxford, United Kingdom) could be applied. Here, the radiolabeled promoter RNAs are crosslinked *in vitro* to the affinity-purified RdRp components, and subsequently the bound radiolabeled 5' promoter RNA is quantified by SDS-PAGE and phosphorimaging (Engelhardt et al., 2005; Walker et al., 2020).

Likewise, I was able to show that NP phosphorylation at Y148 is relevant for the RdRp activity (**Fig. 24**). Despite that several studies have previously shed light on the key molecular function of Y148, phosphorylation at this site was detected for the first time by phosphoproteomics studies in our laboratory (Weber et al., 2019). Importantly, Y148 is one of the residues that form the RNA binding groove of the NP (Lejal et al., 2013; Tarus et al., 2015; Ye et al., 2006). The antiviral property of the compound Naproxe relies on

its capability to compete with the viral RNA for binding to NP, but it cannot compete with viral RNA in case of the NP Y148A mutant (Lejal et al., 2013). This raises several questions: 1) does the Y148 phosphorylation introduce an extra negative charge and thus potentially ablates the RNA-binding affinity of NP, which may explain why the mimicking phosphorylation at this site disrupted polymerase activity and viral rescue? 2) does NP Y148 phosphorylation alter the ability of NP to bind Naproxen? 3) does Naproxen inhibit NP Y148 phosphorylation, especially at doses that differentially affect avian and human IAV? It will be interesting to test these possibilities in future studies. On the other hand, a previous study revealed the importance of NP Y148 in regulating nuclear export and interaction with the nuclear export factor CRM1 (Zheng et al., 2019). In this context, an indispensable role for NP binding to CRM1 has been assigned to the benzene ring of NP Y148, based on the fact that the NP Y148A, rather than NP Y148F, impairs the NP-CRM1 interaction (Zheng et al., 2019). It will thus be very interesting to test the impact of NP Y148E mutant on interaction with CRM1.

Like the phosphorylation mimicking NP Y148E, also NP T378E did not allow virus rescue (**Fig. 23**). In contrast to NP Y148E, NP T378E did not affect RdRp activity, suggesting that the failure to rescue virus carrying this NP mutation cannot be accounted to an effect on the RdRp activity. Notably, NP T378 is located in a region known to be important for NP oligomerization, whereby phosphorylation of this region not only tightly regulates RNP activity, but also the nuclear export of NP (Chan et al., 2010; Yu et al., 2012). This suggests that mimicking constitutive phosphorylation by NP T378E may impair virus propagation by affecting the nuclear RNP export, as RdRp activity is not reduced. It thus will be interesting in the future to study the functional relevance of NP T378E for nuclear RNP export and their interaction with the nuclear export factor CRM1.

In summary, functional analysis of 5 specific phosphorylation events of vRNP components performed in this part of study has revealed that the phospho-mimetic mutants largely prohibited polymerase functions, whereas the phospho-deficient mutants were more compatible for these sites. Mimicking constitutive phosphorylation at PA Y393, S395 and NP Y148 impaired RdRp activity, and PA Y393E and S395E blocked the transcription and replication activity of the RdRp, thus affecting the generation of infectious virus particles. Future experiments employing phospho-specific antibodies against these key residues PA Y393, S395 and NP Y148, T378, as well as analysis of the association between of PA and NP mutants with the vRNA or investigations of protein/protein interactions of such mutants with RdRp components or cellular proteins, will provide a more enhanced functional understanding of the specific phosphorylation events and will help to identify the responsible kinases in the future.

Different mechanisms of inhibitory phosphorylation on IAV proteins have been revealed (Hu et al., 2020). For example, the importance of dynamic phosphorylation of NP at S165 and S407 for IAV replication has been described, as mimicking phosphorylation at these two sites drove NP towards a monomeric form and prevent premature RNP formation (Mondal et al., 2015). Similarly, phosphorylation at PB1 S673 limits the time for polymerase activity to perform transcription and shift it towards replication, thereby fine-tuning the function of RdRp throughout the viral life cycle (Dawson, Wilson, Freiberger, et al., 2020). Moreover, inhibitory phosphorylation on IAV proteins is associated with anti-viral host responses, such as the modification of NS1 at T49 and T80, which lead to a defective suppression of IFN production due to its reduced binding affinity with RIG-I (Kathum et al., 2016; Zheng et al., 2017).

The IAV RdRp is highly flexible, with the surface accessibility of each residue varying in accordance with the polymerase conformation (Dawson, Wilson, Freiberger, et al., 2020). PA Y393 and S395 are buried in the vRNA-bound structure but may be accessible in the monomeric. Phospho-deficient PA YS393, 395EE mutant retained polymerase function whereas constitutive phosphorylation largely inhibits transcription and replication activity, suggesting a possible antiviral signaling mechanism of phosphorylation at these sites.

4.2.2 Multiple functions of influenza virus M1 T108A phosphorylation

In the present study, I analyzed the functional consequences of M1 T108 phosphorylation. Phosphorylation at this site was discovered in MDBK cells infected with the H1N1-type A/WSN/33 IAV strain (Hutchinson et al., 2012), and in MLE-15 cells infected with SC35 or SC35M (Weber et al., 2019).

Sequence alignment analyses revealed that M1 T108 is almost 100% conserved between human and avian IAV strains, and the mutation analysis indicated that M1 T108 phosphorylation is indispensable for the viral propagation due to the fact that recombinant SC35M could not be rescued in the presence of a non-phosphorylatable Ala at this position. This defect rescue occurred even when increased concentrations of the plasmids for RG were used and prolonged incubation periods of MDCK II cells with the supernatant from the transfected cells (data not shown).

How can M1 T108 phosphorylation affect the viral life cycle? The first possibility would involve an effect of M1 T108 phosphorylation on the intracellular localization of the protein, as the M1 T108A mutant was almost never found exclusively in the nucleus. This might be attributable to the position of M1 T108, which is adjacent to the previously

identified NLS (Ye et al., 1995) and thus phosphorylation might contribute to full nuclear import. A phosphorylation-dependent increase of nuclear import has also been described for other viral proteins including the SV40-encoded large T antigen (Xiao et al., 1996), the HBV core antigen (Liao et al., 1995) and the Epstein-Barr virus nuclear antigen 1 (EBNA-1) protein (Kitamura et al., 2006). While phosphorylation of EBNA-1 at S385 increases binding affinity for importin α5 and increases nuclear import, the replacement of S385 with the phosphomimetic aspartic acid decreases the binding affinity for importin α5 (Kitamura et al., 2006). This interesting finding suggests that the response is either dependent on the phosphate moiety or alternatively indicates the need for a spatial and temporal control of the phosphorylation event. This would also explain why the localization changes of the M1 T108E mutant observed in this study were milder and also time-dependent. The described effect on M1 transport by the M1 T108A mutation resembles the one seen by M1 Y132A, strongly supporting a general impact of phosphorylation for M1 transport (Wang et al., 2013).

The functional consequences of certain phosphorylations have been investigated by different experimental approaches such as overexpression or genuine infection. For example, WSN M1 Y132 phosphorylation was functionally studied by overexpression approaches, since the authors failed to rescue respective virus mutants. These experiments showed that M1 Y132 phosphorylation is crucial for virus fitness by regulating M1 transport into nucleus (Wang et al., 2013). In contrast, Mecate-Zambrano *et al*. used genuine infection to reveal the functional importance of WSN M1 Y132 phosphorylation for virion assembly (Mecate-Zambrano et al., 2020). In addition to these differences in methodological approaches, also the genetic background of the virus can largely determine the tolerance of substitutions for viral rescue (Mecate-Zambrano et al., 2020; Patil et al., 2021). These considerations imply that the results based on the experimental conditions used in this study might also not necessarily reflect those that might be obtained for other viral strains such as WSN, or that other IAV strains may allow to study M1 T108 phospho-mutants in a real infection. Nevertheless, it is important to mention that this phospho-site is highly conserved across all IAV subtypes and between human and avian IAV. The second effect of regulated M1 T108 phosphorylation relies on the ability of M1 to support nuclear export of the vRNP. In fact, the nuclear presence of M1 mediated by its NLS is required for vRNPs to be transported to the cytoplasm, where the vRNPs are subsequently transported to the budding site for the production of virus progeny (Bui et al., 2000; Cao et al., 2012; Martin et al., 1991). Accordingly, M1 T108A mutant showed impaired nuclear import of M1 and nuclear export of vRNP.

Besides its role in nuclear vRNP export, M1 plays a critical role in initiating the assembly and budding of progeny virions at the PM where it associates with lipids and other viral

proteins (Hilsch et al., 2014). The intracellular transport of M1 from the cytosol to the PM implies that, in later stages of infection, the M2 protein carries M1 in a piggyback mechanism to the PM (Chen et al., 2008; McCown & Pekosz, 2006). This step seems to be unaffected by M1 T108 modification, as all phospho-mutants showed unchanged membrane co-localization with M2. This indicates that the phosphorylation status of M1 T108 does not affect the membrane association of M1.

Upon binding to the PM, self-assembly of M1 into long, helical polymers surface is promoted and further drives the formation of the matrix shell, which is required not only for the acquisition of membrane curvature to complete virus budding, but also for maintaining morphology and structure stability of virus particles (Calder et al., 2010; Dahmani et al., 2019; Mohd-Kipli et al., 2021). Specifically, M1 polymerization is associated with an extension of helix 9 and the transition of the CTD (C-terminal domain;165–252) from an unfolded to a folded state, upon which it interacts with the NTD (N-terminal domain; residues 1–164) of the neighboring M1 molecule (Baudin et al., 2001; Hofer et al., 2019; Selzer et al., 2020) (**Fig. 34A**). At neutral pH, the tight "stacked" dimeric arrangement of M1 is structurally described, which is frequently observed in virions. In this proposed M1 structure, the M1 T108 lies in the loop between helices 6 and 7 (residues 103–113) and participates in the closer contacts formed by residues between T139/E141 of the h8/h9 loop and I107/T108 of the helix 6/helix 7 loop. This may contribute to reduce the loop mobility seen for the monomer in solution and further support M1 polymerization (Mohd-Kipli et al., 2021).

In the M1 polymer, three different M1 monomers contribute five histidine residues including H110, which participates in the pH-mediated disassembly switch when RNP uncoating occurs in the acidic endosomes of freshly infected cells (Peukes et al., 2020). As M1 T108 is adjacent to the disassembly residue H110 and also directly in the region mediating homopolymerisation of M1 monomers, M1 T108 phosphorylation likely regulates the self-assembly and disassembly of the M1 proteins. Accordingly, the cross-linking experiments showed an increased multimerization of the M1 T108A protein, indicating that dynamically regulated phosphorylation at this residue is specifically important for the disassembly of the M1 polymer thereby contributing to the pH-dependent conformational flexibility of M1 during RNP uncoating (Chiang et al., 2017). Alternatively, M1 phosphorylation could also avoid excess M1 polymerization or maintain the conformational flexibility which is critical for efficient IAV replication (Chiang et al., 2017).This suggests that phosphorylation status at M1 T108 may mediate the balance between polymerization and dimerization of M1 throughout the viral life cycle, although this remains to be substantiated.

M1 T108 phosphorylation also contributes to the regulation of binding to various interaction partners, as shown in **Table 9**.

Table 9. List of identified M1 interactors preferentially binding to WT M1 compared with T108 mutants.

M1 WT/T108A_down (14)			
STRN3	STRIP1	GOLGA3	STK26; STK25
CTTNBP2NL	MTCL1	STRN	NONO
FGFR1OP2	RPL39; RPL39P5	PPP2R1A	
SIKE1	SLMAP	MOB4	
M1 WT/T108E_down (96)			
GOLGA3	RPS12	CFL1	RPL39; RPL39P5
SLMAP	RPS23	EEF1G	STK26; STK25
MOB4	PKM	RPL18	RPS4X
HSPD1	RPL7	RPL4	RPL26; RPL26L1
STRN3	DYNLL1; DYNLL2	RPL10A	DDX5
STRN	LDHB	U2AF1	RPL19
HSP90AB1; HSP90AB3P	STRIP1	RPS10; RPS10P5	SERBP1
ENO1	RPS19	RPS16	RPS27A; UBC; UBB; UBA52
NONO	RPL22	RPL10; RPL10L	CCT8
ACTG1;ACTB	COX6C	HNRNPK	SUB1
GAPDH	RPL5	PRDX1	RPL30
PPP2R1A	ALDOA	ATP5A1	RPLP0; RPLP0P6
EEF2	MTCL1	RPL23A	TXN
CTTNBP2NL	YWHAE	RPS29	PHKG2
FGFR1OP2	LDHA	RPL17	RPS20
SFPQ	ACTA1; ACTC1; ACTA2; ACTG2	RPL36	LUC7L2
NME2; NME2P1	PARP1	HMGB1	RPS13
SIKE1	RPL29	RPLP2	NEDD1
NPM1	RPS9	RPL18A	KCTD3
HNRNPF	ARGLU1	RPS15A	RPL15
PPIA	EIF4A1	RPS14	
HSP90AA1	RPL27A	RPS8	

The WT M1 protein preferentially bound to most members of the STRIPAK complex. The evolutionary conserved STRIPAK complex is a multisubunit complex that contains both kinase and phosphatase subunits; consisting of the PP2A phosphatase in complex with its striatin-family of regulatory subunits (STRN, STRN3, STRN4), the two hippo kinases (MST1/MST2), the three GCKIII kinases (MST3, MST4, STK25) and various scaffolding proteins (Kean et al., 2011; Rodriguez-Cupello et al., 2020). It regulates diverse cellular processes, including cell proliferation and survival, cell polarity, cell migration, and vesicular trafficking (Jeong et al., 2021; Lant et al., 2015). Subsequent results confirmed that M1 and STRIPAX core components-STRN/STRN3 could colocalize and physically interact with each other in both overexpression and real infection conditions (**Fig. 36**, **Fig. 38**). It is presently not clear whether M1 interacts with several proteins contained in this complex or with only one component. Also, the mechanisms enabling phosphorylation-dependent interaction of M1 with the STRIPAK complex are not understood and might involve conformational changes of M1 or alternatively specialized interaction surfaces in the interactor as they mediate also other phosphorylation-regulated protein/protein interactions (Betts et al., 2017).

In line with previous studies, indirect immunofluorescence analysis in this study showed localization of STRN in the cell cortex region in proximity of the PM with additional staining of the cytoplasm (Lahav-Ariel et al., 2019). At 4 h p.i. there was a slight increase in the accumulation of STRN in the cytoplasm where it apparently colocalized with M1 protein over the course of infection (**Fig. 38A**). Likewise, SC35M-infection induced the formation of large bright spots of STRN3 at cytoplasm where it colocalized with M1 (**Fig. 38B**).

After endocytosis of incoming IAV particles, the viral core, consisting of M1 protein and the viral vRNPs that carry the RNA genome, must dissociate from each other in a process called priming and release from the incoming particle after M1 shell disassembly. This ensures that the vRNPs can enter the nucleus for replication and transcription of the viral genome (Banerjee et al., 2014; Miyake et al., 2019; Noda et al., 2012). Although unequivocal colocalization between M1 and STRN/STRN3 occurs at 4 h.p.t when the majority of M1 shell is disassembled (Miyake et al., 2019), the precise steps at which these interactions take place, such as M1 shell disassembly when M1 is exposed as cores, or after M1 is completely uncoated into the cytosol, are still unknown. Thus, it would be interesting to define a more detailed step-by-step model for uncoating of M1 shell and its interaction with the STRN/STRN3 in the future.

A previous study showed that downregulation of E-cadherin in CHO cells resulted in the cytosolic redistribution of STRN (Lahav-Ariel et al., 2019). A similar redistribution was

also observed in SC35M infected 293T cells, consistent with the notion that IAV infection downregulates E-cadherin levels (J. N. Li et al., 2021; Ruan et al., 2020). Moreover, STRN has also been reported to display a distinct staining pattern in 293T cells showing tube-like structures that colocalize with microtubules and tubulin in particular (Kazmierczak-Baranska et al., 2015), thus the disrupted host cytoskeleton homeostasis induced by IAV infection might also affect the subcellular distribution of STRN (Han et al., 2012).

More importantly, the combined reduction of Strn/Strn3 expression by siRNAs impaired IAV replication across various IAV strains: SC35M (H7N7) and $H1N1_{pdm09}$ (**Fig. 38**). This indicates a pro-viral function of the complex in order to support IAV replication. As the STRNs function as the central assembly scaffolds (Jeong et al., 2021), it can be assumed that their downregulation disables the architecture and function of the entire complex. The molecular mechanism allowing STRIPAK complex-dependent support of IAV replication and the involved steps during the viral life cycle are not known. However, several scenarios can be investigated.

First, the Striatin complex is known to regulate cytoskeletal architecture. For example, previous studies mentioned that downregulation of STRN destabilizes the microtubule network and also actin dynamics (Kazmierczak-Baranska et al., 2015; Lahav-Ariel et al., 2019). The actin cytoskeleton and microtubules as a major cellular machinery, is heavily exploited by IAV at multiple stages during the viral life cycles, including its entry, subcellular viral trafficking, and egress (Bedi et al., 2019; Lakadamyali et al., 2003; Simpson et al., 2020). In agreement with these findings, several studies have demonstrated diminished IAV replication following microtubule or actin dynamics disruption by drugs (Amorim et al., 2011; Griffin et al., 1979; Kumakura et al., 2015; Momose et al., 2007).Therefore, it would be interesting to test if the combined depletion of STRN/STRN3 affect the stabilization of cytoskeletal system during IAV infection in the future. Second, it is also known that the depletion of STRN3 leads to increased apoptosis (Tang et al., 2020), and all STRN proteins are implicated in regulating the apoptotic process (Chen, Shi, et al., 2014; Nader et al., 2020; Tanti et al., 2014; Wong et al., 2014). Apoptosis, which is traditionally thought to impede the lytic release of inflammatory damage-associated molecular patterns (DAMPs), is linked to limit IAV replication, as mice with impaired apoptosis exhibit increased viral loads (Downey et al., 2017; Kuriakose et al., 2016; Laghlali et al., 2020; Nogusa et al., 2016; Thapa et al., 2016). This raises the possibility that the induction of apoptotic cell death at early stage of IAV infection would not allow sufficient time for induction of pro-inflammatory responses and viral propagation (Laghlali et al., 2020). In addition, the STRIPAK complex contributes to activation of MAPKs, which is essential for IAV propagation (Pleschka et al., 2001). Since

the depletion of STRN or STRN3 is associated with reduced ERK phosphorylation (Ashton-Beaucage et al., 2014), compromised MAPK activation could be a causal consequence of restricted IAV replication. Another very obvious possibility explaining the contribution of the STRIPAK complex for IAV replication might rely on its ability to directly regulate M1 T108 phosphorylation. All kinases contained in the STRIPAK complex are Ser/Thr kinases and thus it would be exciting to find out whether the combined activity of kinases and phosphatases would control M1 T108 phosphorylation which needs to be balanced and timely and spatially controlled.

In summary, my work shows the functional relevance of several phosphorylations occurring on IAV-encoded proteins including PA, NP and M1. Their possible functions for the IAV life cycle are summarized in **Fig. 39**.

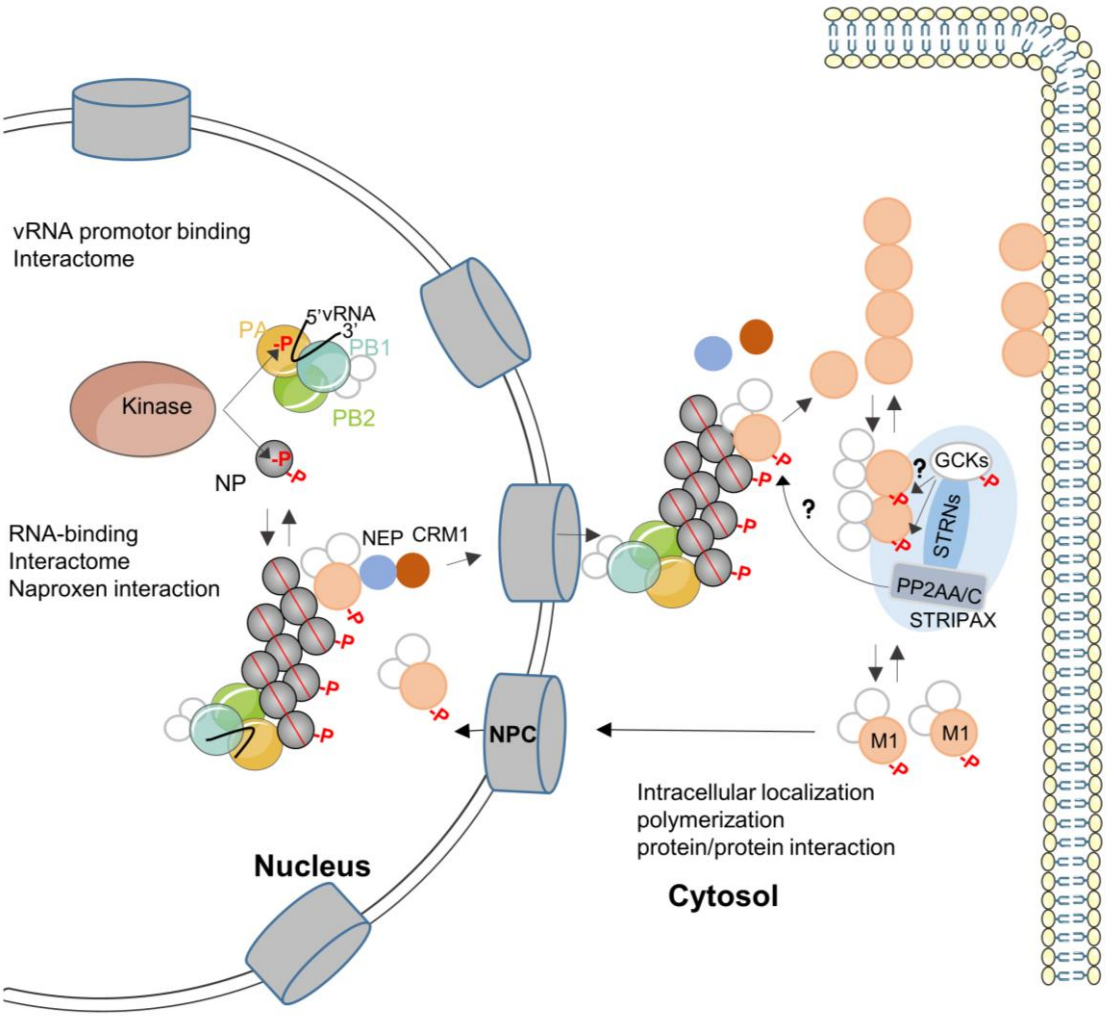

Figure 39: Schematic summary of possible functions of IAV protein phosphorylation investigated in this study.

The PA Y393 and S395 phosphorylation negatively affects the ability of the polymerase to produce vRNA and infectious virions, which might be relevant to regulate the 5' vRNA/cRNA promoters binding during the

viral transcription and replication, and protein-protein interaction. NP Y148 phosphorylation prohibits the polymerase activity, and its role in regulating the viral RNA-binding, protein-protein interactions is suggested. M1 T108 phosphorylation is required for the complete nuclear import of M1, nuclear export of vRNP, and impacts the ability of M1 for the homo polymerization and interaction with other proteins.

5 SUMMARY

This work is divided into two parts, which both address the relevance of phosphorylation events induced by the IAV infection. The first part of the study addressed the functional relevance of kinases activity in IAV-infected cells, which regulate the phosphorylation occurring on cellular proteins. With this regard, PamStation® platform-based analysis of Ser/Thr kinases or Tyr kinases present in IAV-infected cells, was performed to compare the kinase activation patterns triggered by the human circulating IAV isolate A/Hamburg/4/09 ($H1N1_{pdm09}$) and the highly pathogenic avian IAV human isolate A/Thailand/1(KAN-1)/2004 (H5N1). The results indicate that the Tyr phosphorylations of substrate peptides were largely co-regulated by both viruses and are also strongly overrepresented in comparison to Ser/Thr peptide phosphorylations. It allowed to identify 26 of 47 predicated kinases, which are mainly strain-specific and have been implicated in the IAV life cycle, while the function of other 21 kinases on IAV infection is unknown. Subsequently, the perturbation of selected novel kinases with highly specific small molecule inhibitors or siRNAs was conducted to investigate the relevance of these kinases. Received data revealed negative regulation of $H1N1_{pdm09}$ and H5N1 replication by NUAK (novel (nua) kinase) kinases, redundant ephrin A (EphA) receptor Tyr kinases and a $H1N1_{pdm09}$-selective pro-viral function of JAK3 (Janus kinase 3).

The second part of this study was performed to characterize the relevance of phosphorylation occurring on proteins encoded by the IAV strain SC35M (H7N7). For this I integrated all phosphorylations on viral proteins that have been previously detected in our laboratory, together with those found in other literature, along with information on their intramolecular localization in possible functional domains and/or with a suggested relevant function. The subsequent functional analysis focused on phosphorylation sites, which are evolutionally highly conserved, not functionally described but with important functional implications.

Based on mutational analysis results of five phosphorylation sites of PB2 (T471), PA (Y393, S393), NP (Y148, T378), three phosphorylation sites of NS1 (S48, T49, T197), and one phosphorylation site of M1 (T108), three distinct groups of phosphorylation effects could be assigned. The first group of phosphorylations does not have a direct physiological consequence, as reflected by PB2 T471 and NS1 T197, for which neither their phospho-deficient nor phospho-mimetic mutation affects viral replication of SC35M in MLE-15 cell culture. The second group of phosphorylations has a modulatory function, which is exemplified by PA S395 and NS1 ST48, 49. Here, either a phospho-deficient mutation or a phospho-mimetic mutation slightly alters the viral replication. Of particular

interest is the third group of phosphorylations showing a critical role in viral replication. For example, the phospho-mimetic mutation for the vRNP components PA (Y393E), NP (Y148E, T378E), and for the phospho-deficient M1 T108A mutation, which all prevent the production of infections virus. Further functional analysis of selected phosphorylations revealed their distinct biological roles. As such, constitutive phosphorylation on PA Y393 and S395 inhibits polymerase functions to transcribe and replicate the viral genome, which partially also holds true for the phospho-mimetic mutation at NP Y148, which also impaired polymerase activity. Although an inhibitory effect on viral propagation was also seen for the phospho-memetic mutation at NP T378, a different mechanism must be expected, as this mutation leads to an increased polymerase activity.

With regard to the M1 T108 phosphorylation, the experimental results point to the requirement of this phosphorylation for viral propagation via controlling the nuclear M1 import and nuclear vRNP export. Furthermore, a study applying intracellular chemical crosslinking of M1 protein complexes indicates that M1 T108 phosphorylation might avoid excess of M1 polymerization, which may be critical for maintaining conformational flexibility of M1 to switch between assembly and disassembly during viral replication. Further M1 interactome studies revealed a possible role of M1 T108 phosphorylation in regulating protein/protein interaction. This approach disclosed a network of proteins from the STRIPAK complex, in particular its core components STRN/STRN3, acting as novel interacting partners of M1 protein, with preferential binding affinity to WT M1. Loss-of-function experiments also indicate that STRN/STRN3 function as pro-viral factors supporting IAV replication. Moreover, immunofluorescence studies showed the IAV infection led to slight cytoplasmic accumulation of STRN and larger aggregates formation of STRN3.

Collectively, the functional characterization of PA Y393, S395, and NP Y148 phosphorylation on the activity adds new examples for phosphorylation-regulated RNP activity. On the other hand, the identification of virus-supportive phosphorylation M1 T108 and its combinatorial pro-viral interactors could provide new insights into therapeutic interference with IAV replication.

6 ZUSAMMENFASSUNG

Diese Arbeit ist in zwei Teile gegliedert, die sich beide mit der Bedeutung der durch die IAV-Infektion ausgelösten Phosphorylierungsvorgänge befassen. Der erste Teil der Studie befasst sich mit der funktionellen Bedeutung der Kinasenaktivität in IAV-infizierten Zellen. Hier wurden IAV-regulierte Serin/Threonin und Tyrosin-Kinasen durch eine PamStation® Analyse identifiziert. Als IAVs wurden das zirkulierende menschliche IAV-Isolat A/Hamburg/4/09 ($H1N1_{pdm09}$) und das hochpathogene menschliche Vogel-IAV-Isolat A/Thailand/1(KAN-1)/2004 (H5N1) verwendet. Die Ergebnisse zeigen, dass Tyrosin-Phosphorylierungen von Substratpeptiden im Vergleich zu Serin/Threonin-Peptidphosphorylierungen stark überrepräsentiert sind. Auf diese Weise konnten 26 von 47 prädizierten Kinasen identifiziert werden, die hauptsächlich stammspezifisch sind und in den IAV-Lebenszyklus involviert sind, während die Funktion der anderen 21 Kinasen bei der IAV-Infektion unbekannt ist. Anschließend wurde die Perturbation ausgewählter neuer Kinasen mit hochspezifischen niedermolekularen Inhibitoren oder siRNAs durchgeführt, um die Bedeutung dieser Kinasen zu untersuchen. Die erhaltenen Daten zeigten eine negative Regulierung der $H1N1_{pdm09}$- und H5N1-Replikation durch NUAK-Kinasen (novel (nua) kinase), redundante Ephrin A (EphA)-Rezeptortyrosinkinasen und eine $H1N1_{pdm09}$-selektive pro-virale Funktion von JAK3 (Janus kinase 3).

Der zweite Teil dieser Studie wurde durchgeführt, um die Bedeutung der Phosphorylierung von Proteinen zu charakterisieren, die vom IAV-Stamm SC35M (H7N7) kodiert werden. Zu diesem Zweck wurde eine Datenbank mit allen identifizierten Phosphorylierungsstellen erstellt, die dann aufgrund unterschiedlicher Kriterien gefiltert wurde. Dazu zählten die evolutionäre Konservierung und die intramolekulare Lokalisierung in möglichen funktionellen Domänen. Noch nicht analysierte Phosphorylierungsstellen in PB2 (T471), PA (Y393, S393), NP (Y148, T378), NS1 (S48, T49, T197) und M1 (T108) wurden mittels reverser Genetik weiter untersucht. Die erste Gruppe von Phosphorylierungen hat keine direkte physiologische Auswirkung, wie PB2 T471 und NS1 T197 zeigen, bei denen weder ihre phospho-defiziente noch ihre phospho-mimetische Mutation die virale Replikation von SC35M in der MLE-15-Zellkultur beeinflusst. Die zweite Gruppe von Phosphorylierungen hat eine modulierende Funktion, die durch PA S395 und NS1 ST48, 49 veranschaulicht wird. Hier verändert entweder eine phospho-defiziente Mutation oder eine phospho-mimetische Mutation die virale Replikation leicht. Von besonderem Interesse ist die dritte Gruppe von Phosphorylierungen, die eine kritische Rolle bei der viralen Replikation spielen. Zum Beispiel die phospho-mimetische Mutation für die vRNP-Komponenten PA (Y393E), NP

(Y148E, T378E) und für die phospho-defiziente M1-Mutation T108A, die alle die Produktion von Infektionsviren verhindern. Weitere funktionelle Analysen ausgewählter Phosphorylierungen ergaben deren unterschiedliche biologische Funktionen. So hemmt die konstitutive Phosphorylierung an PA Y393 und S395 die Polymerasefunktionen zur Transkription und Replikation des viralen Genoms, was teilweise auch für die phosphormimetische Mutation an NP Y148 gilt, die ebenfalls die Polymeraseaktivität beeinträchtigt. Obwohl auch für die phosphormimetische Mutation an NP T378 eine hemmende Wirkung auf die virale Vermehrung festgestellt wurde, muss ein anderer Mechanismus erwartet werden, da diese Mutation zu einer erhöhten Polymeraseaktivität führt.

In Bezug auf die M1-T108-Phosphorylierung deuten die experimentellen Ergebnisse darauf hin, dass diese Phosphorylierung für die virale Vermehrung erforderlich ist, da sie den nuklearen M1-Import und den nuklearen vRNP-Export kontrolliert. Darüber hinaus deutet eine Studie zur intrazellulären chemischen Vernetzung von M1-Proteinkomplexen darauf hin, dass die M1-T108-Phosphorylierung einen Überschuss an M1-Polymerisation verhindern könnte, was für die Aufrechterhaltung der Konformationsflexibilität von M1 entscheidend sein könnte, um während der viralen Replikation zwischen Aufbau und Abbau zu wechseln. Weitere M1-Interaktom-Studien zeigten eine mögliche Rolle der M1-T108-Phosphorylierung bei der Regulierung der Protein/Protein-Interaktion. Dieser Ansatz enthüllte ein Netzwerk von Proteinen aus dem STRIPAK-Komplex, insbesondere dessen Kernkomponenten STRN/STRN3, die als neuartige Interaktionspartner des M1-Proteins fungieren, mit bevorzugter Bindungsaffinität zu wt M1. Loss-of-function-Experimente zeigen auch, dass STRN/STRN3 als pro-virale Faktoren fungieren, die die IAV-Replikation unterstützen. Darüber hinaus zeigten Immunfluoreszenzstudien, dass die IAV-Infektion zu einer leichten zytoplasmatischen Akkumulation von STRN und zur Bildung größerer Aggregate von STRN3 führte.

Insgesamt liefert die funktionelle Charakterisierung der Phosphorylierung von PA Y393, S395 und NP Y148 neue Beispiele für die durch Phosphorylierung regulierte RNP-Aktivität. Andererseits könnte die Identifizierung der virusunterstützenden Phosphorylierung M1 T108 und ihrer kombinatorischen pro-viralen Interaktoren neue Erkenntnisse über therapeutische Eingriffe in die IAV-Replikation liefern.

7 ABBREVIATIONS

%	percent
% (v/v)	volume/volume percentage (ml/100 ml)
% (w/v)	weight/volume percentage (g/100 ml)
°C	grad Celsius
µg	microgram
µl	microliter
µM	micromolar
aa	amino acid(s)
ADP	adenosine diphosphate
AIV	avian influenza virus
Amp	Ampicillin
AMPK	AMP-activated protein kinase
APS	ammonium persulfate
Arg	Arginine
Asp	Aspartic Acid
ATP	adenosine triphosphate
AKT	protein kinase B
bp	base pair
BSA	bovine serum albumin
cAMP	cyclic adenosine monophosphate
CDK	cyclin-dependent kinase
cDNA	complementary DNA
cds	coding sequence
JNK	c-jun N-terminal kinase
C_T	threshold cycle
CTD	carboxyl-terminal domain
Cys	Cysteine
ddH_2O	deionized distilled water
DFG	Asp-Phe-Gly
DMEM	Dulbecco’s modified eagle medium
DMSO	dimethyl sulfoxide
DNA	deoxyribonucleic acid dsDNA
dNTP	deoxynucleoside triphosphate
DTT	dithiothreitol
dsDNA	double-stranded DNA
EDTA	ethylenediaminetetraacetate
ERK	extracellular-signal regulated kinase

ER	endoplasmic reticulum
Eph	erythropoietin-producing hepatoma
et al.	et alii (and others)
FCS	fetal calf serum
FFU	Foci forming unit(s)
h	hour(s)
h.p.t.	hour(s) post-transfection
h.p.i.	hour(s) post-infection
$H1N1_{pdm2009}$	2009 pandemic H1N1
HDAC	histone deacetylase
HA	hemagglutinin
HPAI	high-pathogenicity avian influenza
His	Histidine
IVs	influenza viruses
IAV	influenza A virus
IBV	influenza B virus
IgG	immunoglobin G
IFN	interferon
M1	matrix proteins 1
M2	matrix proteins 2
MS	mass spectrometry
mg	milligram
ml	milliliter
mM	millimolar
mAb	monoclonal antibody
MAPK	mitogen-activated protein kinase
MOI	multiplicity of infection
mRNA	messenger RNA
min	minute(s)
NF-kB	nuclear factor kB
NUAK1	novel (nua) kinase 1
NLS	nuclear localization signal
NP	nucleocapsid
NA	neuraminidase
NTP	nucleotide triphosphate
N-terminal	amino terminal
NS1	non-structural protein
NEP	nuclear export protein
NES	nuclear export sequence
nt	nucleotide(s)

NP-40	Nonidet P-40
OD	optical density
P/S	penicillin/streptomycin
pAb	polyclonal antibody
PB2	polymerase basic protein 2
PB1	polymerase basic protein 1
PEI	polyethylenimine
PTMs	post-translational modifications
PL	priming loop
PM	plasma membrane
Pro	proline
PBS	phosphate buffered saline
PolyA	polyadenylic acid
PMSF	phenylmethanesulfonylfluoride fluoride
PVDF	polyvinylidene fluoride
qPCR	quantitative real-time polymerase chain reaction
RdRP	RNA-dependent RNA polymerase
RNA	ribonucleic acid
rpm	rounds per minute
SA	sialic acid
Ser	serine
SD	standard deviation
SDS	sodium dodecyl sulfate
SDS-PAGE	SDS polyacrylamide gel electrophoresis
siRNA	small interfering RNA
STRN	striatin
STRN3	striatin 3
STRIPAK Complex	striatin-interacting phosphatase and kinase complex
Thr	threonine
Tyr	tyrosine
TEMED	*N,N,N′,N′*-Tetraacetylethylenediamine
Tween 20	polyoxyethylenesorbiten monolaurate
U	enzyme unit
vRNA	viral RNA
WT	wildtype
vRNPs	viral ribonucleoproteins
α	alpha
β	beta

8 LIST OF FIGURES

9 LIST OF TABLES

10 REFERENCES

Akarsu, H., Burmeister, W. P., Petosa, C., Petit, I., Muller, C. W., Ruigrok, R. W., Baudin, F. (2003). Crystal Structure Of The M1 Protein-Binding Domain Of The Influenza A Virus Nuclear Export Protein (NEP/NS2). EMBO J **22**(18): 4646-4655.

Alack, K., Weiss, A., Kruger, K., Horet, M., Schermuly, R., Frech, T., Eggert, M., Mooren, F. C. (2020). Profiling Of Human Lymphocytes Reveals A Specific Network Of Protein Kinases Modulated By Endurance Training Status. Sci Rep **10**(1): 888.

Alvarado-Facundo, E., Gao, Y., Ribas-Aparicio, R. M., Jimenez-Alberto, A., Weiss, C. D., Wang, W. (2015). Influenza Virus M2 Protein Ion Channel Activity Helps To Maintain Pandemic 2009 H1N1 Virus Hemagglutinin Fusion Competence During Transport To The Cell Surface. J Virol **89**(4): 1975-1985.

Amorim, M. J., Bruce, E. A., Read, E. K., Foeglein, A., Mahen, R., Stuart, A. D., Digard, P. (2011). A Rab11- And Microtubule-Dependent Mechanism For Cytoplasmic Transport Of Influenza A Virus Viral RNA. J Virol **85**(9): 4143-4156.

Ardito, F., Giuliani, M., Perrone, D., Troiano, G., Lo Muzio, L. (2017). The Crucial Role Of Protein Phosphorylation In Cell Signaling And Its Use As Targeted Therapy (Review). Int J Mol Med **40**(2): 271-280.

Ashton-Beaucage, D., Udell, C. M., Gendron, P., Sahmi, M., Lefrancois, M., Baril, C., Guenier, A. S., Duchaine, J., Lamarre, D., Lemieux, S., Therrien, M. (2014). A Functional Screen Reveals An Extensive Layer Of Transcriptional And Splicing Control Underlying RAS/MAPK Signaling In Drosophila. Plos Biol **12**(3): E1001809.

Atkins, C., Evans, C. W., Nordin, B., Patricelli, M. P., Reynolds, R., Wennerberg, K., Noah, J. W. (2014). Global Human-Kinase Screening Identifies Therapeutic Host Targets Against Influenza. J Biomol Screen **19**(6): 936-946.

Balendran, A., Biondi, R. M., Cheung, P. C., Casamayor, A., Deak, M., Alessi, D. R. (2000). A 3-Phosphoinositide-Dependent Protein Kinase-1 (PDK1) Docking Site Is Required For The Phosphorylation Of Protein Kinase Czeta (Pkczeta) And PKC-Related Kinase 2 By PDK1. J Biol Chem **275**(27): 20806-20813.

Banerjee, I., Miyake, Y., Nobs, S. P., Schneider, C., Horvath, P., Kopf, M., Matthias, P., Helenius, A., Yamauchi, Y. (2014). Influenza A Virus Uses The Aggresome Processing Machinery For Host Cell Entry. Science **346**(6208): 473-477.

Bao, Y., Bolotov, P., Dernovoy, D., Kiryutin, B., Zaslavsky, L., Tatusova, T., Ostell, J., Lipman, D. (2008). The Influenza Virus Resource At The National Center For Biotechnology Information. J Virol **82**(2): 596-601.

Barman, S., Adhikary, L., Chakrabarti, A. K., Bernas, C., Kawaoka, Y., Nayak, D. P. (2004). Role Of Transmembrane Domain And Cytoplasmic Tail Amino Acid Sequences Of Influenza A Virus Neuraminidase In Raft Association And Virus Budding. J Virol **78**(10): 5258-5269.

Baudin, F., Petit, I., Weissenhorn, W., Ruigrok, R. W. (2001). In Vitro Dissection Of The Membrane And RNP Binding Activities Of Influenza Virus M1 Protein. Virology **281**(1): 102-108.

Bedi, S., Ono, A. (2019). Friend Or Foe: The Role Of The Cytoskeleton In Influenza A Virus Assembly. Viruses **11**(1).

Bei, Y., Tia, B., Li, Y., Guo, Y., Deng, S., Huang, R., Zeng, H., Li, R., Wang, G. F., Dai, J. (2021). Anti-Influenza A Virus Effects And Mechanisms Of Emodin And Its Analogs Via Regulating Pparalpha/Gamma-AMPK-SIRT1 Pathway And Fatty Acid Metabolism. Biomed Res Int **2021**: 9066938.

Benitez, A. A., Panis, M., Xue, J., Varble, A., Shim, J. V., Frick, A. L., Lopez, C. B., Sachs, D., Tenoever, B. R. (2015). In Vivo Rnai Screening Identifies MDA5 As A Significant Contributor To The Cellular Defense Against Influenza A Virus. Cell Rep **11**(11): 1714-1726.

Benton, D. J., Gamblin, S. J., Rosenthal, P. B., Skehel, J. J. (2020). Structural Transitions In Influenza Haemagglutinin At Membrane Fusion Ph. Nature **583**(7814): 150-153.

Benton, D. J., Wharton, S. A., Martin, S. R., Mccauley, J. W. (2017). Role Of Neuraminidase In Influenza A(H7N9) Virus Receptor Binding. J Virol **91**(11).

Betts, M. J., Wichmann, O., Utz, M., Andre, T., Petsalaki, E., Minguez, P., Parca, L., Roth, F. P., Gavin, A. C., Bork, P., Russell, R. B. (2017). Systematic Identification Of Phosphorylation-Mediated Protein Interaction Switches. Plos Comput Biol **13**(3): E1005462.

Bonaparte, M. I., Dimitrov, A. S., Bossart, K. N., Crameri, G., Mungall, B. A., Bishop, K. A., Choudhry, V., Dimitrov, D. S., Wang, L. F., Eaton, B. T., Broder, C. C. (2005). Ephrin-B2 Ligand Is A Functional Receptor For Hendra Virus And Nipah Virus. Proc Natl Acad Sci U S A **102**(30): 10652-10657.

Bonne Kohler, J., Jers, C., Senissar, M., Shi, L., Derouiche, A., Mijakovic, I. (2020). Importance Of Protein Ser/Thr/Tyr Phosphorylation For Bacterial Pathogenesis. FEBS Lett **594**(15): 2339-2369.

Boon, A. C., Debeauchamp, J., Hollmann, A., Luke, J., Kotb, M., Rowe, S., Finkelstein, D., Neale, G., Lu, L., Williams, R. W., Webby, R. J. (2009). Host Genetic Variation Affects Resistance To Infection With A Highly Pathogenic H5N1 Influenza A Virus In Mice. J Virol **83**(20): 10417-10426.

Bornholdt, Z. A., Prasad, B. V. (2008). X-Ray Structure Of NS1 From A Highly Pathogenic H5N1 Influenza Virus. Nature **456**(7224): 985-988.

Bradley, D., Vieitez, C., Rajeeve, V., Selkrig, J., Cutillas, P. R., Beltrao, P. (2021). Sequence And Structure-Based Analysis Of Specificity Determinants In Eukaryotic Protein Kinases. Cell Rep **34**(2): 108602.

Bui, M., Wills, E. G., Helenius, A., Whittaker, G. R. (2000). Role Of The Influenza Virus M1 Protein In Nuclear Export Of Viral Ribonucleoproteins. J Virol **74**(4): 1781-1786.

Bullough, P. A., Hughson, F. M., Skehel, J. J., Wiley, D. C. (1994). Structure Of Influenza Haemagglutinin At The Ph Of Membrane Fusion. Nature **371**(6492): 37-43.

Calder, L. J., Wasilewski, S., Berriman, J. A., Rosenthal, P. B. (2010). Structural Organization Of A Filamentous Influenza A Virus. Proc Natl Acad Sci U S A **107**(23): 10685-10690.

Cao, A., Alluqmani, N., Buhari, F. H. M., Wasim, L., Smith, L. K., Quaile, A. T., Shannon, M., Hakim, Z., Furmli, H., Owen, D. M., Savchenko, A., Treanor, B. (2018). Galectin-9 Binds Igm-BCR To Regulate B Cell Signaling. Nat Commun **9**(1): 3288.

Cao, S., Liu, X., Yu, M., Li, J., Jia, X., Bi, Y., Sun, L., Gao, G. F., Liu, W. (2012). A Nuclear Export Signal In The Matrix Protein Of Influenza A Virus Is Required For Efficient Virus Replication. J Virol **86**(9): 4883-4891.

Capitanio, J. S., Wozniak, R. W. (2012). Host Cell Factors Necessary For Influenza A Infection: Meta-Analysis Of Genome Wide Studies.

Cargnello, M., Roux, P. P. (2011). Activation And Function Of The Mapks And Their Substrates, The MAPK-Activated Protein Kinases. Microbiol Mol Biol Rev **75**(1): 50-83.

Carrique, L., Fan, H., Walker, A. P., Keown, J. R., Sharps, J., Staller, E., Barclay, W. S., Fodor, E., Grimes, J. M. (2020). Host ANP32A Mediates The Assembly Of The Influenza Virus Replicase. Nature **587**(7835): 638-643.

Chan, C. M., Chu, H., Zhang, A. J., Leung, L. H., Sze, K. H., Kao, R. Y., Chik, K. K., To, K. K., Chan, J. F., Chen, H., Jin, D. Y., Liu, L., Yuen, K. Y. (2016). Hemagglutinin Of Influenza A Virus Binds Specifically To Cell Surface Nucleolin And Plays A Role In Virus Internalization. Virology **494**: 78-88.

Chan, W. H., Ng, A. K., Robb, N. C., Lam, M. K., Chan, P. K., Au, S. W., Wang, J. H., Fodor, E., Shaw, P. C. (2010). Functional Analysis Of The Influenza Virus H5N1 Nucleoprotein Tail Loop Reveals Amino Acids That Are Crucial For Oligomerization And Ribonucleoprotein Activities. J Virol **84**(14): 7337-7345.

Chang, Z., Wang, Y., Zhou, X., Long, J. E. (2018). STAT3 Roles In Viral Infection: Antiviral Or Proviral? Future Virol **13**(8): 557-574.

Chen, B. J., Leser, G. P., Jackson, D., Lamb, R. A. (2008). The Influenza Virus M2 Protein Cytoplasmic Tail Interacts With The M1 Protein And Influences Virus Assembly At The Site Of Virus Budding. J Virol **82**(20): 10059-10070.

Chen, B. J., Leser, G. P., Morita, E., Lamb, R. A. (2007). Influenza Virus Hemagglutinin And Neuraminidase, But Not The Matrix Protein, Are Required For Assembly And Budding Of Plasmid-Derived Virus-Like Particles. J Virol **81**(13): 7111-7123.

Chen, C., Ha, B. H., Thevenin, A. F., Lou, H. J., Zhang, R., Yip, K. Y., Peterson, J. R., Gerstein, M., Kim, P. M., Filippakopoulos, P., Knapp, S., Boggon, T. J., Turk, B. E. (2014). Identification Of A Major Determinant For Serine-Threonine Kinase Phosphoacceptor Specificity. Mol Cell **53**(1): 140-147.

Chen, C., Shi, Z., Zhang, W., Chen, M., He, F., Zhang, Z., Wang, Y., Feng, M., Wang, W., Zhao, Y., Brown, J. H., Jiao, S., Zhou, Z. (2014). Striatins Contain A Noncanonical Coiled Coil That Binds Protein Phosphatase 2A A Subunit To Form A 2:2 Heterotetrameric Core Of Striatin-Interacting Phosphatase And Kinase (STRIPAK) Complex. J Biol Chem **289**(14): 9651-9661.

Cheng, J., Tao, J., Li, B., Shi, Y., Liu, H. (2019). The Tyrosine 73 And Serine 83 Dephosphorylation Of H1N1 Swine Influenza Virus NS1 Protein Attenuates Virus Replication And Induces High Levels Of Beta Interferon. Virol J **16**(1): 152.

Cheng, Y., Tian, H. (2017). Current Development Status Of MEK Inhibitors. Molecules **22**(10).

Chiang, M. J., Musayev, F. N., Kosikova, M., Lin, Z., Gao, Y., Mosier, P. D., Althufairi, B., Ye, Z., Zhou, Q., Desai, U. R., Xie, H., Safo, M. K. (2017). Maintaining Ph-Dependent Conformational Flexibility Of M1 Is Critical For Efficient Influenza A Virus Replication. Emerg Microbes Infect **6**(12): E108.

Chlanda, P., Schraidt, O., Kummer, S., Riches, J., Oberwinkler, H., Prinz, S., Krausslich, H. G., Briggs, J. A. (2015). Structural Analysis Of The Roles Of Influenza A Virus Membrane-Associated Proteins In Assembly And Morphology. J Virol **89**(17): 8957-8966.

Choy, E. H. (2019). Clinical Significance Of Janus Kinase Inhibitor Selectivity. Rheumatology (Oxford) **58**(6): 953-962.

Colinge, J., Cesar-Razquin, A., Huber, K., Breitwieser, F. P., Majek, P., Superti-Furga, G. (2014). Building And Exploring An Integrated Human Kinase Network: Global Organization And Medical Entry Points. J Proteomics **107**: 113-127.

Creeden, J. F., Alganem, K., Imami, A. S., Brunicardi, F. C., Liu, S. H., Shukla, R., Tomar, T., Naji, F., Mccullumsmith, R. E. (2020). Kinome Array Profiling Of Patient-Derived Pancreatic Ductal Adenocarcinoma Identifies Differentially Active Protein Tyrosine Kinases. Int J Mol Sci **21**(22).

Creytens, S., Pascha, M. N., Ballegeer, M., Saelens, X., De Haan, C. A. M. (2021). Influenza Neuraminidase Characteristics And Potential As A Vaccine Target. Front Immunol **12**: 786617.

Cui, L., Mahesutihan, M., Zheng, W., Meng, L., Fan, W., Li, J., Ye, X., Liu, W., Sun, L. (2018). CDC25B Promotes Influenza A Virus Replication By Regulating The Phosphorylation Of Nucleoprotein. Virology **525**: 40-47.

Dadonaite, B., Vijayakrishnan, S., Fodor, E., Bhella, D., Hutchinson, E. C. (2016). Filamentous Influenza Viruses. J Gen Virol **97**(8): 1755-1764.

Dahmani, I., Ludwig, K., Chiantia, S. (2019). Influenza A Matrix Protein M1 Induces Lipid Membrane Deformation Via Protein Multimerization. Biosci Rep **39**(8).

Darling, T. K., Lamb, T. J. (2019). Emerging Roles For Eph Receptors And Ephrin Ligands In Immunity. Front Immunol **10**: 1473.

Das, S. C., Watanabe, S., Hatta, M., Noda, T., Neumann, G., Ozawa, M., Kawaoka, Y. (2012). The Highly Conserved Arginine Residues At Positions 76 Through 78 Of Influenza A Virus Matrix Protein M1 Play An Important Role In Viral Replication By Affecting The Intracellular Localization Of M1. J Virol **86**(3): 1522-1530.

Dawson, A. R., Mehle, A. (2018). Flu's Cues: Exploiting Host Post-Translational Modifications To Direct The Influenza Virus Replication Cycle. Plos Pathog **14**(9): E1007205.

Dawson, A. R., Wilson, G. M., Coon, J. J., Mehle, A. (2020). Post-Translation Regulation Of Influenza Virus Replication. Annu Rev Virol **7**(1): 167-187.

Dawson, A. R., Wilson, G. M., Freiberger, E. C., Mondal, A., Coon, J. J., Mehle, A. (2020). Phosphorylation Controls RNA Binding And Transcription By The Influenza Virus Polymerase. Plos Pathog **16**(9): E1008841.

De Boer, E. C. W., Van Gils, J. M., Van Gils, M. J. (2020). Ephrin-Eph Signaling Usage By A Variety Of Viruses. Pharmacol Res **159**: 105038.

Deng, T., Sharps, J., Fodor, E., Brownlee, G. G. (2005). In Vitro Assembly Of PB2 With A PB1-PA Dimer Supports A New Model Of Assembly Of Influenza A Virus Polymerase Subunits Into A Functional Trimeric Complex. J Virol **79**(13): 8669-8674.

Ding, X., Lu, J., Yu, R., Wang, X., Wang, T., Dong, F., Peng, B., Wu, W., Liu, H., Geng, Y., Zhang, R., Ma, H., Cheng, J., Yu, M., Fang, S. (2016). Preliminary Proteomic Analysis Of A549 Cells Infected With Avian Influenza Virus H7N9 And Influenza A Virus H1N1. Plos One **11**(5): E0156017.

Dou, D., Revol, R., Ostbye, H., Wang, H., Daniels, R. (2018). Influenza A Virus Cell Entry, Replication, Virion Assembly And Movement. Front Immunol **9**: 1581.

Douglass, J., Gunaratne, R., Bradford, D., Saeed, F., Hoffert, J. D., Steinbach, P. J., Knepper, M. A., Pisitkun, T. (2012). Identifying Protein Kinase Target Preferences Using Mass Spectrometry. Am J Physiol Cell Physiol **303**(7): C715-727.

Downey, J., Pernet, E., Coulombe, F., Allard, B., Meunier, I., Jaworska, J., Qureshi, S., Vinh, D. C., Martin, J. G., Joubert, P., Divangahi, M. (2017). RIPK3 Interacts With MAVS To Regulate Type I IFN-Mediated Immunity To Influenza A Virus Infection. Plos Pathog **13**(4): E1006326.

Dubois, J., Terrier, O., Rosa-Calatrava, M. (2014). Influenza Viruses And Mrna Splicing: Doing More With Less. Mbio **5**(3): E00070-00014.

Edwards, A. M., Isserlin, R., Bader, G. D., Frye, S. V., Willson, T. M., Yu, F. H. (2011). Too Many Roads Not Taken. Nature **470**(7333): 163-165.

Ehrhardt, C., Marjuki, H., Wolff, T., Nurnberg, B., Planz, O., Pleschka, S., Ludwig, S. (2006). Bivalent Role Of The Phosphatidylinositol-3-Kinase (PI3K) During Influenza Virus Infection And Host Cell Defence. Cell Microbiol **8**(8): 1336-1348.

Ehrhardt, C., Wolff, T., Pleschka, S., Planz, O., Beermann, W., Bode, J. G., Schmolke, M., Ludwig, S. (2007). Influenza A Virus NS1 Protein Activates The PI3K/Akt Pathway To Mediate Antiapoptotic Signaling Responses. J Virol **81**(7): 3058-3067.

Eisfeld, A. J., Kawakami, E., Watanabe, T., Neumann, G., Kawaoka, Y. (2011). RAB11A Is Essential For Transport Of The Influenza Virus Genome To The Plasma Membrane. J Virol **85**(13): 6117-6126.

Eisfeld, A. J., Neumann, G., Kawaoka, Y. (2015). At The Centre: Influenza A Virus Ribonucleoproteins. Nat Rev Microbiol **13**(1): 28-41.

Ellstrom, P., Jourdain, E., Gunnarsson, O., Waldenstrom, J., Olsen, B. (2009). The "Human Influenza Receptor" Neu5Ac Alpha2,6Gal Is Expressed Among Different Taxa Of Wild Birds. Arch Virol **154**(9): 1533-1537.

Engelhardt, O. G., Smith, M., Fodor, E. (2005). Association Of The Influenza A Virus RNA-Dependent RNA Polymerase With Cellular RNA Polymerase II. J Virol **79**(9): 5812-5818.

Escalona, E., Munoz, M., Pincheira, R., Elorza, A. A., Castro, A. F. (2020). Cytosolic NUAK1 Enhances ATP Production By Maintaining Proper Glycolysis And Mitochondrial Function In Cancer Cells. Front Oncol **10**: 1123.

Fan, H., Walker, A. P., Carrique, L., Keown, J. R., Serna Martin, I., Karia, D., Sharps, J., Hengrung, N., Pardon, E., Steyaert, J., Grimes, J. M., Fodor, E. (2019).

Structures Of Influenza A Virus RNA Polymerase Offer Insight Into Viral Genome Replication. Nature **573**(7773): 287-290.

Fischer, E. H., Krebs, E. G. (1955). Conversion Of Phosphorylase B To Phosphorylase A In Muscle Extracts. J Biol Chem **216**(1): 121-132.

Fodor, E. (2013). The RNA Polymerase Of Influenza A Virus: Mechanisms Of Viral Transcription And Replication. Acta Virol **57**(2): 113-122.

Fodor, E., Te Velthuis, A. J. W. (2020). Structure And Function Of The Influenza Virus Transcription And Replication Machinery. Cold Spring Harb Perspect Med **10**(9).

Fox, A. H., Nakagawa, S., Hirose, T., Bond, C. S. (2018). Paraspeckles: Where Long Noncoding RNA Meets Phase Separation. Trends Biochem Sci **43**(2): 124-135.

Furumoto, Y., Gadina, M. (2013). The Arrival Of JAK Inhibitors: Advancing The Treatment Of Immune And Hematologic Disorders. Biodrugs **27**(5): 431-438.

Garcia, D., Shaw, R. J. (2017). AMPK: Mechanisms Of Cellular Energy Sensing And Restoration Of Metabolic Balance. Mol Cell **66**(6): 789-800.

Garten, W., Bosch, F. X., Linder, D., Rott, R., Klenk, H. D. (1981). Proteolytic Activation Of The Influenza Virus Hemagglutinin: The Structure Of The Cleavage Site And The Enzymes Involved In Cleavage. Virology **115**(2): 361-374.

Gaucherand, L., Porter, B. K., Levene, R. E., Price, E. L., Schmaling, S. K., Rycroft, C. H., Kevorkian, Y., Mccormick, C., Khaperskyy, D. A., Gaglia, M. M. (2019). The Influenza A Virus Endoribonuclease PA-X Usurps Host Mrna Processing Machinery To Limit Host Gene Expression. Cell Rep **27**(3): 776-792 E777.

Gerl, M. J., Sampaio, J. L., Urban, S., Kalvodova, L., Verbavatz, J. M., Binnington, B., Lindemann, D., Lingwood, C. A., Shevchenko, A., Schroeder, C., Simons, K. (2012). Quantitative Analysis Of The Lipidomes Of The Influenza Virus Envelope And MDCK Cell Apical Membrane. J Cell Biol **196**(2): 213-221.

Giacchello, I., Musumeci, F., D'Agostino, I., Greco, C., Grossi, G., Schenone, S. (2021). Insights Into RNA-Dependent RNA Polymerase Inhibitors As Antiinfluenza Virus Agents. Curr Med Chem **28**(6): 1068-1090.

Giese, S., Ciminski, K., Bolte, H., Moreira, E. A., Lakdawala, S., Hu, Z., David, Q., Kolesnikova, L., Gotz, V., Zhao, Y., Dengjel, J., Chin, Y. E., Xu, K., Schwemmle, M. (2017). Role Of Influenza A Virus NP Acetylation On Viral Growth And Replication. Nat Commun **8**(1): 1259.

Gottschalk, A. (1957). Neuraminidase: The Specific Enzyme Of Influenza Virus And Vibrio Cholerae. Biochim Biophys Acta **23**(3): 645-646.

Govorkova, E. A., Rehg, J. E., Krauss, S., Yen, H. L., Guan, Y., Peiris, M., Nguyen, T. D., Hanh, T. H., Puthavathana, P., Long, H. T., Buranathai, C., Lim, W., Webster, R. G., Hoffmann, E. (2005). Lethality To Ferrets Of H5N1 Influenza Viruses Isolated From Humans And Poultry In 2004. J Virol **79**(4): 2191-2198.

Griffin, J. A., Compans, R. W. (1979). Effect Of Cytochalasin B On The Maturation Of Enveloped Viruses. J Exp Med **150**(2): 379-391.

Hahn, A. S., Desrosiers, R. C. (2013). Rhesus Monkey Rhadinovirus Uses Eph Family Receptors For Entry Into B Cells And Endothelial Cells But Not Fibroblasts. Plos Pathog **9**(5): E1003360.

Hahn, A. S., Kaufmann, J. K., Wies, E., Naschberger, E., Panteleev-Ivlev, J., Schmidt, K., Holzer, A., Schmidt, M., Chen, J., Konig, S., Ensser, A., Myoung, J., Brockmeyer, N. H., Sturzl, M., Fleckenstein, B., Neipel, F. (2012). The Ephrin Receptor Tyrosine Kinase A2 Is A Cellular Receptor For Kaposi's Sarcoma-Associated Herpesvirus. Nat Med **18**(6): 961-966.

Hale, B. G., Knebel, A., Botting, C. H., Galloway, C. S., Precious, B. L., Jackson, D., Elliott, R. M., Randall, R. E. (2009). CDK/ERK-Mediated Phosphorylation Of The Human Influenza A Virus NS1 Protein At Threonine-215. Virology **383**(1): 6-11.

Han, J., Perez, J. T., Chen, C., Li, Y., Benitez, A., Kandasamy, M., Lee, Y., Andrade, J., Tenoever, B., Manicassamy, B. (2018). Genome-Wide CRISPR/Cas9 Screen Identifies Host Factors Essential For Influenza Virus Replication. Cell Rep **23**(2): 596-607.

Han, X., Li, Z., Chen, H., Wang, H., Mei, L., Wu, S., Zhang, T., Liu, B., Lin, X. (2012). Influenza Virus A/Beijing/501/2009(H1N1) NS1 Interacts With Beta-Tubulin And Induces Disruption Of The Microtubule Network And Apoptosis On A549 Cells. Plos One **7**(11): E48340.

Hanks, S. K., Quinn, A. M., Hunter, T. (1988). The Protein Kinase Family: Conserved Features And Deduced Phylogeny Of The Catalytic Domains. Science **241**(4861): 42-52.

Hao, W., Wang, L., Li, S. (2020). Roles Of The Non-Structural Proteins Of Influenza A Virus. Pathogens **9**(10).

Hardman, G., Perkins, S., Brownridge, P. J., Clarke, C. J., Byrne, D. P., Campbell, A. E., Kalyuzhnyy, A., Myall, A., Eyers, P. A., Jones, A. R., Eyers, C. E. (2019). Strong Anion Exchange-Mediated Phosphoproteomics Reveals Extensive Human Non-Canonical Phosphorylation. EMBO J **38**(21): E100847.

Hay, A. J., Lomniczi, B., Bellamy, A. R., Skehel, J. J. (1977). Transcription Of The Influenza Virus Genome. Virology **83**(2): 337-355.

Hilsch, M., Goldenbogen, B., Sieben, C., Hofer, C. T., Rabe, J. P., Klipp, E., Herrmann, A., Chiantia, S. (2014). Influenza A Matrix Protein M1 Multimerizes Upon Binding To Lipid Membranes. Biophys J **107**(4): 912-923.

Hofer, C. T., Di Lella, S., Dahmani, I., Jungnick, N., Bordag, N., Bobone, S., Huang, Q., Keller, S., Herrmann, A., Chiantia, S. (2019). Structural Determinants Of The Interaction Between Influenza A Virus Matrix Protein M1 And Lipid Membranes. Biochim Biophys Acta Biomembr **1861**(6): 1123-1134.

Hoffmann, E., Neumann, G., Kawaoka, Y., Hobom, G., Webster, R. G. (2000). A DNA Transfection System For Generation Of Influenza A Virus From Eight Plasmids. Proc Natl Acad Sci U S A **97**(11): 6108-6113.

Hsiang, T. Y., Zhou, L., Krug, R. M. (2012). Roles Of The Phosphorylation Of Specific Serines And Threonines In The NS1 Protein Of Human Influenza A Viruses. J Virol **86**(19): 10370-10376.

Hu, J., Zhang, L., Liu, X. (2020). Role Of Post-Translational Modifications In Influenza A Virus Life Cycle And Host Innate Immune Response. Front Microbiol **11**: 517461.

Huang, K. Y., Lee, T. Y., Kao, H. J., Ma, C. T., Lee, C. C., Lin, T. H., Chang, W. C., Huang, H. D. (2019). Dbptm In 2019: Exploring Disease Association And Cross-Talk Of Post-Translational Modifications. Nucleic Acids Res **47**(D1): D298-D308.

Huang, Q. S., Wood, T., Jelley, L., Jennings, T., Jefferies, S., Daniells, K., Nesdale, A., Dowell, T., Turner, N., Campbell-Stokes, P., Balm, M., Dobinson, H. C., Grant, C. C., James, S., Aminisani, N., Ralston, J., Gunn, W., Bocacao, J., Danielewicz, J., Moncrieff, T., Mcneill, A., Lopez, L., Waite, B., Kiedrzynski, T., Schrader, H., Gray, R., Cook, K., Currin, D., Engelbrecht, C., Tapurau, W., Emmerton, L., Martin, M., Baker, M. G., Taylor, S., Trenholme, A., Wong, C., Lawrence, S., Mcarthur, C., Stanley, A., Roberts, S., Rahnama, F., Bennett, J., Mansell, C., Dilcher, M., Werno, A., Grant, J., Van Der Linden, A., Youngblood, B., Thomas, P. G., Consortium, N. P., Webby, R. J. (2021). Impact Of The COVID-19 Nonpharmaceutical Interventions On Influenza And Other Respiratory Viral Infections In New Zealand. Nat Commun **12**(1): 1001.

Hutchinson, E. C., Denham, E. M., Thomas, B., Trudgian, D. C., Hester, S. S., Ridlova, G., York, A., Turrell, L., Fodor, E. (2012). Mapping The Phosphoproteome Of Influenza A And B Viruses By Mass Spectrometry. Plos Pathog **8**(11): E1002993.

Hutti, J. E., Jarrell, E. T., Chang, J. D., Abbott, D. W., Storz, P., Toker, A., Cantley, L. C., Turk, B. E. (2004). A Rapid Method For Determining Protein Kinase Phosphorylation Specificity. Nat Methods **1**(1): 27-29.

Imamura, K., Imamachi, N., Akizuki, G., Kumakura, M., Kawaguchi, A., Nagata, K., Kato, A., Kawaguchi, Y., Sato, H., Yoneda, M., Kai, C., Yada, T., Suzuki, Y., Yamada, T., Ozawa, T., Kaneki, K., Inoue, T., Kobayashi, M., Kodama, T., Wada, Y., Sekimizu, K., Akimitsu, N. (2014). Long Noncoding RNA NEAT1-Dependent

SFPQ Relocation From Promoter Region To Paraspeckle Mediates IL8 Expression Upon Immune Stimuli. Mol Cell **53**(3): 393-406.

Inazuka, F., Sugiyama, N., Tomita, M., Abe, T., Shioi, G., Esumi, H. (2012). Muscle-Specific Knock-Out Of NUAK Family SNF1-Like Kinase 1 (NUAK1) Prevents High Fat Diet-Induced Glucose Intolerance. J Biol Chem **287**(20): 16379-16389.

Invergo, B. M., Petursson, B., Akhtar, N., Bradley, D., Giudice, G., Hijazi, M., Cutillas, P., Petsalaki, E., Beltrao, P. (2020). Prediction Of Signed Protein Kinase Regulatory Circuits. Cell Syst **10**(5): 384-396 E389.

Jackson, D. A., Caton, A. J., Mccready, S. J., Cook, P. R. (1982). Influenza Virus RNA Is Synthesized At Fixed Sites In The Nucleus. Nature **296**(5855): 366-368.

Jacob, T., Van Den Broeke, C., Favoreel, H. W. (2011). Viral Serine/Threonine Protein Kinases. J Virol **85**(3): 1158-1173.

Jagger, B. W., Wise, H. M., Kash, J. C., Walters, K. A., Wills, N. M., Xiao, Y. L., Dunfee, R. L., Schwartzman, L. M., Ozinsky, A., Bell, G. L., Dalton, R. M., Lo, A., Efstathiou, S., Atkins, J. F., Firth, A. E., Taubenberger, J. K., Digard, P. (2012). An Overlapping Protein-Coding Region In Influenza A Virus Segment 3 Modulates The Host Response. Science **337**(6091): 199-204.

Jaiswal, N., Agarwal, N., Poluri, K. M., Kumar, D. (2020). Effect Of Urea Concentration On Instant Refolding Of Nuclear Export Protein (NEP) From Influenza-A Virus H1N1: A Solution NMR Based Investigation. Int J Biol Macromol **165**(Pt B): 2508-2519.

Jeong, B. C., Bae, S. J., Ni, L., Zhang, X., Bai, X. C., Luo, X. (2021). Cryo-EM Structure Of The Hippo Signaling Integrator Human STRIPAK. Nat Struct Mol Biol **28**(3): 290-299.

Johnson, L. N. (2009). The Regulation Of Protein Phosphorylation. Biochem Soc Trans **37**(Pt 4): 627-641.

Johnson, S. A., Hunter, T. (2005). Kinomics: Methods For Deciphering The Kinome. Nat Methods **2**(1): 17-25.

Jorba, N., Coloma, R., Ortin, J. (2009). Genetic Trans-Complementation Establishes A New Model For Influenza Virus RNA Transcription And Replication. Plos Pathog **5**(5): E1000462.

Joseph, U., Su, Y. C., Vijaykrishna, D., Smith, G. J. (2017). The Ecology And Adaptive Evolution Of Influenza A Interspecies Transmission. Influenza Other Respir Viruses **11**(1): 74-84.

Karlas, A., Machuy, N., Shin, Y., Pleissner, K. P., Artarini, A., Heuer, D., Becker, D., Khalil, H., Ogilvie, L. A., Hess, S., Maurer, A. P., Muller, E., Wolff, T., Rudel, T., Meyer, T. F. (2010). Genome-Wide Rnai Screen Identifies Human Host Factors Crucial For Influenza Virus Replication. Nature **463**(7282): 818-822.

Kash, J. C., Goodman, A. G., Korth, M. J., Katze, M. G. (2006). Hijacking Of The Host-Cell Response And Translational Control During Influenza Virus Infection. Virus Res **119**(1): 111-120.

Kash, J. C., Tumpey, T. M., Proll, S. C., Carter, V., Perwitasari, O., Thomas, M. J., Basler, C. F., Palese, P., Taubenberger, J. K., Garcia-Sastre, A., Swayne, D. E., Katze, M. G. (2006). Genomic Analysis Of Increased Host Immune And Cell Death Responses Induced By 1918 Influenza Virus. Nature **443**(7111): 578-581.

Kathum, O. A., Schrader, T., Anhlan, D., Nordhoff, C., Liedmann, S., Pande, A., Mellmann, A., Ehrhardt, C., Wixler, V., Ludwig, S. (2016). Phosphorylation Of Influenza A Virus NS1 Protein At Threonine 49 Suppresses Its Interferon Antagonistic Activity. Cell Microbiol **18**(6): 784-791.

Kawaguchi, A., Matsumoto, K., Nagata, K. (2012). YB-1 Functions As A Porter To Lead Influenza Virus Ribonucleoprotein Complexes To Microtubules. J Virol **86**(20): 11086-11095.

Kazmierczak-Baranska, J., Peczek, L., Przygodzka, P., Cieslak, M. J. (2015). Downregulation Of Striatin Leads To Hyperphosphorylation Of MAP2, Induces

Depolymerization Of Microtubules And Inhibits Proliferation Of HEK293T Cells. FEBS Lett **589**(2): 222-230.

Kean, M. J., Ceccarelli, D. F., Goudreault, M., Sanches, M., Tate, S., Larsen, B., Gibson, L. C., Derry, W. B., Scott, I. C., Pelletier, L., Baillie, G. S., Sicheri, F., Gingras, A. C. (2011). Structure-Function Analysis Of Core STRIPAK Proteins: A Signaling Complex Implicated In Golgi Polarization. J Biol Chem **286**(28): 25065-25075.

Kemp, B. E., Bylund, D. B., Huang, T. S., Krebs, E. G. (1975). Substrate Specificity Of The Cyclic AMP-Dependent Protein Kinase. Proc Natl Acad Sci U S A **72**(9): 3448-3452.

Kheirollahi, V., Wasnick, R. M., Biasin, V., Vazquez-Armendariz, A. I., Chu, X., Moiseenko, A., Weiss, A., Wilhelm, J., Zhang, J. S., Kwapiszewska, G., Herold, S., Schermuly, R. T., Mari, B., Li, X., Seeger, W., Gunther, A., Bellusci, S., El Agha, E. (2019). Metformin Induces Lipogenic Differentiation In Myofibroblasts To Reverse Lung Fibrosis. Nat Commun **10**(1): 2987.

Kido, H., Murakami, M., Oba, K., Chen, Y., Towatari, T. (1999). Cellular Proteinases Trigger The Infectivity Of The Influenza A And Sendai Viruses. Mol Cells **9**(3): 235-244.

Kido, H., Okumura, Y., Takahashi, E., Pan, H. Y., Wang, S., Chida, J., Le, T. Q., Yano, M. (2008). Host Envelope Glycoprotein Processing Proteases Are Indispensable For Entry Into Human Cells By Seasonal And Highly Pathogenic Avian Influenza Viruses. J Mol Genet Med **3**(1): 167-175.

Kim, D., Ntui, V. O., Zhang, N., Xiong, L. (2015). Arabidopsis Yak1 Protein (Atyak1) Is A Dual Specificity Protein Kinase. FEBS Lett **589**(21): 3321-3327.

Kitamura, R., Sekimoto, T., Ito, S., Harada, S., Yamagata, H., Masai, H., Yoneda, Y., Yanagi, K. (2006). Nuclear Import Of Epstein-Barr Virus Nuclear Antigen 1 Mediated By NPI-1 (Importin Alpha5) Is Up- And Down-Regulated By Phosphorylation Of The Nuclear Localization Signal For Which Lys379 And Arg380 Are Essential. J Virol **80**(4): 1979-1991.

Konig, R., Stertz, S., Zhou, Y., Inoue, A., Hoffmann, H. H., Bhattacharyya, S., Alamares, J. G., Tscherne, D. M., Ortigoza, M. B., Liang, Y., Gao, Q., Andrews, S. E., Bandyopadhyay, S., De Jesus, P., Tu, B. P., Pache, L., Shih, C., Orth, A., Bonamy, G., Miraglia, L., Ideker, T., Garcia-Sastre, A., Young, J. A., Palese, P., Shaw, M. L., Chanda, S. K. (2010). Human Host Factors Required For Influenza Virus Replication. Nature **463**(7282): 813-817.

Kornev, A. P., Taylor, S. S. (2015). Dynamics-Driven Allostery In Protein Kinases. Trends Biochem Sci **40**(11): 628-647.

Koutsakos, M., Wheatley, A. K., Laurie, K., Kent, S. J., Rockman, S. (2021). Influenza Lineage Extinction During The COVID-19 Pandemic? Nat Rev Microbiol **19**(12): 741-742.

Krammer, F., Smith, G. J. D., Fouchier, R. A. M., Peiris, M., Kedzierska, K., Doherty, P. C., Palese, P., Shaw, M. L., Treanor, J., Webster, R. G., Garcia-Sastre, A. (2018). Influenza. Nat Rev Dis Primers **4**(1): 3.

Kumakura, M., Kawaguchi, A., Nagata, K. (2015). Actin-Myosin Network Is Required For Proper Assembly Of Influenza Virus Particles. Virology **476**: 141-150.

Kumar, B., Asha, K., Khanna, M., Ronsard, L., Meseko, C. A., Sanicas, M. (2018). The Emerging Influenza Virus Threat: Status And New Prospects For Its Therapy And Control. Arch Virol **163**(4): 831-844.

Kuriakose, T., Man, S. M., Malireddi, R. K., Karki, R., Kesavardhana, S., Place, D. E., Neale, G., Vogel, P., Kanneganti, T. D. (2016). ZBP1/DAI Is An Innate Sensor Of Influenza Virus Triggering The NLRP3 Inflammasome And Programmed Cell Death Pathways. Sci Immunol **1**(2).

Lachmann, A., Ma'ayan, A. (2009). KEA: Kinase Enrichment Analysis. Bioinformatics **25**(5): 684-686.

Laghlali, G., Lawlor, K. E., Tate, M. D. (2020). Die Another Way: Interplay Between Influenza A Virus, Inflammation And Cell Death. Viruses **12**(4).

Lahav-Ariel, L., Caspi, M., Nadar-Ponniah, P. T., Zelikson, N., Hofmann, I., Hanson, K. K., Franke, W. W., Sklan, E. H., Avraham, K. B., Rosin-Arbesfeld, R. (2019). Striatin Is A Novel Modulator Of Cell Adhesion. FASEB J **33**(4): 4729-4740.

Lahaye, X., Gentili, M., Silvin, A., Conrad, C., Picard, L., Jouve, M., Zueva, E., Maurin, M., Nadalin, F., Knott, G. J., Zhao, B., Du, F., Rio, M., Amiel, J., Fox, A. H., Li, P., Etienne, L., Bond, C. S., Colleaux, L., Manel, N. (2018). NONO Detects The Nuclear HIV Capsid To Promote Cgas-Mediated Innate Immune Activation. Cell **175**(2): 488-501 E422.

Lai, J. C., Chan, W. W., Kien, F., Nicholls, J. M., Peiris, J. S., Garcia, J. M. (2010). Formation Of Virus-Like Particles From Human Cell Lines Exclusively Expressing Influenza Neuraminidase. J Gen Virol **91**(Pt 9): 2322-2330.

Lai, K. O., Chen, Y., Po, H. M., Lok, K. C., Gong, K., Ip, N. Y. (2004). Identification Of The Jak/Stat Proteins As Novel Downstream Targets Of Epha4 Signaling In Muscle: Implications In The Regulation Of Acetylcholinesterase Expression. J Biol Chem **279**(14): 13383-13392.

Lakadamyali, M., Rust, M. J., Babcock, H. P., Zhuang, X. (2003). Visualizing Infection Of Individual Influenza Viruses. Proc Natl Acad Sci U S A **100**(16): 9280-9285.

Lant, B., Yu, B., Goudreault, M., Holmyard, D., Knight, J. D., Xu, P., Zhao, L., Chin, K., Wallace, E., Zhen, M., Gingras, A. C., Derry, W. B. (2015). CCM-3/STRIPAK Promotes Seamless Tube Extension Through Endocytic Recycling. Nat Commun **6**: 6449.

Larson, G. P., Tran, V., Yu, S., Cai, Y., Higgins, C. A., Smith, D. M., Baker, S. F., Radoshitzky, S. R., Kuhn, J. H., Mehle, A. (2019). EPS8 Facilitates Uncoating Of Influenza A Virus. Cell Rep **29**(8): 2175-2183 E2174.

Laure, M., Hamza, H., Koch-Heier, J., Quernheim, M., Muller, C., Schreiber, A., Muller, G., Pleschka, S., Ludwig, S., Planz, O. (2020). Antiviral Efficacy Against Influenza Virus And Pharmacokinetic Analysis Of A Novel MEK-Inhibitor, ATR-002, In Cell Culture And In The Mouse Model. Antiviral Res **178**: 104806.

Ledford, H. (2010). Big Science: The Cancer Genome Challenge. Nature **464**(7291): 972-974.

Lee, B. J., Cansizoglu, A. E., Suel, K. E., Louis, T. H., Zhang, Z., Chook, Y. M. (2006). Rules For Nuclear Localization Sequence Recognition By Karyopherin Beta 2. Cell **126**(3): 543-558.

Lejal, N., Tarus, B., Bouguyon, E., Chenavas, S., Bertho, N., Delmas, B., Ruigrok, R. W., Di Primo, C., Slama-Schwok, A. (2013). Structure-Based Discovery Of The Novel Antiviral Properties Of Naproxen Against The Nucleoprotein Of Influenza A Virus. Antimicrob Agents Chemother **57**(5): 2231-2242.

Li, B., Clohisey, S. M., Chia, B. S., Wang, B., Cui, A., Eisenhaure, T., Schweitzer, L. D., Hoover, P., Parkinson, N. J., Nachshon, A., Smith, N., Regan, T., Farr, D., Gutmann, M. U., Bukhari, S. I., Law, A., Sangesland, M., Gat-Viks, I., Digard, P., Vasudevan, S., Lingwood, D., Dockrell, D. H., Doench, J. G., Baillie, J. K., Hacohen, N. (2020). Genome-Wide CRISPR Screen Identifies Host Dependency Factors For Influenza A Virus Infection. Nat Commun **11**(1): 164.

Li, F., Liu, J., Yang, J., Sun, H., Jiang, Z., Wang, C., Zhang, X., Yu, Y., Zhao, C., Pu, J., Sun, Y., Chang, K. C., Liu, J., Sun, H. (2021). H9N2 Virus-Derived M1 Protein Promotes H5N6 Virus Release In Mammalian Cells: Mechanism Of Avian Influenza Virus Inter-Species Infection In Humans. Plos Pathog **17**(12): E1010098.

Li, J. N., Sun, H. L., Wang, M. Y., Chen, P. S. (2021). E-Cadherin Interacts With Posttranslationally-Modified AGO2 To Enhance Mirisc Activity. Front Cell Dev Biol **9**: 671244.

Li, Y., Sun, L., Zheng, W., Madina, M., Li, J., Bi, Y., Wang, H., Liu, W., Luo, T. R. (2018). Phosphorylation And Dephosphorylation Of Threonine 188 In Nucleoprotein Is Crucial For The Replication Of Influenza A Virus. Virology **520**: 30-38.

Liao, W., Ou, J. H. (1995). Phosphorylation And Nuclear Localization Of The Hepatitis B Virus Core Protein: Significance Of Serine In The Three Repeated SPRRR Motifs. J Virol **69**(2): 1025-1029.

Lindberg, R. A., Quinn, A. M., Hunter, T. (1992). Dual-Specificity Protein Kinases: Will Any Hydroxyl Do? Trends Biochem Sci **17**(3): 114-119.

Liu, H., Grantham, M. L., Pekosz, A. (2018). Mutations In The Influenza A Virus M1 Protein Enhance Virus Budding To Complement Lethal Mutations In The M2 Cytoplasmic Tail. J Virol **92**(1).

Long, J. S., Mistry, B., Haslam, S. M., Barclay, W. S. (2019). Host And Viral Determinants Of Influenza A Virus Species Specificity. Nat Rev Microbiol **17**(2): 67-81.

Luczo, J. M., Stambas, J., Durr, P. A., Michalski, W. P., Bingham, J. (2015). Molecular Pathogenesis Of H5 Highly Pathogenic Avian Influenza: The Role Of The Haemagglutinin Cleavage Site Motif. Rev Med Virol **25**(6): 406-430.

Ludwig, S. (2009). Targeting Cell Signalling Pathways To Fight The Flu: Towards A Paradigm Change In Anti-Influenza Therapy. J Antimicrob Chemother **64**(1): 1-4.

Ludwig, S., Hrincius, E. R., Boergeling, Y. (2021). The Two Sides Of The Same Coin-Influenza Virus And Intracellular Signal Transduction. Cold Spring Harb Perspect Med **11**(1).

Lupberger, J., Zeisel, M. B., Xiao, F., Thumann, C., Fofana, I., Zona, L., Davis, C., Mee, C. J., Turek, M., Gorke, S., Royer, C., Fischer, B., Zahid, M. N., Lavillette, D., Fresquet, J., Cosset, F. L., Rothenberg, S. M., Pietschmann, T., Patel, A. H., Pessaux, P., Doffoel, M., Raffelsberger, W., Poch, O., Mckeating, J. A., Brino, L., Baumert, T. F. (2011). EGFR And Epha2 Are Host Factors For Hepatitis C Virus Entry And Possible Targets For Antiviral Therapy. Nat Med **17**(5): 589-595.

Ma, H., Han, P., Ye, W., Chen, H., Zheng, X., Cheng, L., Zhang, L., Yu, L., Wu, X., Xu, Z., Lei, Y., Zhang, F. (2017). The Long Noncoding RNA NEAT1 Exerts Antihantaviral Effects By Acting As Positive Feedback For RIG-I Signaling. J Virol **91**(9).

Maeda, T., Kawasaki, K., Ohnishi, S. (1981). Interaction Of Influenza Virus Hemagglutinin With Target Membrane Lipids Is A Key Step In Virus-Induced Hemolysis And Fusion At Ph 5.2. Proc Natl Acad Sci U S A **78**(7): 4133-4137.

Manz, B., Matrosovich, M., Bovin, N., Schwemmle, M. (2010). A Polymorphism In The Hemagglutinin Of The Human Isolate Of A Highly Pathogenic H5N1 Influenza Virus Determines Organ Tropism In Mice. J Virol **84**(16): 8316-8321.

Marjuki, H., Alam, M. I., Ehrhardt, C., Wagner, R., Planz, O., Klenk, H. D., Ludwig, S., Pleschka, S. (2006). Membrane Accumulation Of Influenza A Virus Hemagglutinin Triggers Nuclear Export Of The Viral Genome Via Protein Kinase Calpha-Mediated Activation Of ERK Signaling. J Biol Chem **281**(24): 16707-16715.

Marjuki, H., Yen, H. L., Franks, J., Webster, R. G., Pleschka, S., Hoffmann, E. (2007). Higher Polymerase Activity Of A Human Influenza Virus Enhances Activation Of The Hemagglutinin-Induced Raf/MEK/ERK Signal Cascade. Virol J **4**: 134.

Martin, K., Helenius, A. (1991). Nuclear Transport Of Influenza Virus Ribonucleoproteins: The Viral Matrix Protein (M1) Promotes Export And Inhibits Import. Cell **67**(1): 117-130.

Mccown, M. F., Pekosz, A. (2006). Distinct Domains Of The Influenza A Virus M2 Protein Cytoplasmic Tail Mediate Binding To The M1 Protein And Facilitate Infectious Virus Production. J Virol **80**(16): 8178-8189.

Mecate-Zambrano, A., Sukumar, S., Seebohm, G., Ciminski, K., Schreiber, A., Anhlan, D., Greune, L., Wixler, L., Grothe, S., Stein, N. C., Schmidt, M. A., Langer, K., Schwemmle, M., Shi, T., Ludwig, S., Boergeling, Y. (2020). Discrete Spatio-Temporal Regulation Of Tyrosine Phosphorylation Directs Influenza A Virus M1 Protein Towards Its Function In Virion Assembly. Plos Pathog **16**(8): E1008775.

Mehdizadeh, A., Somi, M. H., Darabi, M., Jabbarpour-Bonyadi, M. (2016). Extracellular Signal-Regulated Kinase 1 And 2 In Cancer Therapy: A Focus On Hepatocellular Carcinoma. Mol Biol Rep **43**(2): 107-116.

Mehle, A., Dugan, V. G., Taubenberger, J. K., Doudna, J. A. (2012). Reassortment And Mutation Of The Avian Influenza Virus Polymerase PA Subunit Overcome Species Barriers. J Virol **86**(3): 1750-1757.

Meineke, R., Rimmelzwaan, G. F., Elbahesh, H. (2019). Influenza Virus Infections And Cellular Kinases. Viruses **11**(2).

Mercer, J., Helenius, A. (2009). Virus Entry By Macropinocytosis. Nat Cell Biol **11**(5): 510-520.

Miao, H., Wang, B. (2012). Epha Receptor Signaling--Complexity And Emerging Themes. Semin Cell Dev Biol **23**(1): 16-25.

Miller, C. J., Turk, B. E. (2018). Homing In: Mechanisms Of Substrate Targeting By Protein Kinases. Trends Biochem Sci **43**(5): 380-394.

Miller, C. J., Turk, B. E. (2016). Rapid Identification Of Protein Kinase Phosphorylation Site Motifs Using Combinatorial Peptide Libraries. Methods Mol Biol **1360**: 203-216.

Miyake, Y., Keusch, J. J., Decamps, L., Ho-Xuan, H., Iketani, S., Gut, H., Kutay, U., Helenius, A., Yamauchi, Y. (2019). Influenza Virus Uses Transportin 1 For Vrnp Debundling During Cell Entry. Nat Microbiol **4**(4): 578-586.

Mohd-Kipli, F., Claridge, J. K., Habjanic, J., Jiang, A., Schnell, J. R. (2021). Conformational Triggers Associated With Influenza Matrix Protein 1 Polymerization. J Biol Chem **296**: 100316.

Mok, J., Kim, P. M., Lam, H. Y., Piccirillo, S., Zhou, X., Jeschke, G. R., Sheridan, D. L., Parker, S. A., Desai, V., Jwa, M., Cameroni, E., Niu, H., Good, M., Remenyi, A., Ma, J. L., Sheu, Y. J., Sassi, H. E., Sopko, R., Chan, C. S., De Virgilio, C., Hollingsworth, N. M., Lim, W. A., Stern, D. F., Stillman, B., Andrews, B. J., Gerstein, M. B., Snyder, M., Turk, B. E. (2010). Deciphering Protein Kinase Specificity Through Large-Scale Analysis Of Yeast Phosphorylation Site Motifs. Sci Signal **3**(109): Ra12.

Momose, F., Kikuchi, Y., Komase, K., Morikawa, Y. (2007). Visualization Of Microtubule-Mediated Transport Of Influenza Viral Progeny Ribonucleoprotein. Microbes Infect **9**(12-13): 1422-1433.

Mondal, A., Dawson, A. R., Potts, G. K., Freiberger, E. C., Baker, S. F., Moser, L. A., Bernard, K. A., Coon, J. J., Mehle, A. (2017). Influenza Virus Recruits Host Protein Kinase C To Control Assembly And Activity Of Its Replication Machinery. Elife **6**.

Mondal, A., Potts, G. K., Dawson, A. R., Coon, J. J., Mehle, A. (2015). Phosphorylation At The Homotypic Interface Regulates Nucleoprotein Oligomerization And Assembly Of The Influenza Virus Replication Machinery. Plos Pathog **11**(4): E1004826.

Monteverde, T., Tait-Mulder, J., Hedley, A., Knight, J. R., Sansom, O. J., Murphy, D. J. (2018). Calcium Signalling Links MYC To NUAK1. Oncogene **37**(8): 982-992.

Morens, D. M., Taubenberger, J. K. (2011). Pandemic Influenza: Certain Uncertainties. Rev Med Virol **21**(5): 262-284.

Mostafa, A., Abdelwhab, E. M., Mettenleiter, T. C., Pleschka, S. (2018). Zoonotic Potential Of Influenza A Viruses: A Comprehensive Overview. Viruses **10**(9).

Muhlbauer, D., Dzieciolowski, J., Hardt, M., Hocke, A., Schierhorn, K. L., Mostafa, A., Muller, C., Wisskirchen, C., Herold, S., Wolff, T., Ziebuhr, J., Pleschka, S. (2015). Influenza Virus-Induced Caspase-Dependent Enlargement Of Nuclear Pores Promotes Nuclear Export Of Viral Ribonucleoprotein Complexes. J Virol **89**(11): 6009-6021.

Muramoto, Y., Noda, T., Kawakami, E., Akkina, R., Kawaoka, Y. (2013). Identification Of Novel Influenza A Virus Proteins Translated From PA Mrna. J Virol **87**(5): 2455-2462.

Nader, M., Khalil, B., Kattuah, W., Dzimiri, N., Bakheet, D. (2020). Striatin Translocates To The Cytosol Of Apoptotic Cells And Is Proteolytically Cleaved In A Caspase 3-Dependent Manner. Heliyon **6**(9): E04990.

Nayak, D. P., Balogun, R. A., Yamada, H., Zhou, Z. H., Barman, S. (2009). Influenza Virus Morphogenesis And Budding. Virus Res **143**(2): 147-161.

Neumann, G., Hughes, M. T., Kawaoka, Y. (2000). Influenza A Virus NS2 Protein Mediates Vrnp Nuclear Export Through NES-Independent Interaction With Hcrm1. EMBO J **19**(24): 6751-6758.

Nigdelioglu, R., Meliton, A. Y., Sun, K. A., Witt, L., Wu, D., Hamanaka, R. B., Mutlu, G. M. Serine Glycine One-Carbon Metabolism Drives Effector Responses To Influenza Infection In Macrophages. In *B62. LUNG CYTOPROTECTION AND IMMUNITY DURING INFECTIONS* (Pp. A3860-A3860). Https://Doi.Org/10.1164/Ajrccm-Conference.2018.197.1_Meetingabstracts.A3860

Noda, T., Kawaoka, Y. (2012). Packaging Of Influenza Virus Genome: Robustness Of Selection. Proc Natl Acad Sci U S A **109**(23): 8797-8798.

Noda, T., Murakami, S., Nakatsu, S., Imai, H., Muramoto, Y., Shindo, K., Sagara, H., Kawaoka, Y. (2018). Importance Of The 1+7 Configuration Of Ribonucleoprotein Complexes For Influenza A Virus Genome Packaging. Nat Commun **9**(1): 54.

Nogales, A., Martinez-Sobrido, L. (2016). Reverse Genetics Approaches For The Development Of Influenza Vaccines. Int J Mol Sci **18**(1).

Nogusa, S., Thapa, R. J., Dillon, C. P., Liedmann, S., Oguin, T. H., 3rd, Ingram, J. P., Rodriguez, D. A., Kosoff, R., Sharma, S., Sturm, O., Verbist, K., Gough, P. J., Bertin, J., Hartmann, B. M., Sealfon, S. C., Kaiser, W. J., Mocarski, E. S., Lopez, C. B., Thomas, P. G., Oberst, A., Green, D. R., Balachandran, S. (2016). RIPK3 Activates Parallel Pathways Of MLKL-Driven Necroptosis And FADD-Mediated Apoptosis To Protect Against Influenza A Virus. Cell Host Microbe **20**(1): 13-24.

Olea-Flores, M., Zuniga-Eulogio, M. D., Mendoza-Catalan, M. A., Rodriguez-Ruiz, H. A., Castaneda-Saucedo, E., Ortuno-Pineda, C., Padilla-Benavides, T., Navarro-Tito, N. (2019). Extracellular-Signal Regulated Kinase: A Central Molecule Driving Epithelial-Mesenchymal Transition In Cancer. Int J Mol Sci **20**(12).

Olsen, J. V., Blagoev, B., Gnad, F., Macek, B., Kumar, C., Mortensen, P., Mann, M. (2006). Global, In Vivo, And Site-Specific Phosphorylation Dynamics In Signaling Networks. Cell **127**(3): 635-648.

Olsen, J. V., Vermeulen, M., Santamaria, A., Kumar, C., Miller, M. L., Jensen, L. J., Gnad, F., Cox, J., Jensen, T. S., Nigg, E. A., Brunak, S., Mann, M. (2010). Quantitative Phosphoproteomics Reveals Widespread Full Phosphorylation Site Occupancy During Mitosis. Sci Signal **3**(104): Ra3.

Opitz, B., Rejaibi, A., Dauber, B., Eckhard, J., Vinzing, M., Schmeck, B., Hippenstiel, S., Suttorp, N., Wolff, T. (2007). Ifnbeta Induction By Influenza A Virus Is Mediated By RIG-I Which Is Regulated By The Viral NS1 Protein. Cell Microbiol **9**(4): 930-938.

Oymans, J., Te Velthuis, A. J. W. (2018). A Mechanism For Priming And Realignment During Influenza A Virus Replication. J Virol **92**(3).

Patil, A., Anhlan, D., Ferrando, V., Mecate-Zambrano, A., Mellmann, A., Wixler, V., Boergeling, Y., Ludwig, S. (2021). Phosphorylation Of Influenza A Virus NS1 At Serine 205 Mediates Its Viral Polymerase-Enhancing Function. J Virol **95**(6).

Pearson, G., Robinson, F., Beers Gibson, T., Xu, B. E., Karandikar, M., Berman, K., Cobb, M. H. (2001). Mitogen-Activated Protein (MAP) Kinase Pathways: Regulation And Physiological Functions. Endocr Rev **22**(2): 153-183.

Pennemann, F. L., Mussabekova, A., Urban, C., Stukalov, A., Andersen, L. L., Grass, V., Lavacca, T. M., Holze, C., Oubraham, L., Benamrouche, Y., Girardi, E., Boulos, R. E., Hartmann, R., Superti-Furga, G., Habjan, M., Imler, J. L., Meignin, C., Pichlmair, A. (2021). Cross-Species Analysis Of Viral Nucleic Acid Interacting

Proteins Identifies Taoks As Innate Immune Regulators. Nat Commun **12**(1): 7009.

Perales, B., Sanz-Ezquerro, J. J., Gastaminza, P., Ortega, J., Santaren, J. F., Ortin, J., Nieto, A. (2000). The Replication Activity Of Influenza Virus Polymerase Is Linked To The Capacity Of The PA Subunit To Induce Proteolysis. J Virol **74**(3): 1307-1312.

Pesu, M., Laurence, A., Kishore, N., Zwillich, S. H., Chan, G., O'Shea, J. J. (2008). Therapeutic Targeting Of Janus Kinases. Immunol Rev **223**: 132-142.

Petrich, A., Dunsing, V., Bobone, S., Chiantia, S. (2021). Influenza A M2 Recruits M1 To The Plasma Membrane: A Fluorescence Fluctuation Microscopy Study. Biophys J **120**(24): 5478-5490.

Peukes, J., Xiong, X., Erlendsson, S., Qu, K., Wan, W., Calder, L. J., Schraidt, O., Kummer, S., Freund, S. M. V., Krausslich, H. G., Briggs, J. A. G. (2020). The Native Structure Of The Assembled Matrix Protein 1 Of Influenza A Virus. Nature **587**(7834): 495-498.

Pflug, A., Gaudon, S., Resa-Infante, P., Lethier, M., Reich, S., Schulze, W. M., Cusack, S. (2018). Capped RNA Primer Binding To Influenza Polymerase And Implications For The Mechanism Of Cap-Binding Inhibitors. Nucleic Acids Res **46**(2): 956-971.

Pflug, A., Guilligay, D., Reich, S., Cusack, S. (2014). Structure Of Influenza A Polymerase Bound To The Viral RNA Promoter. Nature **516**(7531): 355-360.

Pflug, A., Lukarska, M., Resa-Infante, P., Reich, S., Cusack, S. (2017). Structural Insights Into RNA Synthesis By The Influenza Virus Transcription-Replication Machine. Virus Res **234**: 103-117.

Pinto, R., Herold, S., Cakarova, L., Hoegner, K., Lohmeyer, J., Planz, O., Pleschka, S. (2011). Inhibition Of Influenza Virus-Induced NF-Kappab And Raf/MEK/ERK Activation Can Reduce Both Virus Titers And Cytokine Expression Simultaneously In Vitro And In Vivo. Antiviral Res **92**(1): 45-56.

Pleschka, S. (2013). Overview Of Influenza Viruses. Curr Top Microbiol Immunol **370**: 1-20.

Pleschka, S. (2008). RNA Viruses And The Mitogenic Raf/MEK/ERK Signal Transduction Cascade. Biol Chem **389**(10): 1273-1282.

Pleschka, S., Wolff, T., Ehrhardt, C., Hobom, G., Planz, O., Rapp, U. R., Ludwig, S. (2001). Influenza Virus Propagation Is Impaired By Inhibition Of The Raf/MEK/ERK Signalling Cascade. Nat Cell Biol **3**(3): 301-305.

Plotch, S. J., Bouloy, M., Ulmanen, I., Krug, R. M. (1981). A Unique Cap(M7gpppxm)-Dependent Influenza Virion Endonuclease Cleaves Capped Rnas To Generate The Primers That Initiate Viral RNA Transcription. Cell **23**(3): 847-858.

Price, G. E., Gaszewska-Mastarlarz, A., Moskophidis, D. (2000). The Role Of Alpha/Beta And Gamma Interferons In Development Of Immunity To Influenza A Virus In Mice. J Virol **74**(9): 3996-4003.

Ptacek, J., Devgan, G., Michaud, G., Zhu, H., Zhu, X., Fasolo, J., Guo, H., Jona, G., Breitkreutz, A., Sopko, R., Mccartney, R. R., Schmidt, M. C., Rachidi, N., Lee, S. J., Mah, A. S., Meng, L., Stark, M. J., Stern, D. F., De Virgilio, C., Tyers, M., Andrews, B., Gerstein, M., Schweitzer, B., Predki, P. F., Snyder, M. (2005). Global Analysis Of Protein Phosphorylation In Yeast. Nature **438**(7068): 679-684.

Raggiaschi, R., Gotta, S., Terstappen, G. C. (2005). Phosphoproteome Analysis. Bioscience Reports **25**(1): 33-44.

Ramazi, S., Zahiri, J. (2021). Posttranslational Modifications In Proteins: Resources, Tools And Prediction Methods. Database (Oxford) **2021**.

Robb, N. C., Te Velthuis, A. J. W., Fodor, E., Kapanidis, A. N. (2019). Real-Time Analysis Of Single Influenza Virus Replication Complexes Reveals Large Promoter-Dependent Differences In Initiation Dynamics. Nucleic Acids Res **47**(12): 6466-6477.

Rodriguez-Cupello, C., Dam, M., Serini, L., Wang, S., Lindgren, D., Englund, E., Kjellman, P., Axelson, H., Garcia-Mariscal, A., Madsen, C. D. (2020). The STRIPAK Complex Regulates Response To Chemotherapy Through P21 And P27. Front Cell Dev Biol **8**: 146.

Roskoski, R., Jr. (2004). Src Protein-Tyrosine Kinase Structure And Regulation. Biochem Biophys Res Commun **324**(4): 1155-1164.

Roskoski, R., Jr. (2019). Targeting ERK1/2 Protein-Serine/Threonine Kinases In Human Cancers. Pharmacol Res **142**: 151-168.

Rossman, J. S., Lamb, R. A. (2011). Influenza Virus Assembly And Budding. Virology **411**(2): 229-236.

Rossman, J. S., Leser, G. P., Lamb, R. A. (2012). Filamentous Influenza Virus Enters Cells Via Macropinocytosis. J Virol **86**(20): 10950-10960.

Ruan, T., Sun, J., Liu, W., Prinz, R. A., Peng, D., Liu, X., Xu, X. (2020). H1N1 Influenza Virus Cross-Activates Gli1 To Disrupt The Intercellular Junctions Of Alveolar Epithelial Cells. Cell Rep **31**(13): 107801.

Samji, T. (2009). Influenza A: Understanding The Viral Life Cycle. Yale J Biol Med **82**(4): 153-159.

Sammaibashi, S., Yamayoshi, S., Kawaoka, Y. (2018). Strain-Specific Contribution Of Eukaryotic Elongation Factor 1 Gamma To The Translation Of Influenza A Virus Proteins. Front Microbiol **9**: 1446.

Sarracino, A., Gharu, L., Kula, A., Pasternak, A. O., Avettand-Fenoel, V., Rouzioux, C., Bardina, M., De Wit, S., Benkirane, M., Berkhout, B., Van Lint, C., Marcello, A. (2018). Posttranscriptional Regulation Of HIV-1 Gene Expression During Replication And Reactivation From Latency By Nuclear Matrix Protein MATR3. Mbio **9**(6).

Savage, S. R., Zhang, B. (2020). Using Phosphoproteomics Data To Understand Cellular Signaling: A Comprehensive Guide To Bioinformatics Resources. Clin Proteomics **17**: 27.

Schmidlin, T., Debets, D. O., Van Gelder, C., Stecker, K. E., Rontogianni, S., Van Den Eshof, B. L., Kemper, K., Lips, E. H., Van Den Biggelaar, M., Peeper, D. S., Heck, A. J. R., Altelaar, M. (2019). High-Throughput Assessment Of Kinome-Wide Activation States. Cell Syst **9**(4): 366-374 E365.

Schmitz, M. L., Kracht, M., Saul, V. V. (2014). The Intricate Interplay Between RNA Viruses And NF-Kappab. Biochim Biophys Acta **1843**(11): 2754-2764.

Schrader, T., Dudek, S. E., Schreiber, A., Ehrhardt, C., Planz, O., Ludwig, S. (2018). The Clinically Approved MEK Inhibitor Trametinib Efficiently Blocks Influenza A Virus Propagation And Cytokine Expression. Antiviral Res **157**: 80-92.

Schreiber, A., Boff, L., Anhlan, D., Krischuns, T., Brunotte, L., Schuberth, C., Wedlich-Soldner, R., Drexler, H., Ludwig, S. (2020). Dissecting The Mechanism Of Signaling-Triggered Nuclear Export Of Newly Synthesized Influenza Virus Ribonucleoprotein Complexes. Proc Natl Acad Sci U S A **117**(28): 16557-16566.

Schutkowski, M., Reimer, U., Panse, S., Dong, L., Lizcano, J. M., Alessi, D. R., Schneider-Mergener, J. (2004). High-Content Peptide Microarrays For Deciphering Kinase Specificity And Biology. Angew Chem Int Ed Engl **43**(20): 2671-2674.

Schwill, M., Tamaskovic, R., Gajadhar, A. S., Kast, F., White, F. M., Pluckthun, A. (2019). Systemic Analysis Of Tyrosine Kinase Signaling Reveals A Common Adaptive Response Program In A HER2-Positive Breast Cancer. Sci Signal **12**(565).

Selman, M., Dankar, S. K., Forbes, N. E., Jia, J. J., Brown, E. G. (2012). Adaptive Mutation In Influenza A Virus Non-Structural Gene Is Linked To Host Switching And Induces A Novel Protein By Alternative Splicing. Emerg Microbes Infect **1**(11): E42.

Selzer, L., Su, Z., Pintilie, G. D., Chiu, W., Kirkegaard, K. (2020). Full-Length Three-Dimensional Structure Of The Influenza A Virus M1 Protein And Its Organization Into A Matrix Layer. Plos Biol **18**(9): E3000827.

Sha, B., Luo, M. (1997). Structure Of A Bifunctional Membrane-RNA Binding Protein, Influenza Virus Matrix Protein M1. Nat Struct Biol **4**(3): 239-244.

Sharma, A., Batra, J., Stuchlik, O., Reed, M. S., Pohl, J., Chow, V. T. K., Sambhara, S., Lal, S. K. (2020). Influenza A Virus Nucleoprotein Activates The JNK Stress-Signaling Pathway For Viral Replication By Sequestering Host Filamin A Protein. Front Microbiol **11**: 581867.

Sharma, K., D'Souza, R. C., Tyanova, S., Schaab, C., Wisniewski, J. R., Cox, J., Mann, M. (2014). Ultradeep Human Phosphoproteome Reveals A Distinct Regulatory Nature Of Tyr And Ser/Thr-Based Signaling. Cell Rep **8**(5): 1583-1594.

Shen, Y. F., Chen, Y. H., Chu, S. Y., Lin, M. I., Hsu, H. T., Wu, P. Y., Wu, C. J., Liu, H. W., Lin, F. Y., Lin, G., Hsu, P. H., Yang, A. S., Cheng, Y. S., Wu, Y. T., Wong, C. H., Tsai, M. D. (2011). E339...R416 Salt Bridge Of Nucleoprotein As A Feasible Target For Influenza Virus Inhibitors. Proc Natl Acad Sci U S A **108**(40): 16515-16520.

Shie, J. J., Fang, J. M. (2019). Development Of Effective Anti-Influenza Drugs: Congeners And Conjugates - A Review. J Biomed Sci **26**(1): 84.

Shimizu, T., Takizawa, N., Watanabe, K., Nagata, K., Kobayashi, N. (2011). Crucial Role Of The Influenza Virus NS2 (NEP) C-Terminal Domain In M1 Binding And Nuclear Export Of Vrnp. FEBS Lett **585**(1): 41-46.

Simon, P. F., De La Vega, M. A., Paradis, E., Mendoza, E., Coombs, K. M., Kobasa, D., Beauchemin, C. A. A. (2016). Avian Influenza Viruses That Cause Highly Virulent Infections In Humans Exhibit Distinct Replicative Properties In Contrast To Human H1N1 Viruses. Sci Rep **6**: 24154.

Simpson, C., Yamauchi, Y. (2020). Microtubules In Influenza Virus Entry And Egress. Viruses **12**(1).

Sipeki, S., Koprivanacz, K., Takacs, T., Kurilla, A., Laszlo, L., Vas, V., Buday, L. (2021). Novel Roles Of SH2 And SH3 Domains In Lipid Binding. Cells **10**(5).

Songyang, Z., Blechner, S., Hoagland, N., Hoekstra, M. F., Piwnica-Worms, H., Cantley, L. C. (1994). Use Of An Oriented Peptide Library To Determine The Optimal Substrates Of Protein Kinases. Curr Biol **4**(11): 973-982.

Stauffer, S., Feng, Y., Nebioglu, F., Heilig, R., Picotti, P., Helenius, A. (2014). Stepwise Priming By Acidic Ph And A High K+ Concentration Is Required For Efficient Uncoating Of Influenza A Virus Cores After Penetration. J Virol **88**(22): 13029-13046.

Stevens, J., Blixt, O., Tumpey, T. M., Taubenberger, J. K., Paulson, J. C., Wilson, I. A. (2006). Structure And Receptor Specificity Of The Hemagglutinin From An H5N1 Influenza Virus. Science **312**(5772): 404-410.

Stieneke-Grober, A., Vey, M., Angliker, H., Shaw, E., Thomas, G., Roberts, C., Klenk, H. D., Garten, W. (1992). Influenza Virus Hemagglutinin With Multibasic Cleavage Site Is Activated By Furin, A Subtilisin-Like Endoprotease. EMBO J **11**(7): 2407-2414.

Stohr, K. (2002). Influenza--WHO Cares. Lancet Infect Dis **2**(9): 517.

Stowe, J., Tessier, E., Zhao, H., Guy, R., Muller-Pebody, B., Zambon, M., Andrews, N., Ramsay, M., Lopez Bernal, J. (2021). Interactions Between SARS-Cov-2 And Influenza, And The Impact Of Coinfection On Disease Severity: A Test-Negative Design. Int J Epidemiol **50**(4): 1124-1133.

Su, W. C., Chen, Y. C., Tseng, C. H., Hsu, P. W., Tung, K. F., Jeng, K. S., Lai, M. M. (2013). Pooled Rnai Screen Identifies Ubiquitin Ligase Itch As Crucial For Influenza A Virus Release From The Endosome During Virus Entry. Proc Natl Acad Sci U S A **110**(43): 17516-17521.

Subbarao, E. K., London, W., Murphy, B. R. (1993). A Single Amino Acid In The PB2 Gene Of Influenza A Virus Is A Determinant Of Host Range. J Virol **67**(4): 1761-1764.

Sugiyama, K., Obayashi, E., Kawaguchi, A., Suzuki, Y., Tame, J. R., Nagata, K., Park, S. Y. (2009). Structural Insight Into The Essential PB1-PB2 Subunit Contact Of The Influenza Virus RNA Polymerase. EMBO J **28**(12): 1803-1811.

Sugiyama, N. (2020). Mass Spectrometry-Based Discovery Of In Vitro Kinome Substrates. Mass Spectrom (Tokyo) **9**(1): A0082.

Sugiyama, N., Imamura, H., Ishihama, Y. (2019). Large-Scale Discovery Of Substrates Of The Human Kinome. Sci Rep **9**(1): 10503.

Szklarczyk, D., Gable, A. L., Lyon, D., Junge, A., Wyder, S., Huerta-Cepas, J., Simonovic, M., Doncheva, N. T., Morris, J. H., Bork, P., Jensen, L. J., Mering, C. V. (2019). STRING V11: Protein-Protein Association Networks With Increased Coverage, Supporting Functional Discovery In Genome-Wide Experimental Datasets. Nucleic Acids Res **47**(D1): D607-D613.

Takeda, M., Leser, G. P., Russell, C. J., Lamb, R. A. (2003). Influenza Virus Hemagglutinin Concentrates In Lipid Raft Microdomains For Efficient Viral Fusion. Proc Natl Acad Sci U S A **100**(25): 14610-14617.

Takeuchi, K., Lamb, R. A. (1994). Influenza Virus M2 Protein Ion Channel Activity Stabilizes The Native Form Of Fowl Plague Virus Hemagglutinin During Intracellular Transport. J Virol **68**(2): 911-919.

Tang, Y., Fang, G., Guo, F., Zhang, H., Chen, X., An, L., Chen, M., Zhou, L., Wang, W., Ye, T., Zhou, L., Nie, P., Yu, H., Lin, M., Zhao, Y., Lin, X., Yuan, Z., Jiao, S., Zhou, Z. (2020). Selective Inhibition Of STRN3-Containing PP2A Phosphatase Restores Hippo Tumor-Suppressor Activity In Gastric Cancer. Cancer Cell **38**(1): 115-128 E119.

Tang, Y. S., Xu, S., Chen, Y. W., Wang, J. H., Shaw, P. C. (2021). Crystal Structures Of Influenza Nucleoprotein Complexed With Nucleic Acid Provide Insights Into The Mechanism Of RNA Interaction. Nucleic Acids Res **49**(7): 4144-4154.

Tanti, G. K., Goswami, S. K. (2014). SG2NA Recruits DJ-1 And Akt Into The Mitochondria And Membrane To Protect Cells From Oxidative Damage. Free Radic Biol Med **75**: 1-13.

Tarus, B., Bertrand, H., Zedda, G., Di Primo, C., Quideau, S., Slama-Schwok, A. (2015). Structure-Based Design Of Novel Naproxen Derivatives Targeting Monomeric Nucleoprotein Of Influenza A Virus. J Biomol Struct Dyn **33**(9): 1899-1912.

Taubenberger, J. K., Kash, J. C. (2010). Influenza Virus Evolution, Host Adaptation, And Pandemic Formation. Cell Host Microbe **7**(6): 440-451.

Taubenberger, J. K., Reid, A. H., Lourens, R. M., Wang, R., Jin, G., Fanning, T. G. (2005). Characterization Of The 1918 Influenza Virus Polymerase Genes. Nature **437**(7060): 889-893.

Taylor, S. S., Kornev, A. P. (2011). Protein Kinases: Evolution Of Dynamic Regulatory Proteins. Trends Biochem Sci **36**(2): 65-77.

Taylor, S. S., Radzio-Andzelm, E., Hunter, T. (1995). How Do Protein Kinases Discriminate Between Serine/Threonine And Tyrosine? Structural Insights From The Insulin Receptor Protein-Tyrosine Kinase. FASEB J **9**(13): 1255-1266.

Te Velthuis, A. J., Fodor, E. (2016). Influenza Virus RNA Polymerase: Insights Into The Mechanisms Of Viral RNA Synthesis. Nat Rev Microbiol **14**(8): 479-493.

Thapa, R. J., Ingram, J. P., Ragan, K. B., Nogusa, S., Boyd, D. F., Benitez, A. A., Sridharan, H., Kosoff, R., Shubina, M., Landsteiner, V. J., Andrake, M., Vogel, P., Sigal, L. J., Tenoever, B. R., Thomas, P. G., Upton, J. W., Balachandran, S. (2016). DAI Senses Influenza A Virus Genomic RNA And Activates RIPK3-Dependent Cell Death. Cell Host Microbe **20**(5): 674-681.

Tong, S., Zhu, X., Li, Y., Shi, M., Zhang, J., Bourgeois, M., Yang, H., Chen, X., Recuenco, S., Gomez, J., Chen, L. M., Johnson, A., Tao, Y., Dreyfus, C., Yu, W., Mcbride, R., Carney, P. J., Gilbert, A. T., Chang, J., Guo, Z., Davis, C. T., Paulson, J. C., Stevens, J., Rupprecht, C. E., Holmes, E. C., Wilson, I. A., Donis, R. O. (2013). New World Bats Harbor Diverse Influenza A Viruses. Plos Pathog **9**(10): E1003657.

Tsukamoto, K., Ashizawa, H., Nakanishi, K., Kaji, N., Suzuki, K., Okamatsu, M., Yamaguchi, S., Mase, M. (2008). Subtyping Of Avian Influenza Viruses H1 To H15 On The Basis Of Hemagglutinin Genes By PCR Assay And Molecular Determination Of Pathogenic Potential. J Clin Microbiol **46**(9): 3048-3055.

Turrell, L., Hutchinson, E. C., Vreede, F. T., Fodor, E. (2015). Regulation Of Influenza A Virus Nucleoprotein Oligomerization By Phosphorylation. J Virol **89**(2): 1452-1455.

Ubersax, J. A., Ferrell, J. E., Jr. (2007). Mechanisms Of Specificity In Protein Phosphorylation. Nat Rev Mol Cell Biol **8**(7): 530-541.

Uhlendorff, J., Matrosovich, T., Klenk, H. D., Matrosovich, M. (2009). Functional Significance Of The Hemadsorption Activity Of Influenza Virus Neuraminidase And Its Alteration In Pandemic Viruses. Arch Virol **154**(6): 945-957.

Vreede, F. T., Jung, T. E., Brownlee, G. G. (2004). Model Suggesting That Replication Of Influenza Virus Is Regulated By Stabilization Of Replicative Intermediates. J Virol **78**(17): 9568-9572.

Walker, A. P., Fodor, E. (2019). Interplay Between Influenza Virus And The Host RNA Polymerase II Transcriptional Machinery. Trends Microbiol **27**(5): 398-407.

Walker, A. P., Sharps, J., Fodor, E. (2020). Mutation Of An Influenza Virus Polymerase 3' RNA Promoter Binding Site Inhibits Transcription Elongation. J Virol **94**(13).

Walther, T., Karamanska, R., Chan, R. W., Chan, M. C., Jia, N., Air, G., Hopton, C., Wong, M. P., Dell, A., Malik Peiris, J. S., Haslam, S. M., Nicholls, J. M. (2013). Glycomic Analysis Of Human Respiratory Tract Tissues And Correlation With Influenza Virus Infection. Plos Pathog **9**(3): E1003223.

Wandzik, J. M., Kouba, T., Cusack, S. (2021). Structure And Function Of Influenza Polymerase. Cold Spring Harb Perspect Med **11**(9).

Wandzik, J. M., Kouba, T., Karuppasamy, M., Pflug, A., Drncova, P., Provaznik, J., Azevedo, N., Cusack, S. (2020). A Structure-Based Model For The Complete Transcription Cycle Of Influenza Polymerase. Cell **181**(4): 877-893 E821.

Wang, J., Sun, J., Hu, J., Wang, C., Prinz, R. A., Peng, D., Liu, X., Xu, X. (2020). A77 1726, The Active Metabolite Of The Anti-Rheumatoid Arthritis Drug Leflunomide, Inhibits Influenza A Virus Replication In Vitro And In Vivo By Inhibiting The Activity Of Janus Kinases. FASEB J **34**(8): 10132-10145.

Wang, J., Zheng, X., Peng, Q., Zhang, X., Qin, Z. (2020). Eph Receptors: The Bridge Linking Host And Virus. Cell Mol Life Sci **77**(12): 2355-2365.

Wang, Q., Li, Q., Liu, T., Chang, G., Sun, Z., Gao, Z., Wang, F., Zhou, H., Liu, R., Zheng, M., Cui, H., Chen, G., Li, H., Yuan, X., Wen, J., Peng, D., Zhao, G. (2018). Host Interaction Analysis Of PA-N155 And PA-N182 In Chicken Cells Reveals An Essential Role Of UBA52 For Replication Of H5N1 Avian Influenza Virus. Front Microbiol **9**: 936.

Wang, S., Zhao, Z., Bi, Y., Sun, L., Liu, X., Liu, W. (2013). Tyrosine 132 Phosphorylation Of Influenza A Virus M1 Protein Is Crucial For Virus Replication By Controlling The Nuclear Import Of M1. J Virol **87**(11): 6182-6191.

Wang, Z., Yang, H., Chen, Y., Tao, S., Liu, L., Kong, H., Ma, S., Meng, F., Suzuki, Y., Qiao, C., Chen, H. (2017). A Single-Amino-Acid Substitution At Position 225 In Hemagglutinin Alters The Transmissibility Of Eurasian Avian-Like H1N1 Swine Influenza Virus In Guinea Pigs. J Virol **91**(21).

Watanabe, K., Shimizu, T., Noda, S., Tsukahara, F., Maru, Y., Kobayashi, N. (2014). Nuclear Export Of The Influenza Virus Ribonucleoprotein Complex: Interaction Of Hsc70 With Viral Proteins M1 And NS2. FEBS Open Bio **4**: 683-688.

Watanabe, T., Kawakami, E., Shoemaker, J. E., Lopes, T. J., Matsuoka, Y., Tomita, Y., Kozuka-Hata, H., Gorai, T., Kuwahara, T., Takeda, E., Nagata, A., Takano, R., Kiso, M., Yamashita, M., Sakai-Tagawa, Y., Katsura, H., Nonaka, N., Fujii, H., Fujii, K., Sugita, Y., Noda, T., Goto, H., Fukuyama, S., Watanabe, S., Neumann, G., Oyama, M., Kitano, H., Kawaoka, Y. (2014). Influenza Virus-Host Interactome

Screen As A Platform For Antiviral Drug Development. Cell Host Microbe **16**(6): 795-805.

Waters, K., Gao, C., Ykema, M., Han, L., Voth, L., Tao, Y. J., Wan, X. F. (2021). Triple Reassortment Increases Compatibility Among Viral Ribonucleoprotein Genes Of Contemporary Avian And Human Influenza A Viruses. Plos Pathog **17**(10): E1009962.

Weber, A., Dam, S., Saul, V. V., Kuznetsova, I., Muller, C., Fritz-Wolf, K., Becker, K., Linne, U., Gu, H., Stokes, M. P., Pleschka, S., Kracht, M., Schmitz, M. L. (2019). Phosphoproteome Analysis Of Cells Infected With Adapted And Nonadapted Influenza A Virus Reveals Novel Pro- And Antiviral Signaling Networks. J Virol **93**(13).

Weinheimer, V. K., Becher, A., Tonnies, M., Holland, G., Knepper, J., Bauer, T. T., Schneider, P., Neudecker, J., Ruckert, J. C., Szymanski, K., Temmesfeld-Wollbrueck, B., Gruber, A. D., Bannert, N., Suttorp, N., Hippenstiel, S., Wolff, T., Hocke, A. C. (2012). Influenza A Viruses Target Type II Pneumocytes In The Human Lung. J Infect Dis **206**(11): 1685-1694.

Weiss, A., Neubauer, M. C., Yerabolu, D., Kojonazarov, B., Schlueter, B. C., Neubert, L., Jonigk, D., Baal, N., Ruppert, C., Dorfmuller, P., Pullamsetti, S. S., Weissmann, N., Ghofrani, H. A., Grimminger, F., Seeger, W., Schermuly, R. T. (2019). Targeting Cyclin-Dependent Kinases For The Treatment Of Pulmonary Arterial Hypertension. Nat Commun **10**(1): 2204.

Willemsen, J., Wicht, O., Wolanski, J. C., Baur, N., Bastian, S., Haas, D. A., Matula, P., Knapp, B., Meyniel-Schicklin, L., Wang, C., Bartenschlager, R., Lohmann, V., Rohr, K., Erfle, H., Kaderali, L., Marcotrigiano, J., Pichlmair, A., Binder, M. (2017). Phosphorylation-Dependent Feedback Inhibition Of RIG-I By DAPK1 Identified By Kinome-Wide Sirna Screening. Mol Cell **65**(3): 403-415 E408.

Wilson, C., Agafonov, R. V., Hoemberger, M., Kutter, S., Zorba, A., Halpin, J., Buosi, V., Otten, R., Waterman, D., Theobald, D. L., Kern, D. (2015). Kinase Dynamics. Using Ancient Protein Kinases To Unravel A Modern Cancer Drug's Mechanism. Science **347**(6224): 882-886.

Wilson, L. J., Linley, A., Hammond, D. E., Hood, F. E., Coulson, J. M., Macewan, D. J., Ross, S. J., Slupsky, J. R., Smith, P. D., Eyers, P. A., Prior, I. A. (2018). New Perspectives, Opportunities, And Challenges In Exploring The Human Protein Kinome. Cancer Res **78**(1): 15-29.

Wise, H. M., Foeglein, A., Sun, J., Dalton, R. M., Patel, S., Howard, W., Anderson, E. C., Barclay, W. S., Digard, P. (2009). A Complicated Message: Identification Of A Novel PB1-Related Protein Translated From Influenza A Virus Segment 2 Mrna. J Virol **83**(16): 8021-8031.

Wise, H. M., Hutchinson, E. C., Jagger, B. W., Stuart, A. D., Kang, Z. H., Robb, N., Schwartzman, L. M., Kash, J. C., Fodor, E., Firth, A. E., Gog, J. R., Taubenberger, J. K., Digard, P. (2012). Identification Of A Novel Splice Variant Form Of The Influenza A Virus M2 Ion Channel With An Antigenically Distinct Ectodomain. Plos Pathog **8**(11): E1002998.

Wong, M., Hyodo, T., Asano, E., Funasaka, K., Miyahara, R., Hirooka, Y., Goto, H., Hamaguchi, M., Senga, T. (2014). Silencing Of STRN4 Suppresses The Malignant Characteristics Of Cancer Cells. Cancer Sci **105**(12): 1526-1532.

Wong, S. W., Bergquam, E. P., Swanson, R. M., Lee, F. W., Shiigi, S. M., Avery, N. A., Fanton, J. W., Axthelm, M. K. (1999). Induction Of B Cell Hyperplasia In Simian Immunodeficiency Virus-Infected Rhesus Macaques With The Simian Homologue Of Kaposi's Sarcoma-Associated Herpesvirus. J Exp Med **190**(6): 827-840.

Wu, J., Ma, Q. N., Lam, K. S. (1994). Identifying Substrate Motifs Of Protein Kinases By A Random Library Approach. Biochemistry **33**(49): 14825-14833.

Xiao, C. Y., Hubner, S., Elliot, R. M., Caon, A., Jans, D. A. (1996). A Consensus Camp-Dependent Protein Kinase (PK-A) Site In Place Of The Ccn Motif Casein Kinase

II Site Simian Virus 40 Large T-Antigen Confers PK-A-Mediated Regulation Of Nuclear Import. J Biol Chem **271**(11): 6451-6457.

Xu, W., Chen, M., Ge, N., Xu, J. (2012). Hemagglutinin From The H5N1 Virus Activates Janus Kinase 3 To Dysregulate Innate Immunity. Plos One **7**(2): E31721.

Xue, L., Tao, W. A. (2013). Current Technologies To Identify Protein Kinase Substrates In High Throughput. Front Biol (Beijing) **8**(2): 216-227.

Yanguez, E., Hunziker, A., Dobay, M. P., Yildiz, S., Schading, S., Elshina, E., Karakus, U., Gehrig, P., Grossmann, J., Dijkman, R., Schmolke, M., Stertz, S. (2018). Phosphoproteomic-Based Kinase Profiling Early In Influenza Virus Infection Identifies GRK2 As Antiviral Drug Target. Nat Commun **9**(1): 3679.

Ye, Q., Krug, R. M., Tao, Y. J. (2006). The Mechanism By Which Influenza A Virus Nucleoprotein Forms Oligomers And Binds RNA. Nature **444**(7122): 1078-1082.

Ye, Z., Liu, T., Offringa, D. P., Mcinnis, J., Levandowski, R. A. (1999). Association Of Influenza Virus Matrix Protein With Ribonucleoproteins. J Virol **73**(9): 7467-7473.

Ye, Z., Robinson, D., Wagner, R. R. (1995). Nucleus-Targeting Domain Of The Matrix Protein (M1) Of Influenza Virus. J Virol **69**(3): 1964-1970.

Yu, M., Liu, X., Cao, S., Zhao, Z., Zhang, K., Xie, Q., Chen, C., Gao, S., Bi, Y., Sun, L., Ye, X., Gao, G. F., Liu, W. (2012). Identification And Characterization Of Three Novel Nuclear Export Signals In The Influenza A Virus Nucleoprotein. J Virol **86**(9): 4970-4980.

Yue, H., Zhang, M., Xing, L., Wang, K., Rao, X., Liu, H., Tian, J., Zhou, P., Deng, Y., Shang, J. (2020). The Epidemiology And Clinical Characteristics Of Co-Infection Of SARS-Cov-2 And Influenza Viruses In Patients During COVID-19 Outbreak. J Med Virol **92**(11): 2870-2873.

Zagorac, I., Fernandez-Gaitero, S., Penning, R., Post, H., Bueno, M. J., Mouron, S., Manso, L., Morente, M. M., Alonso, S., Serra, V., Munoz, J., Gomez-Lopez, G., Lopez-Acosta, J. F., Jimenez-Renard, V., Gris-Oliver, A., Al-Shahrour, F., Pineiro-Yanez, E., Montoya-Suarez, J. L., Apala, J. V., Moreno-Torres, A., Colomer, R., Dopazo, A., Heck, A. J. R., Altelaar, M., Quintela-Fandino, M. (2018). In Vivo Phosphoproteomics Reveals Kinase Activity Profiles That Predict Treatment Outcome In Triple-Negative Breast Cancer. Nat Commun **9**(1): 3501.

Zhang, J., Ma, K., Li, B., Chen, Y., Qiu, Z., Xing, J., Huang, J., Hu, C., Huang, Y., Li, H., Liu, D., Liao, M., Qi, W. (2021). A Risk Marker Of Tribasic Hemagglutinin Cleavage Site In Influenza A (H9N2) Virus. Commun Biol **4**(1): 71.

Zhao, Y., Adjei, A. A. (2014). The Clinical Development Of MEK Inhibitors. Nat Rev Clin Oncol **11**(7): 385-400.

Zheng, W., Cai, X., Li, S., Li, Z. (2018). Autophosphorylation Mechanism Of The Ser/Thr Kinase Stk1 From Staphylococcus Aureus. Front Microbiol **9**: 758.

Zheng, W., Cao, S., Chen, C., Li, J., Zhang, S., Jiang, J., Niu, Y., Fan, W., Li, Y., Bi, Y., Gao, G. F., Sun, L., Liu, W. (2017). Threonine 80 Phosphorylation Of Non-Structural Protein 1 Regulates The Replication Of Influenza A Virus By Reducing The Binding Affinity With RIG-I. Cell Microbiol **19**(2).

Zheng, W., Fan, W., Zhang, S., Jiao, P., Shang, Y., Cui, L., Mahesutihan, M., Li, J., Wang, D., Gao, G. F., Sun, L., Liu, W. (2019). Naproxen Exhibits Broad Anti-Influenza Virus Activity In Mice By Impeding Viral Nucleoprotein Nuclear Export. Cell Rep **27**(6): 1875-1885 E1875.

Zheng, W., Li, J., Wang, S., Cao, S., Jiang, J., Chen, C., Ding, C., Qin, C., Ye, X., Gao, G. F., Liu, W. (2015). Phosphorylation Controls The Nuclear-Cytoplasmic Shuttling Of Influenza A Virus Nucleoprotein. J Virol **89**(11): 5822-5834.

Zhu, G., Liu, Y., Shaw, S. (2005). Protein Kinase Specificity. A Strategic Collaboration Between Kinase Peptide Specificity And Substrate Recruitment. Cell Cycle **4**(1): 52-56.

Zolotukhin, A. S., Michalowski, D., Bear, J., Smulevitch, S. V., Traish, A. M., Peng, R., Patton, J., Shatsky, I. N., Felber, B. K. (2003). PSF Acts Through The Human

Immunodeficiency Virus Type 1 Mrna Instability Elements To Regulate Virus Expression. Mol Cell Biol **23**(18): 6618-6630.

11 LIST OF PUBLICATIONS:

A. Publications that have evolved from this dissertation

1. *****Liu, L., *****Weiß, A., Saul, VV., Schermuly, RT., Pleschka, S., & SCHMITZ, ML. (2022). Comparative kinase activity profiling of pathogenic influenza A viruses reveals new anti- and pro-viral protein kinases. J Gen Virol. 2022 Jun;103(6). doi: 10.1099/jgv.0.001762.. * **Co-first author**

In revision

2. Liu, L., Weber, A., Linne, U., Pleschka, S., Kracht M., & SCHMITZ, ML. (2022). Phosphorylation of influenza matrix protein 1 at T108 controls its multimerization state and functional association with the STRIPAK complex. MBio, in revision.

In review

3. Liu, L., Madhugiri, R., Saul, VV., Pleschka, S., & SCHMITZ, ML. (2022). RNA-binding of the influenza virus polymerase subunit PA is inhibited by Y393 phosphorylation. J. Virol, in review.

B. Oral and poster presentations at scientific meetings

1. Liu. L., Weiß, A., Saul, V V., Schermuly, R T., Schmitz, M. L. and Pleschka S. Comparative kinase activity profiling of pathogenic influenza A viruses reveals new anti- and pro-viral protein kinases, Poster presentation at 31st Annual Meeting of the Society for Virology, Germany, 30 March – 2 April 2022
2. Liu, L., Weber, A., Linne, U., Kuznetsova, I., Shehata, M., Kracht, M., Schmitz, M. L. and Pleschka S. Functional impact of a specific M1 protein phosphorylation site on IAVpropagation; Poster presentation at 30st Annual Meeting of the Society for Virology, Germany, 24 March – 26 March 2021
   and 7th International Influenza Meeting 2020, 28-29 September, Münster, Germany.

During PhD studies

1. Luo, T., Liu, L., Shen, X., Irwin, DM., Liao, M., Shen, Y. The evolutionary dynamics of H1N1/pdm2009 in India. Infect Genet Evol. 2018 Nov; 65:276-282.
2. Guo, F., Li, Y., Yu, S., Liu, L., Luo, T., Pu, Z., Xiang, D., Shen, X., Irwin, DM., Liao, M., Shen, Y. Adaptive Evolution of Human-Isolated H5Nx Avian Influenza A Viruses. Front Microbiol. 2019 Jun 12; 10:1328.

12 EHRENWÖRTLICHE ERKLÄRUNG

„Hiermit erkläre ich, dass ich die vorliegende Arbeit selbständig und ohne unzulässige Hilfe oder Benutzung anderer als der angegebenen Hilfsmittel angefertigt habe. Alle Textstellen, die wörtlich oder sinngemäß aus veröffentlichten oder nichtveröffentlichten Schriften entnommen sind, und alle Angaben, die auf mündlichen Auskünften beruhen, sind als solche kenntlich gemacht. Bei den von mir durchgeführten und in der Dissertation erwähnten Untersuchungen habe ich die Grundsätze guter wissenschaftlicher Praxis, wie sie in der „Satzung der Justus-Liebig-Universität Gießen zur Sicherung guter wissenschaftlicher Praxis“ niedergelegt sind, eingehalten sowie ethische, datenschutzrechtliche und tierschutzrechtliche Grundsätze befolgt. Ich versichere, dass Dritte von mir weder unmittelbar noch mittelbar geldwerte Leistungen für Arbeiten erhalten haben, die im Zusammenhang mit dem Inhalt der vorgelegten Dissertation stehen, und dass die vorgelegte Arbeit weder im Inland noch im Ausland in gleicher oder ähnlicher Form einer anderen Prüfungsbehörde zum Zweck einer Promotion oder eines anderen Prüfungsverfahrens vorgelegt wurde. Alles aus anderen Quellen und von anderen Personen übernommene Material, das in der Arbeit verwendet wurde oder auf das direkt Bezug genommen wird, wurde als solches kenntlich gemacht. Insbesondere wurden alle Personen genannt, die direkt und indirekt an der Entstehung der vorliegenden Arbeit beteiligt waren. Mit der Überprüfung meiner Arbeit durch eine Plagiatserkennungssoftware bzw. ein internetbasiertes Softwareprogramm erkläre ich mich einverstanden.“

Gießen, 26. April 2022

Ort/Datum	Unterschrift

13 ACKNOWLEDGEMENTS

There are so many people who have helped me throughout my PhD journey.
I would like to thank my supervisor, Prof. Dr. M. Lienhard Schmitz, for accepting me into his working group and the opportunity to work on this project. I first arrived in the group as an amateur researcher in evolutionary virology, he then took me to the wonderful world of protein phosphorylation and biochemistry, since then has supported me throughout my studies for scientific guidance and many constructive discussions on the way to the publications. He appreciates me on my every little progress/achievement, and many "down" times were there encouraging and motivating me. Working under his supervision I have grown a lot as a scientist and as a person, and I deeply appreciate all this.
I also would like to thank my supervisor Prof. Dr. Stephan Pleschka. I am so grateful to have both supervisors, and he was also so supportive to constantly provide suggestions, discussions, and finalize my thesis. So much of what I learned under his tutelage has proven incredibly valuable for my knowledge in virology.
I would like to thank also the talented peers of the AG Schmitz and AG Pleschka past and present: Markus Seibert, Shashi Chillappagari, Vera Saul, Ratnal Belapurkar, Ines Höfliger, Yvonne Horn, Markus Schwinn, Ahmed Mostafa, Jan Dreute, Maximilian Pfisterer, Mahmoud Shehata, Irina Kuznetsova, Christin Müller, Maja Treusch, Olesja Ritter and Tabea Riedlinger who helped me in work, gave good advises and shared 'tips and tricks' throughout these years. Special gratitude also to Ramakanth Madhugiri and Ganesh Bylapudi for their help during my work at the institute of medical virology. I thank Alexander Perniß and Wei Peng from Institute for Anatomy and Cell Biology, JLU, for the help with the confocal microscope. Going for a PhD is by no means an easy endeavor, but I count myself incredibly fortunate to have studied in the company of such excellent peers.
I would also like to thank all collaboration partners who contributed to my work. There are many others including my friends who have enriched my time at JLU. You are too many to name in person but I would like to thank you all.
Finally, I owe a debt of gratitude to my family and most of all to my parents and my sister. Thank you, my boyfriend, for the bioinformatic support, and for the help with the translation in German language. Thank you for always being here as my emotional outlet giving me endless trust. This thesis is dedicated to them.

CURRICULUM VITAE

Der Lebenslauf wurde aus der elektronischen Version der Arbeit entfernt.

The curriculum vitae was removed from the electronic version of the paper.